THE ROTATION OF PORPHYROBLASTS AND EXTENDED BELEMNITES DURING TECTONIC STRAIN

A thesis submitted for the degree of Ph.D. of the

UNIVERSITY OF LONDON

BY

KHANDEKER MOSHARRAF HOSSAIN

December 1973

Department of Geology,

Imperial College,

London S.W.7.

ABSTRACT

The work presented in the thesis is a study (theoretical, experimental and field) of the geometrical properties of rotated porphyroblasts (Part I) and extended belemnites (Part II) during tectonic strain. The theoretical study is undertaken with the assumption that rock, under certain conditions, behaves as a viscous fluid.

The theory of the motion of rigid particles immersed in a viscous matrix is extended and used to analyse the behaviour of rigid porphyroblasts and the surrounding matrix. The results of experiments simulating the motion of rigid inclusions are in good agreement with those predicted from the theory. The history of rigid rotation and deformation of the inclusions is complex and depends on the type of deformation (irrotational strain or simple shear), shape, axial ratio and initial orientation of the included object.

The second part of the thesis is a theoretical and experimental study of the geometrical properties of the extended belemnites. The theoretical analysis uses the theory of motion of rigid inclusions and assumes that a belemnite before deformation can be considered as an elliptical inclusion (in 2D) set in a viscous matrix. There is a discrepancy between the theoretical and experimental results. Natural examples of extended belemnites from Leytron, Valais, Switzerland are also studied to verify the geological implications of the theoretical and experimental analyses. The study shows that the amount of strain calculated from extended belemnites is considerably less than the actual strain suffered by the surrounding matrix.

The formation of structural patterns around rigid inclusions during deformation is discussed. The stress patterns around a rigid circular inclusion are derived theoretically and their influence in the formation of 'pressure shadows' and 'pressure fringes' examined.

"Dedicated to the martyrs of the
Liberation War of my homeland
whose sacrifice made Bangladesh a
political and geographical reality."

ACKNOWLEDGEMENTS

I would like to thank Professor J. G. Ramsay for suggesting this topic of research and for his helpful supervision. Help from my colleagues has been invaluable and I would particularly like to thank Dr. N. J. Price, Mr. R. J. Lisle, Dr. P. R. Cobbold and Mr. Sugata Sengupta. I am grateful to Dr. J. W. Cosgrove who has taken a pain-staking job to read and criticise the thesis which has been very helpful in improving the manuscript.

Help from the technical staff of the Royal School of Mines particularly Mr. J. Gee & Mrs. Helen Richardson for help with the photography and Mr. Denman and his staff for building one of the strain boxes, is gratefully acknowledged.

During the course of this work the Liberation War of Bangladesh broke out. I would like to extend sincere thanks to Prof. J. G. Ramsay, Dr. N.J. Price and all my colleagues for their understanding and encouragement during this emotional stress. But for their constant help it would not have been possible to complete this work.

The research was carried out as a part of a post-graduate study under the technical assistance programme of the Colombo-plan scholarship which is gratefully acknowledged.

Finally, I am grateful to my wife, Bilquis for her patience and helpful presence during my stay in England.

LIST OF CONTENTS

Page

PART II

Page

CHAPTER 1. INTRODUCTION

1.1 GENERAL STATEMENT

The motion of a particle immersed in a viscous fluid has been studied in the field of suspensions and emulsions since 1911, when Einstein published a mathematical solution for the motion of a spherical particle suspended in a viscous fluid. A small particle included in a deforming fluid may be transported or rotated due to the force exerted on it by the motion of the fluid. Rocks under certain conditions behave as viscous fluids. There is a considerable field evidence to show that rocks can undergo large-scale flow during tectonic strain or seidmentary processes. Inclusions embedded in rocks, under such deformation, may behave in a similar way to particles suspended in a viscous fluid.

Inclusions of known original shape (e.g. pebbles, porphyroblasts and fossils) that undergo rotation and distortion during the deformation of the surrounding rock provide useful data for the determination of the strain history of the adjacent rocks. There are many factors (e.g. initial orientation, axial ratio of the object and the viscosity contrast between the object and matrix) controlling the motion of an inclusion and each factor contributes to the modification of strain in the surrounding rock. Unless there is no competency contrast between the matrix and the inclusion, the inclusion always behaves in a different manner to the surrounding matrix during deformation. One of the objectives of this thesis is to examine how far the behaviour of inclusions complies with that of the matrix.

The deformation history of an inclusion and its matrix can not generally be determined from the final position of an inclusion. A careful model simulation of inclusions in a viscous matrix and a study of progressive development of different structures around inclusions gives an insight into the deformation history. Inclusions of various shapes are commonly observed in nature. Another objective of this work is to explain the geometric arrangements of the rotated inclusions with respect to the features (stretching lineation) in the matrix and to determine influence of the shapes of inclusions on their motion.

After deformation a considerable amount of inhomogeneous strain exists in the matrix around an inclusion. This work attempts to explain the development of these regions of inhomogeneous strain and to account for the structures (e.g. pressure shadows and pressure fringes) that develop within them.

When an inclusion that is able to extend (either by being non-rigid or having planes of weakness cutting across it, e.g. belemnite) is situated in a deforming viscous matrix, it suffers both rotation and extension if it lies within the extension field of the strain ellipse. Deformed belemnites, for example, are found in the nature as fragmented rigid bodies which have been stretched and generally rotated by the force exerted on them by the surrounding matrix. Many geologists have measured the extension of belemnite specimens in an attempt to determine the amount of elongation that has been suffered by the surrounding rock. The second part of the thesis is devoted to the investigation (theoretically and experimentally) of whether the amount of elongation obtained from the measurements of extended belemnites represent the true elongation suffered by the rock matrix.

The result obtained from the model simulation of any structure can be very valuable and often can be utilized directly in the interpretation of field data. The study of field examples of extended belemnites from Leytron, Valais, Switzerland described in chapter 9, is an attempt to apply the techniques and interpretations developed during experimentations.

The thesis is divided into three parts : Part I (chapter 2 to 6) is a study of the behaviour of rotated porphyroblasts and associated structures, and Part II (chapter 7 to 9) is a study of the behaviour of extended belemnites. Part III (chapter 10) is the summary and conclusions of the results obtained from Parts I and II.

In chapter 2 (Part I), a review of published works on the nomenclature, description and interpretation of rotated structures in and around porphyroblasts has been undertaken. The confusion that has arisen due to casual nomenclature that has been used to describe some of the rotated structures is discussed and the terms have been defined strictly in accordance with Spry (1969). The inhomogeneities in the matrix around an inclusion give rise to the formation of two structures, namely "pressure fringes" and "pressure shadows". The mechanism of formation of these two structures has been verified theoretically and experimentally. Chapter 3 deals with the theoretical analysis of the behaviour of rigid porphyroblasts set in a matrix undergoing deformation by either irrotational strain or simple shear. The basic derivations have been taken from Jeffery (1922) and Gay (1966, 1968) and are extended in the present work.

A lozenge-shaped irrotational strain box and a simple shear box have been used to simulate the behaviour of rigid porphyroblasts and belemnites set in a deforming viscous matrix. Wooden strips and rods were used to simulate rigid inclusions (porphyroblasts and belemnites) and linseed oil putty to simulate the rock matrix.

Gay's (1966) method for calculating the amount of shear strain (γ_s) from the geometry of the simple shear box has been criticised and a new technique for determining γ_s from the change in apical angle during deformation, has been developed.

Thirty-nine runs of experiments set in the two strain boxes have been performed to investigate the motion of rigid objects set in a deforming viscous matrix. The experiments were performed in order to determine the effect of the initial orientation, the axial ratio of the object and the type of deformation (irrotational strain or simple shear) on the motion of the object. A quantitative analysis of the experimental results has been made and these results compared with the results predicted from the theory. The behaviour of the matrix material around different porphyroblasts has been studied experimentally by determining the 'strain pattern' and 'flow lines' in the matrix.

Part II of the thesis consists of the results derived from the theoretical, experimental and field analysis of stretched belemnites. The results obtained from 29 experimental runs have been compared with those derived from the theory. A marked disagreement is found between the experimental and theoretical results. An attempt is made to explain this disagreement.

Hundred and ninety-six (196) specimens of stretched belemnites have been measured from the field. The results obtained from these measurements have been interpreted applying techniques developed from the experimental and theoretical study of extended belemnites.

All the results derived from the theory, calculated from the experimental simulations and measured from field observations have been recorded in tables and are presented in the Appendices. A few examples of experiments simulating the progressive development of rotated porphyroblasts and extended belemnites are also illustrated in plates I to XXXII at the back of the thesis.

1.2 LIST OF SYMBOLS

α	Initial apical angle of the strain boxes.
α_1	Apical angle of the strain boxes after deformation.
β_1	Complimentary apical angle of the strain boxes after deformation.
β	Angle of deflection of a line from any position.
γ_s	Amount of simple shear.
$\dot{\gamma}_s$	Rate of simple shear.
ε	Eccentricity of an ellipse; $\varepsilon^2 = \frac{a^2 - b^2}{a^2}$
λ'	Reciprocal quadratic elongation.
λ'_1, λ'_2	Reciprocal principal quadratic elongation.
$\sqrt{\lambda_1}, \sqrt{\lambda_2}$	Major and minor semi-axes of the strain ellipse. Also used to denote the principal strains.
$\sqrt{\lambda_1/\lambda_2}$	Axial ratio of the strain ellipse; strain ratio.
ν	Poisson's ratio of the matrix outside a rigid inclusion.
ν_i	Poisson's ratio of the material inside an inclusion.
κ	$3 - 4\nu$
$\sigma_r, \sigma_\theta, \tau_{r\theta}$	Resolved stresses with respect to polar co-ordinates r, θ.
σ_1, σ_3	Principal stresses.
θ', ϕ', ψ'	Euler's angles.
ψ	Angle of shear.
ϕ_i, ϕ_f	Initial and final orientation of an elliptical object measured with reference to the normal to the principal extension direction.
θ_{ie}, θ_{fe}	Initial and final orientation of an elliptical object with reference to the principal extension direction.

θ_{is}, θ_{fs} Initial and final orientation of an elliptical object with reference to the shearing direction.

θ_b Initial orientation of a belemnite specimen.

θ'_b Final orientation of a belemnite specimen.

θ_f Initial orientation of a fragment containing in a belemnite specimen.

θ'_f Final orientation of a fragment containing in a belemnite specimen.

τ Shear stress.

τ_{max} Maximum shear stress.

ω Angular velocity.

Ω Orientation of the greatest principal stress.

Φ Angle between the fracture plane and the maximum principal stress.

φ_i Angle of internal friction.

$\emptyset(z)$ A stress function.

$\emptyset'(z)$ A stress function subjected to differentiation.

$\emptyset''(z)$ A stress function subjected to two times differentiation.

$(1 + e_1)$ same as $\sqrt{\lambda}_1$.

$(1 + e_2)$ same as $\sqrt{\lambda}_2$.

a,b,c Lengths of the semi-axes of an ellipsoid. Also lengths of axes of a belemnite specimen.

a/b Axial ratio of an elliptical object. Also axial ratio of a belemnite body.

$\underline{a},\underline{b},\underline{c},\underline{g},\underline{h},\underline{f}$ and η, ϑ, ξ Components of distortion and rotation of a fluid.

A,B,C Real constants for the material outside an inclusion.

A_i, B_i, C_i Real constants for the material inside an inclusion.

e	Extension
G	Modulus of rigidity of the material outside an inclusion.
G_i	Modulus of rigidity of the material inside an inclusion.
ln.	Natural logarithm.
K	G_i/G
$l_1, l_2, l_3, m_1, m_2, m_3, n_1, n_2, n_3$	Direction cosines between two sets of co-ordinate axes.
l	Original length of a belemnite specimen.
l_o	Length of an individual fragment of a belemnite.
l_1	Extended length of a belemnite specimen.
M	Moment of couple.
M_f	Moment of frictional couple.
N	Normal stress.
P_1	Applied stress along OY direction.
P_2	Applied stress along OX direction.
R	Radius of a circular inclusion. Also used to represent strain ratio.
r, θ	Polar co-ordinates.
S_i	Inclusion trail inside a porphyroblast.
S_e	Inclusion trail outside a porphyroblast.
T	Tangential stress.
u,v,w	Components of fluid velocity parallel to the x,y,z axes. Also used to denote displacement components.
u',v',w'	Components of fluid velocity parallel to the x',y',z' axes. Also displacement components of deformation.
W_1, W_2, W_3	Rates of rotations of ellipsoid about its own x,y,z axes.
x,y,z	Co-ordinate axes fixed parallel to the particle semi-axes a.b.c. Also represent co-ordinates of any point.
x',y',z'	Co-ordinate axes for strain or flow. Also to represent co-ordinates of any point after deformation.

x_o, y_o Initial lengths of the diagonals of the lozenge-shaped strain box.

x_1, y_1 Lengths of the diagonals of the lozenge-shaped box after deformation.

PART I

PART - I

CHAPTER 2. ROTATED STRUCTURES IN AND AROUND PORPHYROBLASTS

2.1 INTRODUCTION

Relatively rigid inclusions showing different amounts of deformation and rotation (real or apparent) from that of their matrix are commonly observed in metamorphic rocks. Concretions, pebbles, boudins, fossils and porphyroblast of any mineral included in the rock matrix are termed here rigid inclusions. The present study is involved mainly with an investigation of the geometric forms of rotated structures in and around pre-tectonic porphyroblasts.

Porphyroblasts which have undergone a differential rotation to that of their matrix as a result of deformation will be termed 'Rotated porphyroblasts'. These rotated porphyroblasts leave behind some geometrical evidence from which the behaviour of the included porphyroblast and surrounding matrix can be determined. This evidence is preserved in such features as rotational-, snowball and helicitic structures many of which have been described by previous workers (Flett, 1912; Niggli, 1912; Kreig, 1918; Schmidt, 1918; Baily, 1923; Becke, 1924; Mugge, 1930; Harker, 1939; Turner, 1948; Collette, 1959; Zwart, 1960, 1962,; Peacey, 1961; Howkins, 1961; Spry, 1963, 1969; Johnson, 1963; Chadwick, 1965; Powell, 1966; Powell and Treagus, 1967, 1970; Cox, 1969; Wilson, 1971). The differentiation of various types of rotated porphyroblasts has largely been obtained by studying S-inclusion patterns. This S-plane is a non-genetic nomenclature referring to any surface (bedding, foliation and etc.). When the surface is present inside porphyroblast it is termed S_i and when situated outside it is known S_e. The structural forms known as snowball- and helicitic structure occur in syntectonic and post-tectonic porphyroblasts respectively. Because of the occasional geometrical similarity of the forms of the internal marker lines of S_i in these rotational-, snowball- and helicitic structures, some confusion in nomenclature has arisen in the past. Spry (1969) clarified the situation and suggested ways by which they might be unambiguously distinguished.

As this thesis is mainly concerned with rotation of pre-tectonic porphyroblasts, the structures associated with the syntectonic and post-tectonic porphyroblasts will not be considered in any detail. A study of previous works shows that the terms rotational-, snowball- and helicitic structure have been used interchangeably by some previous workers without reference to the genesis of the structure. To avoid all such confusion, the more generalised term 'rotated structures' will be used throughout this thesis for defining the structures developed by the rotation of pre-tectonic porphyroblasts. The structures known as 'pressure shadows' and 'pressure fringes' found in the matrix around the pre-tectonic porphyroblasts can also be used to analyse the deformation history of the rocks.

2.2 DESCRIPTIONS OF ROTATED STRUCTURES

An investigation of the morphology of the inclusion trails inside (S_i) and outside (S_e) porphyroblasts has enabled the history of deformation of the enclosing rock to be determined. The amount of total differential rotation of the porphyroblasts can easily be obtained by measuring $S_i \wedge S_e$. Previous evaluations of this angle shows a considerable range from 50°-60° (Zwart, 1960); 120° (Spry, 1963); 130° (Rast, 1958); 173° (Schmidt, 1918) and 540° (Flett, 1912). Some of these results may be over-estimates as the $S_i \wedge S_e$ was not necessarily measured from a thin section cut perpendicular to the axis of rotation. However, accurate measurements of the angle between S_i and S_e can be derived by using the method proposed by Powell and Treagus (1967, 1970). It is observed from a study by Powell and Treagus (1970) that the serial sections of a garnet porphyroblast from Norwegian schists exhibit a gradual change of inclusion trails (Fig. 2.1). Many authors have measured the total amount of differential rotation from the inner and outer S-trails of the crystal which led to the obvious misleading interpretation. Powell and Treagus (1967) suggested that the rotation axis of a crystal in thin section may be located by reference to the sections with inclusion trails of straight, ()) −,)(− and () patterns (Fig. 2.2). Having located the rotation axis, the amount of differential rotation that has been suffered by the crystal can be obtained from the section perpendicular to the axis of rotation.

Another aspect of the rotational effects is often seen in the geometric form of S_e in the matrix material around the porphyroblasts. Structures known as 'pressure shadows' and 'pressure fringes' are often developed in the zones of low strain around pre-tectonic rigid or semi-rigid porphyroblasts.

2.2.1 Rotated structures in and around pre-tectonic porphyroblasts

The inclusion trails (S_i) inside pre-tectonic porphyroblasts are straight whereas those outside (S_e) the object are curved. Occasionally crystals grow with complete assimilation of all pre-existing material and show no traces of internal trails. The curved S_e generally show a morphology termed "wrapping around" the inclusion (Figs.2.3 ; 2.4,a,b; 2.5).

The relationship of S_i and S_e is comparatively simple when porphyroblasts are completely rigid. Geometrical complications arise

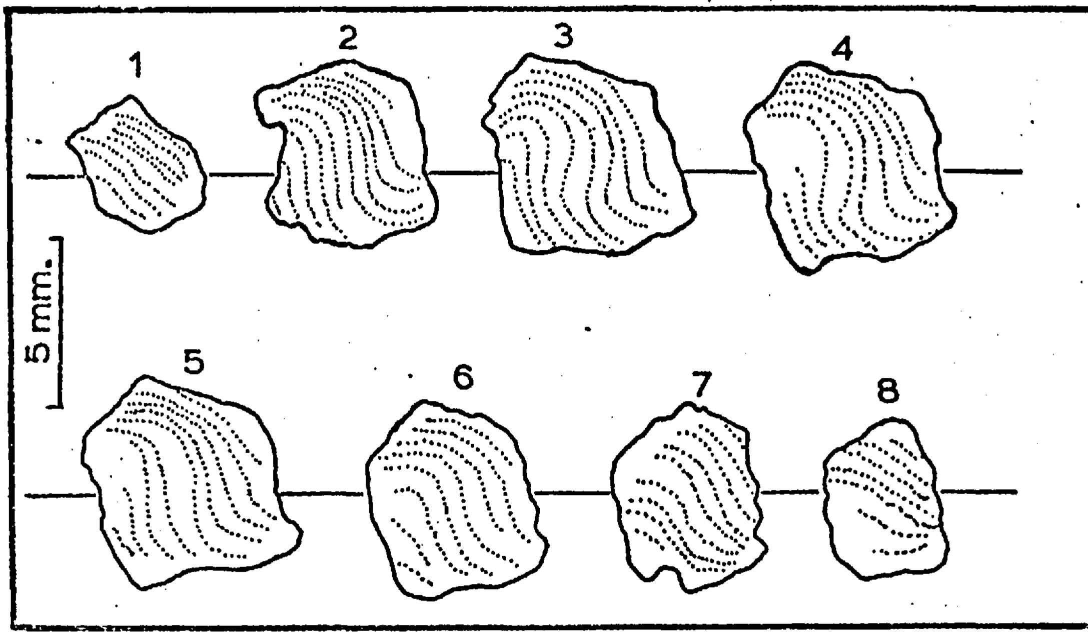

Fig. 2.1 Serial sections of a garnet from Norwegian schists showing the change of shape of inclusion trails through the same crystal. (After Powell and Treagus, 1970).

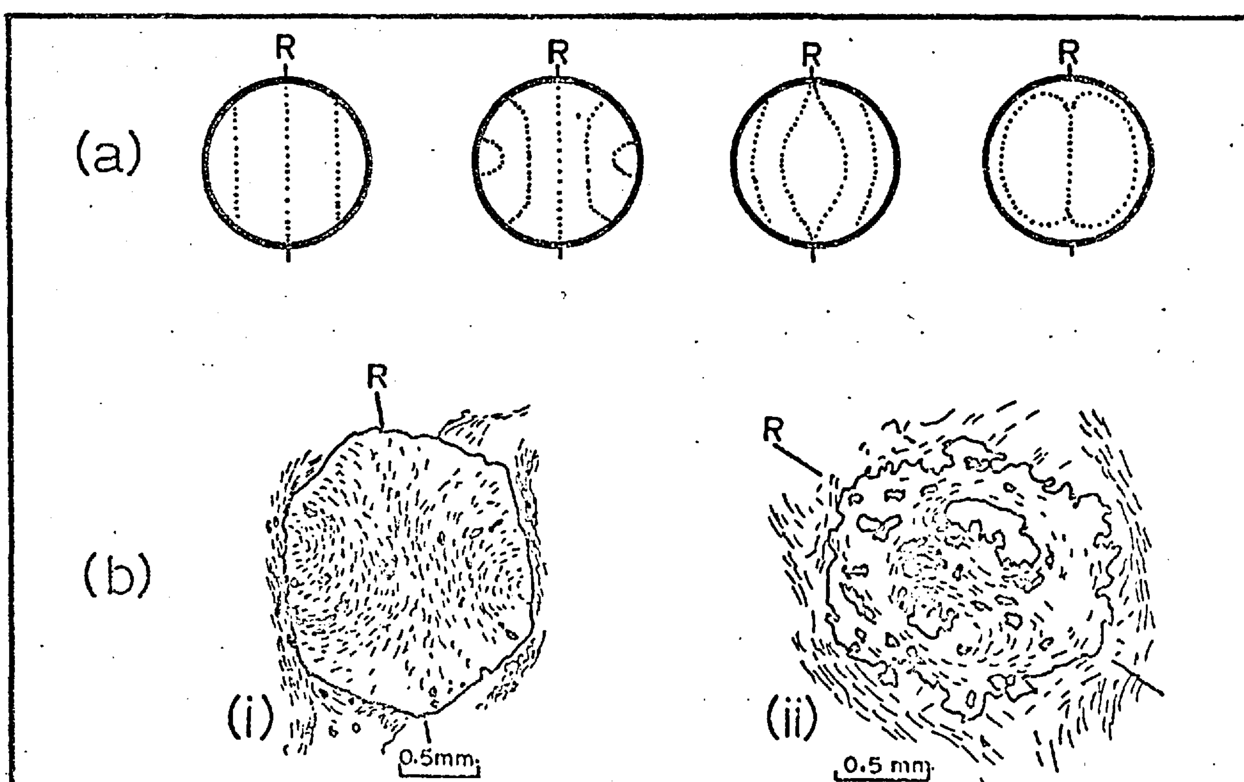

Fig. 2.2 (a) Inclusion patterns by which the axis of rotation (R) can be located in a thin section.

(b) Natural examples of inclusion patterns from which the axis of rotation can be determined. (i) Thin section of a garnet from the Dalradian of Glen Shee showing)(pattern (after Powell and Treagus, 1970). (ii) Drawn from a thin section from Cox (1969) showing the OD pattern of inclusion.

where the object or porphyroblast is ductile or semi-ductile. Objects such as this suffer simultaneous deformation and rotation during tectonic strain. The final orientation of S_i inside such object represent a combination of the body rotation and the internal deformation of the porphyroblast due to its shape change. If the initial and final orientation of these porphyroblasts are known, it may be possible to compute the amount of strain and body rotation.

2.2.2 Rotated structures in and around syn-tectonic and post-tectonic porphyroblasts

The rotated structures preserved in syn-tectonic porphyroblasts referred to as 'rotational-', 'snowball-' and helicitic structures have long been known in the literature. Spry (1969) has defined these terms so that they are no longer interchangeable (Fig. 2.4).

Certain crystals which are rotated by tectonic strain at the same time as they grow give rise to the formation of rotational- and snowball structures. These two structures are syn-tectonic and are differentiated by the amount of rotation that has taken place during deformation. When the apparent angle of rotation is less than 90° the structure is generally called as rotational structure (Fig. 2.4,a) and if it is greater than 90° it is called snowball structure (Fig. 2.4,b). The growth of post-tectonic crystals in a schistosity that already contain deflection (e.g. microfolds) may results in the formation of 'helicitic structures' (Fig. 2.4,c). These structures may resemble rotational structures but do not represent syntectonic growth of the crystal.

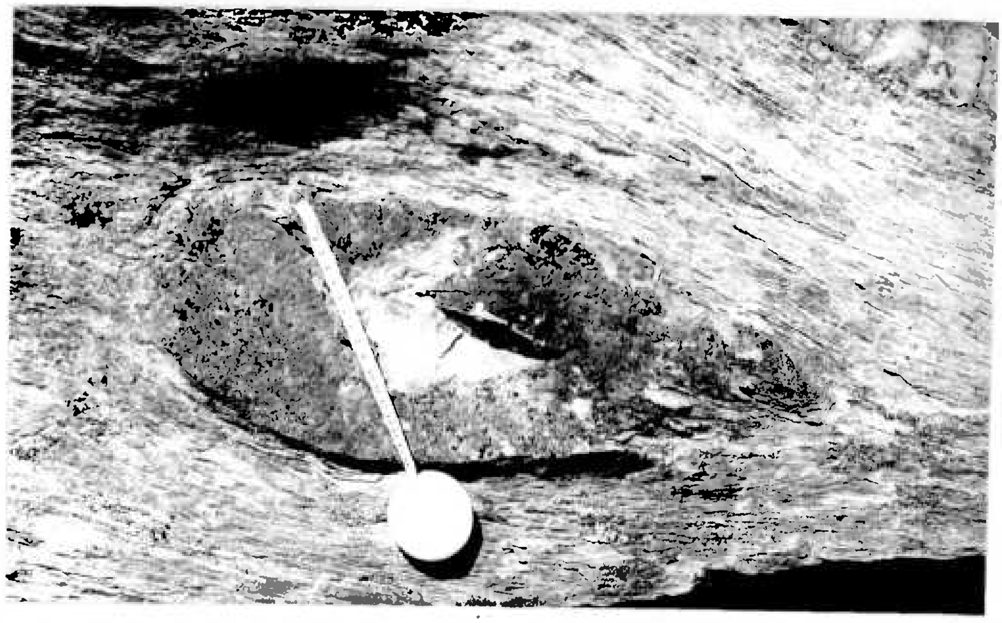

Fig. 2.3 "Wrapping around" schistosity shown by slates around a large inclusion (Concretion), Leytron, Valais, Switzerland.

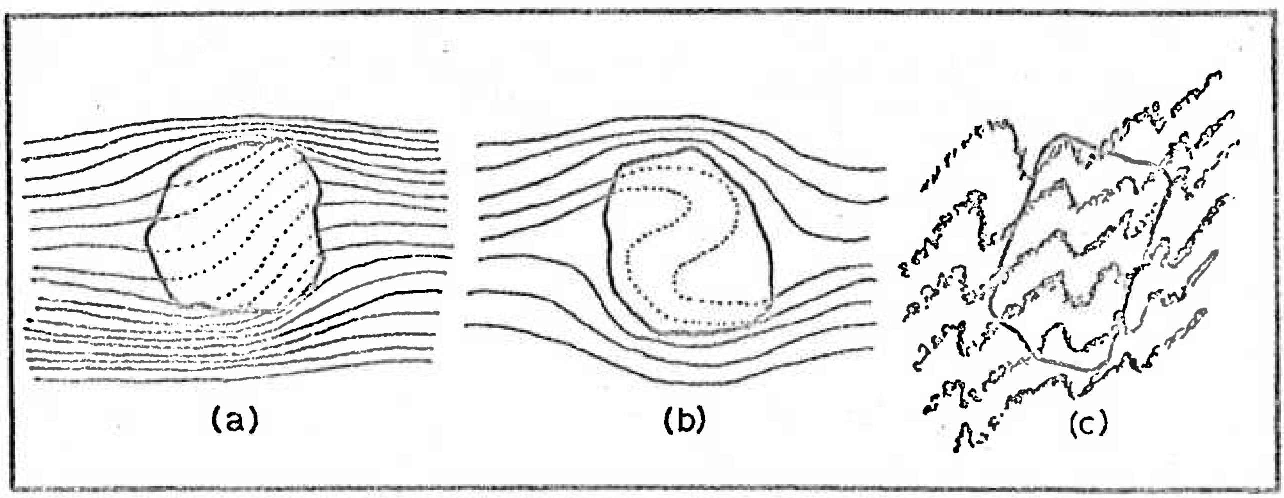

Fig. 2.4 Models describing the distinction between rotational-, snowball- and helicitic structures. (a) Rotational- (b) Snowball- and (c) helicitic structures (after Spry, 1969).

2.3 DEVELOPMENT OF SHADOWS AND FRINGES AROUND PORPHYROBLASTS

Any rigid or semi-rigid porphyroblast embedded in a rock matrix undergoing deformation, sets up stress and strain variations around itself, and these set up a variety of different textures in its immediate environment. The local deformation is marked by inhomogeneities referred to as 'pressure shadows', 'pressure fringes', 'halos de etirement' and 'streckungshofe' etc. (Knopf, 1929; Pabst, 1931; Bain, 1933; Miles, 1945; Fairbairn, 1950; Frankel, 1957; Ramsay, 1967; Joplin, 1968; and Spry, 1969). Most of these terms have never been strictly defined and they have generally been used interchangeably. Bain (1933) and Spry (1969) have suggested refinements of these terms which enable the terms to be employed more exactly.

The term 'pressure shadows' was originally used by Harker (1889) to describe the formation of fibrous quartz concentrations in eye-like sections around pyrite. Moss (1927) described a similar sort of structure as 'streckungshofe'. The elongated and wedge-shaped quartz, calcite or chlorite associated with the pyrite porphyroblasts were also termed 'pressure shadows' by Pabst (1931). Frankel (1957) described muscovite flakes around pyrite porphyroblasts as pressure shadows referring to the general terminology of Harker (1889) and Pabst (1931). Bain (1933) was the first to describe the appearance of these areas comprised of chlorite flakes around pyrite crystals as 'pressure fringes'. Spry (1969) supported the term proposed by Bain (1933) to describe the new mineral formation around such crystals and further suggested that the term 'pressure shadows' should be used for relatively undisturbed areas around rigid porphyroblasts.

2.3.1 Pressure shadows

A pressure shadow is that region of the rock matrix adjacent to a relatively rigid object which is protected from deformation by the presence of the object (Spry, 1969). Such pressure shadows develop around many types of relatively resistant objects such as fossils, worm-tubes, pebbles and large rigid crystals (porphyroblasts).

From field and experimental observations, it is seen that any initial planar structure becomes curved around a rigid object (Figs. 2.5 and 2.6). The relatively low strain regions around a rigid inclusion have an approximately ellipsoidal form, and are here strictly described as 'pressure shadows'. The shapes of the shadow regions do not always conform to that of the porphyroblasts. The elliptical zones often contain coarse, granular and un-oriented quartz in contrast to the other quartz in the matrix which has elongated, fine grained and oriented crystals.

Pressure shadows and pressure fringes both develop in the low strain areas around a porphyroblast. The pressure shadow areas are characterised by the influx of material (often quartz or calcite) into the low strain area, the new mineral often show no crystallographic orientation and develop within the matrix material.

2.3.2 Pressure fringes

Pressure fringe is a term used to describe the texture arising from the growth of new minerals adjacent to a rigid porphyroblast as a result of the pulling away of the material from the porphyroblast contact (Fig. 2.7). The shape of the area of new crystalline material in the pressure fringe is dependent on the type of deformation and the shape of the included object (Fig. 2.7, a and b). The minerals inside fringes are often fibrous in habit with their long axis parallel

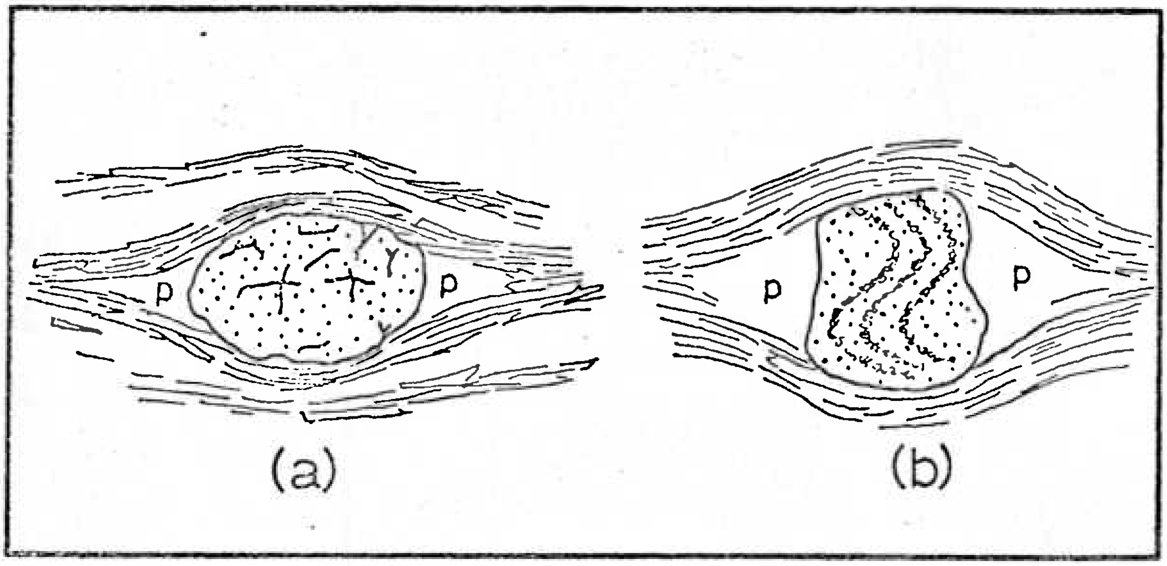

Fig. 2.5 Development of pressure shadow regions (P) around a rigid or semi-rigid inclusions. (a) Shadow regions around an elliptical inclusion (2D). (b) Shadow regions around a rectangular (approxly.) shaped inclusion. Both the illustrations are drawn from Spry (1969).

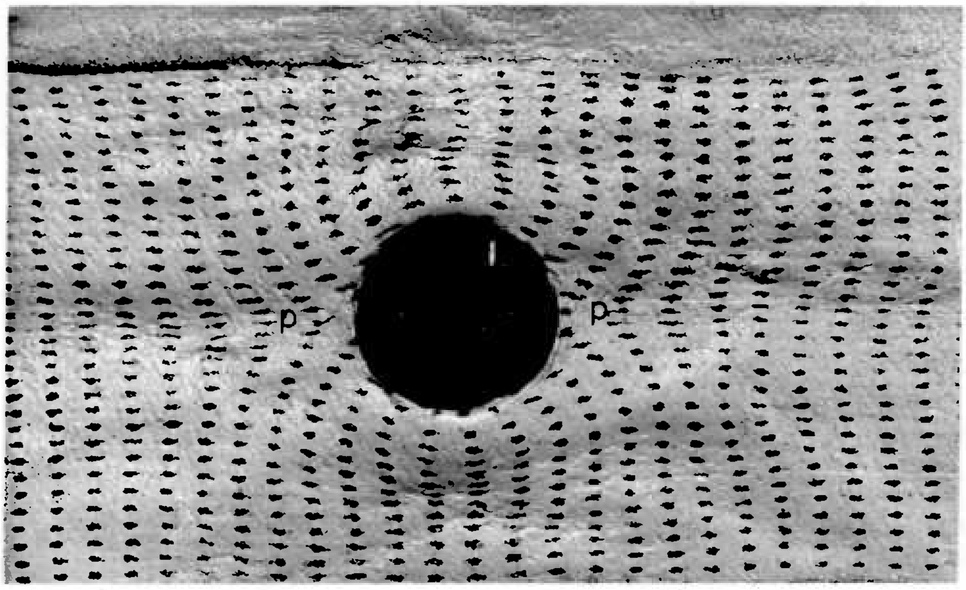

Fig. 2.6 Experimental simulation of pressure shadow regions (P) around a rigid equidimensional (circular) inclusion.

to the maximum principal extension direction. The fibres may be straight, curved or even irregular according to the complexity of the deformation history during their growth (Durney, 1972). The minerals most commonly found in pressure fringes are fibrous quartz, calcite, chlorite and muscovite.

Pressure fringes are commonly observed around pretectonic porphyroblasts. When rocks with included objects are subject to deformation, the porphyroblast-matrix interface often appear to become detached and the disconnected surfaces are pulled apart in a direction parallel to the principal extension direction. Crystallisation of new minerals takes place in the interspace between the object and matrix. The crystals of pressure fringe minerals grow as the deformation continues and the amount of separation of the initial surfaces increases. These crystals grown in the fringe zone are therefore syn-tectonic.

The elliptical cross-section shape of pressure fringes is sometimes similar to that of pressure shadow zones. Pressure fringes can, however, be distinguished from pressure shadows on account of oriented mineral growth completely distinct from those textures seen in the matrix away from the pressure fringe area.

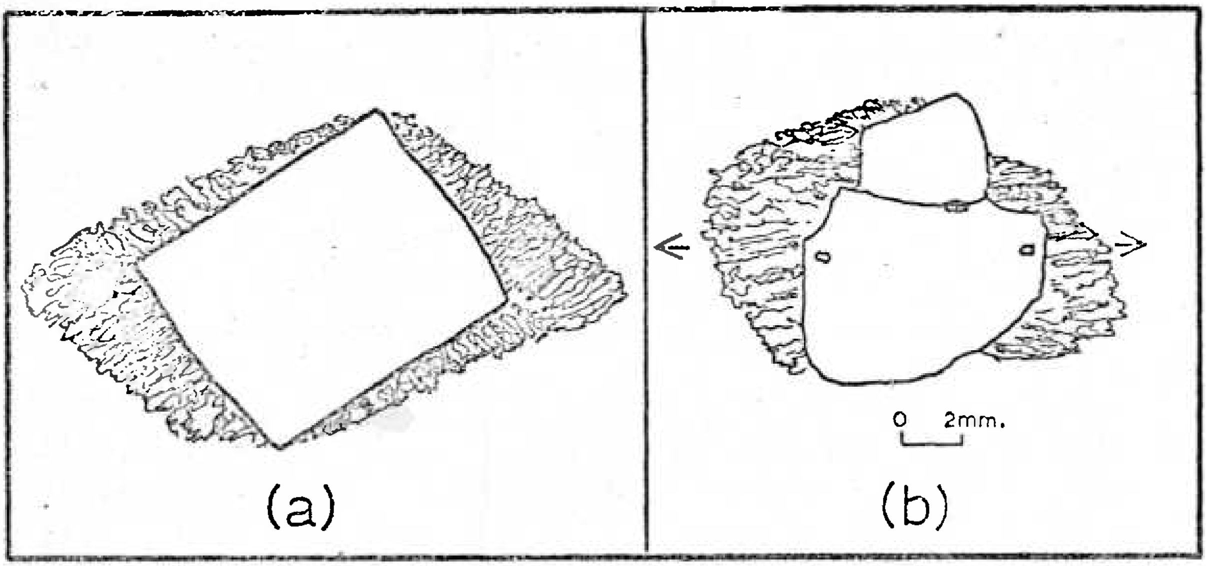

Fig. 2.7 Natural examples of pressure fringe regions around rectangular (a) and semi-circular inclusions (b). (a) Quartz filled pressure fringe regions around pyrite cube, Rio Tinto, Spain (Drawn from Ramsay, 1967, fig. 4-40). (b) Quartz filled pressure fringe regions around a semi-circular pyrite crystal. City Deep Mine, Witwatersrand (Drawn from a photomicrograph, Frankel, 1957, fig. 7).

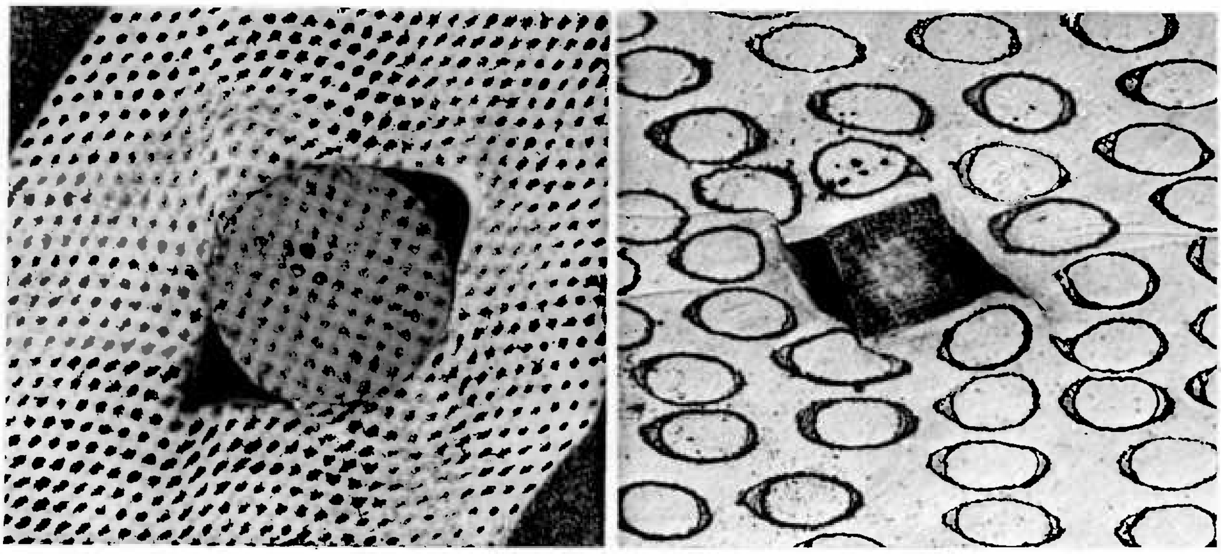

(a) (b)

Fig. 2.8 Experimental production of 'open spaces' simulating pressure fringe regions.

(a) Around a rigid circular inclusion undergoing simple shear deformation.

(b) Around a rigid rectangular inclusion undergoing irrotational deformation.

CHAPTER 3. THEORIES OF THE MECHANISMS OF RIGID PORPHYROBLAST ROTATION

3.1 INTRODUCTION

This chapter deals with the mathematical theories of rotation of pre-tectonic rigid porphyroblasts in materials undergoing deformation by progressive pure shear and progressive simple shear. The accuracy of the original equations deduced by Einstein (1896) and Jeffery (1922) which have later been discussed by Gay (1966, 1968) will be reviewed. The equation for the motion of rigid objects embedded in a fluid undergoing simple shear deformation proposed by Gay, does not take into account the initial orientation of the object. This equation is discussed and a more complete expression is obtained.

Since the end of the last century, many research workers in the field of physical sciences have shown concern regarding the properties of fluid in which small particles are suspended. It is observed that during deformation the presence of any particle in a viscous matrix influences the behaviour of adjacent material. Einstein (1896) investigated the properties of a spherical particle immersed in viscous fluid and determined the mathematical expressions describing the rotational properties of the particle. This work was extended by Jeffery (1922) to cover the behaviour of ellipsoidal particles included in viscous matrix. This latter contribution is clearly a more general analysis than that of Einstein. Subsequent work (Taylor, 1932, 1934; Trevelyan and Mason, 1951; Bartok and Mason, 1958, 1959; Ramscheidt and Mason, 1961) has extended and experimentally verified the predictions of Einstein and Jeffery.

Gay (1966, 1968) discussed the theory of the motion of rigid particles by extending the methods of previous work by Jeffery (1922) and Taylor (1932, 1934) on the properties of suspensions and emulsions.

The results obtained by Jeffery were applicable to deformation by simple shear. Gay (1966, 1968) extended the analysis to derive the mathematical solution for deformation by pure shear. The analysis of the behaviour of a particle immersed in viscous fluid is applicable to that of porphyroblasts included in a ductile host rock if it is assumed that the rock behaves as a highly viscous fluid.

Chapter 5 describes experiments performed to test the behaviour of rigid pre-tectonic porphyroblasts included in a ductile matrix. In order to draw much benefit from these experimental results, it is useful to discuss the predictions of these theories and so a review of the theories proposed by Jeffery (1922) and Gay (1966, 1968) with some modifications and extension will now be given.

3.2 BASIC ASSUMPTIONS AND EQUATIONS

As previously stated, it is assumed that rocks, under certain condition, behave like highly viscous fluid with a small Reynold's number and deform by laminar flow. It is also assumed that in the experiments, the matrix in which the rigid objects are included behaved as a linear viscous fluid and that no slip or separation takes place at the porphyroblast-matrix interface.

The basic equations describing the deformation by fluid flow and particle motion are obtained by using Gay's method. The systems of co-ordinate axes are illustrated in figure 3.1,a. The relationships can be obtained by following the system of direction cosines,

$$\begin{aligned} x &= l_1x' + m_1y' + n_1z' \\ y &= l_2x' + m_2y' + n_2z' \\ z &= l_3x' + m_3y' + n_3z' \end{aligned} \tag{3.1}$$

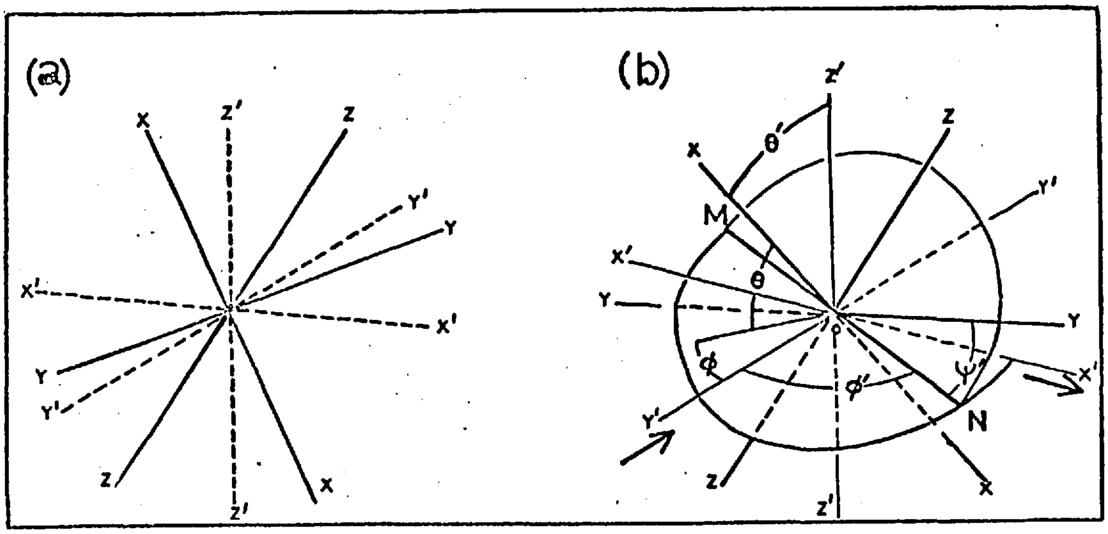

Fig. 3.1 (a) System of co-ordinate axes.

x,y,z - axes parallel to the semi-axes of the elliptical object.

x',y',z' - Axes for the undisturbed motion of the fluid.

(b) System of Euler's angles θ', ϕ', ψ' used to fix the position of the axes of an ellipsoid of revolution during simple shear (after Gay, 1968).

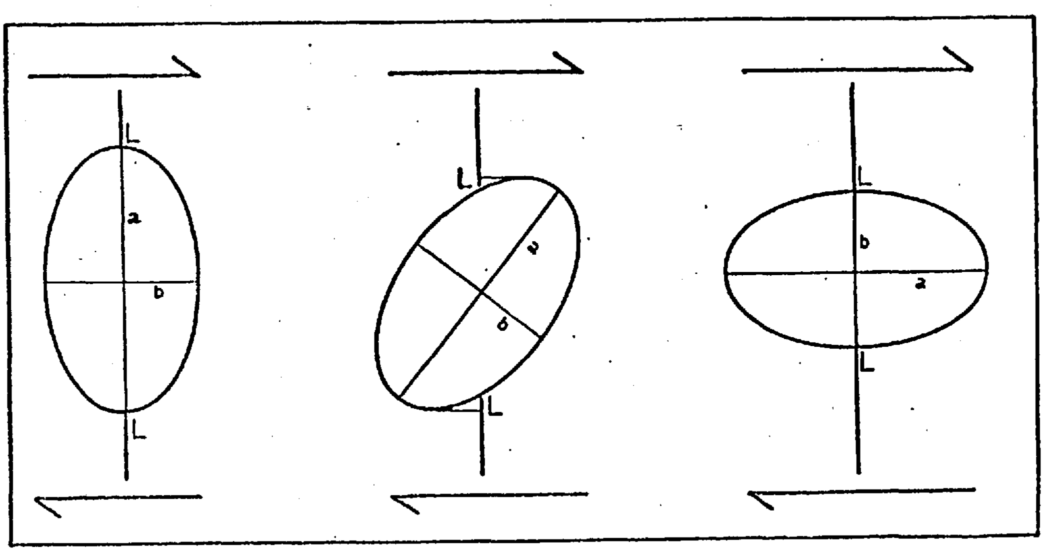

Fig. 3.2 Change in the arm of the couple length of an elliptical particle set in a matrix during simple shear deformation.

By referring figure 3.1,b, it can be seen that the direction cosines can be expressed as

$$
\begin{aligned}
l_1 &= -\sin\theta'.\cos\phi' \\
l_2 &= \cos\psi'.\sin\phi' - \cos\theta'.\sin\psi'.\cos\phi' \\
l_3 &= -\sin\psi'.\sin\phi' + \cos\theta'.\cos\psi'.\cos\phi' \\
m_1 &= \sin\theta'.\sin\phi' \\
m_2 &= \cos\psi'.\cos\phi' - \cos\theta'.\sin\psi'.\sin\phi' \\
m_3 &= -\sin\psi'.\cos\phi' - \cos\theta'.\cos\psi'.\sin\phi' \\
n_1 &= \cos\theta' \\
n_2 &= \sin\theta'.\sin\psi'. \\
n_3 &= \sin\theta'.\cos\psi'
\end{aligned}
\qquad (3.2)
$$

The components of velocity for each point are

$$
\begin{aligned}
u' &= dx'/dt \\
v' &= dy'/dt \\
w' &= dz'/dt
\end{aligned}
\qquad (3.3)
$$

in the x, y and z directions respectively.

These velocity components for pure shear deformation are described as

$$
\begin{aligned}
u' &= cx' \\
v' &= -cy' \\
w' &= 0
\end{aligned}
\qquad (3.4)
$$

where c is a constant.

And those for simple shear deformation are

$$
\begin{aligned}
u' &= \dot{\gamma}_s y' \\
v' &= 0 \\
w' &= 0
\end{aligned}
\qquad (3.5)
$$

3.3 THE ROTATION OF RIGID PORPHYROBLASTS IN A MATRIX UNDERGOING PURE SHEAR

Gay (1966, 1968) used the original equations of motion of rigid particle presented by Jeffery (1922) to describe the behaviour of rigid inclusion set in a viscous matrix. The expressions describing the motion of fluid around the particle simulating a porphyroblast are

$$\begin{aligned} u &= \underline{a}x + \underline{h}y + \underline{g}z + \eta z - \vartheta y \\ v &= \underline{h}x + \underline{b}y + \underline{f}z + \vartheta x - \xi z \qquad (3.6) \\ w &= \underline{g}x + \underline{f}y + \underline{c}z + \xi y - \eta x \qquad \text{(Jeffery, 1922, eq. 2)} \end{aligned}$$

where $u = dx/dt$, $v = dy/dt$, $w = dz/dt$, are the undisturbed velocity compoenets for each point in the fluid parallel to x, y, z axes and $\underline{a}$, $\underline{b}$, $\underline{c}$, $\underline{g}$, $\underline{f}$, $\underline{h}$, and ξ, η, ϑ are the components of distortion and the components of rotation of the fluid respectively.

Other equations defining the motion of any ellipsoid subjected to forces exerted by the surrounding fluid are

$$\begin{aligned} (b^2 + c^2).w_1 &= b^2(\xi + \underline{f}) + c^2(\xi - \underline{f}) \\ (c^2 + a^2).w_2 &= c^2(\eta + \underline{g}) + a^2(\eta - \underline{g}) \qquad (3.7) \\ (a^2 + b^2).w_3 &= a^2(\vartheta + \underline{h}) + b^2(\vartheta - \underline{h}) \qquad \text{(Jeffery's eq. 37)} \end{aligned}$$

where a, b, c are the lengths of the semi-axes of the ellipsoid and w_1, w_2, w_3 are the respective rates of rotations of ellipsoid about its own x, y and z axes.

The motion of an ellipsoid and the systems of Euler's angles used to fix the position of the axes of the ellipsoid are illustrated in figure 3.1,b. The derivations of the equations to describe these angles are given by Gay (1966, 1968). The resultant equation of motion of an elliptical object (in 2D) included in viscous matrix is given by

$$\ln \text{Cot}\, \varnothing_f = \ln \text{Cot}\, \varnothing_i + (a^2 - b^2)/(a^2 + b^2).\ \ln \sqrt{\lambda_2/\lambda_1} \qquad (3.8)$$

(Gay, 1968, equation 10.a)

This equation relates final ($\varnothing_f$) and initial ($\varnothing_i$) orientation of the particle to deformation. The angle $\varnothing_f$ and $\varnothing_i$ are measured with respect to the normal to the extension direction of the strain ellipse. But for the convenience of measurements, these parameters are changed so that the angle of orientation can be measured with reference to the extension direction. Let the new angle be denoted by θ which relates with $\varnothing$ as $\theta = 90 - \varnothing$. Modifying this parameter, the equation 3.8 can be transformed into

$$\ln \tan \theta_{fe} = \ln \tan \theta_{ie} + (a^2 - b^2)/(a^2 + b^2).\ \ln \sqrt{\lambda_2/\lambda_1} \qquad (3.9)$$

where θ_{fe} and θ_{ie} are the final and initial orientations measured with reference to the extension direction respectively in the case of pure shear. This is the required equation for the motion of elliptical porphyroblasts set in a matrix undergoing pure shear.

By substituting a = b in equation 3.9, the expression is reduced to

$$\begin{aligned} \ln \tan \theta_{fe} &= \ln \tan \theta_{ie} \\ \text{i.e.} \quad \theta_{fe} &= \theta_{ie} \end{aligned} \qquad (3.10)$$

which is the equation for spherical or equidimensional object. This equation confirms the statement by Ramsay (1962, 1967) that the equidimensional objects do not rotate during pure shear deformation.

The theoretical motion of a rigid porphyroblast set in viscous matrix with various axial ratio and initial orientation was investigated using equation 3.9 and a computer. The results are recorded in table 1 and presented graphically in figure 3.3. The

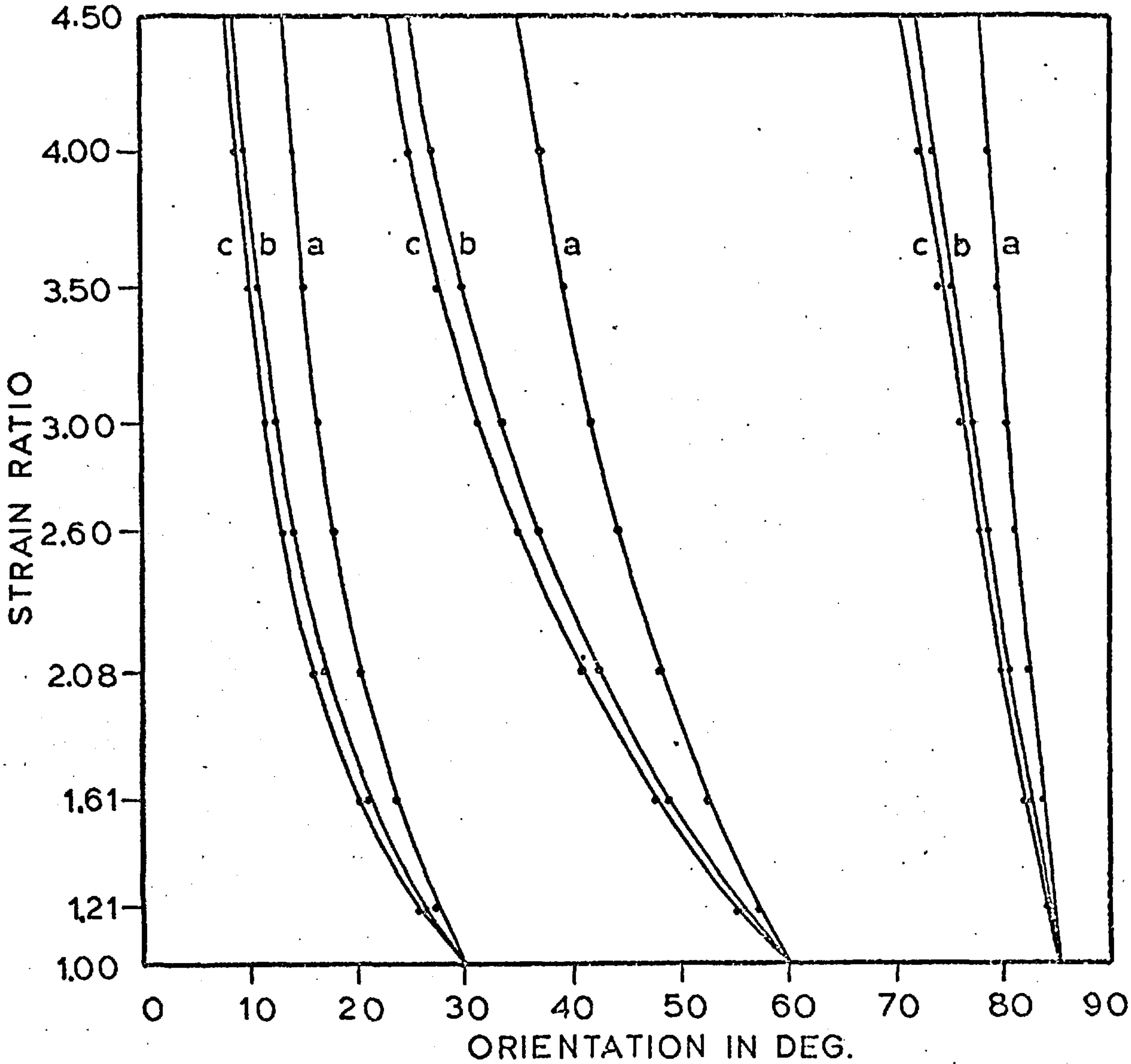

Fig. 3.3 Graphical representation of eq. 3.9 showing the motion of elliptical inclusions set in a matrix during progressive pure shear deformation. The curves 'a', 'b', 'c' represent the graphs for inclusions having axial ratio a/b = 2:1, a/b = 4:1 and a/b = 6:1 respectively.

amounts of rotation calculated from the difference of final and initial orientation are also recorded in table 1 and are illustrated in figure 3.4, a and b.

The following predictions can be made from this analysis:

(a) Equidimensional objects subjected to pure shear deformation do not rotate (equation 3.10).

(b) The final orientation (θ_{fe}) of the elliptical porphyroblasts is a function of the strain and their initial orientation (Fig. 3.3). It is seen that the amount of rotation is greatest when the object lies initially at an angle between 40° to 70° with reference to the extension direction. The rotation is least where the long axis of the object lies close to or almost normal to the extension direction i.e. when $\theta_{ie} = 0^{\circ}$ and $\theta_{ie} = 90^{\circ}$. Any object lying parallel to or normal to the extension direction show no or very little rotation after deformation (Fig. 3.5).

(c) The amount of rotation of an elliptical object depends on its axial ratio. It increases with increase of axial ratio of the porphyroblasts (Fig. 3.4, a and b).

(d) Rotation also depends on the value of the finite strain; the rate of rotation is greatest at the initial stage of development and least during the later stages of deformation (Fig. 3.4, a and b).

3.4 THE ROTATION OF RIGID PORPHYROBLASTS IN A MATRIX UNDERGOING SIMPLE SHEAR

During simple shear deformation of a ductile medium containing rigid objects leads to rotation of the objects irrespective of their shape and initial orientation. The equations which express the behaviour of rigid particles contained within a linear viscous fluid were obtained by Einstein (1896) and Jeffery (1922). Gay (1966, 1968)

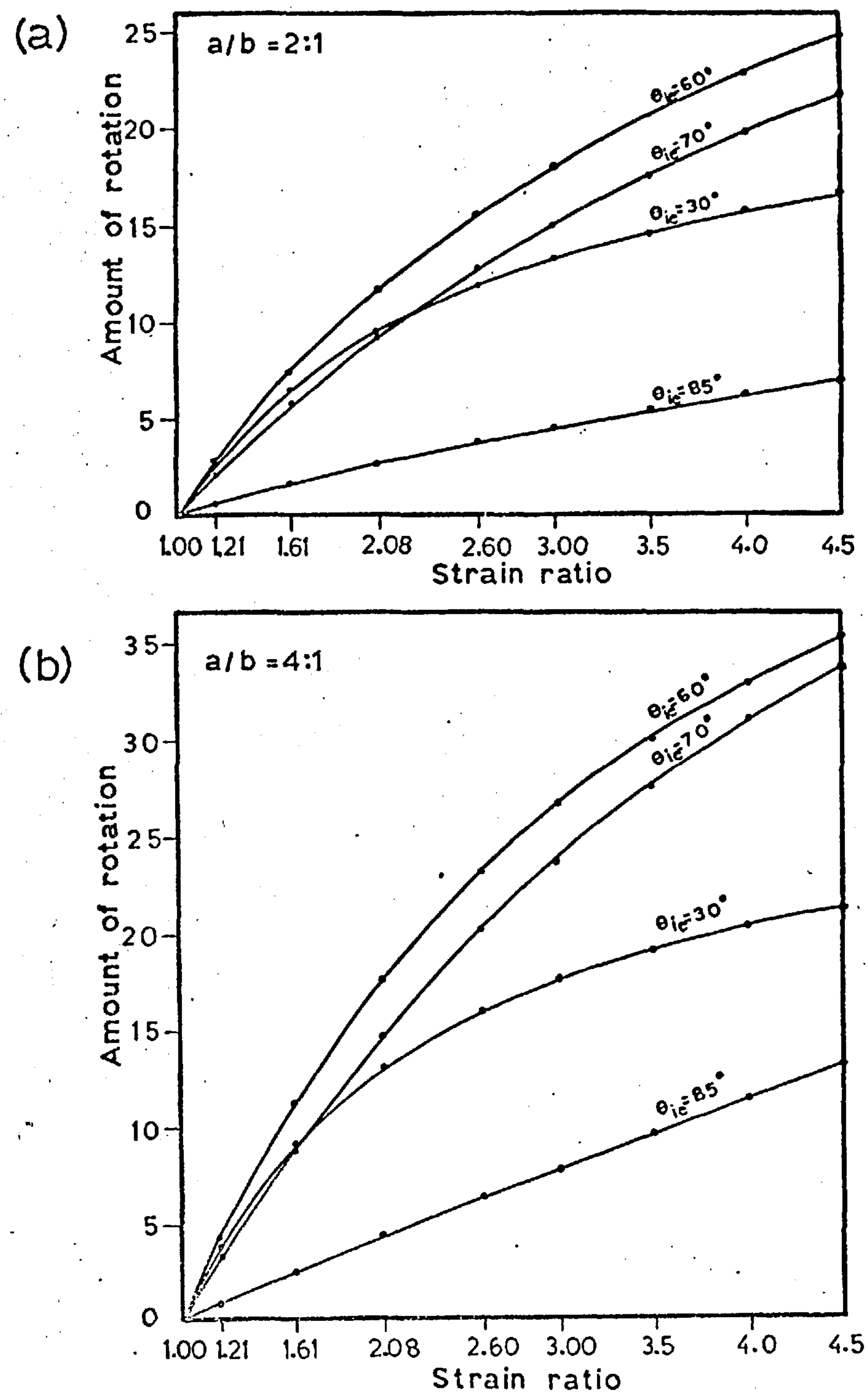

Fig. 3.4 Effect of initial orientation θ_{ie} (measured with reference to the principal extension direction) and axial ratio (a/b) of the elliptical inclusions on their amount of rotation during progressive pure shear deformation.

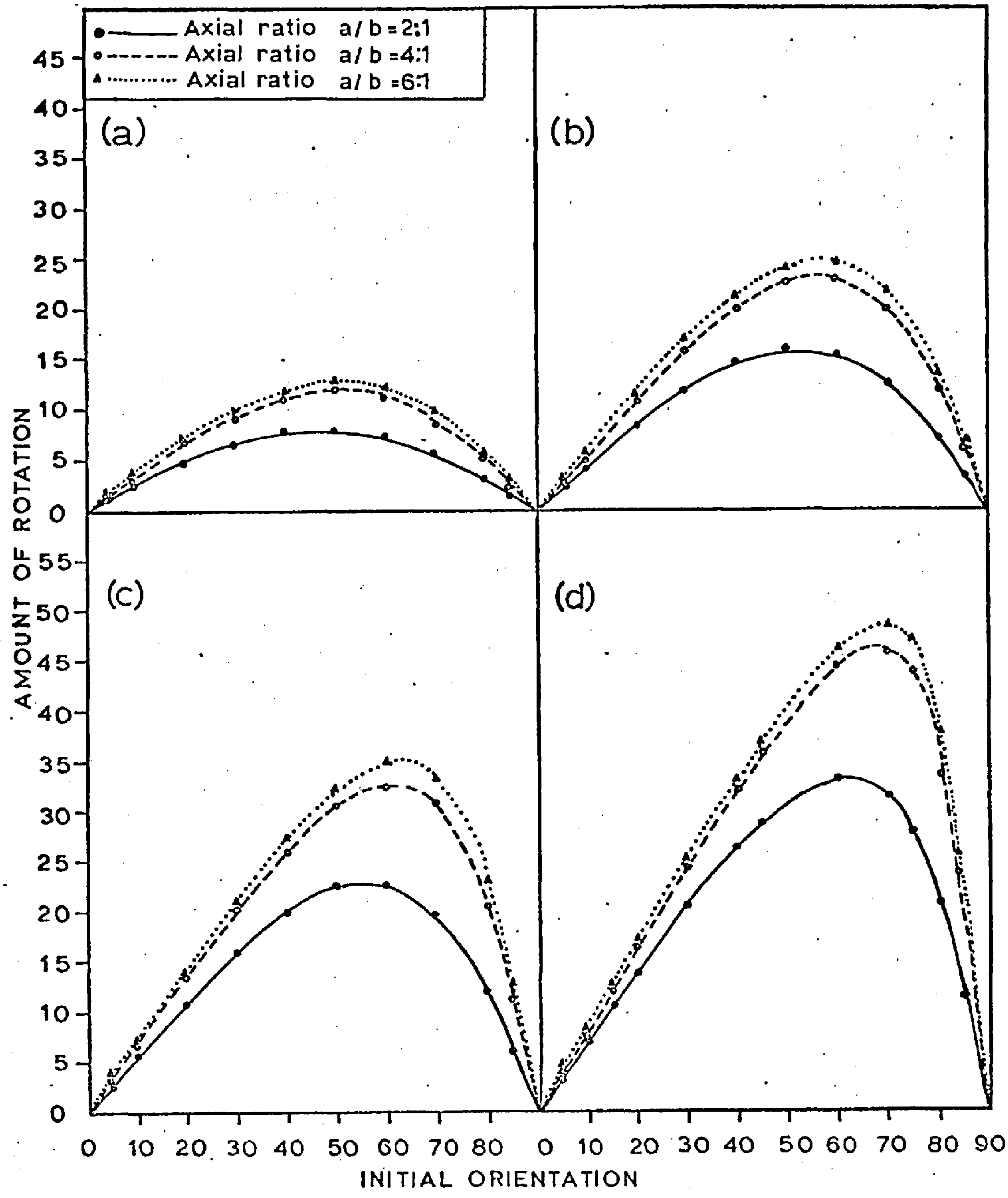

Fig. 3.5 Theoretical relationship between the amount of rotation and the initial orientation (θ_{ie}) of elliptical inclusions undergoing progressive pure shear deformation.
(a) $\sqrt{\lambda_1/\lambda_2}$ = 1.61; (b) $\sqrt{\lambda_1/\lambda_2}$ = 2.60; (c) $\sqrt{\lambda_1/\lambda_2}$ = 4.0; (d) $\sqrt{\lambda_1/\lambda_2}$ = 8.0

extended their work and discussed the geological implications of it.

3.4.1 The behaviour of spherical particles

Let us first consider the case of a spherical rigid object immersed in a deforming viscous fluid. The resolved normal forces acting on the object as a result of the deformation of the surrounding fluid, causes no translation but the component tangential force will produce couple which will cause rotation of the sphere. The moment (M) of the couple acting on the object is given by

$$M = 2\pi a^2 \tau = 2\pi a^2 \mu \dot{\gamma}_s \qquad (3.11)$$

where $2a$ = length of arm of the couple

πa = the area on which tangential forces act

τ = shearing stress of the fluid = $\mu\dot{\gamma}_s$.

This moment of couple must be equal to the moment of frictional couple acting on a sphere rotating with constant angular velocity (ω). Lamb (1932, p-588, eq. 4) deduced this frictional moment (M_f) as

$$M_f = -4\pi a^2 \omega \qquad (3.12)$$

Equating M and M_f, and remembering that $\dot{\gamma}_s = 2\omega$, the following expression is derived,

$$d\gamma_s/dt = 2.d\varnothing/dt \qquad (3.13)$$

This is the equation first derived by Einstein (1896) and later used by Gay (1966, 1968).

If $\varnothing_i$ and $\varnothing_f$ are the initial and final orientations measured from the normal to the shearing direction and θ_{is} and θ_{fs} are the initial and final orientations with reference to the shearing direction, then the relationships between these angles are $\theta_{is} = 90-\varnothing_i$ and $\theta_{fs} = 90-\varnothing_f$.

A more useful expression can be obtained by integrating equation 3.13 over the limits from ϕ_i to ϕ_f and 0 to γ_s, it gives

$$\phi_f - \phi_i = 1/2.\gamma_s \qquad (3.14)$$

Replacing ϕ_f and ϕ_i by θ_{fs} and θ_{is} respectively, the above equation is expressed as

$$\theta_{fs} = \theta_{is} - 1/2.\gamma_s \qquad (3.15)$$

The final orientations of the spherical objects with reference to the initial orientations for given strains are calculated from equation 3.15 (table 2) and are graphically presented in figure 3.6. An unmarked spherical object can not have any definable direction of orientation. The angle of rotation ($\theta_{fs} - \theta_{is}$) might be measured in deformed porphyroblasts of this shape by the maximum difference in orientation of the fabric or schistosity preserved inside and outside the porphyroblast. It can be seen from the graphs of figure 3.6 that spherical objects rotate at a constant rate during simple shear deformation.

3.4.2 The behaviour of elliptical particles

The couple acting on an elliptical particle due to the force exerted by the fluid matrix under simple shear deformation causes the object to rotate. The couple on an elliptical particle, unlike that on a spherical particle, varies as the ellipse rotates (fig. 3.2). The moment of couple (M) acting on the particle and the moment of frictional couple (M_f) are given by

$$\left.\begin{aligned} M &= 2\pi a^2(1-\varepsilon^2 \sin^2\phi).\tau \\ M_f &= 2\pi\mu\,\omega(a^2 + b^2) \end{aligned}\right\} \qquad (3.16)$$

where 'ε' is the eccentricity of the ellipse.

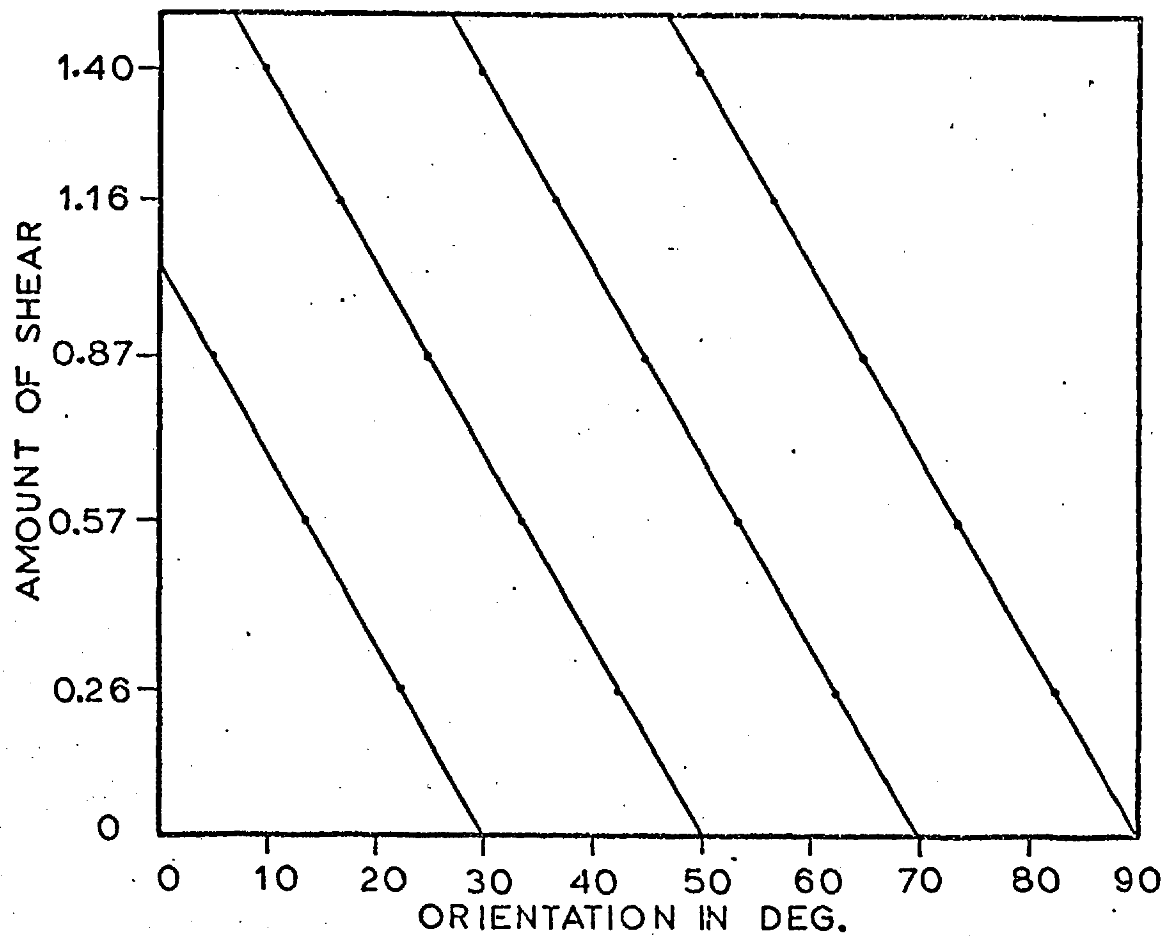

Fig. 3.6 Graphical solution of eq. 3.15 showing the motion of rigid equidimensional (spherical) object set in a matrix undergoing progressive simple shear deformation. Orientations are measured with reference to the shearing direction.

Equating M and M_f, gives

$$\omega = a^2/(a^2 + b^2).\ \dot{\gamma}_s(1-\varepsilon^2 \sin^2\emptyset)$$

$$\text{i.e.} \quad \int d\emptyset/(1-\varepsilon^2 \sin^2\emptyset) = a^2/(a^2 + b^2).\ \int d\gamma_s \qquad (3.17)$$

Solving equation 3.17, we get

$$\tan \emptyset = a/b.\ \tan[a.b/(a^2 + b^2).\gamma_s] \qquad (3.18)$$

(Jeffery, 1922, eq. 43)

This solution is not complete because an important factor, initial orientation of the elliptical particle, was not taken into consideration.

To obtain a complete solution for the final orientation with reference to the initial orientation, the left hand side of equation 3.17 has to be integrated between limits from initial and final orientation and right hand side of the same equation with limits from 0 to γ_s. Changing Gay's parameter $\emptyset$ to θ, according to the relationship of $\theta = 90-\emptyset$, the equation 3.17 gives,

$$\int_{\theta_{is}}^{\theta_{fs}} d\theta/1-\varepsilon^2.\text{Cos}^2\theta = a^2/(a^2 + b^2).\ \int_0^{\gamma_s} d\gamma_s \qquad (3.19)$$

$$\text{or,} \quad \text{Cot}\ \theta_{fs} = a/b.\ \tan[a.b/(a^2 + b^2).\gamma_s + \tan^{-1}(b/a.\text{Cot}\ \theta_{is})] \qquad (3.20)$$

This is the exact equation for the motion of elliptical porphyroblast in the system undergoing simple shear.

The final orientations of elliptical objects of having any a/b ratio and initial orientations have been calculated from equation 3.20 (table 3) and the results are presented graphically in figures 3.7 and 3.8. From the interpretation of the results, the following conclusions may be drawn:

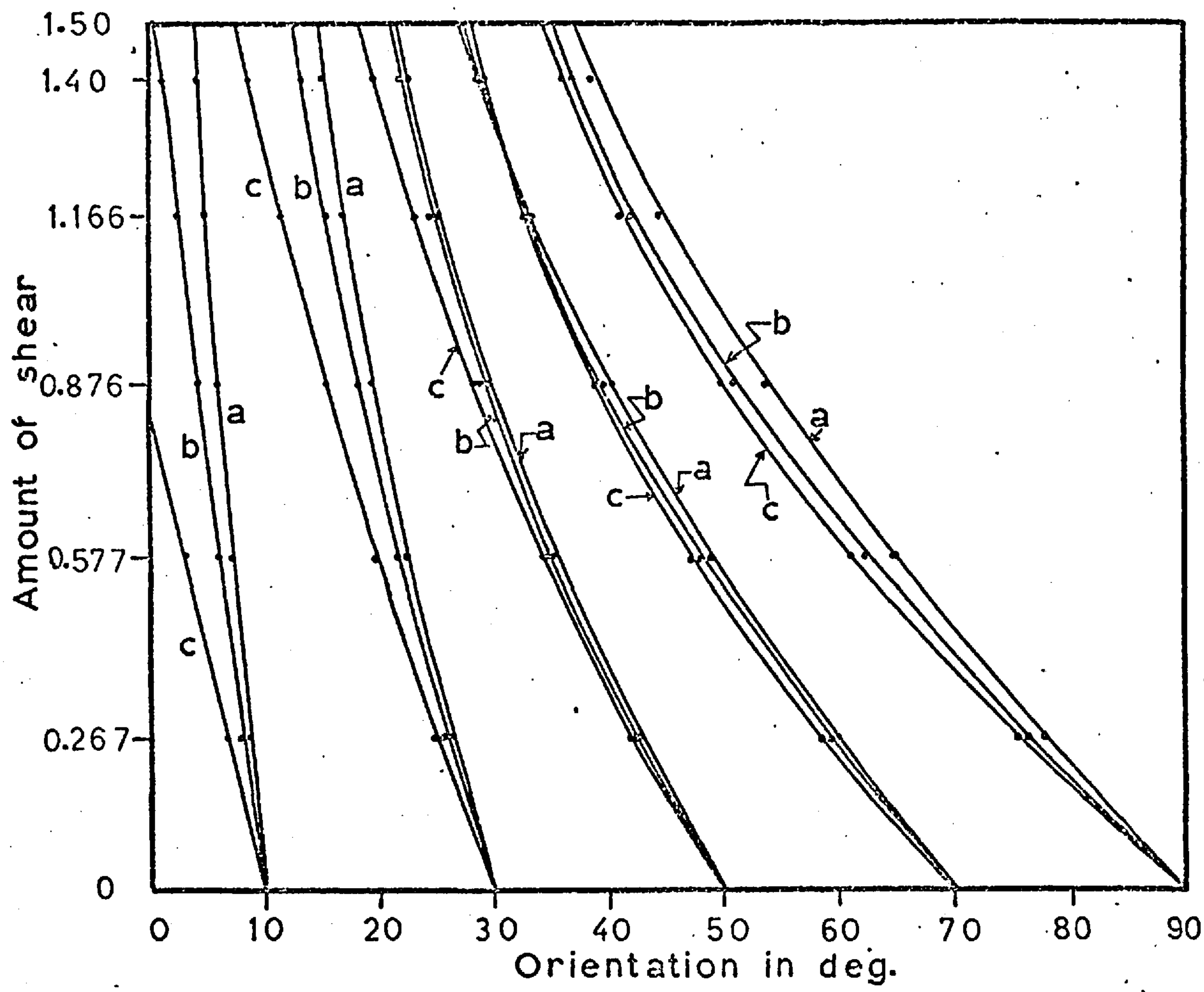

Fig. 3.7 Graphical representation of eq. 3.20 illustrating the motion of rigid elliptical inclusions undergoing progressive simple shear deformation.
(a) a/b = 2:1; (b) a/b = 3:1; (c) a/b = 4:1
Orientations are measured with reference to the shearing direction.

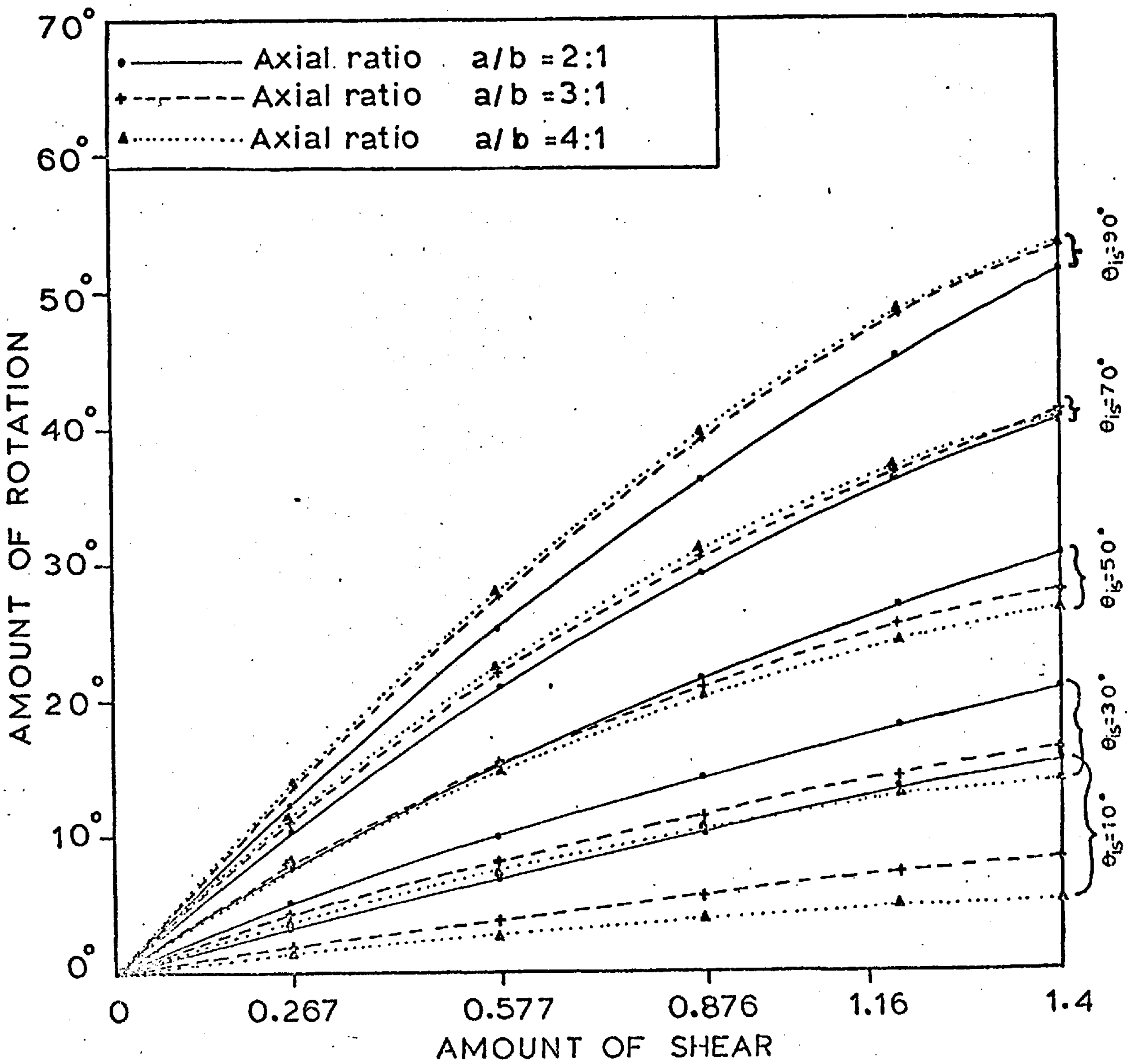

Fig. 3.8 Theoretical relationship between the amount of rotation and the applied shear strain (γ_s). θ_{is} represents initial orientation of an inclusion with reference to the shearing direction.

(a)The final orientation of the elliptical objects is dependent on their initial orientation and their axial ratio (a/b) (fig. 3.7).

(b) The rate of rotation of the object is greatest where its long axis makes a high angle to the shearing direction (fig. 3.8).

(c) The variation in the amount of rotation with change in axial ratio of the object is complex (fig. 3.8).

CHAPTER 4. EXPERIMENTAL PROGRAMME

4.1 INTRODUCTION

Over the last 150 years, various types of experiments have been performed to investigate geological problems. Two main types of laboratory experimentations are common in the field of geology : (i) scale models and (ii) high pressure deformation of rock. The present investigation has used scale models to simulate the rigid rotation of porphyroblasts and the deformation of belemnites.

This type of investigation was first undertaken by J. Hall in 1815, when he simulated fold shapes by compressing a pile of cloth sheets. Later, Favre (1878) and Cadell (1888) used wet clay and plaster of paris respectively as model materials and made model studies of folds and faults. Since that time, many workers have used models to simulate structural processes, to test theoretical hypothesis or to bridge the gap between theoretical predictions and field observations.

The aim of this chapter is to describe the instruments, model materials, experimental procedures and the methods of analysing the results of the experiments. A lozenge-shaped irrotational strain box and a simple shear box have been used to perform all the experiments described in this thesis. A discussion of the history of deformation of the material inside the lozenge-shaped box is given. Gay's simple shear box is then described together with the modifications which have been made to obtain high strains in the model materials.

4.2 MODEL STUDY PROBLEMS

Experimental work with models is often used to test theoretical predictions about the formation of geological structures. It also helps in investigating the progressive development and deformation history of a structure, a feature which is not usually possible from observations of naturally deformed rocks. Theoretical studies, supported by experimental verifications have been used to predict the history of rigid rotation of inclusions and the nature of strain around such objects. These model studies have been carried out with definite objectives and with controlled materials.

Many workers (including Cadell, 1888; Paulke, 1912; Hubbert, 1951; Cloos, 1955; Bucher, 1956; Sanford, 1959; Biot et al, 1961; Ramberg, 1955; Donath, 1968; Gosh, 1968; Cobbold et al, 1971) have undertaken experiments with a variety of materials, although some of them failed to simulate natural structures very exactly. The reasons for this ambiguity may be : (i) The relevance to geology of some of the early results was not certain or the experimental conditions were not carefully controlled. (ii) Much of the early work was developed in ignorance of the theory of scale model proportions. (iii) The boundary conditions of some of the early models were over-simplified when compared to the natural situations. (iv) And finally, the impossibility of reducing all the parameters of the model correctly which might cause the ambiguity in results.

The theory of scale models have been discussed in detail by Hubbert (1937) and Currie (1966). The practical application of the conclusions drawn from the theory of dimensional analysis of small scale models of large structures poses modelling problems which can be incompletely resolved as the strength or rigidity of material varies with the size of the body (Hubbert, 1937). The model size problem is investigated in the present experiments by varying sizes and shapes of inclusions. The scale of models used to simulate the progressive deformation of stretched belemnites is very close to the original scale of the natural example (compare figures 4.1 and 4.2).

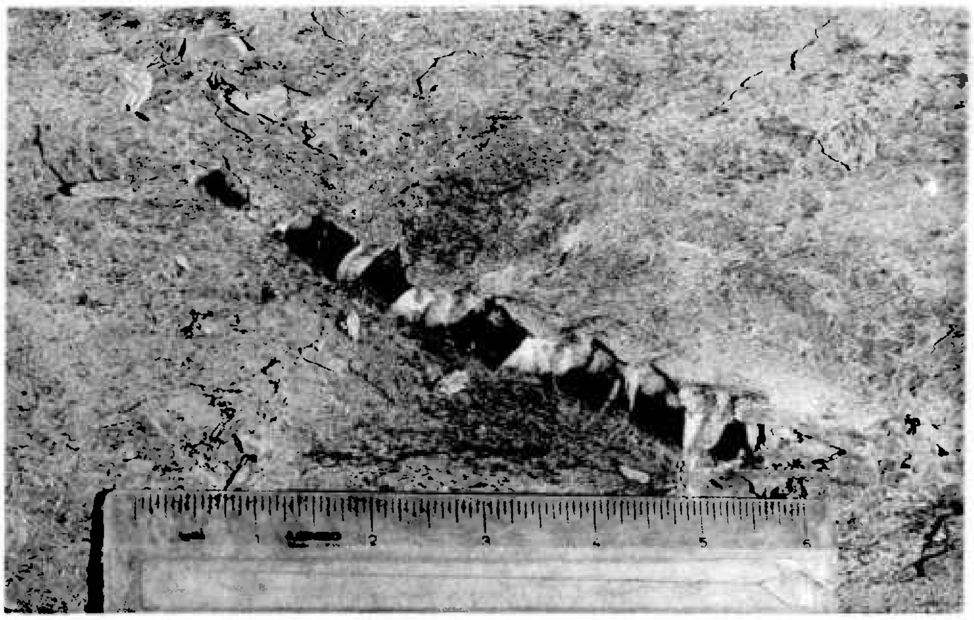

Fig. 4.1 Natural example of an extended belemnite from Leytron, Valais, Switzerland.

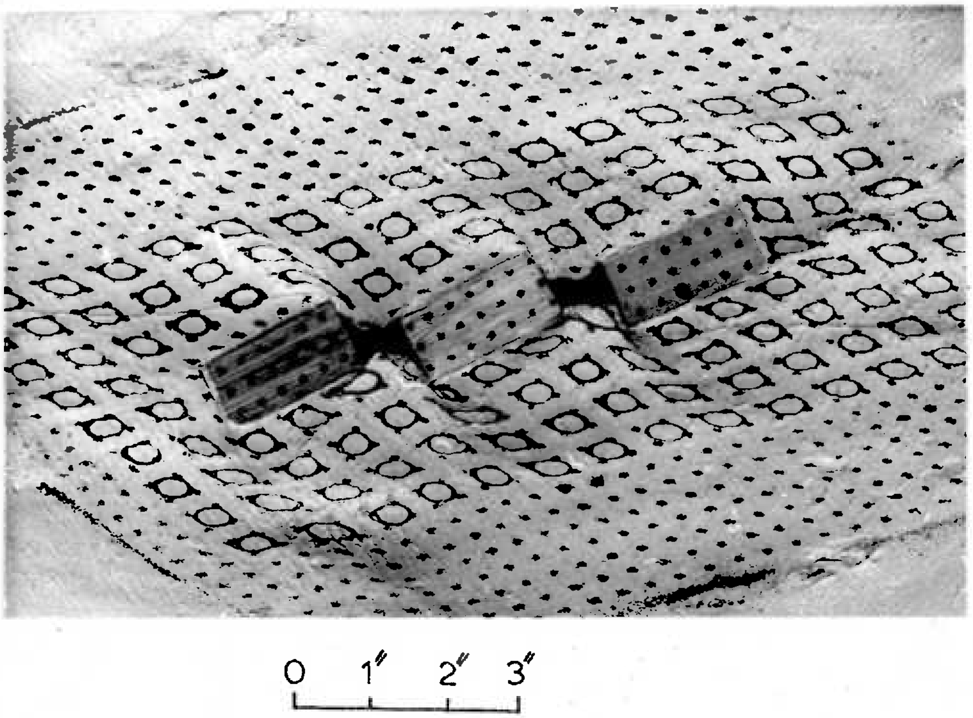

Fig. 4.2 Experimental simulation of an extended belemnite set in a matrix during irrotational strain deformation.

There are a few number of features of the model studies which can lead to some difficulties of direct interpretation. For example, the properties of the model material chosen to represent rigid particles and belemnite fragments may not be completely appropriate, and the assumption that there is a pre-existing plane of weakness between the fragments of belemnite may limit the direct application of the experimental results to the geometry of the natural examples. It does seem, however, that the results of many of these model studies can be used to ascertain the validity of theoretical predictions and assist the interpretation of field observations.

4.3 MODEL MATERIALS

The model materials used in the experiments were chosen to simulate the behaviour of completely rigid inclusions in a ductile matrix. The matrix material was selected so that the included objects did not sink under their own weight and so that adhesion between matrix and included object was maintained throughout deformation. Care was taken that the matrix material did not undergo chemical reaction with the inclusion and that there are no changes in the physical properties during the course of experiment. The materials were chosen for their convenience and ease of handling and particularly for the suitability of imprinting markers on the surface so that finite strains could be computed.

Linseed oil putty was selected as a matrix material for experimental work. The complex rheological properties of putty have been described by Durney (1968). Putty flows when deformed at an intermediate strain rate but it ruptures at high strain rates. The experiments described below were all conducted at strain rates within the ductile range. Putty is composed of approximately 90% fine grained calcium carbonate and 10% linseed oil and it has a tendency to dry out when exposed to air.

Wooden rods and strips were used to simulate the rigid objects. Wooden material was chosen because of its excellent adhesive properties (after treated by oil) and because it was a simple material to cut into any required shape and size.

4.4 IRROTATIONAL STRAIN BOX (LOZENGE-SHAPED BOX)

An irrotational strain box used in these experiments termed the 'Lozenge-shaped shear box' by Beech (1969) was constructed by N. C. Gay (1966) according to a design by Professor J. G. Ramsay. The essential features of the box are shown in figure 4.3. The box consists of four rigid sides hinged together to form a rhomb. The shape of the rhomb changes with the progressive change of its apical angle (fig. 4.4 and 4.5). Small holes have been drilled at equally spaced intervals near the base of the sides and thin nylon has been threaded through these holes. This net-work of thin cord enables the material inside the box to deform homogeneously. The shape of the box was changed by applying pressure by hand on opposite corners so that two of the principal strains are parallel to the diagonals of the box and the third is normal to the surface of the model material.

4.4.1 Geometry of the box

The area of the box changes with the changes of apical angle (fig. 4.5). It increases progressively from $\alpha_0 = 0^{\circ}$ to $\alpha_1 = 90^{\circ}$ reaching a maximum at $\alpha_1 = 90^{\circ}$, and then decreases with further increase of the apical angle. Hence, the box does not produce progressive pure shear deformation. The final area of the box is equal to the initial area when the complimentary apical angle β_1 reaches

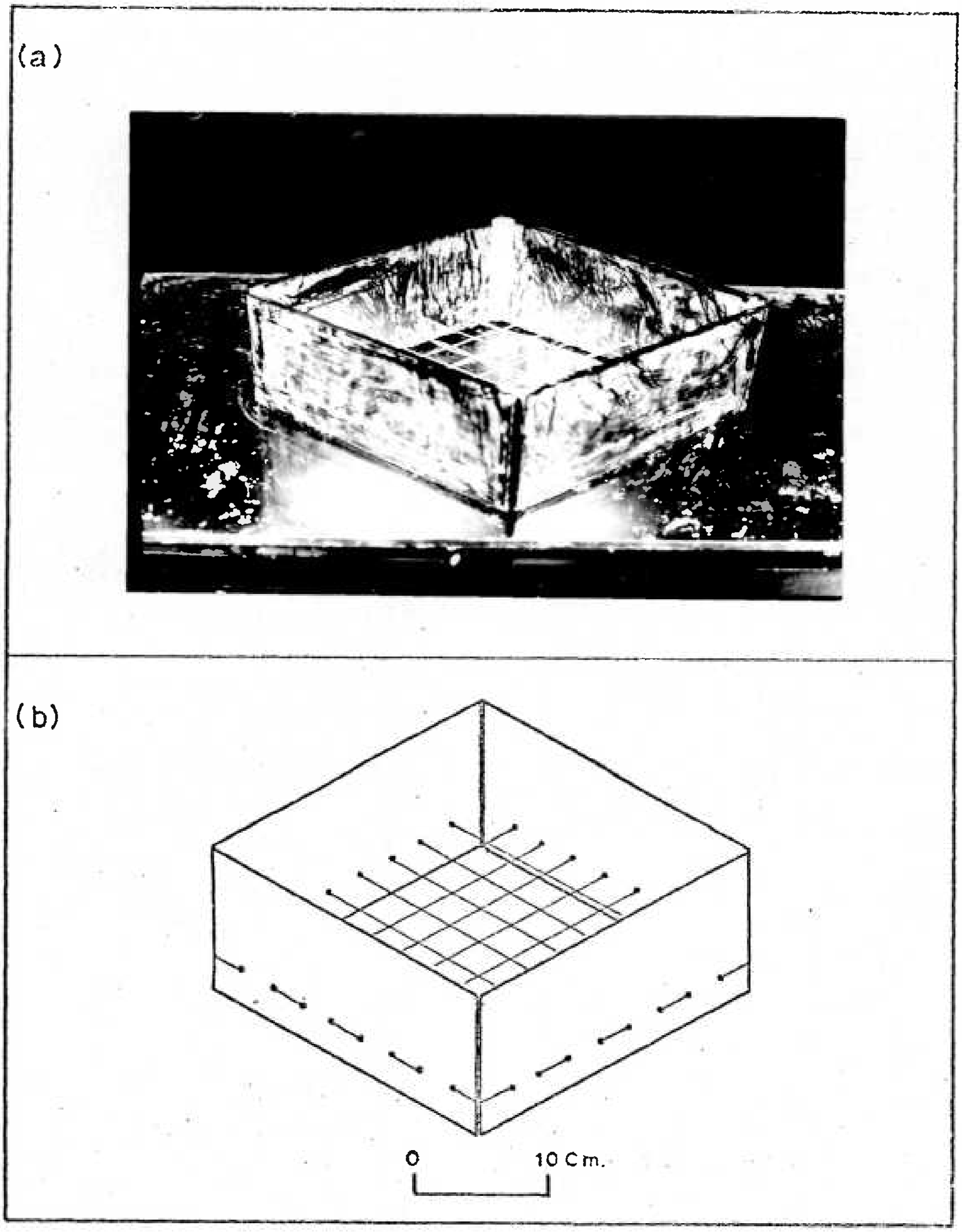

Fig. 4.3 Lozenge-shaped irrotational strain box.

(a) Photograph taken vertically.

(b) Drawing showing the side view of the box.

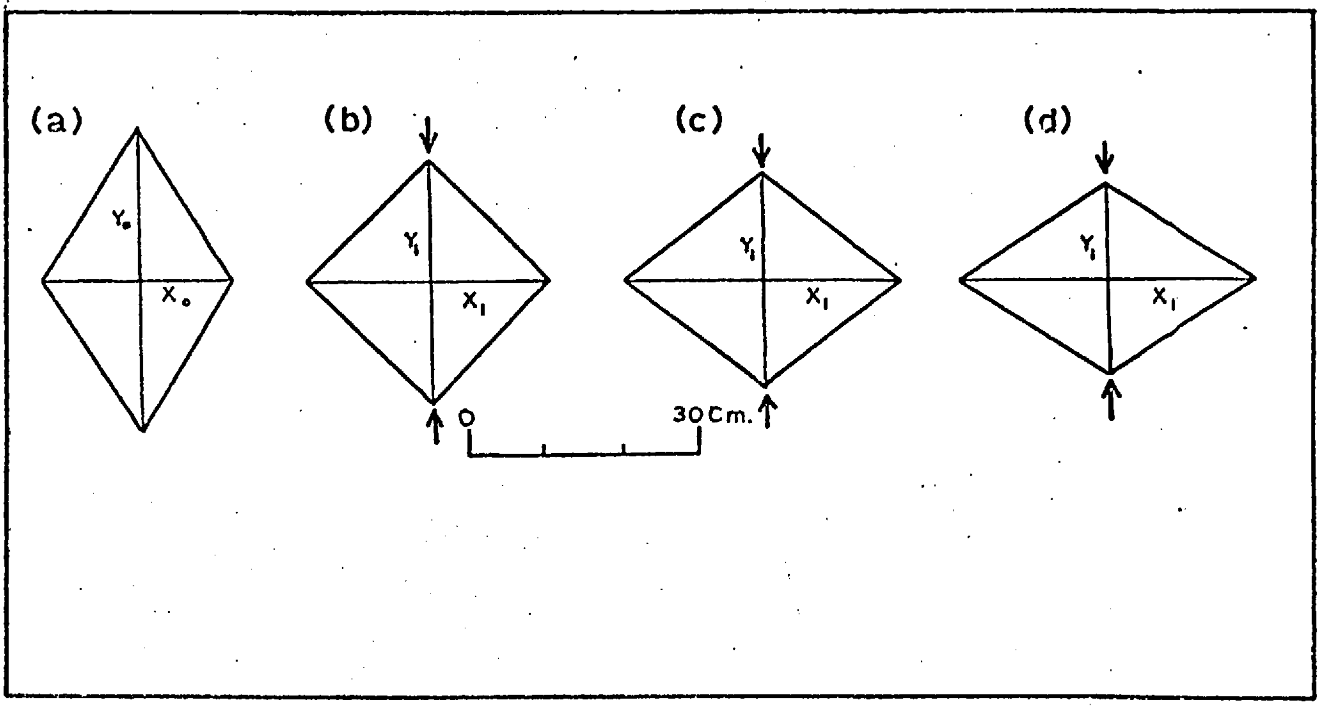

Fig. 4.4 Plan of deformation of the irrotational strain box.

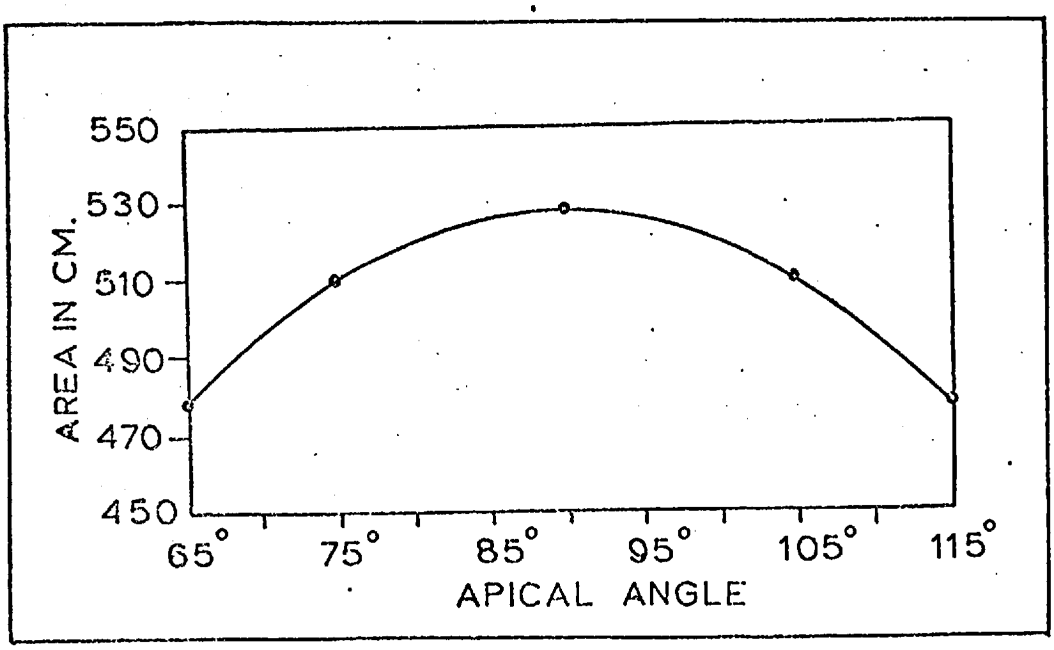

Fig. 4.5 Graphical representation showing the relationship between the area of the irrotational strain box and its apical angle (α) during progressive deformation.

the value which is equal to α_0 ($\beta_1 = \alpha_0$, fig. 4.4). When this has been achieved, the model materials in the box show a finite pure shear deformation.

The two principal bulk strains developed in the surface of the model can be obtained from the geometry of the box (Hossain, 1970)

$$\begin{aligned} 1 + e_1 &= x_1/x_0 \\ 1 + e_2 &= y_1/y_0 \end{aligned} \tag{4.1}$$

where x_1, y_1 are the new lengths of the diagonal of the box and x_0, y_0 are the initial lengths respectively (fig. 4.4). The values of bulk strains obtained from equation 4.1 are recorded in table 4.

4.4.2 Homogeneity of strain inside the box

Experiments were carried out to check the homogeneity and the amount of strain developed in a homogeneous model material inside the box during deformation. Two thirds of the box were filled with linseed oil putty and circular markers were printed on a smoothed surface. The shape of the box was then changed and the different stages of development were recorded photographically (plate I). The strain ellipses on the model surface showed that irrotational strain had occurred. Except in regions near the boundary and the corners of the box, the ellipses showed approximately homogeneous deformation (fig. 4.6). In all later experiments it was decided to restrict observations to the central homogeneously strained region of the model surface.

Values of the principal strains $\sqrt{\lambda_1}$ and $\sqrt{\lambda_2}$ were calculated from the dimensions of the long and short axis of the strain ellipses. The observed strains are compared with theoretically predicted strains (fig. 4.7). It can be seen that there is a close correspondence between the experimental results and theoretical predictions.

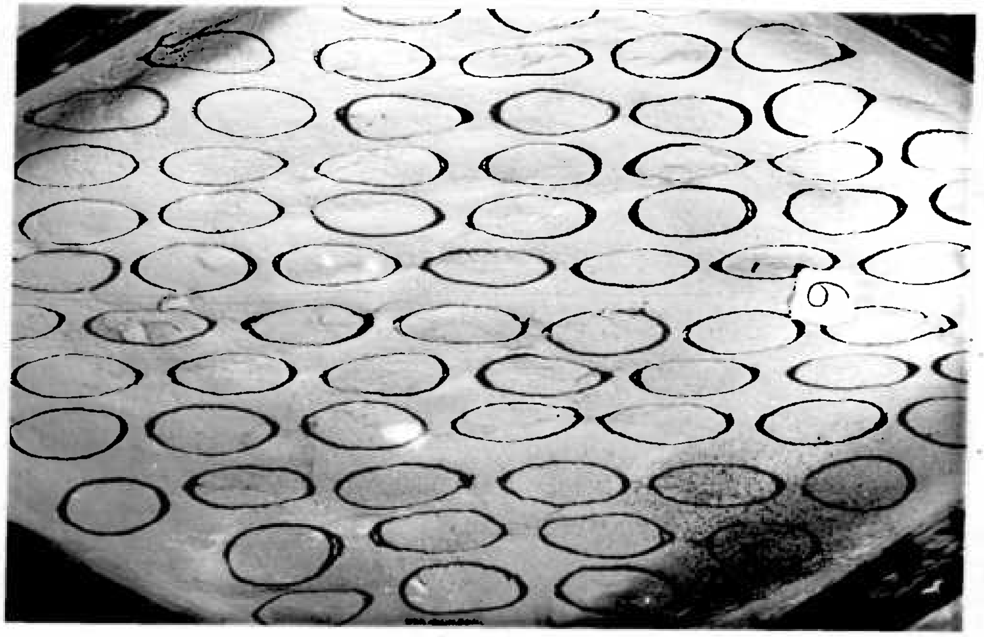

Fig. 4.6 Strain markers showing approximately homogeneous deformation of the material at the central region of the irrotational strain box after finite deformation ($\sqrt{\lambda_1/\lambda_2}$ = 2.60).

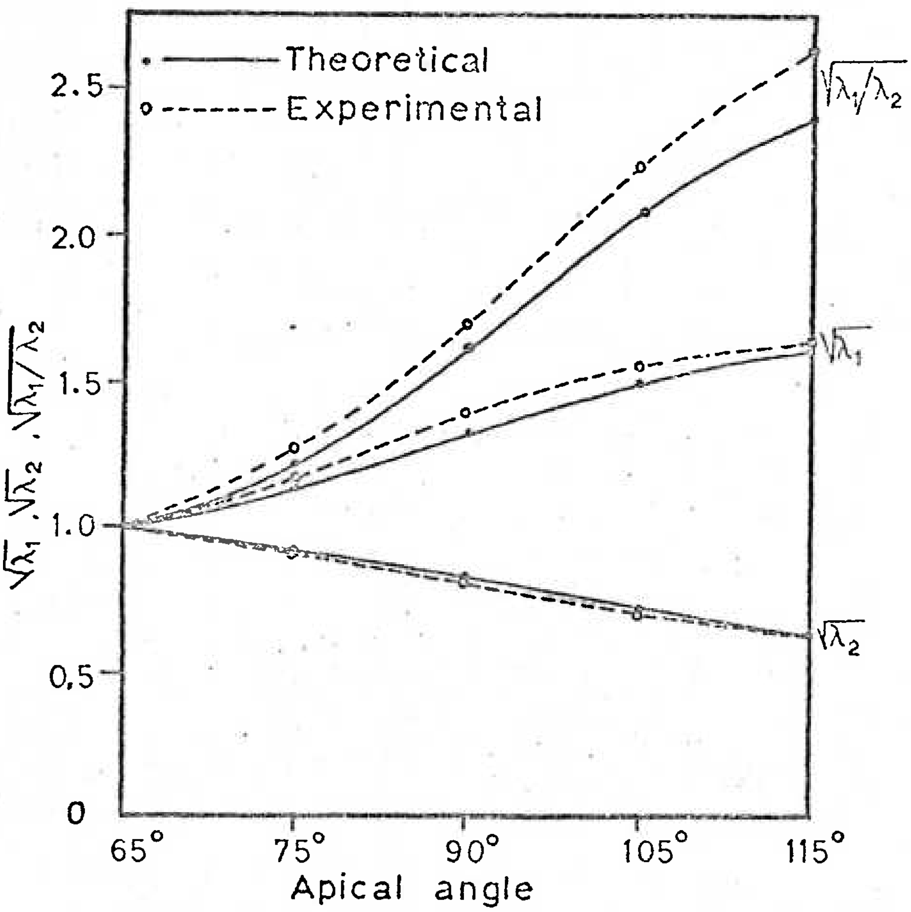

Fig. 4.7 Deformation history of the material deformed inside the Lozenge-shaped irrotational strain box.

4.4.3 Deformation history of the box

As the box is not suitable for obtaining progressive pure shear, a check was needed to investigate the effect of variable strain history during deformation. This can be done by plotting the deformation paths (in 2D). The two dimensional deformation path can be easily obtained from the observed strains (table 4) and is shown in figure 4.8. The deformation path lies in "field-2" i.e. $1 + e_1$ is greater than $1 + e_2$ (Ramsay, 1967) and both the predicted and observed strain paths correlate well.

This box has been used to investigate the properties of finite pure shear (cf. Gay, 1966; Beech, 1969; Hossain, 1970). Another check was made to see how close the strains obtained from this box deviate from those due to perfect pure shear. From the definition of pure shear deformation (Ramsay, 1967, p-56), the relationship of the principal strains in 2D can be expressed as

$$1 + e_1 = 1/1 + e_2 \qquad (4.2)$$

By considering this relationship the predicted and observed results are compared (fig. 4.9). The graphs for predicted and observed results of the box show a good correlation.

4.5 SIMPLE SHEAR BOX

The simple shear box used in the laboratory was designed by N. C. Gay (1966) on the basis of Becker's (1904) "scission Engine" and Ramberg's (1959) "shearing apparatus" principle. One disadvantage with Gay's box was its inability to produce during one experimental run, shear strains higher than $\gamma_s = 0.7$ when operated by motor and $\gamma_s = 0.932$ when operated by hand. In order to procure higher strains, the box was slightly modified. The plans of the modified box are shown in figures 4.10 and 4.11. The apparatus consists of 100

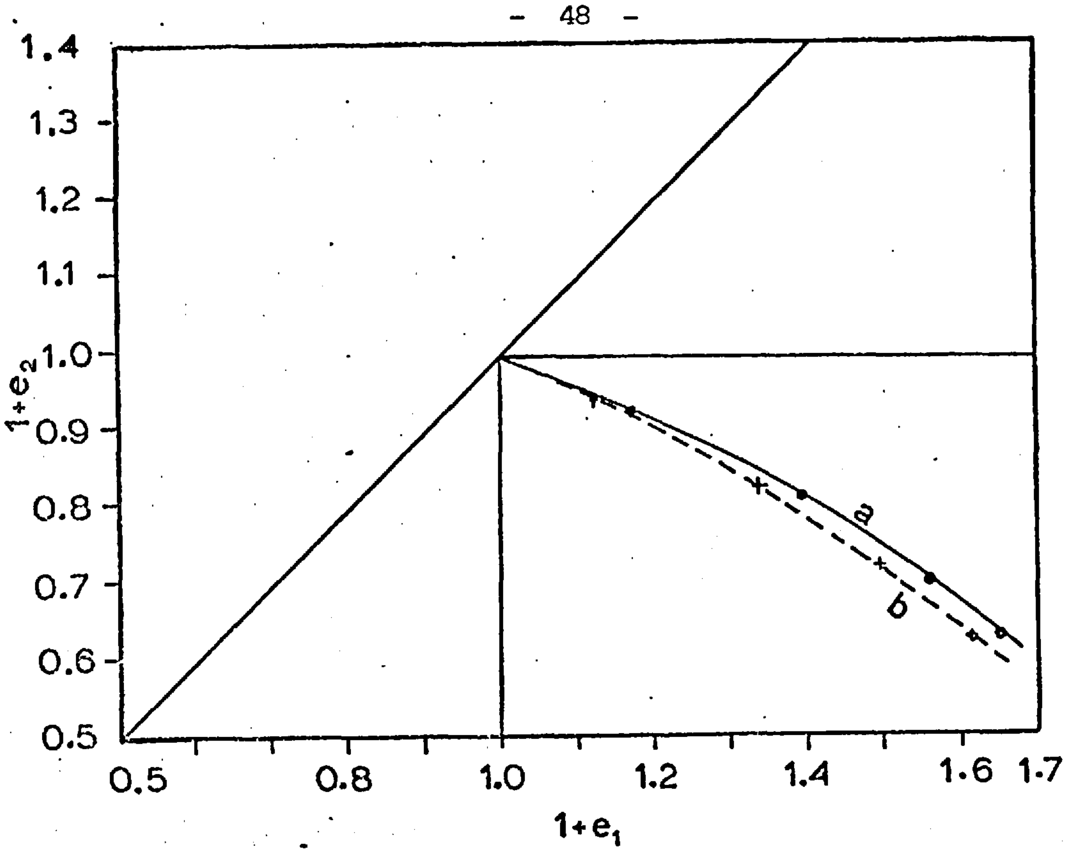

Fig. 4.8 Deformation path (in 2D) shown on the surface of the matrix material (putty) deforming inside the irrotational strain box.

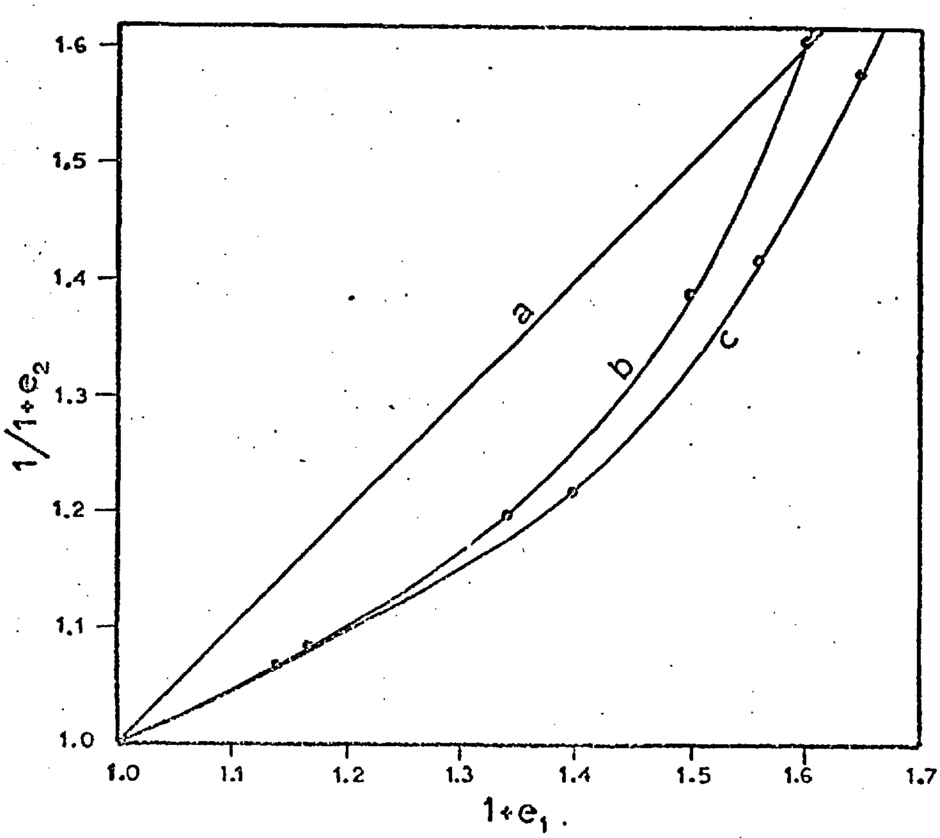

Fig. 4.9 Relationship between the pure shear condition and the strain produced in the material deformed inside the irrotational strain box. (a) Pure shear graph. (b) Theoretically predicted strain state. (c) Experimental graph.

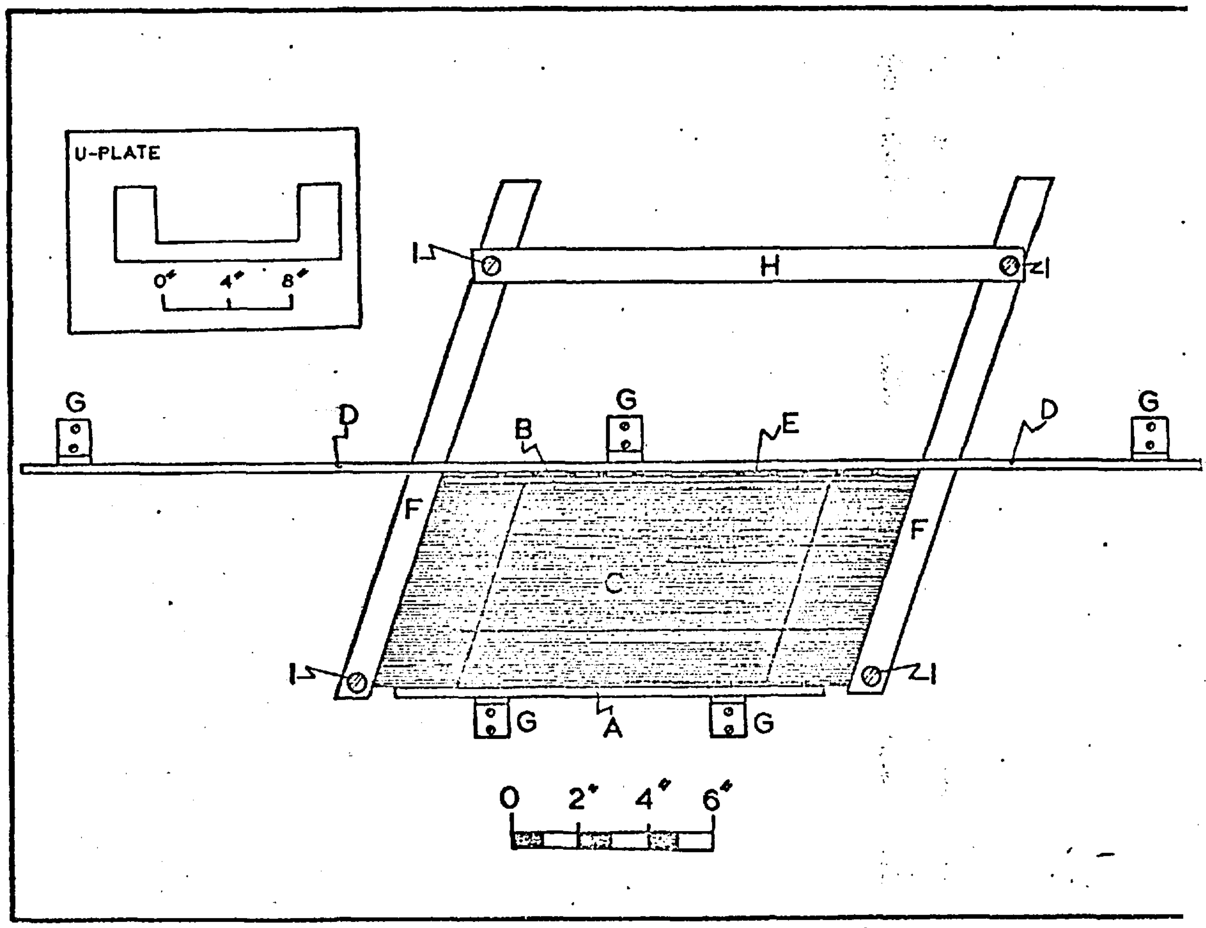

Fig. 4.10 Plan of the modified simple shear box.

A - fixed aluminium plate

B - Movable aluminium plate

C - U-shaped plates

D - A rod to support the movable plate

E - Rail fixed on the movable plate

F - side bar

G - Guid post

H - A bar to keep the side bars tight

I - Pivoted screw

J - Base plate

U-shaped aluminium plates which are clamped together to form a hollow box between two rectangular aluminium plates. One of these aluminium plates is fixed while the other is displaced by a moving arm which displaces all the U-shaped plates.

4.5.1 Geometry of the box

The simple shear box was designed in such a way that any deformation in the box will follow the linear transformation given by

$$\begin{aligned} x' &= x + \gamma_s y \\ y' &= y \end{aligned} \qquad (4.3)$$

where x, y are the co-ordinates of any point in the unstrained position and x', y' are those in the deformed position. Any initial circle of unit radius drawn on the material inside the box, when deformed by simple shear, is transformed into an ellipse

$$x^2 + 2\gamma_s xy + y^2(1 + \gamma_s^2) = 1 \qquad (4.4)$$

The lengths of the major and minor axis ($\sqrt{\lambda_1}$, $\sqrt{\lambda_2}$) of the above ellipse (Jaeger, 1962, p-27 to 28) are

$$\begin{aligned} \sqrt{\lambda_1} &= \sqrt{(\gamma_s/2)^2 + 1} + \gamma_s/2 \\ \sqrt{\lambda_2} &= \sqrt{(\gamma_s/2)^2 + 1} - \gamma_s/2 \end{aligned} \qquad (4.5)$$

The orientation of the major axis of the strain ellipse with reference to the shearing direction is given by

$$\tan\theta = \gamma_s/1 + \gamma_s^2 - (1/\lambda_1) \qquad (4.6)$$

(Ramsay, 1967, p. 87)

which can also be expressed,

$$\theta = \pi/2 - 1/2 \cdot \tan^{-1}(\gamma_s/2) \qquad (4.7)$$

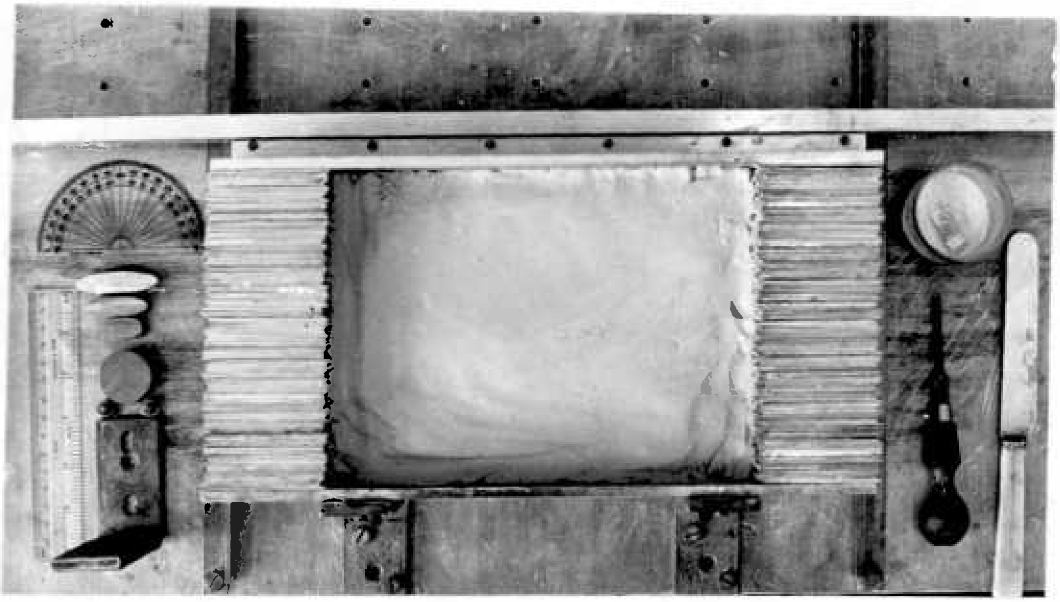

Fig. 4.11 The modified simple shear box. Picture taken from the vertical position.

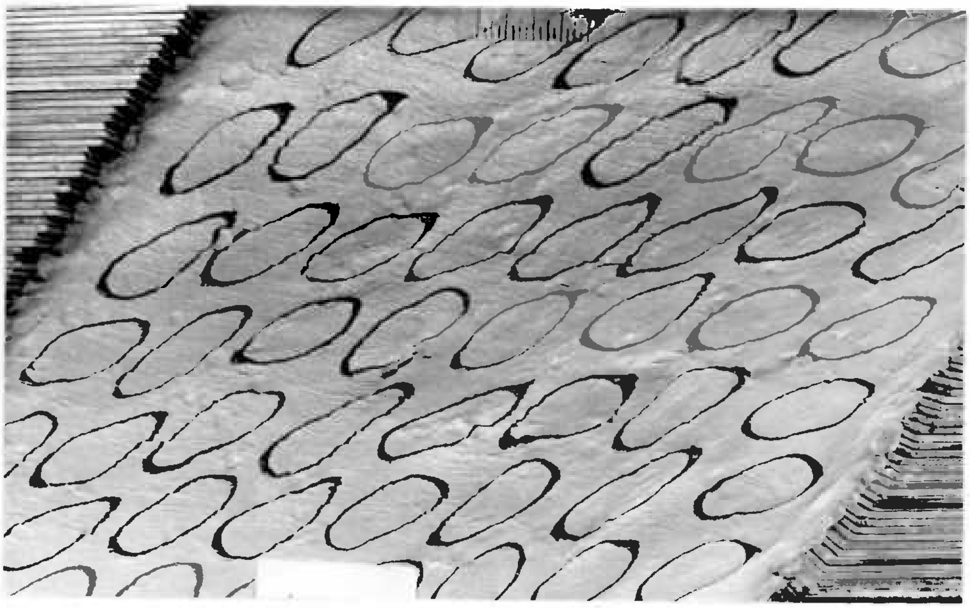

Fig. 4.12 Ellipses produced experimentally show approximately homogeneous strain on the surface of the matrix (putty) at the central region of the modified simple shear box after its finite deformation ($\gamma_s = 1.4$).

Graphical solutions of equations 4.5 and 4.7 are shown in figure 4.17.

4.5.2 Deformation history and homogeneity of the box

The different stages of deformation during one run of an experiment were recorded photographically (plate II). The shapes of experimentally produced strain ellipses show that the finite deformation (γ_s = 1.4) is approximately homogeneous in the centre of the box (fig. 4.12) and that slight variation in strain do occur near the corners of the box. Heterogeneity of strain is greatest during the late stages of deformation. In the two diagonally opposite corners where the angles between the walls are increasing, the material became depressed whereas in the two other corners material bulged up during deformation. This complexity undoubtedly causes some inhomogeneity in distribution of strain particularly near the corners of the box. To avoid such complexity as much as possible, all the experiments performed in the box were restricted to the central part as shown in figure 4.12.

4.6 A MODIFIED METHOD OF CALCULATION OF THE AMOUNT OF SHEAR

The shear strain γ_s can be expressed as a function of angle of shear ψ,

$$\gamma_s = \tan \psi \tag{4.8}$$

Both Gay's box and the modified box were set up by fixing the initial apical angle at an angle greater than 90° i.e. at $\alpha_o = 115^\circ$ and $\alpha_o = 125^\circ$ respectively to obtain higher shearing angle ψ. Gay (1966) obtained total shearing angles of up to $\psi = 50^\circ$ (fig. 4.13) and derived the amount of shear up to γ_s = 1.2 (?). The present investigation into the method of calculation of γ_s shows that the shearing angle ψ was misinterpreted by Gay. Hence, another method of calculating γ_s has been developed.

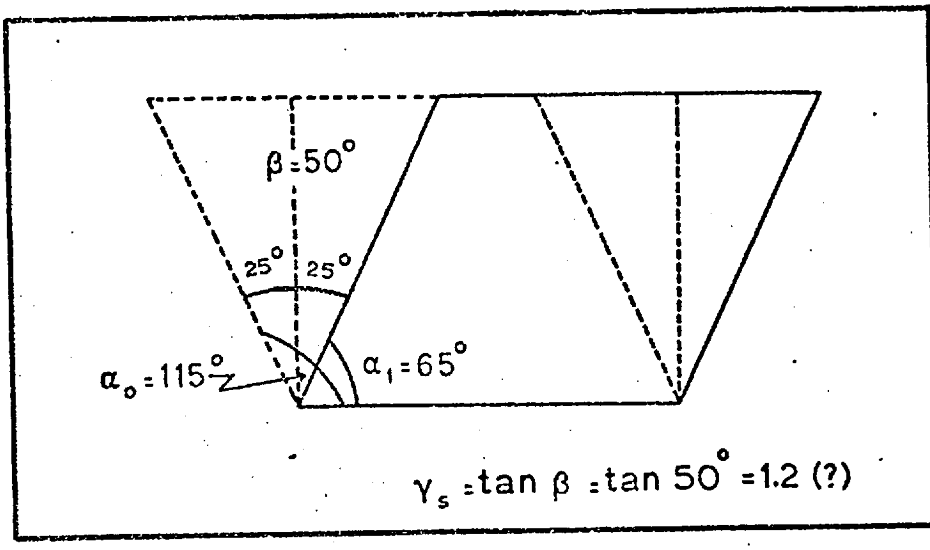

Fig. 4.13 Model demonstrating Gay's method of calculation of the amount of shear (γ_s) from the geometry of the simple shear box.

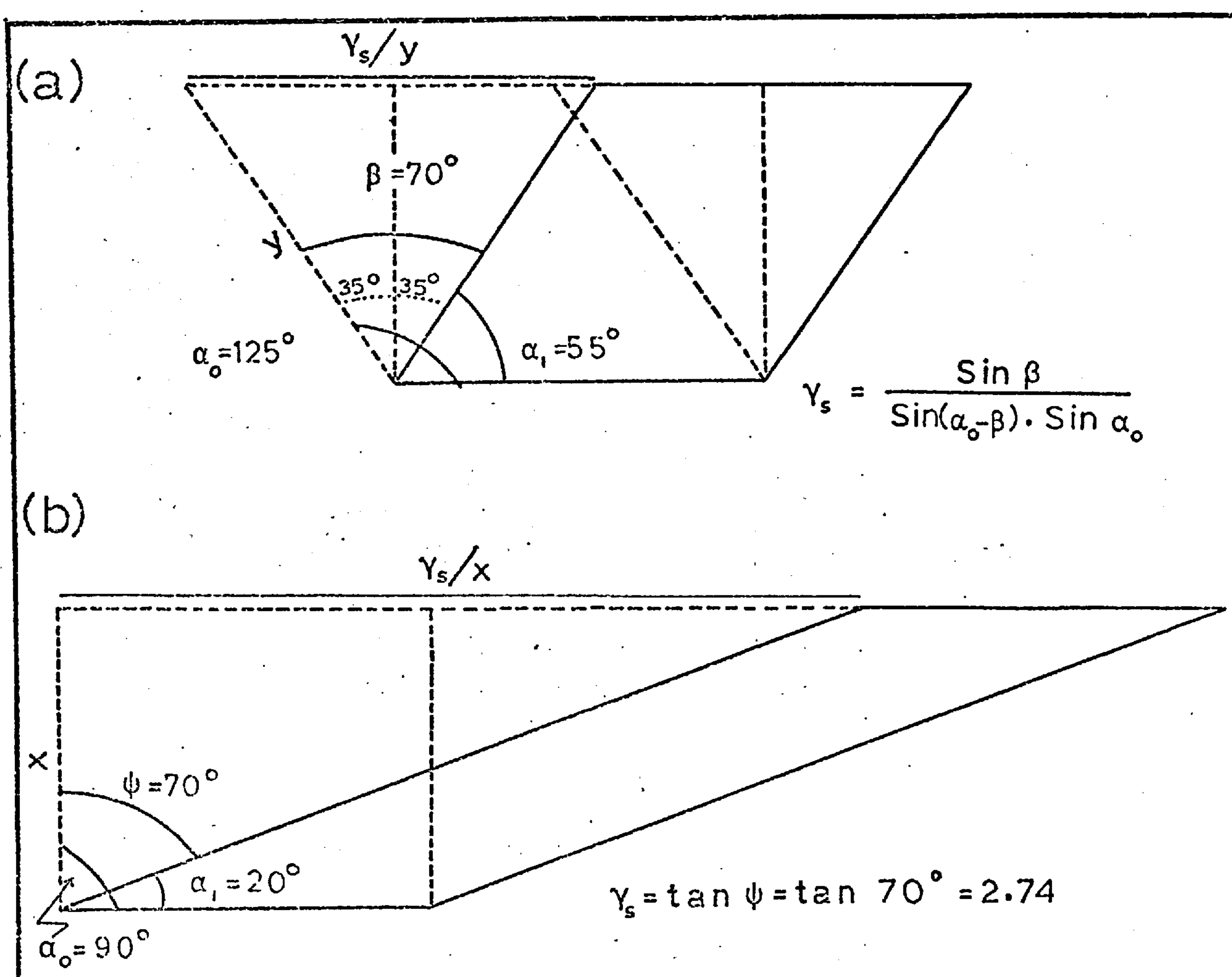

Fig. 4.14 Modified method of calculation of the amount of simple shear (γ_s) from the geometry of the simple shear box.

(a) Initial apical angle of the box $\alpha_o = 125^\circ$

(b) Initial apical angle of the box $\alpha_o = 90^\circ$

The shearing angle ψ is a measure of the deflection of a pair of lines originally at right angles (Ramsay, 1967, p.53). The relationship between ψ and γ_s in the box has been determined for the two cases : (i) $\alpha_o = 90^\circ$ and (ii) $\alpha_o = 125^\circ$. Comparing figures 4.14,a and 4.14,b, it is clearly observed that the physical lengths of γ_s/x and γ_s/y are different because they are related to the apical angle (α_o).

A general solution for the determination of ψ and γ_s for any α_o can be evaluated from figure 4.15. Let us consider any angular deflection β in a box whose apical angle α_o is greater than 90°. Note, β is not equal to ψ, see figure 4.15.

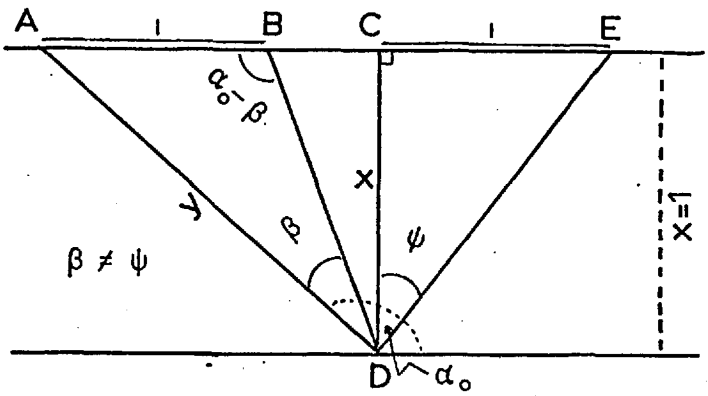

Fig. 4.15 Determination of shearing angle ψ from the deflection of a line which was set originally at an angle greater than 90° (i.e. $\alpha_o > 90^\circ$).

The length 'l' traversed due to the deflection of β is the same everywhere in the line AE. Measuring 'l' from the right angle position 'C' and joining ED, the required angle of shear ψ can be evaluated (fig. 4.15).

By following the sine rule in ΔABD, a relationship can be obtained,

$$1/\sin\beta = y/\sin(\alpha_o - \beta) \quad (4.9)$$

where α_o is the initial apical angle and y is the length of AD.

In ΔCED, $\tan\psi = 1$ (4.10)

since 'x' is taken as unity.

Substituting equation 4.10 in eq. 4.9, gives

$$\tan\psi/\sin\beta = y/\sin(\alpha_o - \beta) \quad (4.11)$$

Similarly from ΔACD, it follows that

$$y = 1/\sin\alpha_o \quad (4.12)$$

Substituting eq. 4.12 into eq. 4.11, gives the general solution

$$\tan\psi = \sin\beta/\sin(\alpha_o - \beta) \cdot \sin\alpha_o \quad (4.13)$$

If the box is set in such a way that α_o is 90° the above expression (eq. 4.13) will be reduced to

$$\tan\psi = \tan\beta$$

$$\text{i.e.} \quad \psi = \beta \quad (4.14)$$

which conforms with the definition of angle of shear ψ.

For the comparative study of the deformation history of the box initially set at $\alpha_o = 125^\circ$, the amount of shear strain along with the corresponding principal strains are derived by using both Gay's and the modified method. The results of the two methods were not consistent (fig. 4.16). One run of experiment was performed to check the predicted results. Experimental results (table 5) measured directly from the deformed ellipses show a close consistency (fig. 4.17) with the results calculated from the theory using modified method. This new technique for calculating γ_s is, therefore, used in all future analyses.

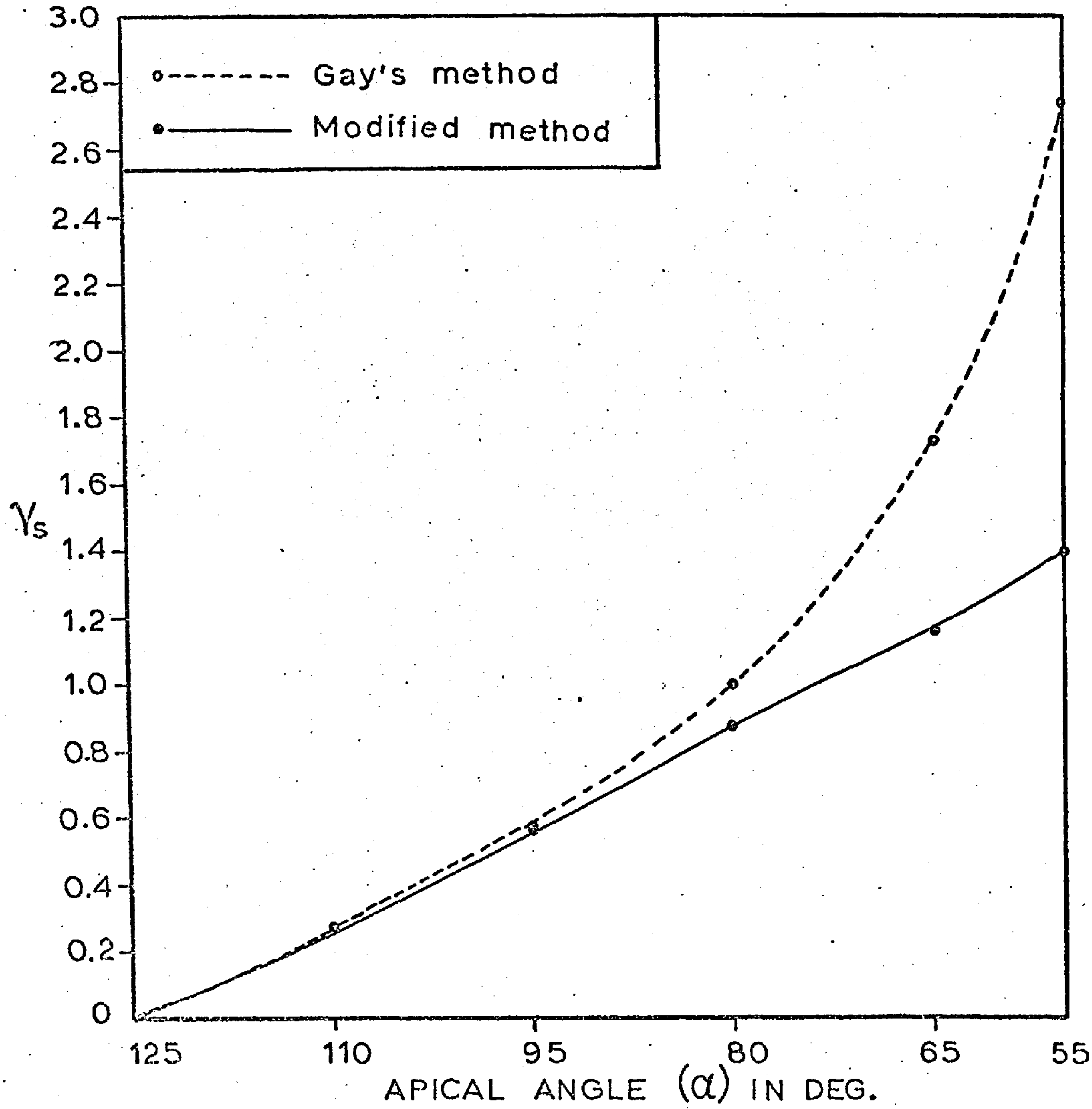

Fig. 4.16 Comparative study of Gay's method and the modified method of the calculation of γ_s from the geometry of the simple shear box.

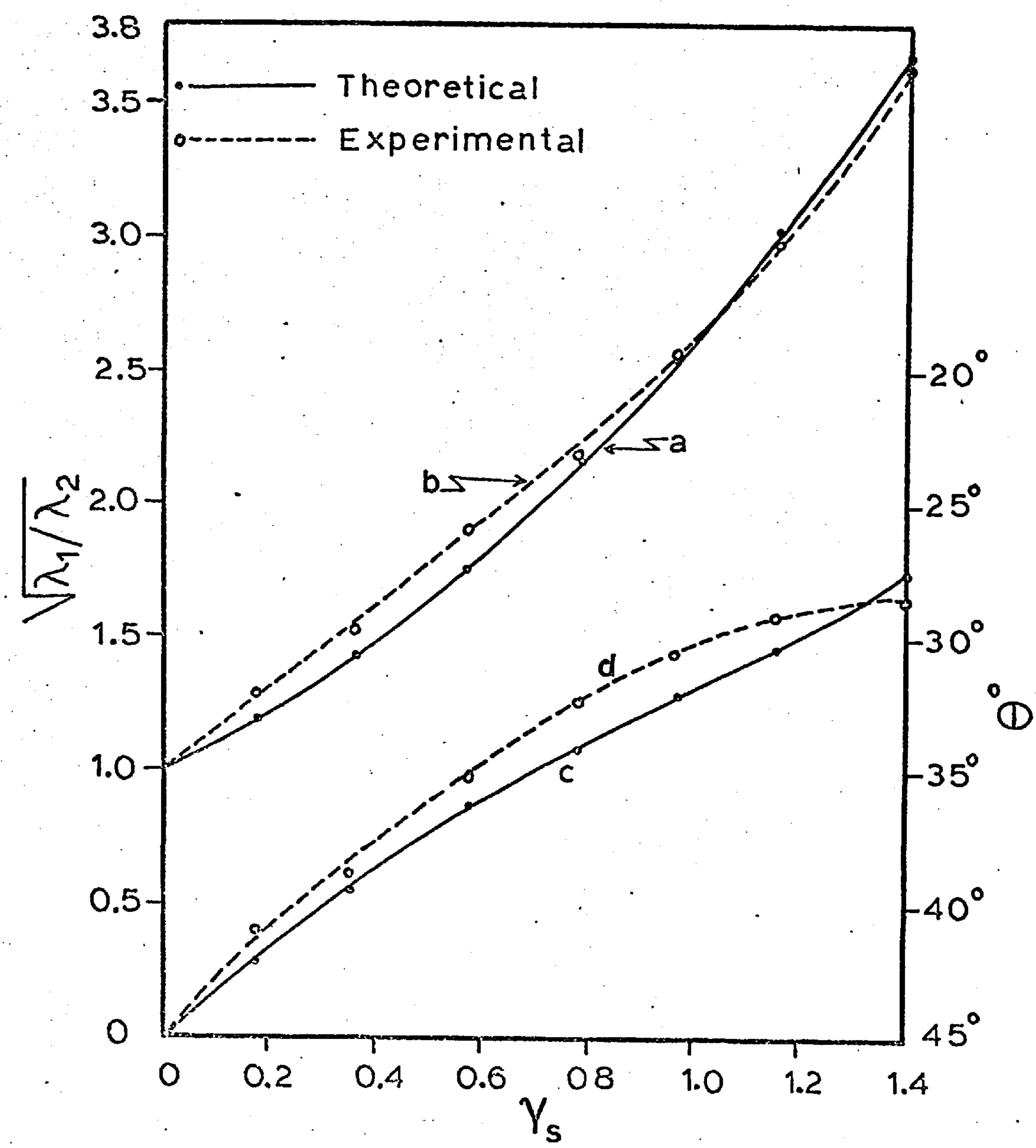

Fig. 4.17 Progressive development of the observed (from an experiment) and predicted (from theory) strains in the matrix deformed inside the modified simple shear box.

4.7 EXPERIMENTAL PROCEDURE

The deformation procedures for the two boxes are slightly different and are discussed separately.

The lozenge-shaped irrotational strain box was set on a greased glass plate and two thirds of it was filled with linseed oil putty. The sides of the box were then positioned at the desired initial apical angle (in all experiments $\alpha_o = 65^o$). Wooden particles simulating prophyroblasts and strips of rectangular wooden blocks put together to form a rigid layer representing a belemnite, were pressed into the surface of putty. The surface of the putty and the object were levelled very carefully to prevent the development of an uncontrolled inhomogeneity during deformation. A rectangular grid or circular markers (or both in some cases) were imprinted on the surface of putty as strain markers. These markers were printed using graphite powder which did not disturb any movement of the putty. The box was then allowed to deform by applying pressure at the two diagonally opposite corners by hand. The deformation of the box was stopped after reaching the desired apical angle (α_1). Starting from an initial position ($\alpha_o = 65^o$) to final stage ($\alpha_1 = 115^o$), five different stages of deformation were recorded at various apical angles ($\alpha_o = 65^o$, $\alpha_1 = 75^o$, $\alpha_1 = 90^o$, $\alpha_1 = 105^o$ and $\alpha_1 = 115^o$).

Simple shear box was set up with the U-plates together to form a hollow box. The plates were thoroughly greased in order to allow them to slide past each other smoothly. The matrix materials and inclusions were placed in the strain box and strain markers were printed as described above. The box was then positioned at its initial apical angle ($\alpha_o = 125^o$) and deformed by allowing the movable plate to slide sideways. The progressive stages of deformation were recorded at different apical angles (e.g. $\alpha_o = 125^o$, $\alpha_1 = 110^o$, $\alpha_1 = 95^o$,

$\alpha_1 = 80^{\circ}$, $\alpha_1 = 65^{\circ}$ and $\alpha_1 = 55^{\circ}$).

The matrix materials for both the cases were thoroughly kneaded after each experimental run to remove any anisotropy and changes of properties of materials (e.g. removal of oil in the putty around wooden blocks) that developed during the run. As putty tends to dry out when exposed to the air for a few days, linseed oil was added to retain constant ductility of the material during successive experiments.

The different stages of deformation were recorded photographically using a 35 mm. camera and necessary measurements were taken from the photographs using a milimetre rule. Some errors of measurements were inevitable and it was assumed that the smaller the changes measured, the higher the proportional error and vice-versa.

CHAPTER 5. EXPERIMENTAL RESULTS OF THE MOTION OF THE RIGID INCLUSIONS

5.1 INTRODUCTION

Observations on natural examples of porphyroblasts suggest that the matrix around each crystal has undergone a complex deformation history. Two simple types of deformations: (i) irrotational strain and (ii) simple shear have been investigated experimentally. The experiments represented here were performed in two boxes, described in Chapter 4.

The theory (Chapter 3) indicates that the distortion of the matrix and the rigid rotation of the inclusion is a function of several variables. One of the most important is the shape of the object included in the matrix. Two types of shapes, equidimensional (circular) and elliptical, were selected for the experiments. The behaviour of the included objects and the surrounding matrix depends upon their shape defined by the diameter of the equidimensional objects and axes a, b of the elliptical objects.

A theoretical study shows that the finite orientation of an inclusion is dependent on its initial orientation. To examine this aspect experimentally and to obtain the relationship between the finite and initial orientations, several runs of experiments were undertaken each with a different value for initial orientation. The number of experimental runs carried out is shown in the table A.

Table A

<table>
<tr><th colspan="2" rowspan="2">Shape</th><th colspan="2">No. of experiments performed (varying θ_i)</th></tr>
<tr><th>Inside irrotational strain box</th><th>Inside simple shear box</th></tr>
<tr><td colspan="2">Equidimensional</td><td>4</td><td>3</td></tr>
<tr><td rowspan="3">Elliptical</td><td>a/b = 2:1</td><td>4</td><td>4</td></tr>
<tr><td>a/b = 3:1</td><td>4</td><td>4</td></tr>
<tr><td>a/b = 4:1</td><td>4</td><td>4</td></tr>
</table>

The orientation of the grid lines inside (S_i) and outside (S_e) the inclusions were measured from the photographs taken progressively during deformation. These measurements were made with reference to the extension direction in the irrotational strain experiments and with reference to the shearing direction in simple shear experiments. The results of all the experiments are recorded in Appendix B (table 6 - 10). The effect of various factors (e.g. initial orientation, axial ratio a/b, the type of deformation) on rotation is investigated experimentally by varying shapes, sizes and initial orientation of the porphyroblasts.

5.2 FINITE ORIENTATION AND THE AMOUNT OF ROTATION OF RIGID INCLUSIONS

The motions of rigid inclusions undergoing irrotational or simple shear deformation were measured and the results are compared with the theoretically predicted motions. The finite orientation and the amount of rotation were evaluated from grid markers.

5.2.1 Equidimensional Inclusions

Irrotational Strain

When rigid equidimensional inclusions are subjected to irrotational strain they remain stationary while the surrounding material suffers rotation (plates III and IV). The orientations of the grid markers measured from four different experiments are recorded in table 6 which are graphically represented in figure 5.1. These results agree well with the theoretical prodictions and satisfy the equation 3.10 derived from the theory of pure shear deformation. Any grid markers around the inclusions which are not parallel to the principal finite elongation directions rotate, and do so by differing

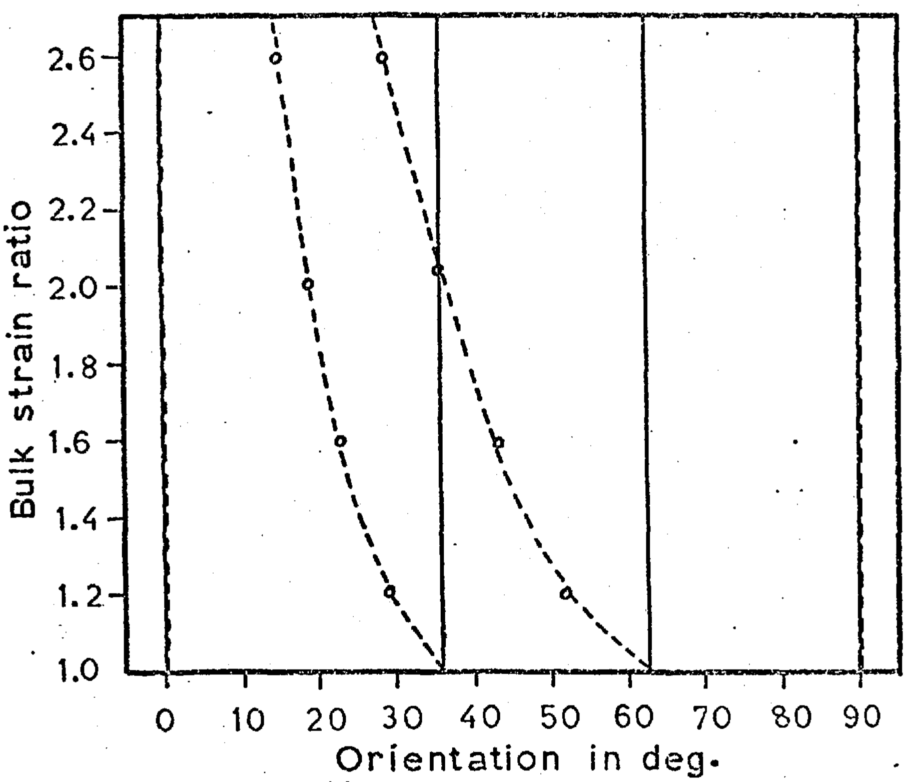

Fig. 5.1 Behaviour of an equidimensional (circular) inclusion and its surrounding matrix undergoing progressive deformation in the irrotational strain box. Solid and broken lines represent experimental results for the inclusion and the matrix respectively.

amounts depending on their initial orientation. Those lines oriented parallel or normal to the extension direction of the box show no rotation (fig. 5.1).

Simple shear

Rigid equidimensional inclusions undergoing simple shear deformation always undergo a rotation (plates XI and XII). Three different experiments were carried out with objects of differing size (diameter). Experimental results (table 7) and theoretical predictions for the motion of equidimensional inclusions under simple shear deformation are compared in figure 5.2,and it is found that the experimental results closely conform to the theoretical predictions. The relationships between the rotation of inclusions and that of the matrix materials were also examined. It is observed that the matrix material always suffers a greater rotation than the inclusions (fig. 5.3).

5.2.2 Elliptical Inclusions

With elliptical inclusions, finite orientation and the amount of rotation can not be determined as simple as with equidimensional objects. The shape and initial orientation of an elliptical inclusion influence its rotation. The type of deformation is an important factor controlling the direction and the amount of rotation. Twenty four experimental runs were carried out with the two types of deformation. The results of some of the experimental runs are shown in plates V to X and plates XIII to XVIII.

Irrotational Strain

The results of the experiments performed by changing the shape and initial orientation θ_{ie} of rigid object (measured with

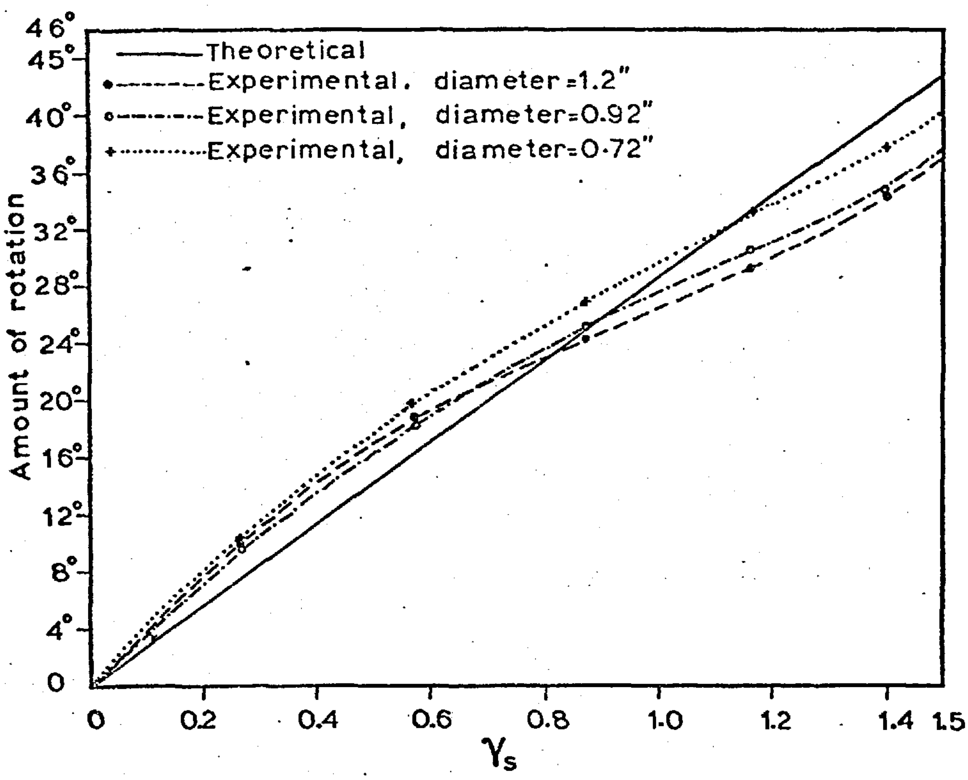

Fig. 5.2 Motion of rigid equidimensional inclusions (with varying diameter) set in a matrix undergoing simple shear deformation. γ_s represents amount of simple shear.

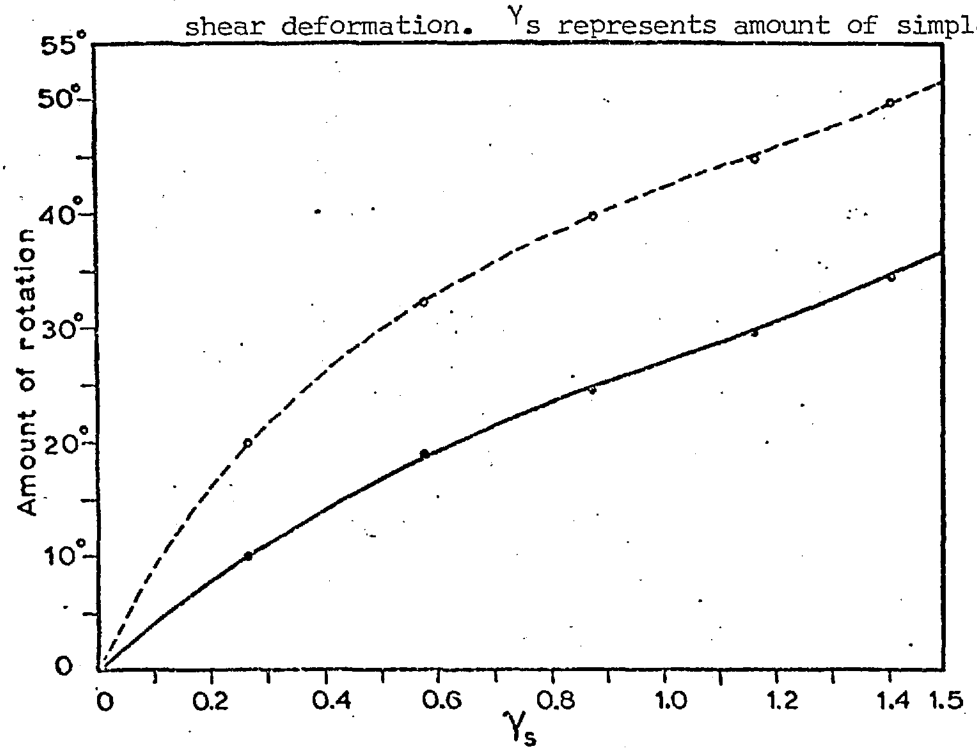

Fig. 5.3 Relationship between the motion of an equidimensional inclusion and the matrix in which the inclusion is embedded during progressive simple shear deformation. γ_s is the amount of simple shear.

reference to the extension direction) undergoing irrotational bulk strain are recorded in table 8.

The finite orientations of the elliptical inclusions at different stages of deformation for various θ_{ie} values are shown in figure 5.4 and these are compared with the predictions derived from the theory. The theoretical curves here relate to pure shear deformation - but the observed results were obtained from the experiments performed in the strain box which does not give progressive pure shear deformation. The exact relationship between the irrotational strain and true pure shear condition were discussed earlier (fig. 4.9 in chapter 4). Surprisingly, the curves constructed from experimental observations of the motion of elliptical inclusion undergoing irrotational strain and curves predicted by the theory of pure shear are in close agreement (fig. 5.4). Where the elliptical objects were originally oriented with $\theta_{ie} = 0^{\circ}$ or 90°, they did not rotate.

Simple Shear

Table 9 shows the results of all the experiments performed in the simple shear box and these results are graphically presented in figure 5.5 along with the theoretical curves. It can be seen that within the limits of experimental error, the experimental and theoretical graphs are in agreement.

The experimental results for the amount of rotation of the elliptical inclusions are plotted in figure 5.6 which show that the amount of rotation increases with an increase of strain. It is most significant that the curve for $\theta_{is} = 126^{\circ}$ in all the cases (a, b and c of fig. 5.6) intersects the curve for $\theta_{is} = 90^{\circ}$ (in the case of simple shear deformation, θ_{is} represent the initial orientation of an elliptical object measured with reference to the shearing direction). In

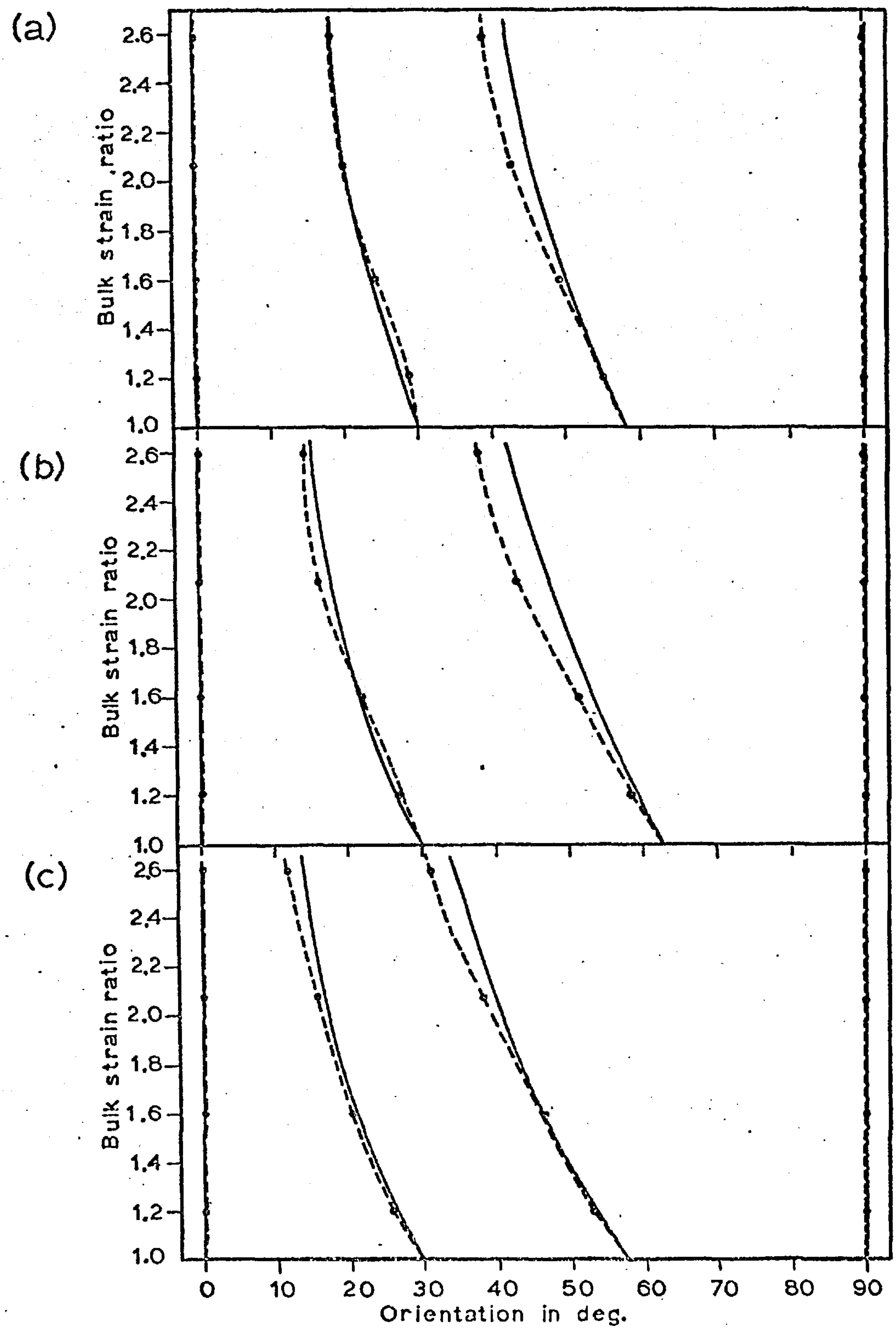

Fig. 5.4 Motion of rigid elliptical inclusions set in a matrix (putty) undergoing progressive irrotational strain deformation. Solid and broken lines represent theoretical and experimental results respectively.
(a) a/b = 2:1; (b) a/b = 3:1; (c) a/b = 4:1

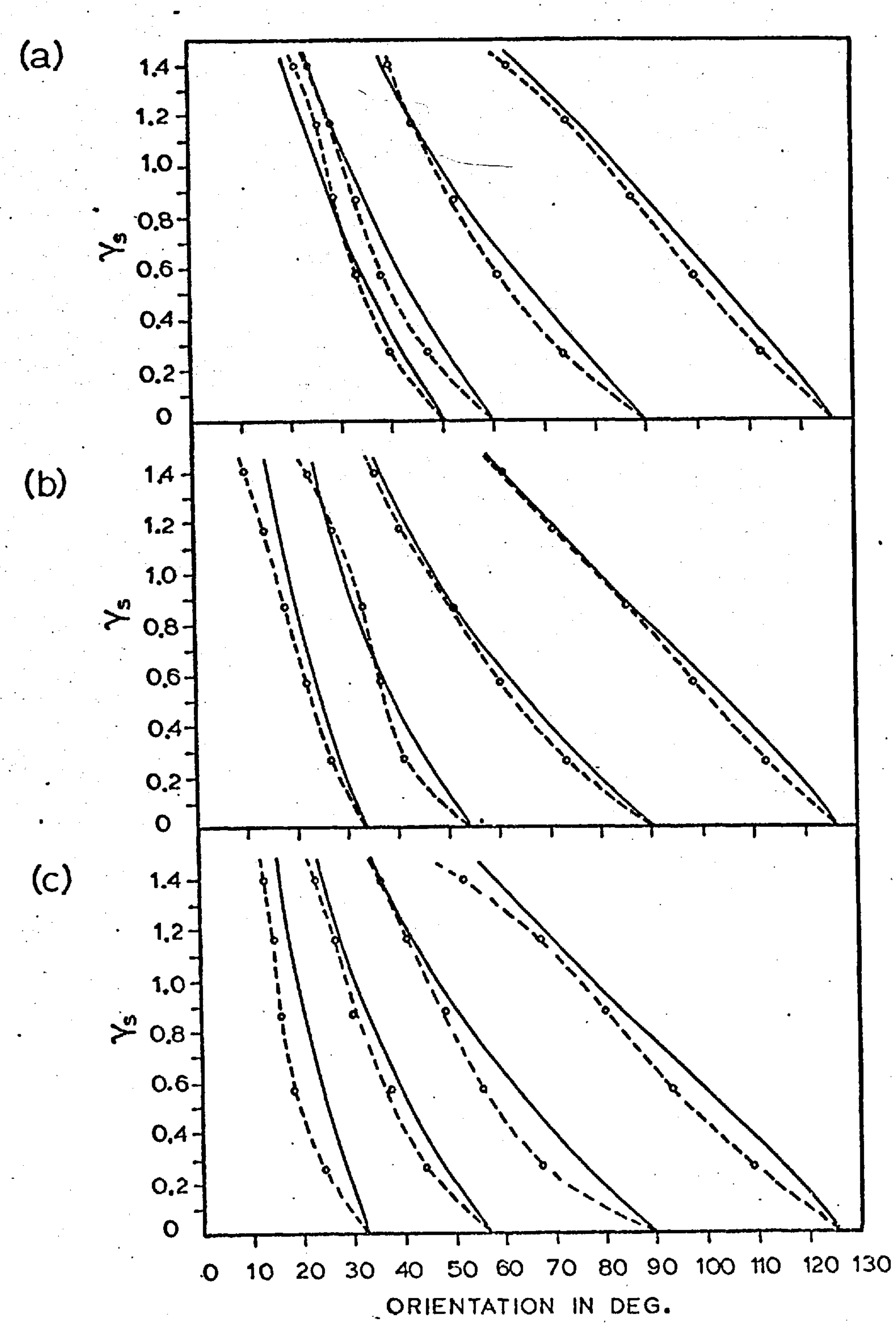

Fig. 5.5 Motion of rigid elliptical inclusions set in a matrix undergoing progressive simple shear deformation. Solid and broken lines represent theoretical and experimental curves respectively.
(a) a/b = 2:1; (b) a/b = 3:1; (c) a/b = 4:1

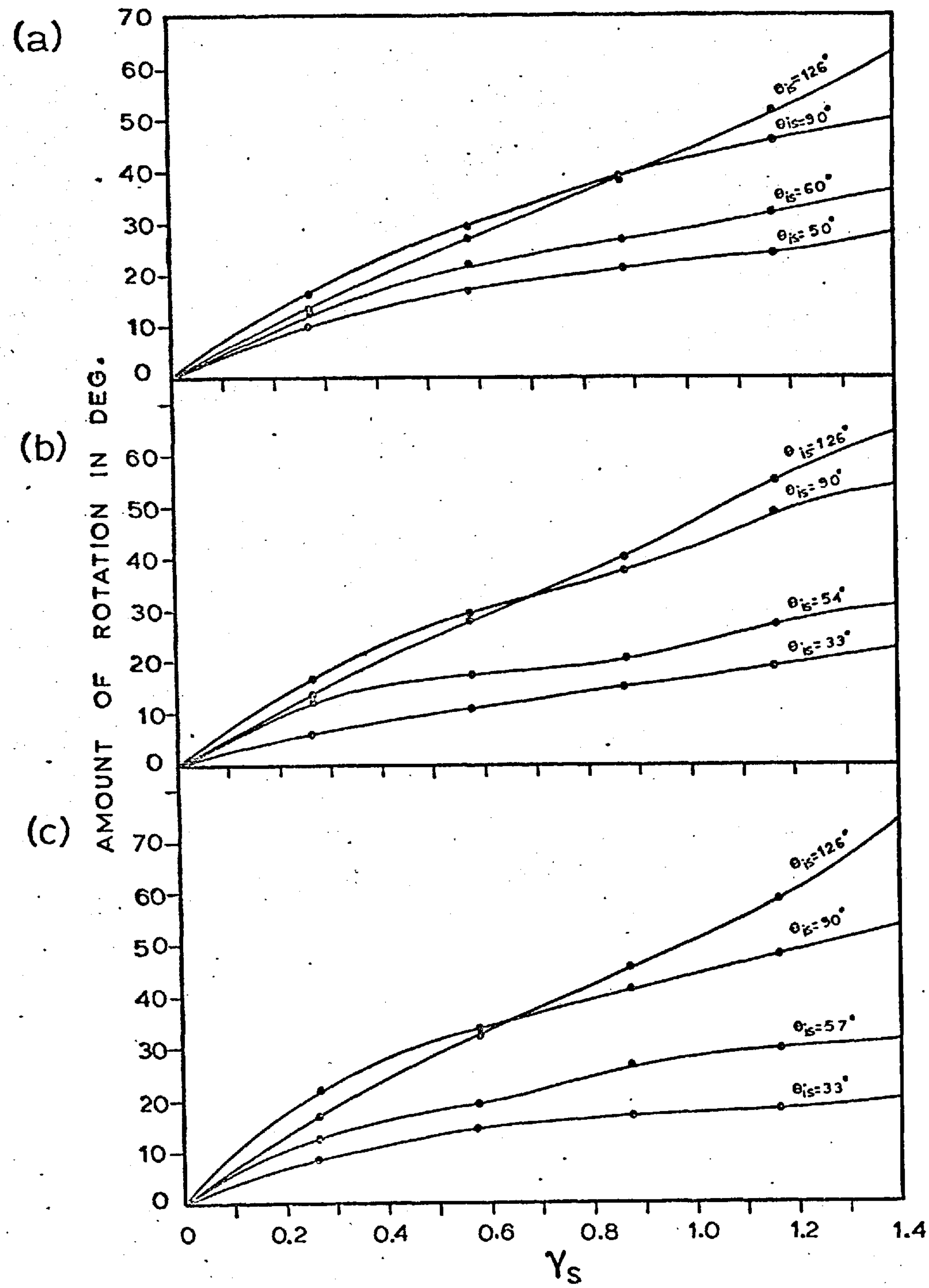

Fig. 5.6 Rotation of rigid elliptical inclusions during progressive simple shear deformation. γ_s represents the amount of simple shear and θ_{is} represents initial orientation of the inclusion with respect to the shearing direction.

(a) a/b = 2:1; (b) a/b = 3:1; (c) a/b = 4:1

all three experiments the rotation rate for $\theta_{is} = 126^{\circ}$ is slower than that for $\theta_{is} = 90^{\circ}$ during the early stages of deformation and is higher during the later stages of deformation. On the other hand, comparison of the curves for $\theta_{is} = 90^{\circ}$ for different a/b ratios demonstrates that the rate of rotation decreases progressively with deformation. The curves for $\theta_{is} < 90^{\circ}$ clearly correspond with the overall trend of that for $\theta_{is} = 90^{\circ}$. If the initial orientation of the inclusion is such that $\theta_{is} < 90^{\circ}$, it is also observed that for any given strain the amount of rotation decreases with the decrease of θ_{is} (initial orientation measured with reference to the shearing direction).

By measuring the orientations of internal (S_i)and external (S_e) marker lines (table 10), the relationship between the rotation of the inclusions and the surrounding matrix was determined. The graphical representation (fig. 5.7) of the results shows that the difference in orientation between (S_i) and (S_e) is generally small and that the difference is non-linearly related to the amount of shear. The results indicate that an elliptical inclusion may sometimes rotate more than the matrix and that the rotation difference depends on the initial orientation θ_{is}. For the case of $\theta_{is} = 90^{\circ}$, the amount of rotation of the matrix is slightly more than that of the inclusion, whereas, with experiments carried out with $\theta_{is} = 33^{\circ}$ and with $\theta_{is} = 58^{\circ}$, the situation is reversed (fig. 5.7). Whether the inclusion rotates faster or slower than the matrix is found to depend on its initial orientation with respect to the extension direction of the finite strain ellipse.

5.3 EFFECT OF AXIAL RATIO (a/b) OF RIGID INCLUSIONS ON ROTATION

5.3.1 Equidimensional Inclusions

From the theoretical point of view, the amount and the rate

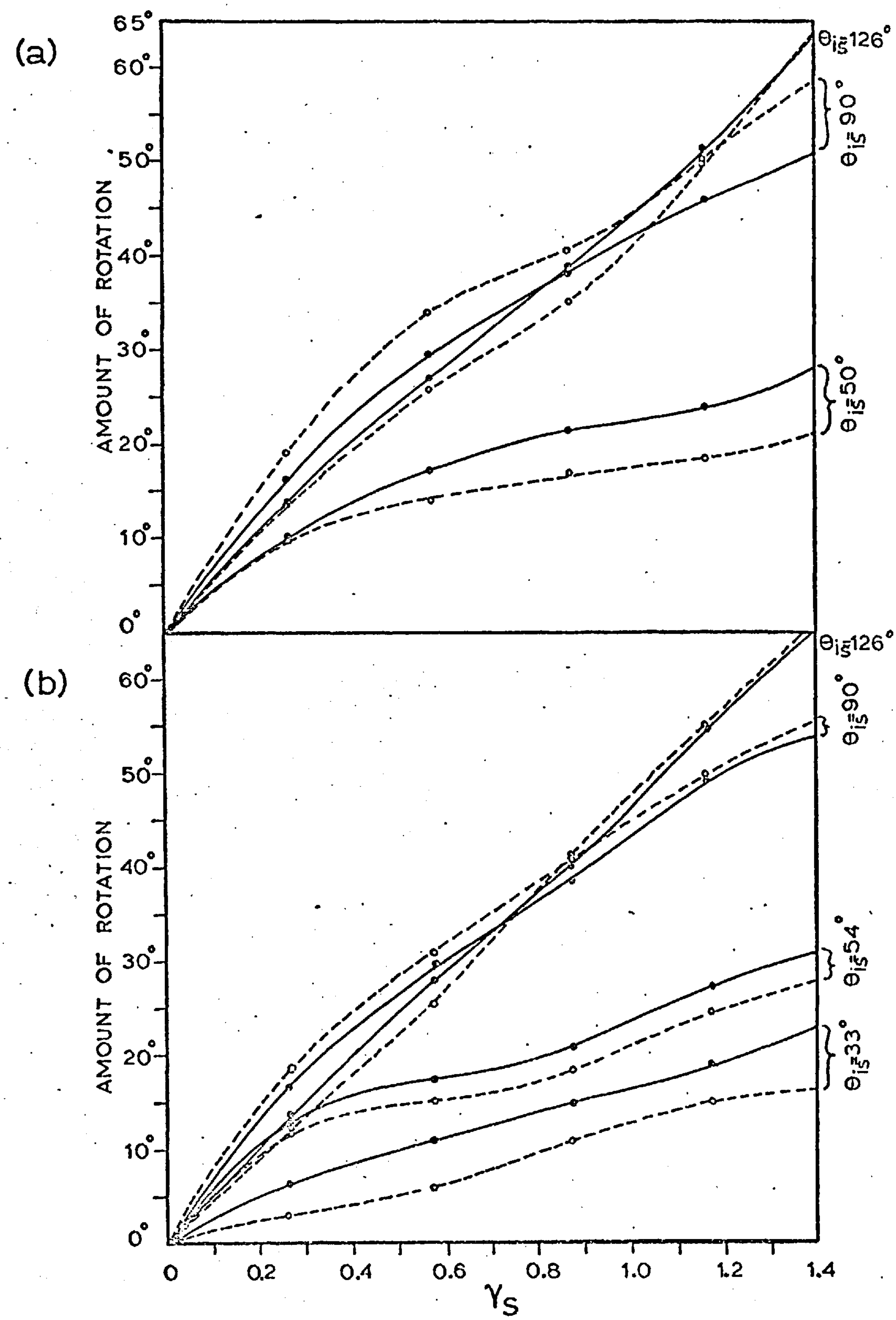

Fig. 5.7 Comparative study of the rotation of rigid elliptical inclusions and their surrounding matrix during progressive simple shear deformation. Solid lines and broken lines represent the graphs for the inclusions and the matrix respectively.

of rotation should not be affected by the variation of the sizes of the object undergoing simple shear deformation. Three experiments with various sizes (large = 1.2" diameter, medium = 0.92" diameter and small = 0.72" diameter) were performed to examine these predictions. The results are presented in figure 5.2 along with the theoretical plot and show that the graphs for observed results are approximately linear. This is in agreement with the theoretical prediction. Within the limits of experimental error, it can be seen that the rate of rotation of equidimensional inclusions is approximately constant.

5.3.2 Elliptical Inclusions

Irrotational strain

A few experiments were carried out with rigid elliptical objects of fixed initial orientation but varying axial ratios. The amount of rotation varied with the axial ratio of the elliptical object. The experimental results are illustrated in figure 5.8. Theoretical results show a close conformity with the experimental curves and that the greatest rotation occurs where the axial ratio is largest.

Simple shear

The results of experiments performed by varying axial ratio a/b and keeping constant initial orientation are presented in figure 5.9. The amount of rotation increases with increase in the amount of shear strain γ_s. The curves for different inclusions are close indicating that the axial ratio of the elliptical inclusions have little influence on the rate of rotation during simple shear.

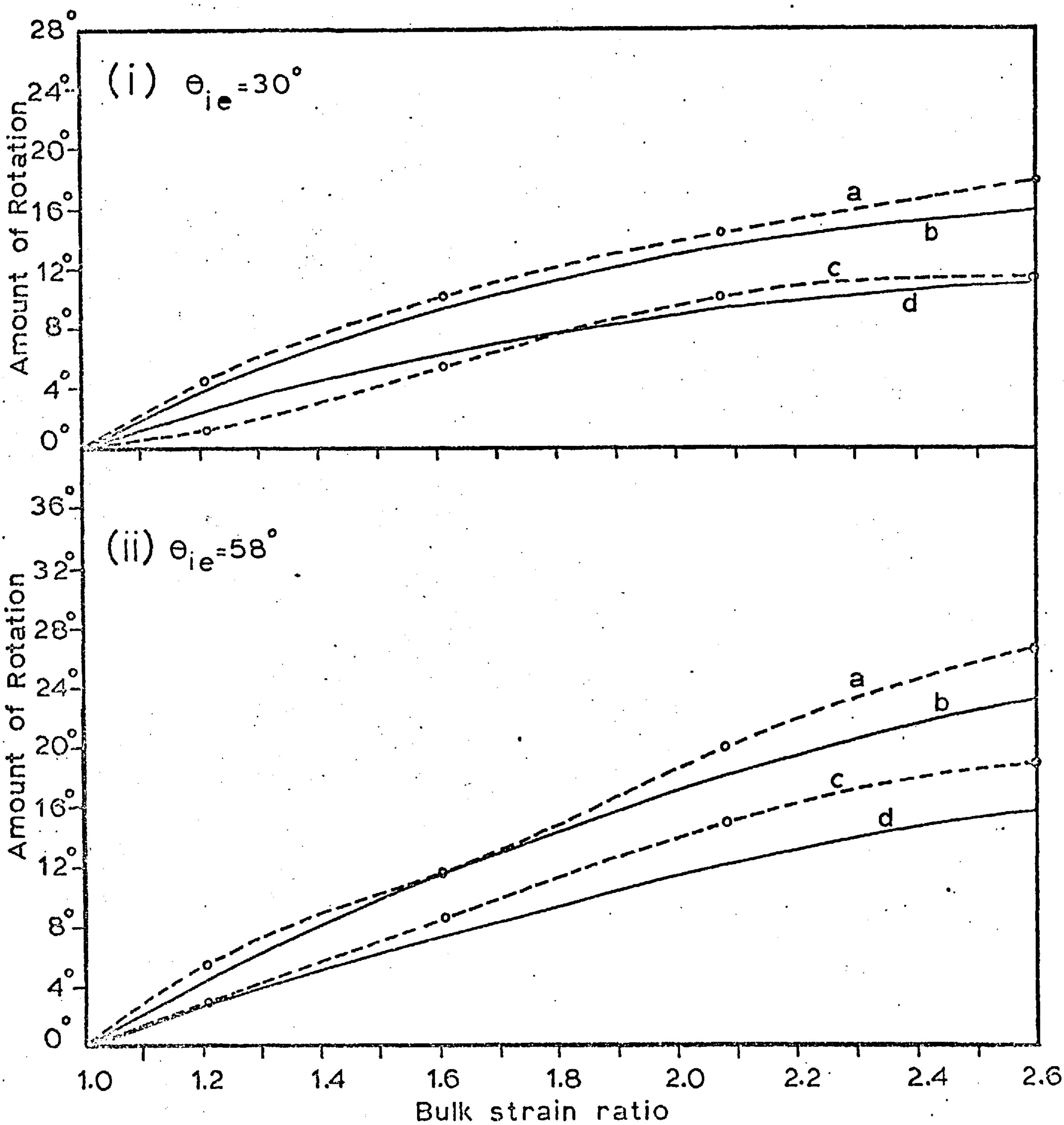

Fig 5.8 Effect of axial ratio (a/b) of elliptical inclusions on the amount of rotation during progressive irrotational strain deformation. θ_{ie} represents the initial orientation of the inclusion with reference to the principal extension direction.

(a) Experimental curve for an elliptical inclusion having a/b = 4:1

(b) Theoretical curve for an elliptical inclusion a/b = 4:1

(c) Experimental curve for an elliptical inclusion a/b = 2:1

(d) Theoretical curve for an elliptical inclusion a/b = 2:1

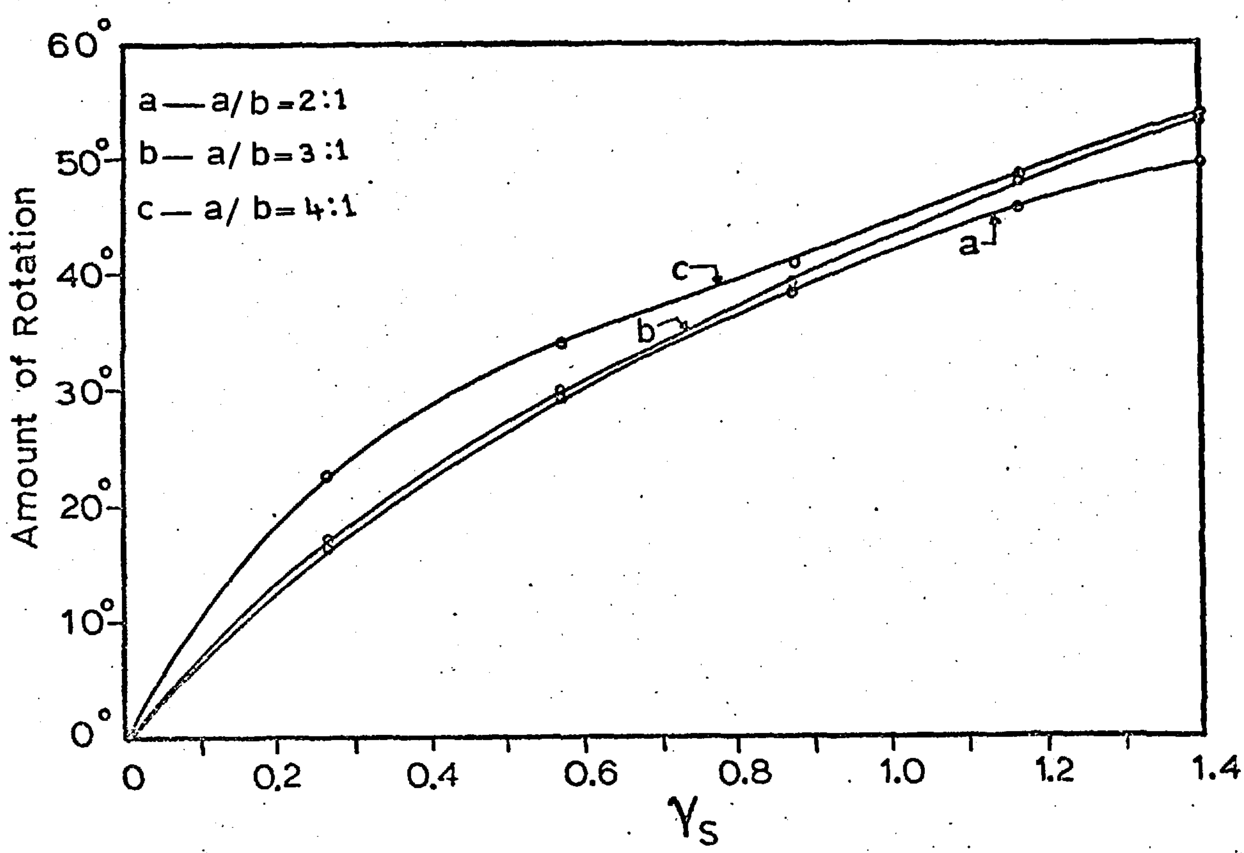

Fig. 5.9 Effect of the axial ratio (a/b) of elliptical inclusions on the amount of rotation during progressive simple shear deformation. All the three inclusions were originally oriented at $\theta_{is} = 90^{\circ}$ (measured with reference to the shearing direction).

5.4 EFFECT OF INITIAL ORIENTATION OF RIGID INCLUSIONS ON ROTATION

5.4.1 Equidimensional Inclusions

Equidimensional objects do not rotate during irrotational strain deformation and suffer a constant rate of rotation when deformed under simple shear.

5.4.2 Elliptical Inclusions

The shapes of the orientation curves are dependent on the initial orientation of the inclusions (fig. 5.4). These curves clearly indicate that the amount of rotation approaches zero as the initial orientation (θ_{ie}) comes closer to values 0° or 90° (i.e. parallel or normal to the extension direction of strain ellipse).

To investigate this relationship more precisely, three experiments were carried out with an inclusion having a/b = 3:1 and with varying initial orientation. The amount of rotation after deformation (strain ratio R = 2.6) are presented graphically in figure 5.10 along with the theoretical predictions. The overall shape of the curve constructed from the experimental data shows a marked similarity with the theoretically predicted curve. It is seen from this figure (5.10) that the amount of rotation for given strain clearly depends on the initial orientation of the inclusion.

Simple shear

The results of four experiments performed with an elliptical inclusion (a/b = 3:1) with various initial orientation θ_{is} (the angle measured with reference to shearing direction) are graphically presented in figure 5.11. A predicted curve is also plotted in figure 5.11 from the theory. The shape of the observed graph shows some conformity with that of the predicted curve, but the amount of observed rotation is

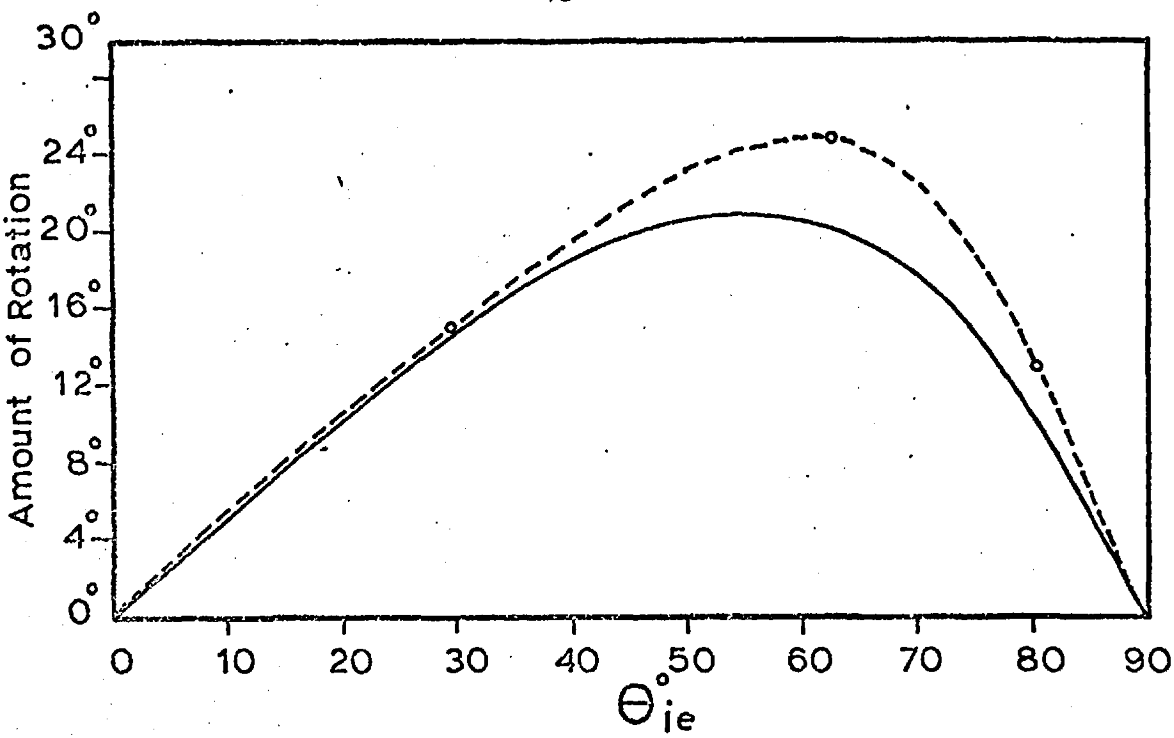

Fig. 5.10 Relationship between the amount of rotation and initial orientation (θ_{ie}) of an elliptical inclusion (a/b = 3:1) after finite deformation ($\sqrt{\lambda_1/\lambda_2}$ = 2.6) inside the irrotational strain box. Broken line represents experimental results and solid line is the graph predicted from the theory.

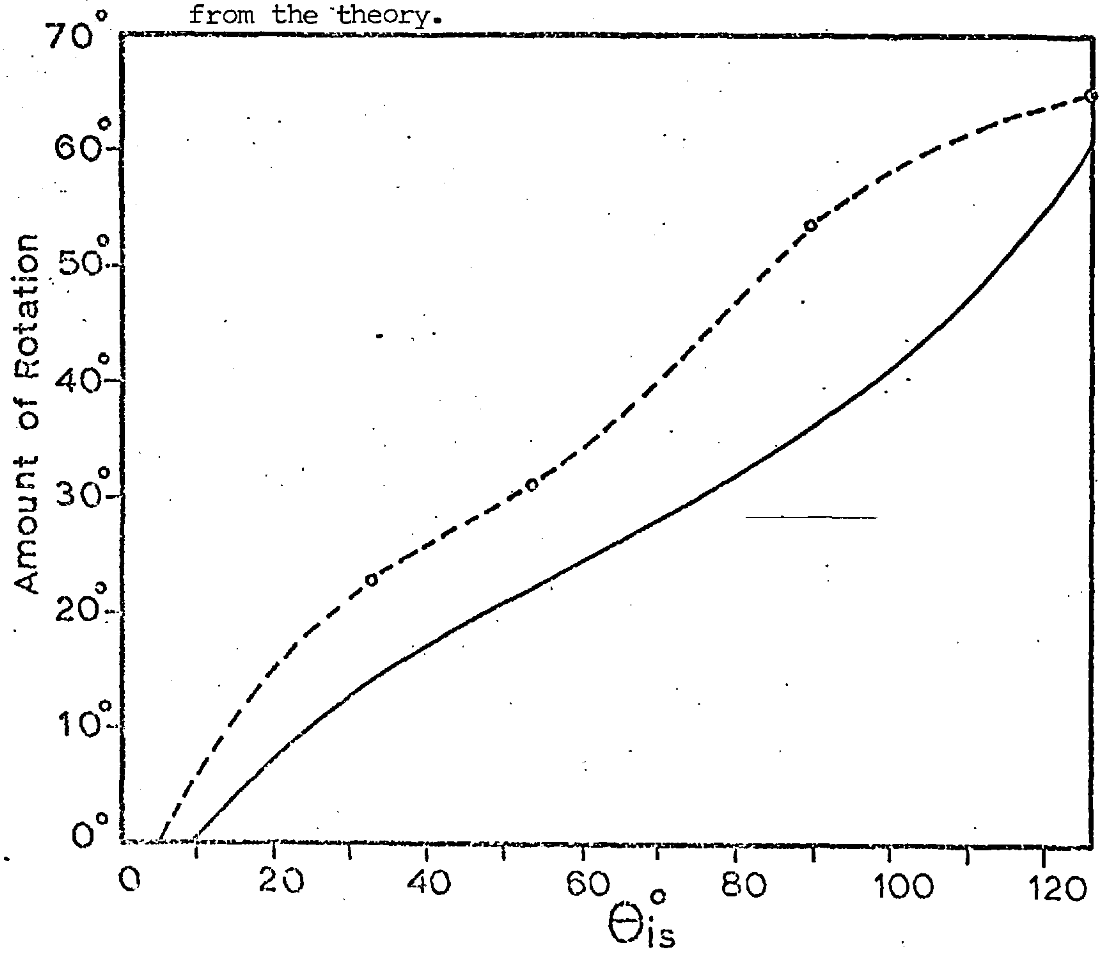

Fig. 5.11 Relationship between the amount of rotation and the initial orientation (θ_{is}) of an elliptical inclusion (a/b = 3:1) at the finite deformation (γ_s = 1.4) inside the simple shear box.

higher than that of the predicted results. The observation of the figure (5.11) shows that the amount of rotation increases with the increase of initial orientation (θ_{is}) of the inclusions.

The overall shapes of the curves of figures 5.10 and 5.11 are completely different. This shape difference is one of the characteristic features that can be used to distinguish between the two types of deformation.

5.5 BEHAVIOUR OF THE MATERIAL AROUND RIGID INCLUSIONS

The behaviour of the ductile matrix material in the complex strain zone around rigid inclusions was studied experimentally using grids and circular markers to evaluate the inhomogeneity of strain. The geometry of the distortions around the inclusions have been described using two methods: (i) displacement vector analysis and (ii) strain analysis. The simplest method of demonstrating movements that have taken place is by evaluating the displacement vectors. These vectors are obtained by joining the respective initial and final position of the points of grids. They can be determined for successive stages of deformation. The differences in vectors between the consecutive stages of deformation define the displacement difference vectors which indicate the flow of matrix during the deformation increment between the two stages.

Strain analysis is an important method of evaluating the principal aspects of the deformation tensor at different localities around the rigid object. A new technique for evaluating strain from the deformed grids by using a computer was developed with the collaboration of P. R. Cobbold (1973). This technique was used for the strain analysis in the matrix around rigid inclusions and is described in Appendix F.

5.5.1 Behaviour of the Matrix Around Equidimensional Inclusions

Irrotational strain

Displacement vectors constructed from two series of experiments are shown in figure 5.12 and 5.13. Although the grid lines simulating schistosity around a rigid inclusion exhibit different patterns (plates III and IV), the resultant vectors of the two cases show similar pattern. The vectors show variations in magnitude and in orientation around the object (figs. 5.12 and 5.13).

As θ_{ie} (initial orientation measured with reference to extension direction) has no significance in these experiments with equidimensional objects, only one series of experiments was necessary for strain analysis. Figure 5.14 shows the progressive changes in the shapes of finite strain ellipses defined by the values and orientations of the principal finite strain axes. The inspection of the figure 5.14 also shows that the maximum and minimum values of the strain are distributed symmetrically at four positions around the object.

Simple shear

Displacement vectors derived from one experiment (plate XI) are shown in figure 5.15. The progressive displacement of the material around the inclusion demonstrates that the material generally flow towards the shearing direction and not to the extension direction of the strain ellipse. The materials on either side of the shear box flow in opposite directions and there are certain regions where little or no displacement takes place (fig. 5.15).

Strain values and orientations were calculated from the deformed grids in the matrix around the equidimensional inclusion and

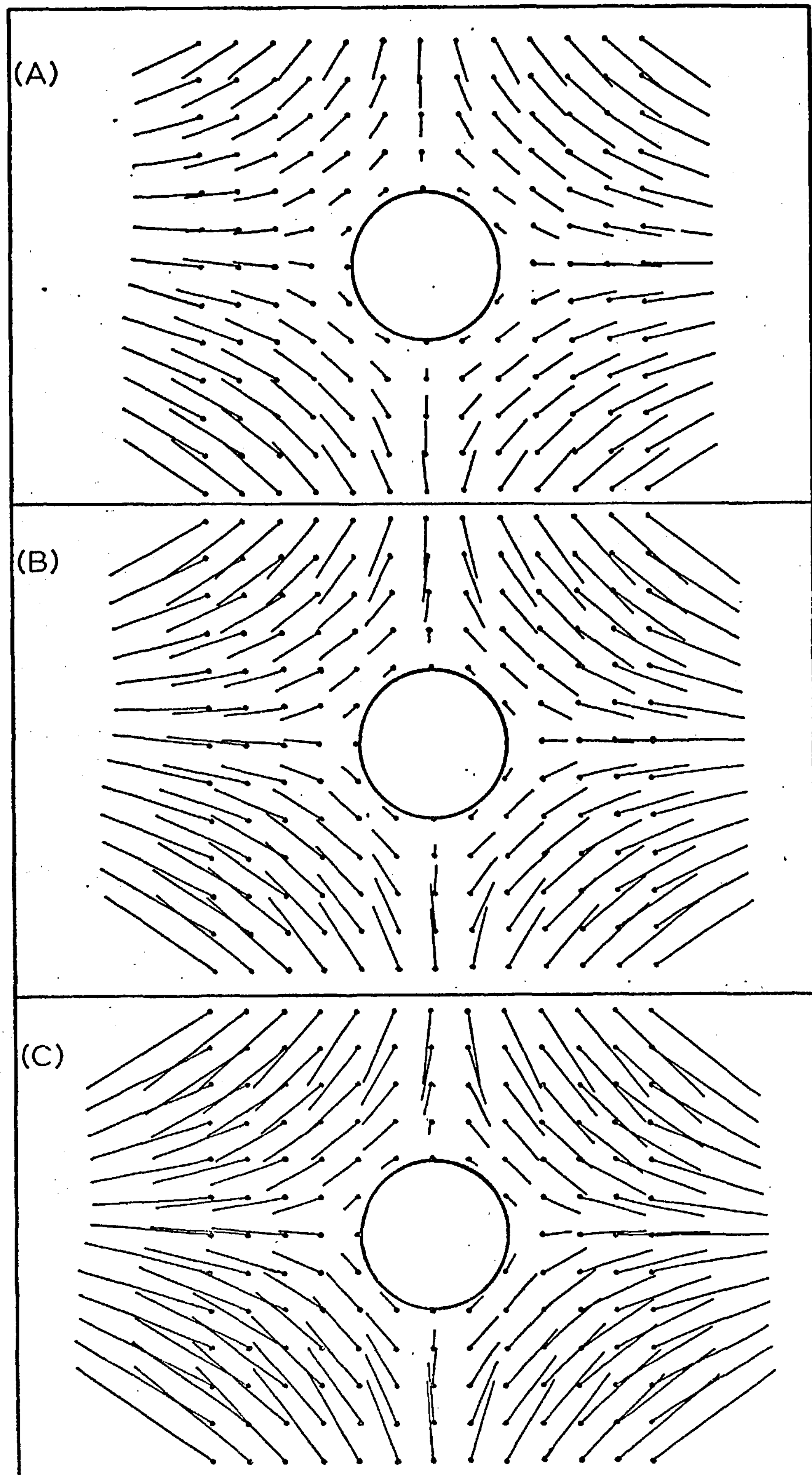

Fig. 5.12 Flow pattern of the matrix material around a rigid equidimensional inclusion undergoing progressive irrotational strain deformation. Grid lines were printed parallel and normal to the extension direction.

(A) $\sqrt{\lambda_1/\lambda_2} = 1.61$; (B) $\sqrt{\lambda_1/\lambda_2} = 2.08$; (C) $\sqrt{\lambda_1/\lambda_2} = 2.60$

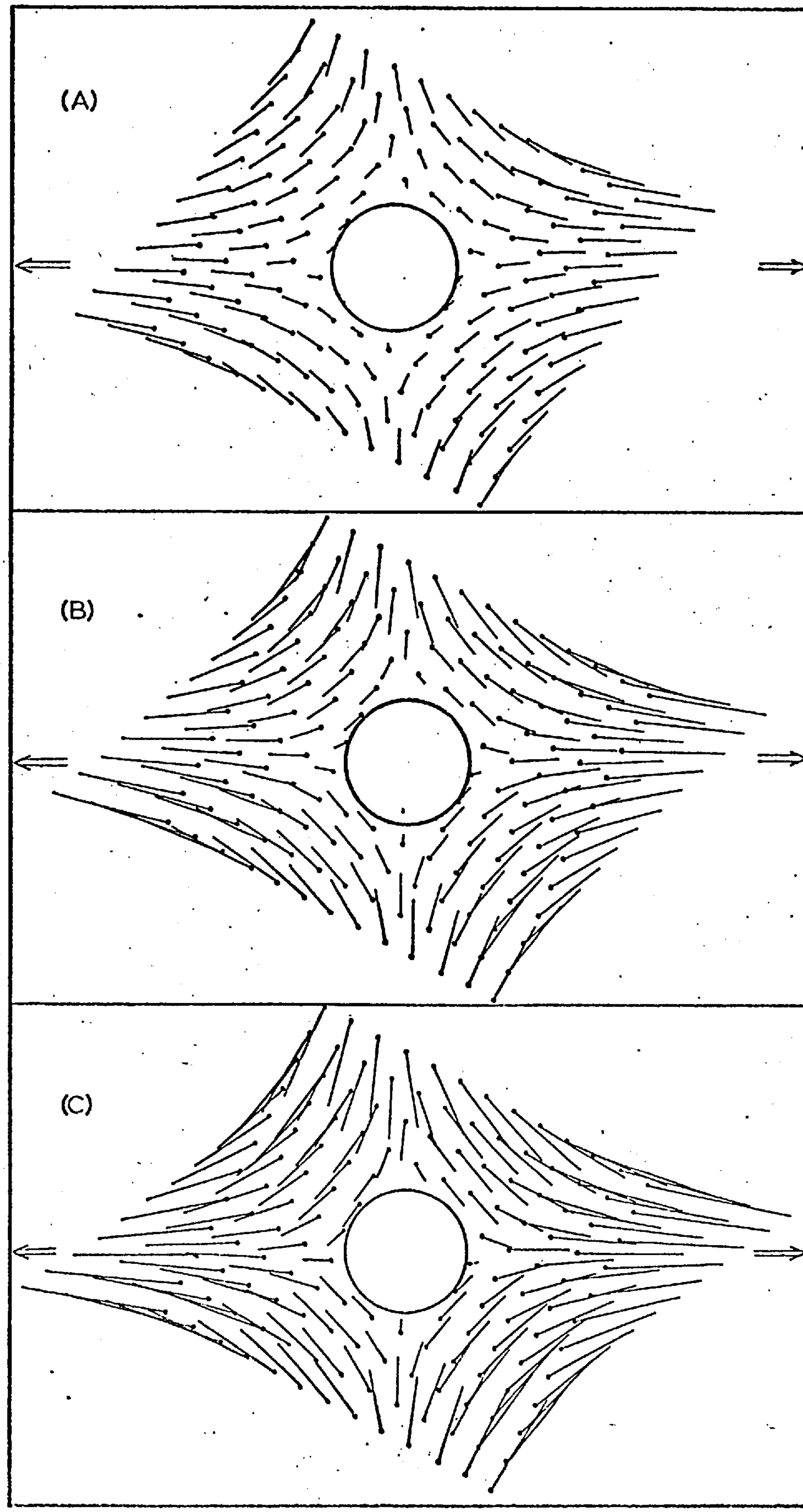

Fig. 5.13 Flow pattern of the matrix material around a rigid equi-dimensional (circular) inclusion during progressive irrotation strain deformation. The initial grid lines were printed at an angle to the extension direction.

(A) $\sqrt{\lambda_1/\lambda_2}=1.61$; (B) $\sqrt{\lambda_1/\lambda_2}=2.08$; (C) $\sqrt{\lambda_1/\lambda_2}=2.60$

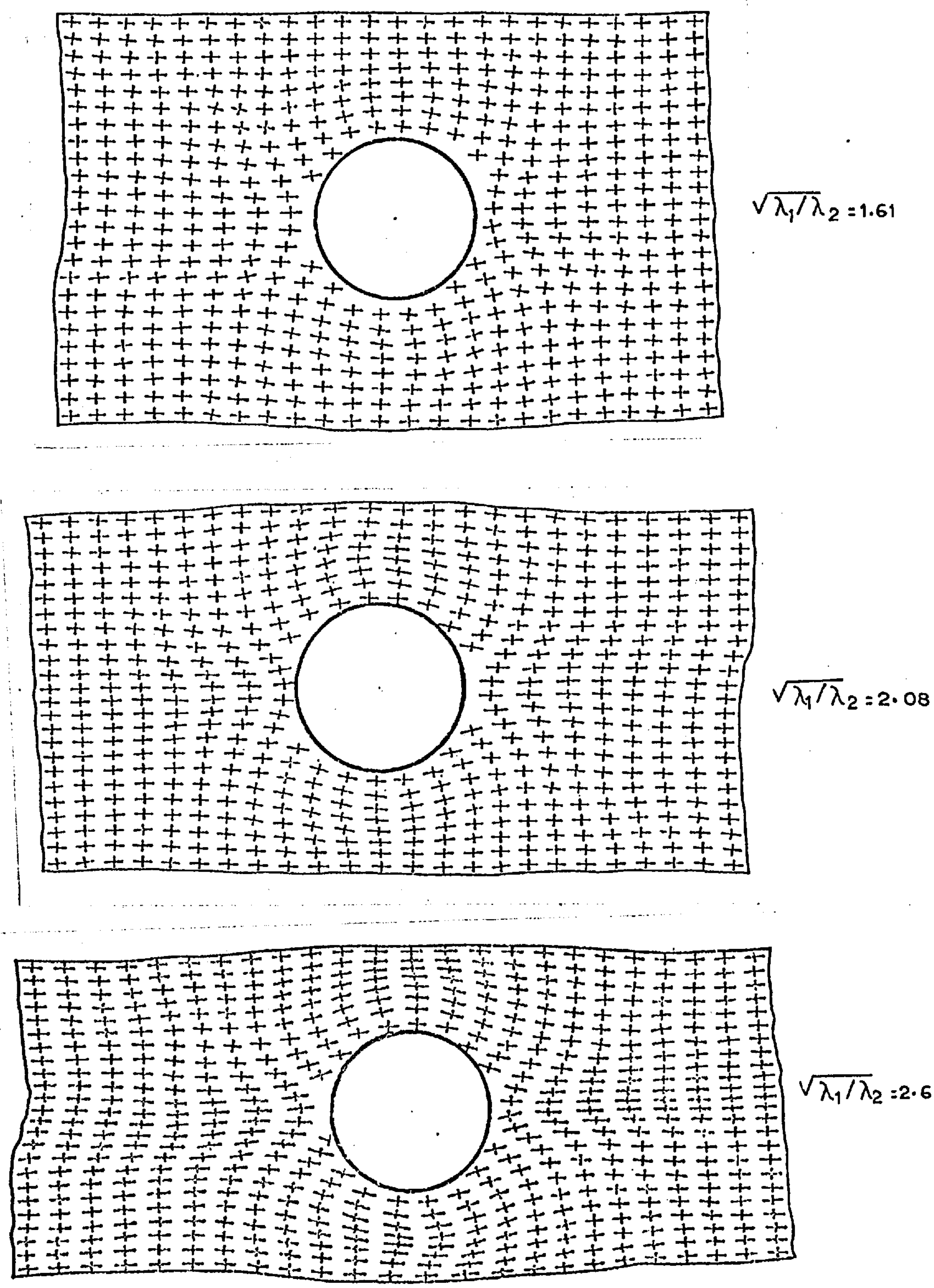

Fig. 5.14 Distribution of the magnitude and orientation of the principal axes of the strain ellipses in the matrix around a rigid equidimensional inclusion undergoing progressive irrotational strain deformation.

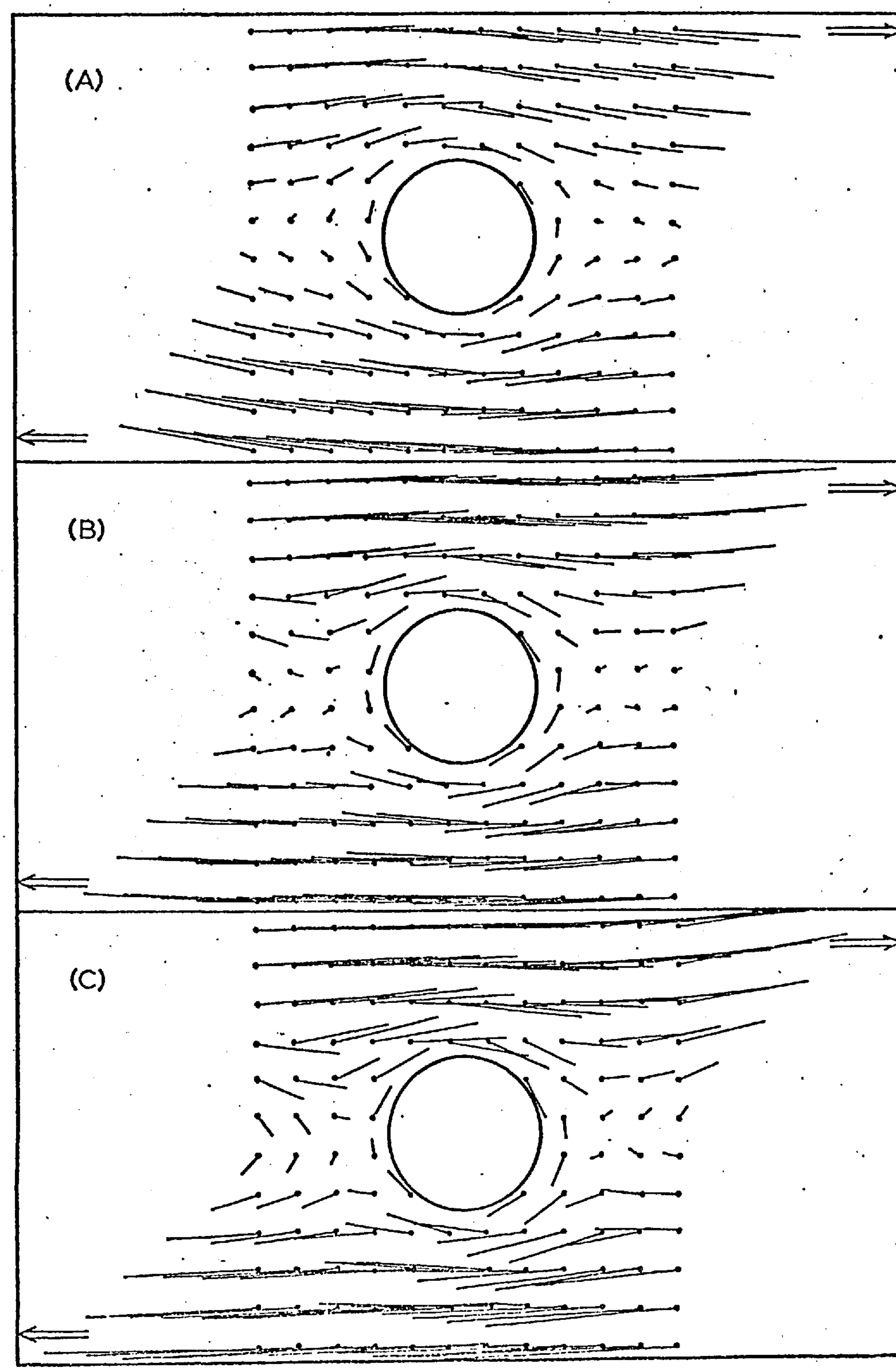

Fig. 5.15 Flow pattern of the matrix around a rigid equidimensional (circular) inclusion undergoing progressive simple shear deformation.

(A) $\gamma_s = 0.577$; (B) $\gamma_s = 0.876$; (C) $\gamma_s = 1.166$

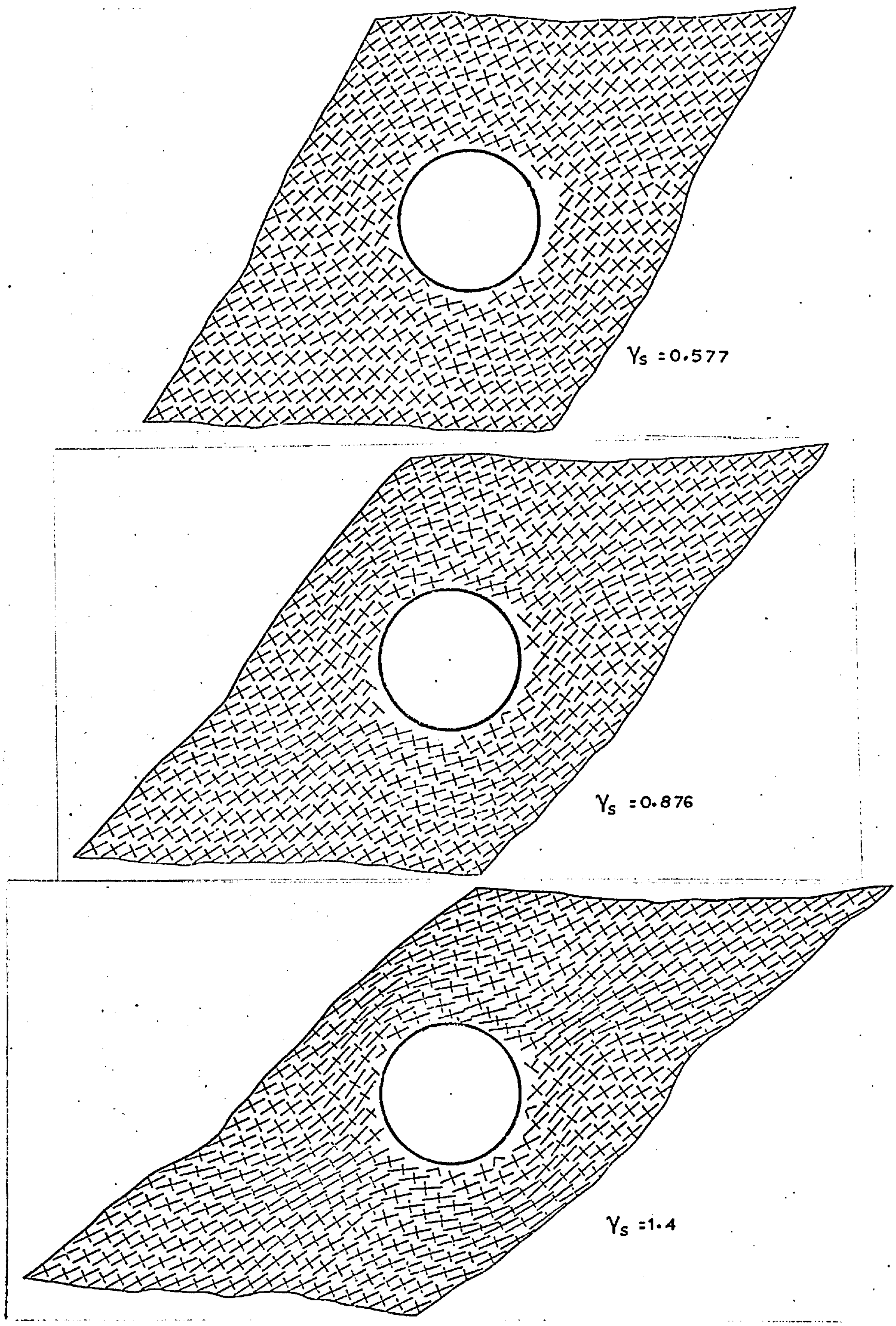

Fig. 5.16 Distribution of the magnitude and orientation of the principal axes of the strain ellipses in the matrix around a rigid equidimensional inclusion undergoing progressive simple shear deformation.

the computer plot for the strain values are presented in figure 5.16. The maximum and minimum strains were found to be systematically distributed in four different positions. The flow direction and the direction of the major axes of the bulk strain ellipse are not parallel to each other (compare figures 5.15 and 5.16).

Inspection of figures 5.14 and 5.16 shows that a similar pattern of strain around a rigid circular inclusion is developed in both irrotational strain and simple shear deformation. However, the patterns of the flow of the material around the inclusion are very different for the two types of deformation (figs. 5.12, 5.13 and 5.15).

5.5.2 Behaviour of the Matrix Around Elliptical Inclusions

Irrotational strain

Displacement vectors evaluated for different stages of deformation up to a total bulk strain of R = 2.6 from one series of experiments of obliquely oriented elliptical inclusions are shown in figure 5.17. The general pattern of the vectors is somewhat similar to that developed around an equidimensional object. There is, however, a slight variation due to the shape and orientation of the inclusion.

The nature of finite strains at successive stages during one series of experiments were determined from the grid data (fig. 5.18) in order to illustrate the distribution of strains in the matrix around an elliptical inclusion. Comparing the strain distribution around circular and elliptical inclusions (compare figures 5.14 and 5.18), it can be seen that there is very little difference between the two strain patterns. The deflection of the

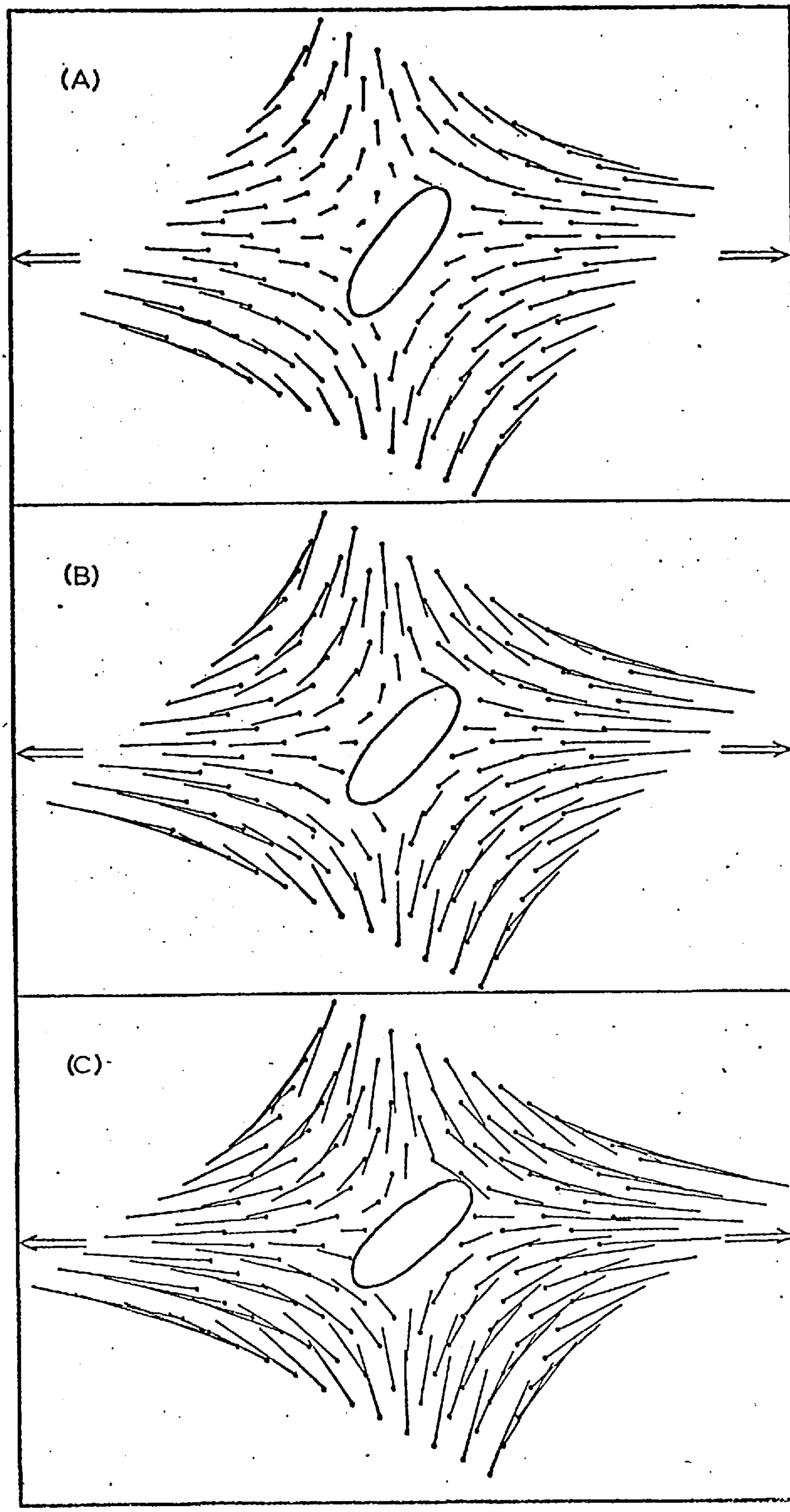

Fig. 5.17 Displacement vectors showing the flow pattern of the matrix material around an elliptical inclusion undergoing progressive irrotational strain deformation. (A) $\sqrt{\lambda_1/\lambda_2} = 1.61$; (B) $\sqrt{\lambda_1/\lambda_2} = 2.08$; (C) $\sqrt{\lambda_1/\lambda_2} = 2.60$.

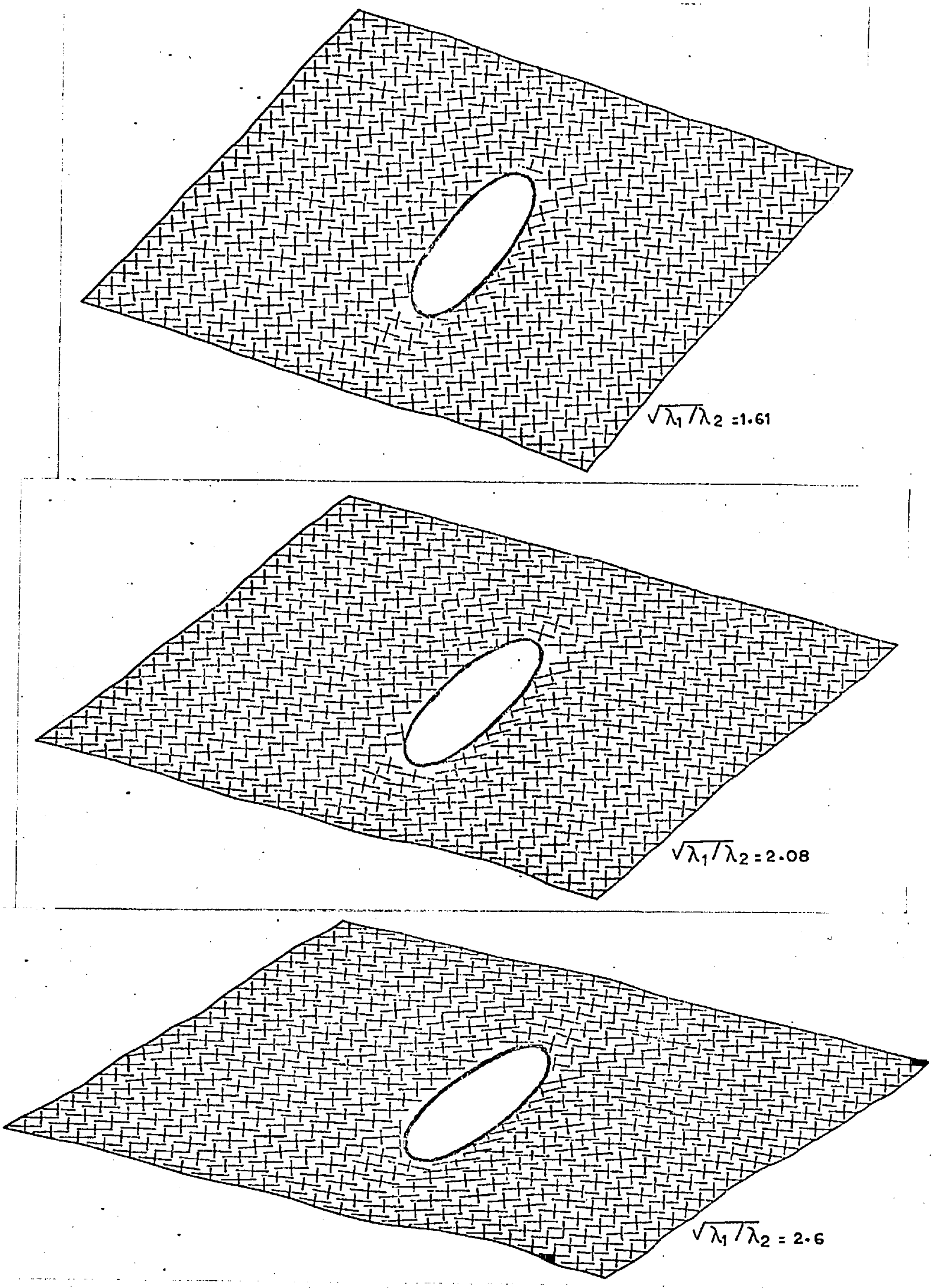

Fig. 5.18 Distribution of the magnitude and orientation of the principal axes of the strain ellipse in the matrix around an elliptical inclusion undergoing progressive irrotational strain deformation.

axes of strain ellipses in the matrix near the elliptical object is influenced by the shape of the inclusion.

Simple shear

The displacement vectors (fig. 5.19) describing the flow lines were derived from the simple shear experiments performed using an elliptical inclusion. In these experiments (having small amount of shear), The strain pattern around an inclusion deformed by simple shear do not show any significant difference to that developed during irrotational strain (compare figures 5.14 and 5.16). Hence the computation of strain ellipses in the matrix around an inclusion would not be sufficient to determine whether these strains ellipses were produced by the irrotational strain or simple shear deformation.

5.6 DEVELOPMENT OF PRESSURE SHADOWS AND PRESSURE FRINGES ADJACENT TO RIGID INCLUSIONS

The regions around inclusions commonly known as pressure shadows and pressure fringes have been investigated experimentally. Although shadow regions cannot generally be developed in the experiments, fringe regions can be directly simulated by the formation of 'open spaces' in the matrix adjacent to the rigid inclusion.

The geometry of the low strain regions has been assessed by studying the behaviour of the grid markers. Examples of the shadow areas developed in the low strain zone adjacent to the rigid inclusions derived from the experiments are illustrated in figures 5.20 and 5.21. Where the grid lines are initially parallel to the extension direction of the bulk strain ellipse, they are deflected around the object during irrotational strain deformation (fig. 5.20,a). The least deformed areas located where the grid lines are widely

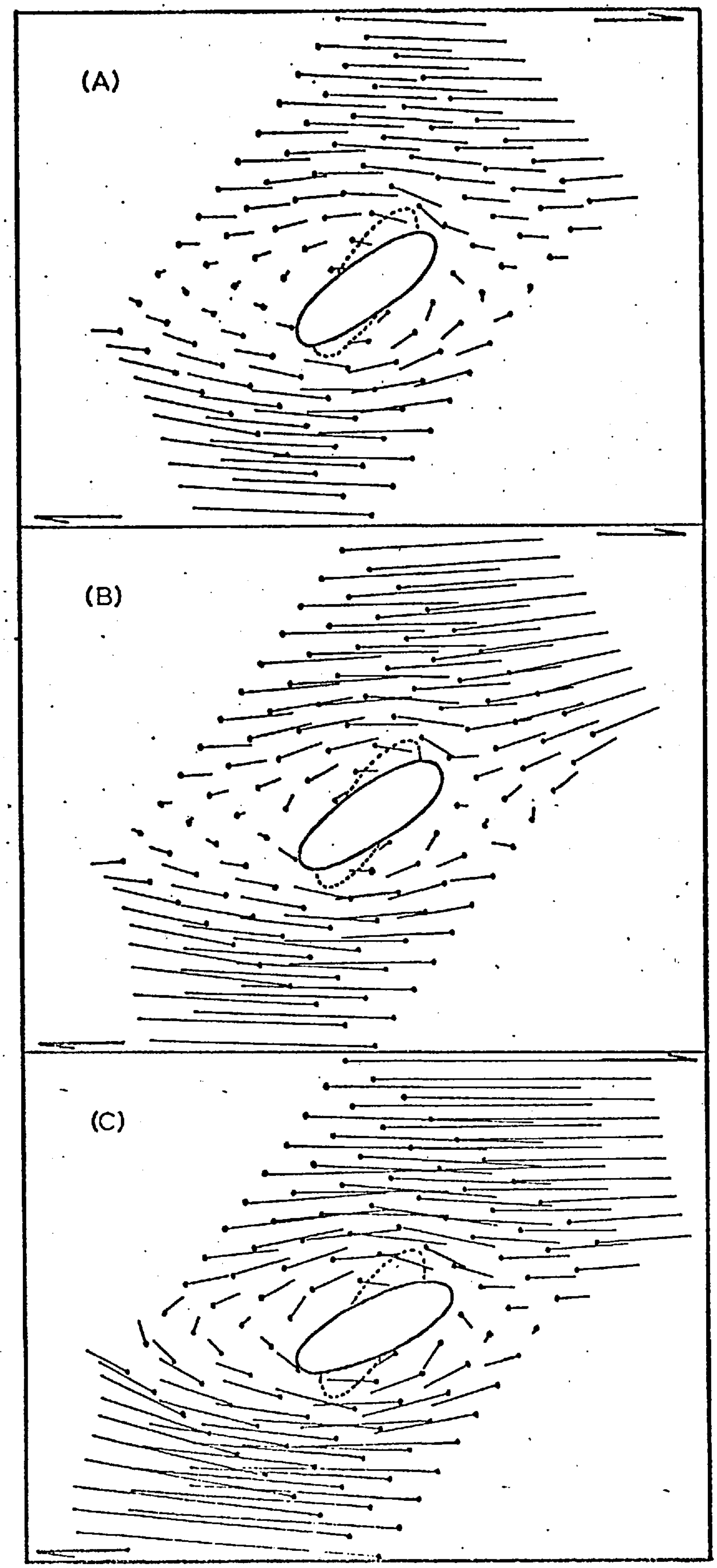

Fig. 5.19 Flow lines of the matrix material around a rigid elliptical inclusion during progressice simple shear deformation.
(A) $\gamma_s = 0.577$; (B) $\gamma_s = 0.876$; (C) $\gamma_s = 1.166$.

spaced adjacent to the object are shown as dotted areas (figs. 5.20 and 5.21). Grid line markers normal to the extension direction of the bulk strain show the low pressure areas even more clearly. During deformation, these lines gradually move apart in a direction parallel to the extension direction of the strain ellipse, and this displacement is less pronounced in the regions of low deformation. Hence, the area where the maxima of the curvature of these grid lines are situated, may be taken as the area of least deformation (fig. 5.20,b).

A few experiments were undertaken using relatively stiff matrix material and during deformation 'open spaces' developed at some localities adjacent to the rigid inclusion (Plates XIX, XX and XXI). Two examples of fringe regions (open spaces) around the rigid inclusions of different shapes developed during deformation are illustrated in figure 2.8. The shape of the 'open spaces' varies with the shape of the object.

These models only illustrate the shape of the fringe areas. In order to evaluate the likely orientation of fibrous minerals that might grow in these spaces under geological condition the progressive opening of the spaces was studied. The progressive development of the 'open spaces' for two examples has been investigated and the probable patterns of the fringe mineral growth obtained (fig. 5.22). The progressive "displacement trends" show straight and curved pattern for irrotational strain and simple shear deformation respectively.

Pressure shadow and pressure fringe regions both develop in the same area adjacent to the inclusions and the presence of one or the other depends on the amount of strain and the properties of the material. Pressure fringe areas are clearly distinguished from the pressure shadow regions in that the matrix has actually been pulled away from the inclusion and in nature the gap formed filled with new minerals.

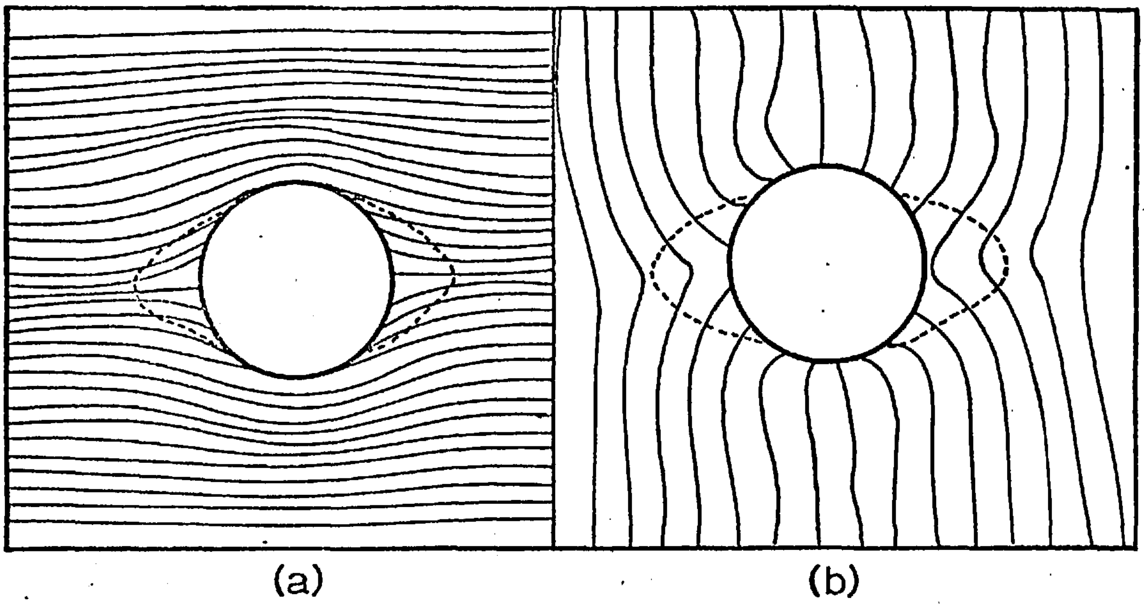

Fig. 5.20 Low strain zone (shown by the dotted line) assessed by the behaviour of the grid lines around a rigid circular object after finite irrotational strain deformation ($\sqrt{\lambda_1/\lambda_2} = 2.6$).
(a) Grid lines parallel to the principal extension direction.
(b) Grid lines normal to the principal extension direction.

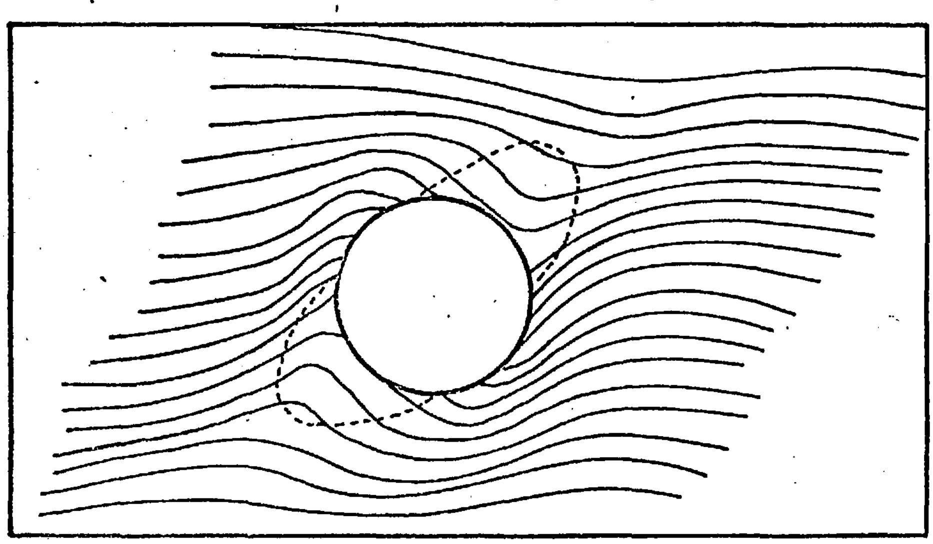

Fig. 5.21 Area of low strain (shown by the dotted line) in the matrix around a rigid equidimensional inclusion deformed under simple shear ($\gamma_s = 1.4$).

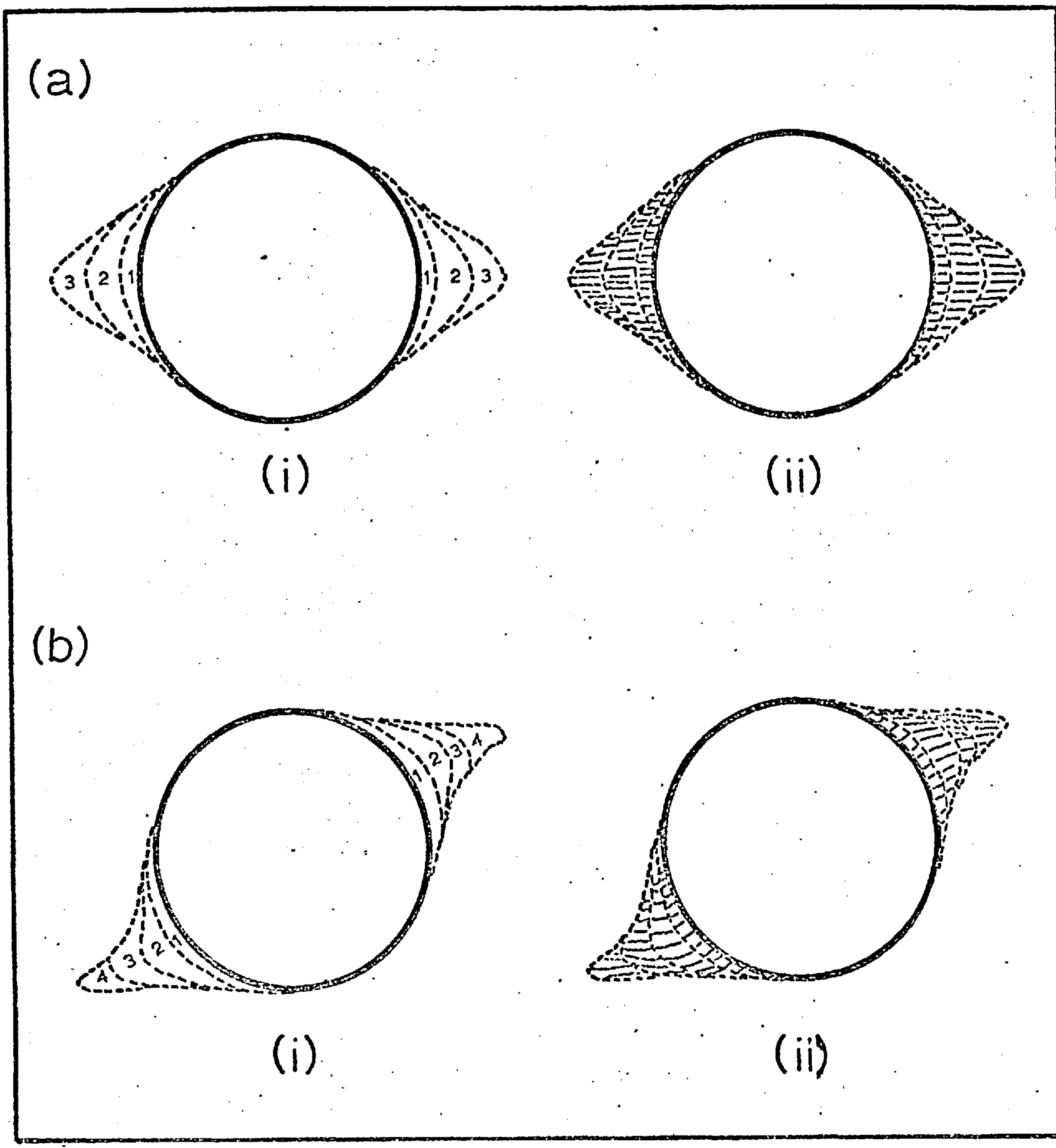

Fig. 5.22 Progressive development of open spaces around rigid inclusions simulating pressure fringe regions and a probable pattern of mineral growth inside these regions.
(a) During irrotation strain experiment. (i) Open spaces (ii) Fibrous mineral growth patterns.
(b) During simple shear experiment. (i) open spaces (ii) Probable patterns of mineral growth.

CHAPTER 6. STRESS DISTRIBUTION AROUND THE EQUIDIMENSIONAL INCLUSION

6.1 INTRODUCTION

In the previous chapters, theoretical and experimental studies have dealt with the distribution of strains and their dependence on the deformation history of the material around inclusions. The state of strain results from the displacements produced by an applied stress. It is therefore, important to investigate the state of stress and its role in the formation of the structure. It is generally impossible to determine from the geometry of deformed rocks the magnitude of the stress associated with the deformation. The evaluation of the stress conditions around a certain structure can be made mathematically, or by using finite element or photoelastic models. Photoelastic studies are widely used in Rock mechanics and Engineering Geology. These studies provide two sets of information: (i) Isoclinics and (ii) Isochromatics from which stress trajectories and the distribution of the differential stress can be evaluated. The following study presents a theoretical analysis of the stress distribution in the matrix around the rigid inclusion. The complete analytical solution for stress around an inclusion of various shapes is complex. The solution is developed for a circular inclusion and the geological implication of their result is discussed.

The problem of stress distribution in and around a particle has been treated previously by Goodier (1933), Sezawa (1933), Coutinho (1949), Muskhelishvili (1953), Eshelby (1957) and Wilson (1961). The stress distribution around a hole has been studied among others by Nadai (1950), Savin (1961) and Jaeger and Cook (1969). Recently, Strömgård (1972) presented the results of a study of stress around a rigid inclusion. All these studies analyse how a uniform stress field is disturbed by the presence of a hole or an inclusion. The basic equations (Jaeger and Cook, 1969) are extended in this chapter and a complete solution for the stress distribution around a circular rigid inclusion is determined.

6.2 THEORETICAL ANALYSIS

From the Saint Venants principle it follows that any disturbance will be confined to the neighbourhood of the inclusion. It is assumed that the matrix material is homogeneous and has the ideal properties of linear elasticity. It is also assumed that the matrix material is firmly attached to the boundary of the included object so that the continuity of stress and displacement is maintained.

6.2.1 General solution

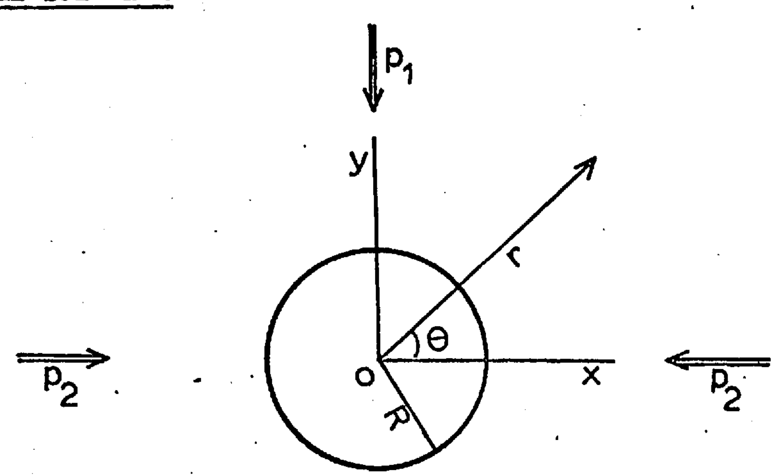

Fig. 6.1. A rigid circular inclusion under uniform stress from infinity.

Let a circular inclusion inside homogeneous matrix be subjected to uniform stress P_1 along OY direction and P_2 along OX direction from infinity (fig. 6.1). For the case of uniaxial stress, P_2 is zero and only P_1 is applied on the inclusion and its surrounding matrix. 'r' and 'θ' are the parameters of polar co-ordinates and 'R' is the radius of the circular inclusion. It is assumed that the material outside the inclusion (i.e. in the region $r > R$) is linearly elastic with shear modulus and Poisson's ratio G and ν respectively and that the material inside the inclusion has elastic moduli G_i and ν_i.

The stresses in an infinite region due to the applied stress P_1 can be represented by a standard stress function (jaeger and Cook, 1969, p.236) as

$$\begin{aligned} \phi(Z) &= \frac{1}{4} P_1 Z \\ \psi(Z) &= -\frac{1}{2} P_1 Z \end{aligned} \qquad (6.1)$$

The matrix material in this region contains a circular inclusion. In this situation, as suggested by Jaeger and Cook (1969), some terms must be added to the above function to represent the effect of the inclusion. The expression (6.1) becomes

$$\begin{aligned} \phi(Z) &= \frac{1}{4} P_1 \, [Z + (A/Z)R^2] \\ \psi(Z) &= -\frac{1}{2} P_1 \, [Z + (B/Z)R^2 + (C/Z^3)R^3] \end{aligned} \qquad (6.2)$$

where A, B and C are the real constants. Following the similar argument, the stress function in the region inside the inclusion can be expressed as

$$\begin{aligned} \phi_i(Z) &= \frac{1}{4} P_1 \, [A_i Z + (B_i/R^2)Z^3] \\ \psi_i(Z) &= -\frac{1}{2} P_1 \, C_i Z \end{aligned} \qquad (6.3)$$

The values of these constants were discussed by Jaeger and Cook (1969) and their conclusion will be outlined here.

The amount of displacement (u and v) can be determined from the stress function by using the standard equation,

$$2G(u + iv) = \varkappa\, \varnothing(Z) - Z\, \overline{\varnothing'(Z)} - \overline{\psi(Z)}$$

where $\varkappa = 3 - 4\nu$.

Using equation 6.2, the equation for the displacement at the boundary of the inclusion (i.e. r = R) can be obtained and is given by

$$4G(u_r + iv_\theta)/P_1R = \frac{1}{2}(\varkappa - 1) + B + (\frac{1}{2}\varkappa A + 1)e^{-2i\theta} + (\frac{1}{2}A + C)e^{2i\theta} \quad (6.4)$$

where u_r and v_θ are the displacements with respect to polar co-ordinates etc.

Using equation 6.3, the required expression for the displacement at the region r = R is obtained

$$4G_i(u_{ri} + iv_{\theta i})/P_1R = \frac{1}{2}A_i(\varkappa_i - 1) + \frac{1}{2}\varkappa_i B_i e^{2i\theta} + (C_i - \frac{3}{2}B_i)e^{-2i\theta} \quad (6.5)$$

where $\varkappa = 3 - 4\nu$

$\varkappa_i = 3 - 4\nu_i$ for plane strain

Equating the coefficient of both the equations (6.4 and 6.5) and writing $K = G_i/G$, gives

$$\begin{aligned} K(\varkappa - 1 + 2B) &= A_i(\varkappa_i - 1) \\ K(\varkappa A + 2) &= 2C_i - 3B_i \\ K(A + 2C) &= \varkappa_i B_i \end{aligned} \quad (6.6)$$

Let us now consider the normal and tangential stress at the boundary of the inclusion (i.e. in the region r = R). The relationship between the resolved stresses (σ_r, σ_θ and $\tau_{r\theta}$) and the stress function is given by

$$\sigma_r + \sigma_\theta = \sigma_x + \sigma_y = 2[\emptyset'(Z) + \overline{\emptyset'(Z)}]$$

and

$$\sigma_\theta - \sigma_r + 2i\tau_{r\theta} = [\sigma_y - \sigma_x + 2i\tau_{xy}] = 2[\overline{Z}\ \emptyset''(Z) + \psi'(Z)]e^{2i\theta} \qquad (6.7)$$

where $Z = re^{i\theta}$ and $e^{2i\theta} = \text{Cos}\ 2\theta$.

At the boundary, the difference of the normal and tangential stress (N and T respectively) can be expressed as

$$N - iT = \emptyset'(Z) + \overline{\emptyset'(Z)} - [\overline{Z}\ \emptyset''(Z) + \psi'(Z)]e^{2i\theta} \qquad (6.8)$$

Differentiating equation 6.2 and substituting it in equation 6.8, gives

$$2(N - iT)/P_1 = 1 - B - (\tfrac{3}{2} A + 3C)e^{-2i\theta} + (1 - \tfrac{1}{2}A)e^{2i\theta} \qquad (6.9)$$

Similarly from equation 6.3,

$$2(N - iT)/P_1 = A_i + (C_i - \tfrac{3}{2} B_i)e^{2i\theta} + \tfrac{3}{2} B_i e^{-2i\theta} \qquad (6.10)$$

Now equating the coefficient of equation 6.9 and 6.10, we obtain

$$\begin{aligned} A_i &= 1 - B \\ B_i &= -A - 2C \\ 2C_i - 3B_i &= 2 - A \end{aligned} \qquad (6.11)$$

From equations 6.6 and 6.11, the final solution for the real constants can be determined,

$$\begin{aligned} B_i &= 0 \\ A_i &= K(\varkappa + 1)/(2K + \varkappa_i - 1) \\ C_i &= K(\varkappa + 1)/(K\varkappa + 1) \end{aligned} \qquad (6.12)$$

and

$$\begin{aligned} A &= 2(1 - K)/(K\varkappa + 1) \\ B &= [\varkappa_i - 1 - K(\varkappa - 1)]/(2K + \varkappa_i - 1) \\ C &= (K - 1)/(K\varkappa + 1) \end{aligned} \qquad (6.13)$$

The general solution for the stress distribution in the matrix around a circular inclusion is obtained by differentiating equation 6.2, substituting it into equation 6.7, σ_r, σ_θ and $\tau_{r\theta}$ can be determined

$$\begin{aligned}
\sigma_r &= \frac{1}{2}P_1\left(1 - \frac{BR^2}{r^2}\right) + \frac{1}{2}P_1\left(1 - \frac{2AR^2}{r^2} - \frac{3CR^4}{r^4}\right)\cos 2\theta \\
\sigma_\theta &= \frac{1}{2}P_1\left(1 + \frac{BR^2}{r^2}\right) - \frac{1}{2}P_1\left(1 - \frac{3CR^4}{r^4}\right)\cos 2\theta \qquad (6.14) \\
\tau_{r\theta} &= -\frac{1}{2}P_1\left(1 + \frac{AR^2}{r^2} + \frac{3CR^4}{r^4}\right)\sin 2\theta
\end{aligned}$$

6.2.2 Solution for the Rigid Circular Inclusion

The required solution for the distribution of the different aspects of stresses in the matrix due to the applied uniaxial stress loaded under plane strain are obtained by solving the values for real constants. The rigidity contrast K, in this case is infinity, as the matrix material is assumed to be ductile. For plane strain, the other variable $\varkappa$ is given by $\varkappa = 3 - 4\nu$. Substituting $\nu = \frac{1}{2}$ for non-compressible material, the value of $\varkappa = 1$. Similarly $\varkappa_i$ is also equal to 1.

Now substituting $K = G/G_i = \infty$ and $\varkappa = 1$, $\varkappa_i = 1$ in equation 6.13, the required values of the real constants are

$$\begin{aligned}
A &= -2 \\
B &= 0 \qquad (6.15) \\
C &= 1
\end{aligned}$$

Finally, the expressions for the resolved stresses (σ_r, σ_θ and $\tau_{r\theta}$) in the material around rigid circular inclusion loaded under plane strain are obtained by substituting equation 6.15 into equation 6.14. This gives

(i) In case of applied uniaxial stress,

$$\sigma_r = \frac{1}{2}P_1 + \frac{1}{2}P_1(1 + \frac{4R^2}{r^2} - \frac{3R^4}{r^4})\text{Cos } 2\theta$$

$$\sigma_\theta = \frac{1}{2}P_1 - \frac{1}{2}P_1(1 - \frac{3R^4}{r^4})\text{Cos } 2\theta \qquad (6.16)$$

$$\tau_{r\theta} = -\frac{1}{2}P_1(1 - \frac{2R^2}{r^2} + \frac{3R^4}{r^4})\text{Sin } 2\theta$$

(ii) For the applied bi-axial stress,

$$\sigma_r = \frac{1}{2}(P_1 + P_2) + \frac{1}{2}(P_1 - P_2)(1 + \frac{4R^2}{r^2} - \frac{3R^4}{r^4})\text{Cos } 2\theta$$

$$\sigma_\theta = \frac{1}{2}(P_1 + P_2) - \frac{1}{2}(P_1 - P_2)(1 - \frac{3R^4}{r^4})\text{Cos } 2\theta \qquad (6.17)$$

$$\tau_{r\theta} = -\frac{1}{2}(P_1 - P_2)(1 - \frac{2R^2}{r^2} + \frac{3R^4}{r^4})\text{Sin } 2\theta$$

From the above resolved stresses, the distribution of the principal stresses and their orientation in the matrix around the rigid circular inclusion can be obtained using the following relationship

$$\sigma_1 = \frac{\sigma_r + \sigma_\theta}{2} + \frac{1}{2}[(\sigma_r - \sigma_\theta)^2 + 4\tau_{r\theta}]^{\frac{1}{2}}$$

$$\sigma_3 = \frac{\sigma_r + \sigma_\theta}{2} - \frac{1}{2}[(\sigma_r - \sigma_\theta)^2 + 4\tau_{r\theta}]^{\frac{1}{2}} \qquad (6.18)$$

$$\Omega = \frac{1}{2}\tan^{-1}(\frac{2\tau_{r\theta}}{\sigma_r - \sigma_\theta})$$

where σ_1 and σ_3 are the greatest and least principal stresses respectively and Ω is the orientation of the greatest principal stress.

Geologically significant aspects of the state of stresses, such as, the maximum shearing stress (τ_{max}), tensile stress zone and the mean stress can easily be determined when σ_1 and σ_3 are known. The values of τ_{max} and the mean stress are obtained from the relationships,

$$\tau_{max} = \frac{1}{2}(\sigma_1 - \sigma_3)$$
$$\text{Mean stress} = \frac{1}{2}(\sigma_1 + \sigma_3) \qquad (6.19)$$

6.3 INTERPRETATION OF THE RESULTS AND GEOLOGICAL IMPLICATIONS

All the following calculations were made from equations 6.16, 6.17, 6.18 and 6.19 using a computer. The stress trajectories and contours of values of principal stresses etc. were constructed by hand.

6.3.1 Stress Trajectories and Fracture Patterns

Stress trajectories or isostatics are the orthogonal system of curves representing the directions of the principal stresses at every point. These sets of curves are very useful for deducing the potential deformation (specially fracture) patterns in the field of geology, rock mechanics and engineering.

Jaeger and Cook (1969) described the geometry of shear fractures developed in the material during compressive stresses. The angles, which the planes of these fractures made with the axis of maximum principal stress is given by

$$\Phi = \pm(45^{\circ} - \varphi_i/2)$$

where φ_i is the angle of internal friction of the material. The results of many experiments performed to determine φ_i are listed in Jaeger and Cook (1969, p.59). It is observed that the value of φ_i is always positive and less than 45° irrespective of the rock type. Hence, the angle of fracture Φ is always less than 45° with reference to the greatest principal stress σ_1 direction.

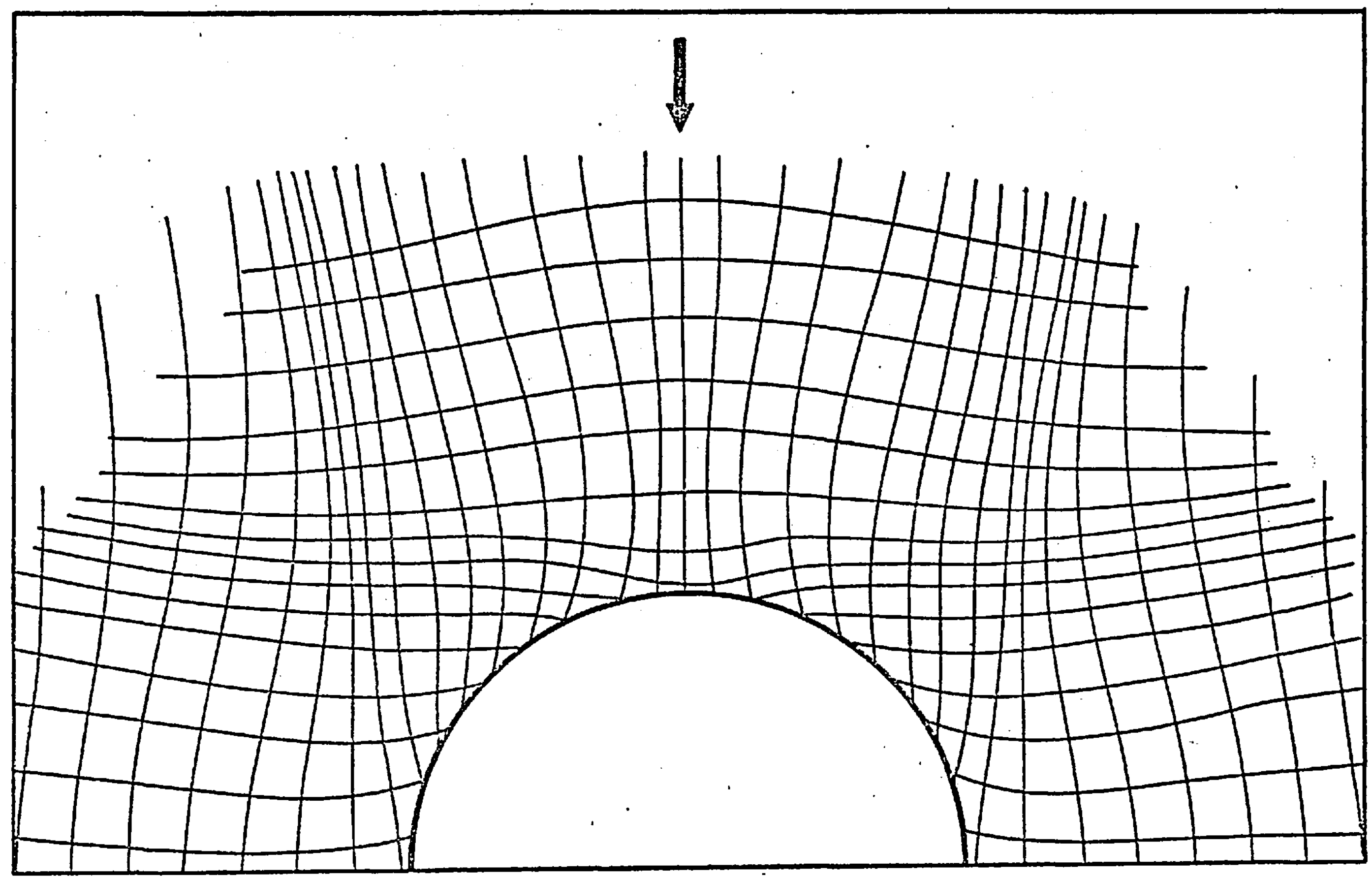

Fig. 6.2 Principal stress trajectories around a rigid circular (equidimensional) inclusion.

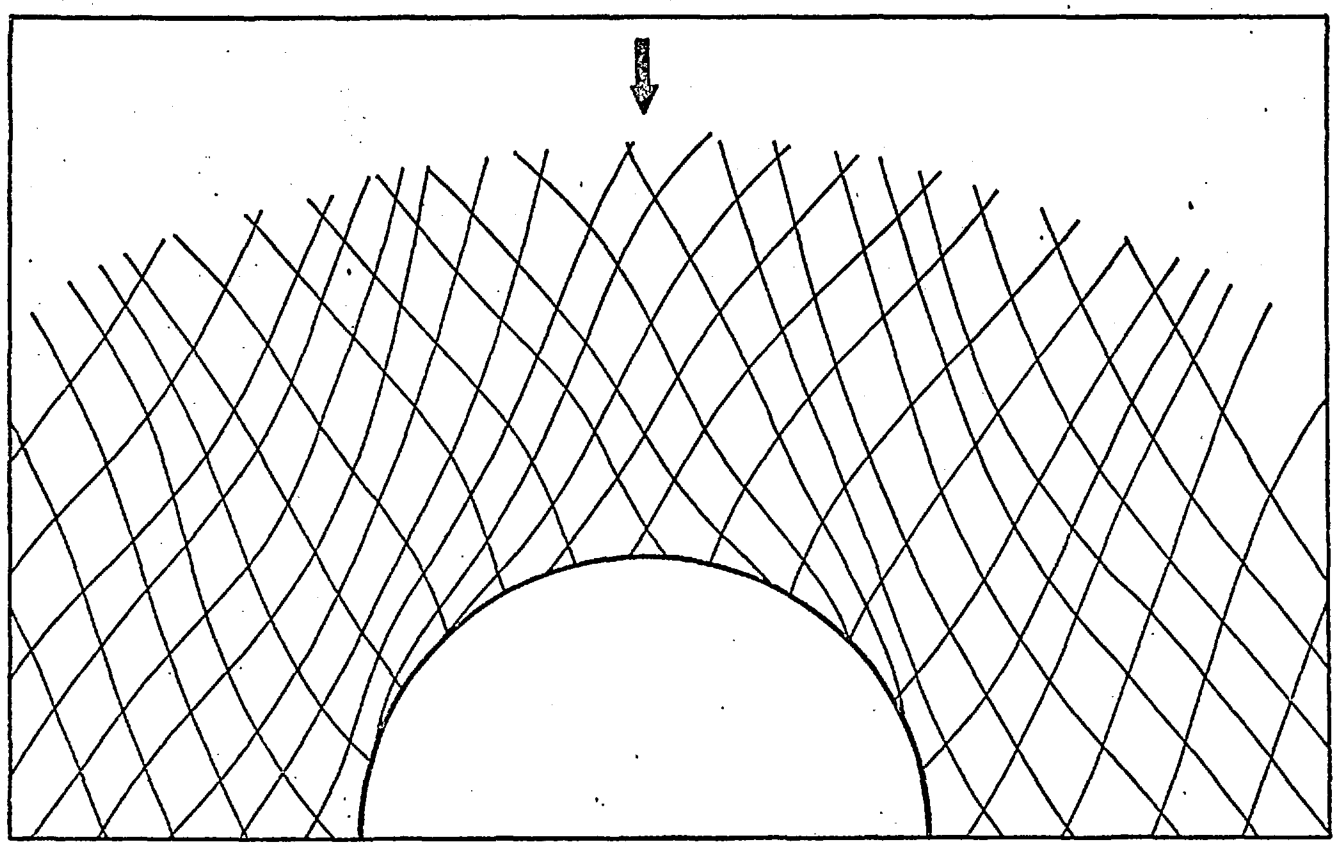

Fig. 6.3 Fracture pattern around a rigid circular inclusion.

The stress trajectories in the matrix around a rigid equidimensional inclusion are obtained from equations 6.16 and 6.18, and are shown in fig. 6.2. The direction of the principal stresses observed from the computer output is constant for any value of applied stress. The orthogonal trajectories shown in fig. 6.2 show a marked deflection around the rigid object.

Having established the stress field, it is possible to compute the orientation of any shear fractures which might be developed around the rigid object, should the matrix undergo brittle failure. Fractures initiate along two planes having certain value of Φ with the direction of σ_1. As φ_i depends on the type of the rock material, the angle of potential fracture is variable. For most rocks, Φ falls between 20° and 40°, hence the choice of 30° for Φ seems appropriate (Hafner, 1951). The two sets of potential shear failure curves are plotted in figure 6.3.

6.3.2 Distribution of the Principal Stresses and their Influence in the Material Around the Rigid Inclusion

The values of greatest (σ_1) and least (σ_3) principal stresses for an applied stress P_1 have been evaluated from equation 6.18. These values vary from point to point in the matrix around the rigid inclusion. Because the values of greatest principal stress (σ_1) could be geologically significant their distribution have been illustrated by joining the points of equal value of σ_1/P_1 in figure 6.4. The variations in value of σ_1 (compressive, -ve; and tensile, +ve) are symmetrically distributed around the inclusion. High local compressive stresses are found on the side of the inclusion facing the direction of greatest regional compression and high local tensile stresses are found on the sides facing the direction normal to the greatest regional compression.

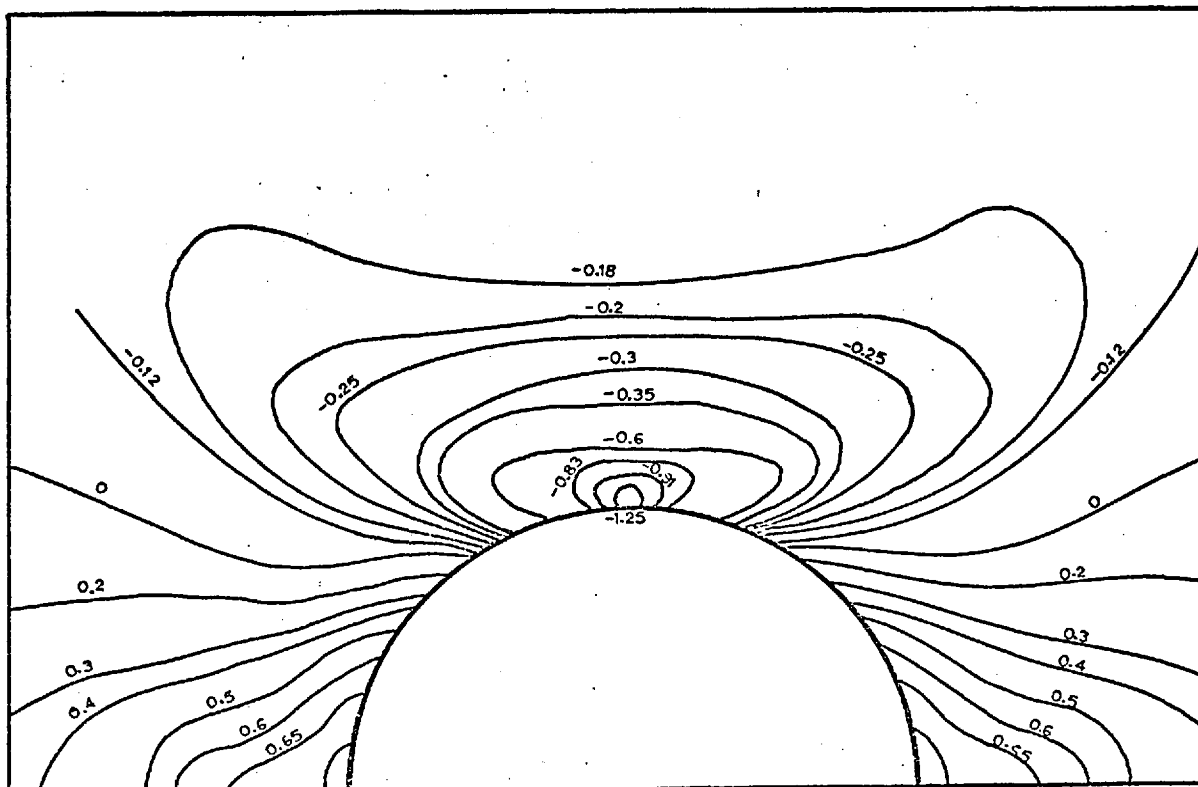

Fig. 6.4 Distribution of maximum principal stress (σ_1/P_1) around a rigid circular inclusion under applied uniaxial stress.

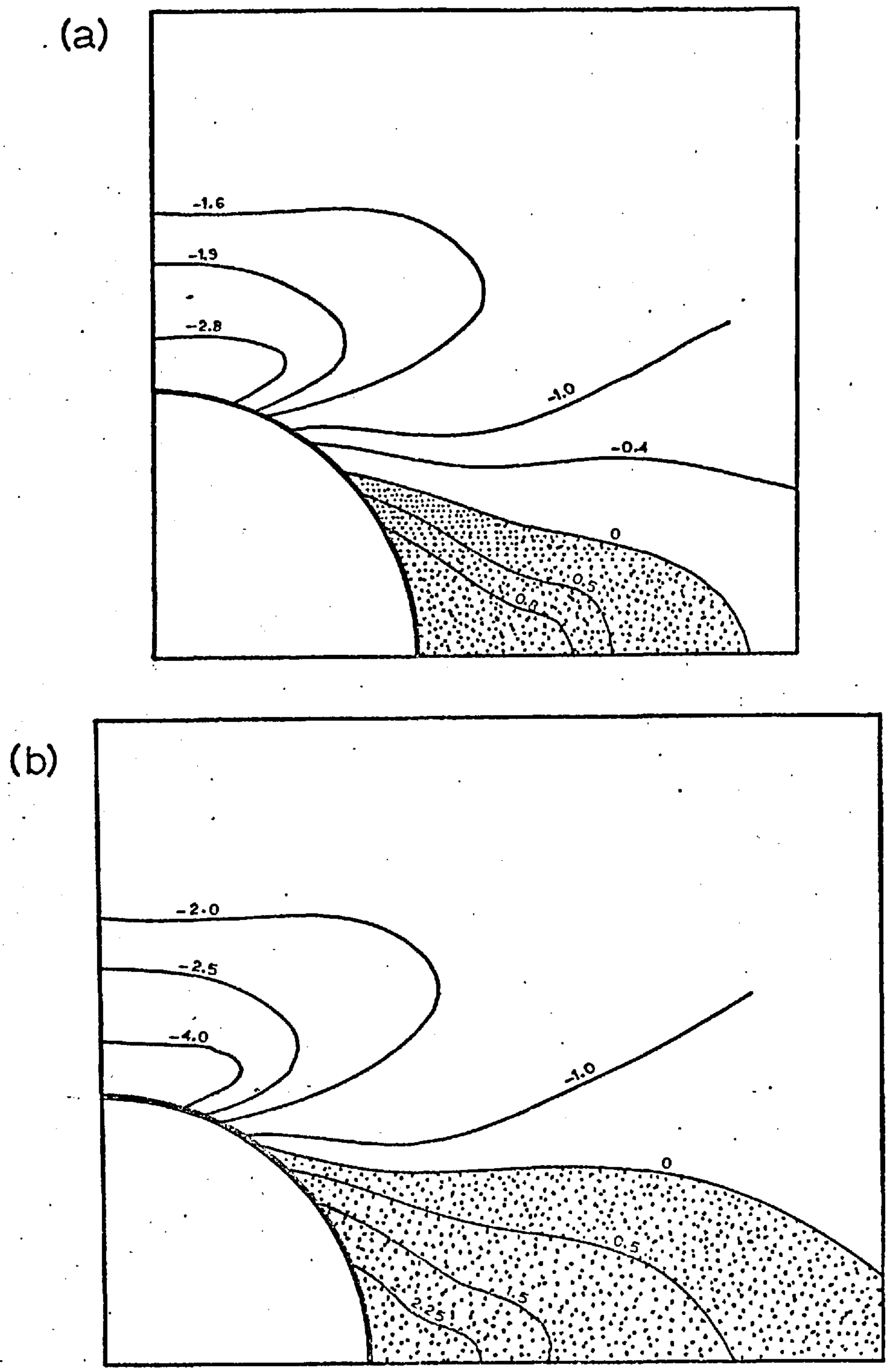

Fig. 6.5 Areas of tensile stress $\sigma_1/P_1 > 0$ (dotted regions) adjacent to a rigid circular inclusion.

(a) $P_2/P_1 = 0.33$ (i.e. $P_1 = 3$)

(b) $P_2/P_1 = 0.2$ (i.e. $P_1 = 5$)

It is well known that tension fractures can be developed in regions of tensile stress where $\sigma_1/P_1 > 0$. The regions of tensile stress for two cases of an applied bi-axial stress condition are shown in figure 6.5. The extent and shape of the tensile zone is related to the applied stress ratio P_2/P_1. Tensile fractures developed in this area might accommodate pressure solution and be deposition sites of material derived from the surrounding area. In natural rocks tensile fractures that are subsequently filled with minerals (quartz, calcite) often develop at the matrix - inclusion junction to form pressure fringes. Strömgård (1972) suggested that the secretionary type of mineral growth associated with tensile fracture at the matrix - inclusion interface does not occur if $P_2/P_1 > 0.5$. In this situation minerals migrate into the low strain areas but are deposited in a more diffused manner with the matrix and form a pressure shadow.

Observations of naturally deformed rocks and experimental results show that the initiation of fractures usually starts along the inclusion - matrix contact (figs. 2.7 and 2.8 in chapter 2, and plates XIX, XX and XXI). Pressure fringes appear to be generated by the dialation of an initial tensile fracture at the matrix - inclusion interface.

6.3.3 Maximum Shearing Stress (τ_{max}) or the Differential Principal Stress

Contoured values of the maximum shear stresses calculated from equation 6.19 are illustrated in figure 6.6. The maxima and minima of τ_{max} are symmetrically distributed around the object and are located at some distance from the boundary of the inclusion. The experimental study by Strömgård (1972) shows that the theoretically predicted pattern of τ_{max} around the inclusion is in good agreement

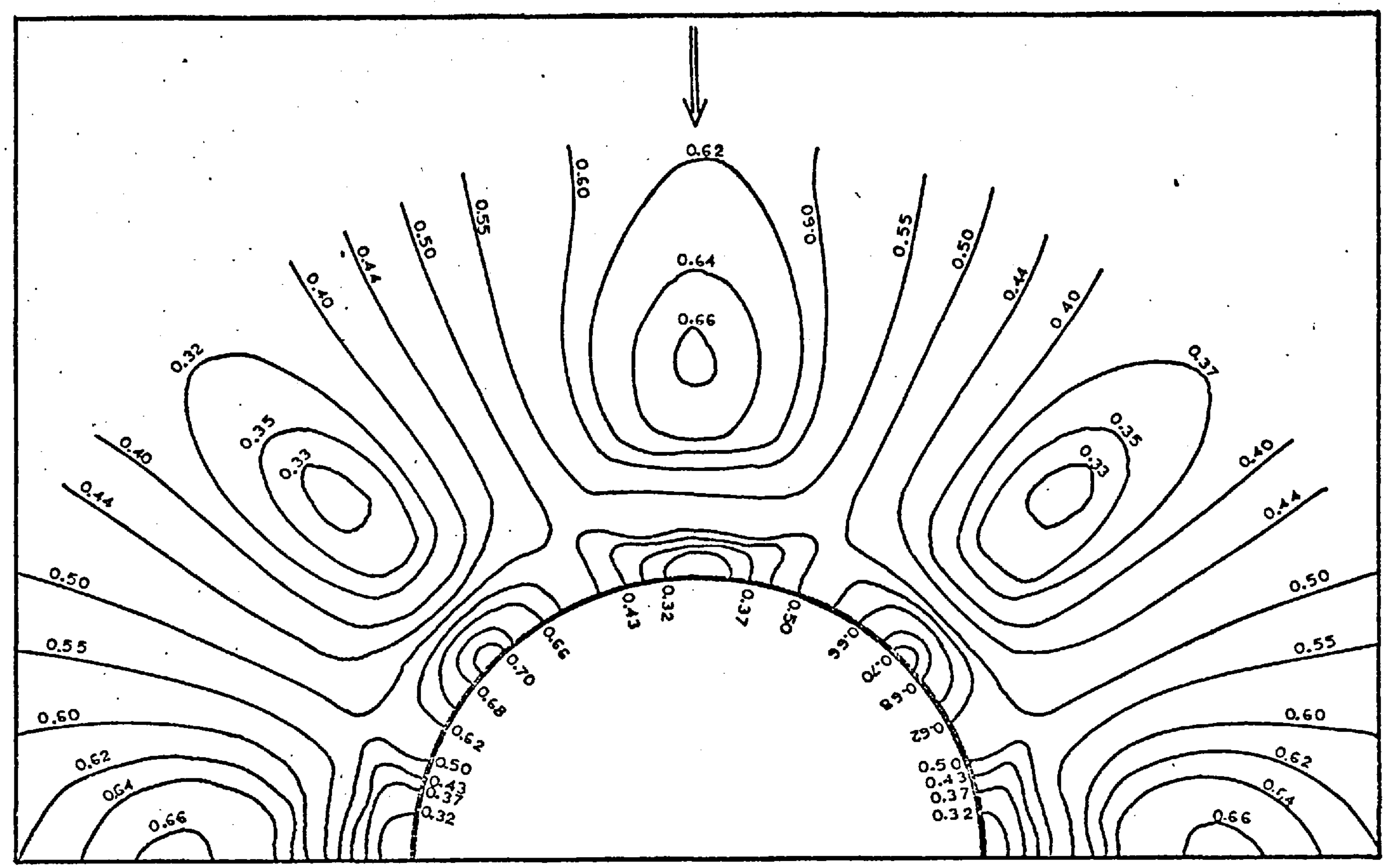

Fig. 6.6 Distribution of τ_{max}/P_1 in the matrix around a rigid circular inclusion under uniaxial stress.

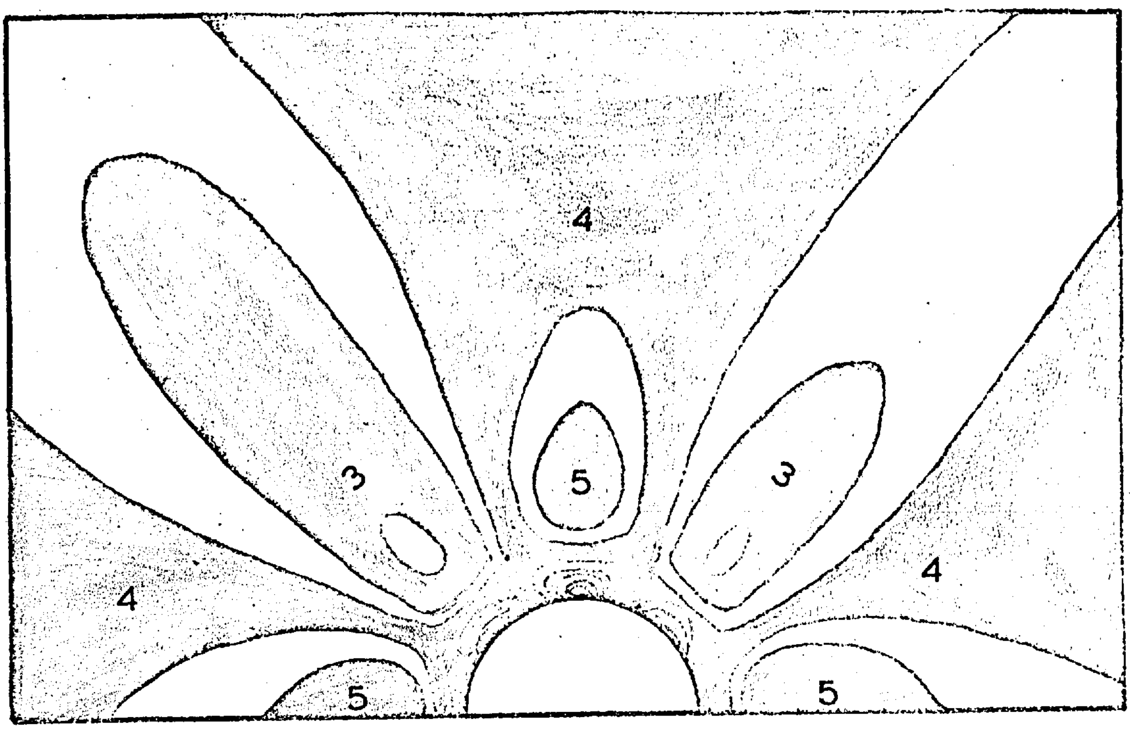

Fig. 6.7 A photo-elastic model showing the distribution of isochromatics. Numerical numbers represent the fringe order. (After Stromgard, 1972)

with the pattern determined photoelastically (fig. 6.7).

6.3.4 Role of Mean Stress in the Development of Pressure Fringes and Pressure Shadows

Mean stress or pressure in the matrix around the rigid circular inclusion has been evaluated from equations 6.18 and 6.19 and the variations are shown in figure 6.8. The highest value of mean stress lies along the plane parallel to the applied compressive stress (i.e. along OY) whereas the lowest value of mean stress lies along the plane normal to the compressive stress (i.e. along OX direction). The magnitude of the mean stress at any point in the matrix varies proportionally with the applied compression.

Field and experimental observations show that the pressure fringes and pressure shadows are formed in the regions which coincide with areas of low mean stress around the inclusion. Ramberg (1952, 1961) and Gresens (1966) have studied the problem of diffusion and mineralogical differentiation as a result of pressure variation. Many factors are involved in the diffusion and movement of the material from one place to another, but it is thought that minerals migrate from high pressure zone into adjacent low pressure zones. It seems likely that new minerals would crystallise in the low mean stress zones to form pressure fringes and pressure shadows and that this material would be derived from areas in the surrounding matrix where the mean stress was high.

Two main factors are involved in the formation of pressure shadows and pressure fringes. The variation of the mean stress governs the migration of material and the tensile zone near the object (determined by the nature of the greatest principal stress σ_1) provides the area for deposition. Surprisingly, the areas of tensile

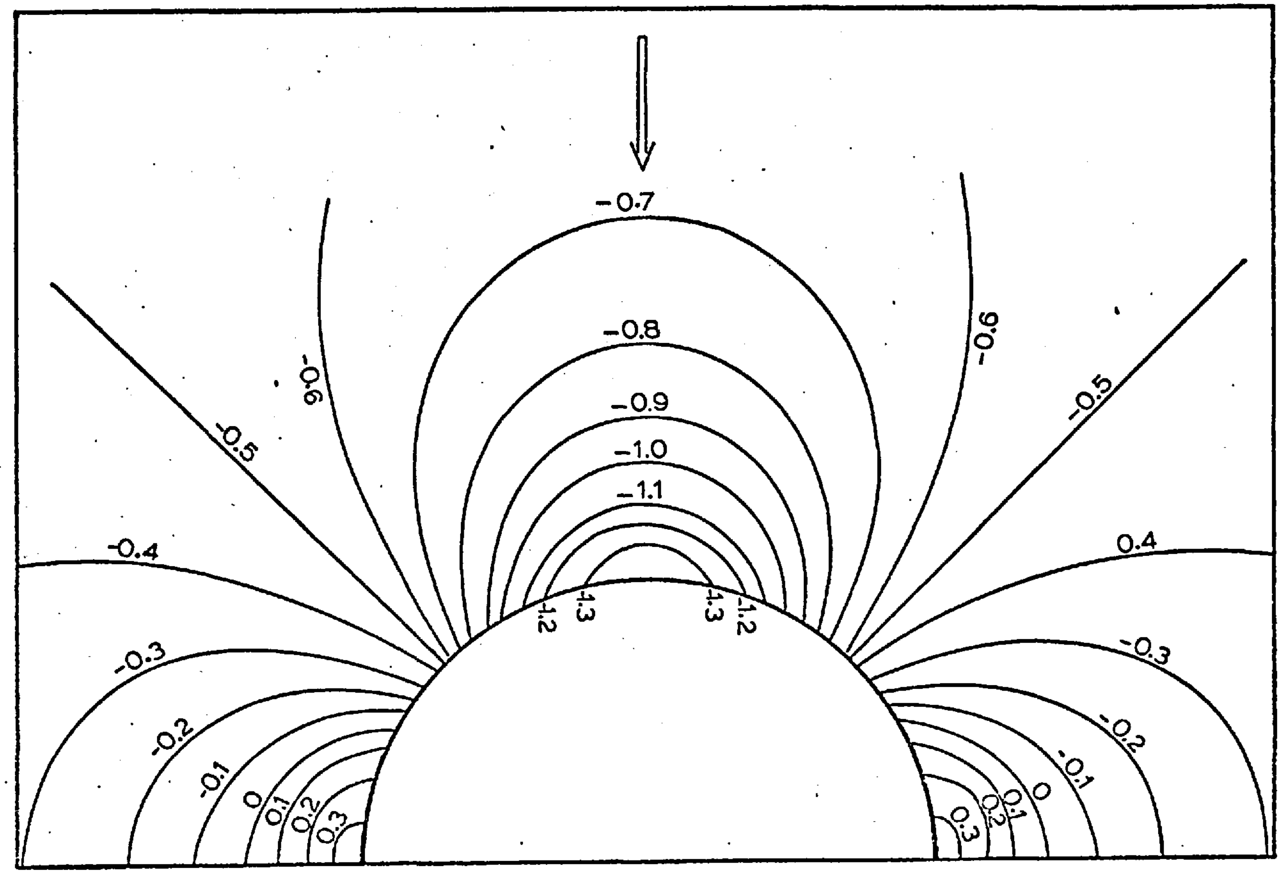

Fig. 6.8 Distribution of mean stress ($\bar{\sigma}/P_1$) in the matrix around a rigid circular inclusion under uniaxial stress.

stress and the regions of low mean stress approximately coincide (figs. 6.4 and 6.8). The type of structures (whether pressure shadows or pressure fringes) that develop in these low mean stress regions is controlled by the magnitude of the ratio of the applied regional compressive stresses P_2/P_1.

PART II

PART II

CHAPTER 7. THE EVOLUTION AND THEORETICAL ANALYSIS OF STRETCHED BELEMNITES

7.1 INTRODUCTION

The presence of objects of known original shape (fossils, oolites, pebbles and other porphyroblasts) in sedimentary rocks is particularly useful in evaluating the amount of deformation of the surrounding rocks as a result of sedimentary and tectonic processes. Belemnites are particularly valuable in this respect, because the belemnite guards are resistant to distortion by flow. The guards become fragmented and the length of the original guard may be calculated by reassembling the fragments (Daubree, 1876; Heim, 1919; Brace, 1960; Badoux, 1963, and Ramsay, 1967).

Experiments have been carried out to investigate the behaviour of fragments of rigid material chosen to simulate the behaviour of naturally deformed belemnites. The basic principles associated with the development of boudinage structure are found to be similar to those associated with the formation of stretched belemnites. By considering belemnite specimen to be a fragmented rigid inclusion, the established solution for the motion of rigid inclusions in a viscous matrix can be used to determine the amount of elongation ($\sqrt{\lambda} = 1 + e$). A technique of constructing models simulating stretched belemnites and a method of evaluating the amount of elongation from the models are also described. A comparison is made of the results obtained from the theoretical models with those derived from the experimental simulations of stretched belemnites (in chapter 8).

7.2 THE DEVELOPMENT OF STRETCHED BELEMNITES

Belemnites are composed of material of different composition or structure from that of the surrounding matrix. Examination of the structure of the guards of naturally fragmented belemnites shows that the guards generally behave as rigid bodies. The contact between the guards of a belemnite is composed of fibrous calcite crystals, the long axis of which are arranged perpendicular to the long axis of the belemnite body. This fibrous structure provides a weakness which assists fragmentation and separation of the parts during deformation. The guards being resistant to breaking are then preserved in the host rock (figs. 9.4 and 9.5). The regions between the separated fragments are often filled with fibrous crystals of quartz and calcite probably precipitated from interstitial fluids during the course of deformation.

The geometry of the stretched belemnites is very similar to that of the boudins (figs. 7.1 and 7.2). The shape of boudins is often modified during deformation but that of the belemnite fragments generally remains rectangular. Rectangular shaped boudins (fig. 7.2) are common where there is a high ductility contrast between the boudinaged layer and surrounding matrix. There is a close resemblence between the strain in the matrix around these rectangular boudins and the strain in the matrix around extended belemnites. The development of stretched belemnites discussed below draws on many of the ideas regarding the formation of rectangular boudins.

Field and experimental observations show that separation of the fragments of belemnites is caused by an extension along the long axis of the belemnite body. When a belemnite lies oblique to the major axis of the strain ellipse but within the extension field, the separated fragments are generally arranged to form an 'en-echelon'

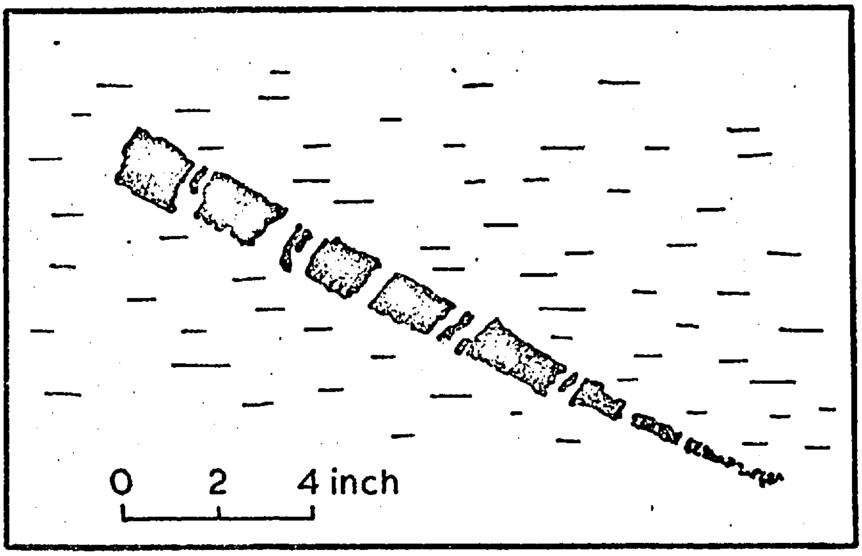

Fig. 7.1 Sketch of an extended belemnite specimen from Leytron, Valais, Switzerland.

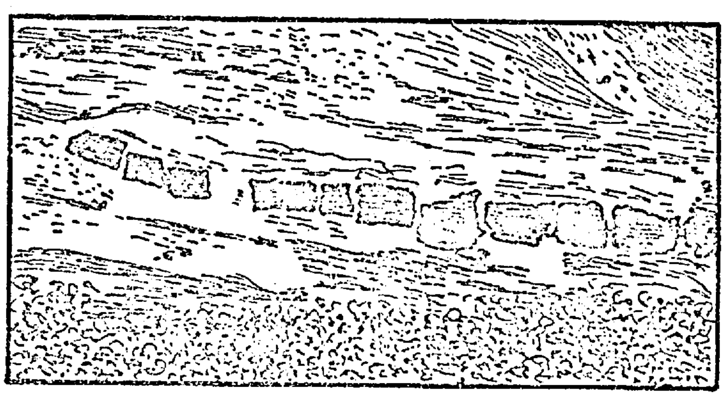

Fig. 7.2 An example of rectangular boudins of amphibolite in granite gneiss, West Greenland. Thickness of the layer is 3 cm. (Drawing from a photograph after Ramberg, 1955, plate 2B)

structure (fig. 7.2).

7.3 THE THEORETICAL ANALYSIS OF THE DEVELOPMENT OF STRETCHED BELEMNITES

A complete mathematical solution for calcating a value for the extension using fragmented belemnites is complicated by the many factors which are involved (initial orientation, axial ratio of the belemnite body, axial ratio of the individual fragments of belemnite and the values of finite strain). Field observations (fig. 7.1) provide the information on the final orientation (θ_b'), the deformed length and the original length of the belemnite body. Using these parameters, it is possible to determine approximately a value for the finite elongation in one direction. It is also possible to compute theoretically the elongation suffered by a belemnite knowing the final orientation (θ_b') and the length of the belemnite specimen and making use of the solution for the motion of elliptical inclusion (in 2D) inside a viscous matrix.

Basic Assumptions

It is assumed that the behaviour of belemnite specimens embedded in rocks is similar to the behaviour of rigid inclusions embedded in a viscous matrix. In the model work carried out it is also assumed that the matrix materials are viscous fluids and that they always remain in contact with the boundary of the included object (i.e. the object does not 'slip'). Belemnites oriented at an angle to the direction of major axis of strain ellipse undergo rotation as well as separation during deformation. Experimental observations (plates XXII to XXXII) show that the whole body simulating a belemnite even after the fragments have separated, rotates as a single body towards the extension direction. It is also seen that the separated fragments tend to behave independently of the whole body. In the analysis below, the belemnite body, after being stretched, is first considered as a single elliptical body (in 2D) with a high axial ratio a/b and then as separated fragments.

For the purpose of determining theoretical models of stretched belemnites the solutions for the motions of elliptical rigid inclusions (described in chapter 3) are utilized. They are:

(i) For pure shear deformation:

$$\ln \tan \theta'_b = \ln \tan \theta_b + \frac{a^2 - b^2}{a^2 + b^2} \cdot \ln \sqrt{\lambda_2/\lambda_1} \qquad (3.9)$$

where θ_b and θ'_b are the initial and final orientation of a belemnite specimen with reference to the major axis of strain ellipse. 'a' and 'b' represent the length and width of the belemnite body.

(ii) For simple shear deformation:

$$\text{Cot } \theta'_b = a/b.\tan[\frac{a \cdot b}{a^2+b^2} \cdot \gamma_s + \tan^{-1}(\frac{b}{a}.\text{Cot } \theta_b)]$$

where θ_b and θ'_b are the initial and final orientations respectively of a belemnite specimen with reference to the shearing direction.

Reconstruction of stretched belemnite (Theoretical model)

The reconstruction of stretched belemnite models has been made using equations (3.9 and 3.20). Measurements have been taken from these models to determine the amount of their extension. The results obtained from these models have been analysed in order to examine the geometrical parameters of stretched belemnites.

Consider a belemnite specimen of known axial ratio a/b embedded in a ductile matrix and whose long axis is at an angle to the extension direction before deformation. Using eqs. 3.9 and 3.20 the finite orientation of a belemnite specimen (θ'_b) has been calculated for two types of finite strains (pure shear and simple shear). The belemnite specimen as a whole suffers rotation about its mid-point towards the major axis of strain ellipse.

The general method of constructing such models and determining extension from the geometrical properties of the reconstructions will first be discussed. Three rigid rectangular objects placed together in such a way that they represent a belemnite body (in 2D) with axial ratio (or length/width) a/b = 6:1 and they are included in a ductile matrix making an angle $\theta_b = 60^\circ$ with reference to the major axis of the strain ellipse (fig. 7.3). The reference lines 'GH' and 'IJ' are parallel to the principal extension direction and shearing direction for pure shear and simple shear deformation respectively. It is assumed that the body of the model (belemnite) has developed fractures which divide it into three fragments of equal size, a/b = 2:1. The points used for measuring the length of the whole object are the two middle points 'a' and 'c' of fragments x and z, since the amount of extension at the two ends of x and z cannot be measured accurately. The reference lines were, therefore, drawn through these points. The final orientation of the specimen (θ_b') is then calculated and a solid line 'AB' is drawn through the point 'b' at an angle θ_b' with reference to GH. The line 'AB' cuts across the reference lines at 'a' and 'c'. These points are the new positions of the fragments 'x' and 'z' after deformation. Hence, the length 'a'c'' is the extended length of 'ac' and the direction of 'AB' represents the average orientation of the belemnite model (fig. 7.3). Before completing the construction, the rotation made by the individual fragments is calculated. The fragments, when separated from each other tend to behave in a way governed by their individual shapes and axial ratios. Knowing their axial ratio, the final orientation of fragments (θ_f') is

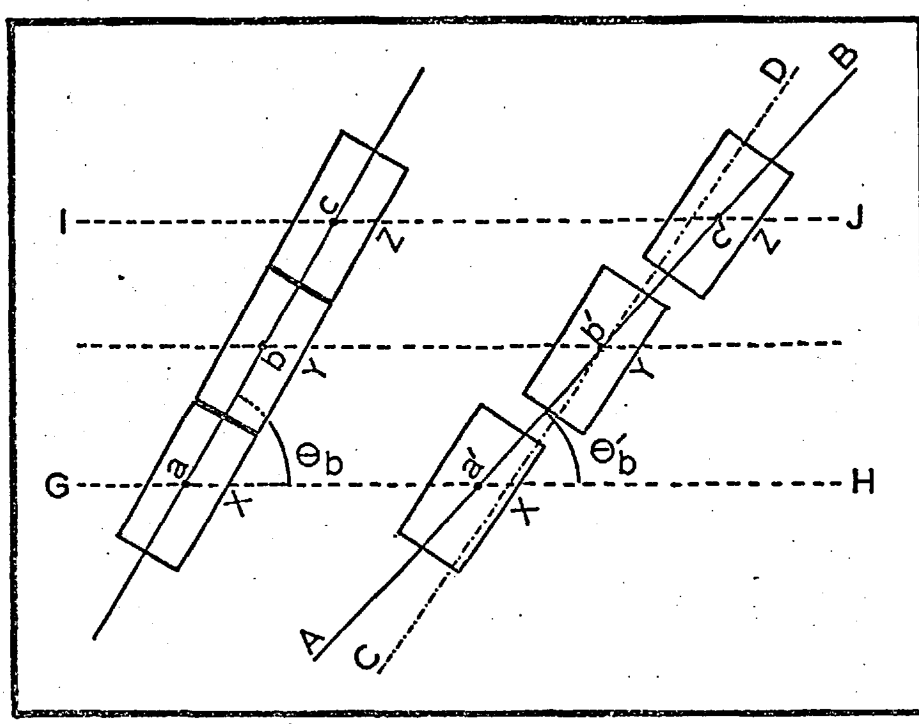

Fig. 7.3 Theoretical model illustrating the method of construction of extended belemnites undergoing homogeneous deformation.

obtained from equations 3.9 and 3.20 and is represented by the dotted line 'CD' through the point 'b' in fig. 7.3. The final reconstruction is performed by drawing the original fragments at their respective deformed positions and keeping them parallel to the dotted line 'CD'. The required amount of extension is then determined by measuring the original length (ac) and deformed length (a'c') of the specimen and using the relationship, $e = \frac{a'c' - ac}{ac}$. Repeating this procedure, for different values of finite strain, it has been possible to compute the progressive development of "stretched belemnites". Several models of stretched belemnites have been investigated by varying their axial ratio, initial orientation and the type of deformation. Two of the models (one for each type of deformation) are illustrated in figures 7.4 and 7.5. The amount of elongation derived from a number of such examples is recorded in tables 11 and 12 (Appendix C).

7.4 INTERPRETATION OF RESULTS

The results of the theoretical analysis of stretched belemnite indicate that the amount of extension of belemnites is dependent mainly on the initial orientation of the whole belemnite body (θ'_b), the type of deformation (irrotational strain or simple shear) and the axial ratio of belemnites.

The results show that a simple relationship exists between the amount of extension of belemnites and their initial orientation (θ_b) in case of irrotational strain deformation (fig. 7.6). It is seen from the graphs in fig. 7.6 that the amount of extension of belemnite models lying finally within the extension field, increases progressively with the decrease of their initial orientation with reference to the major principal axis of the strain ellipse. The amount of extension is largest when the belemnite specimen lies at $\theta_b = 0^o$ (i.e. parallel

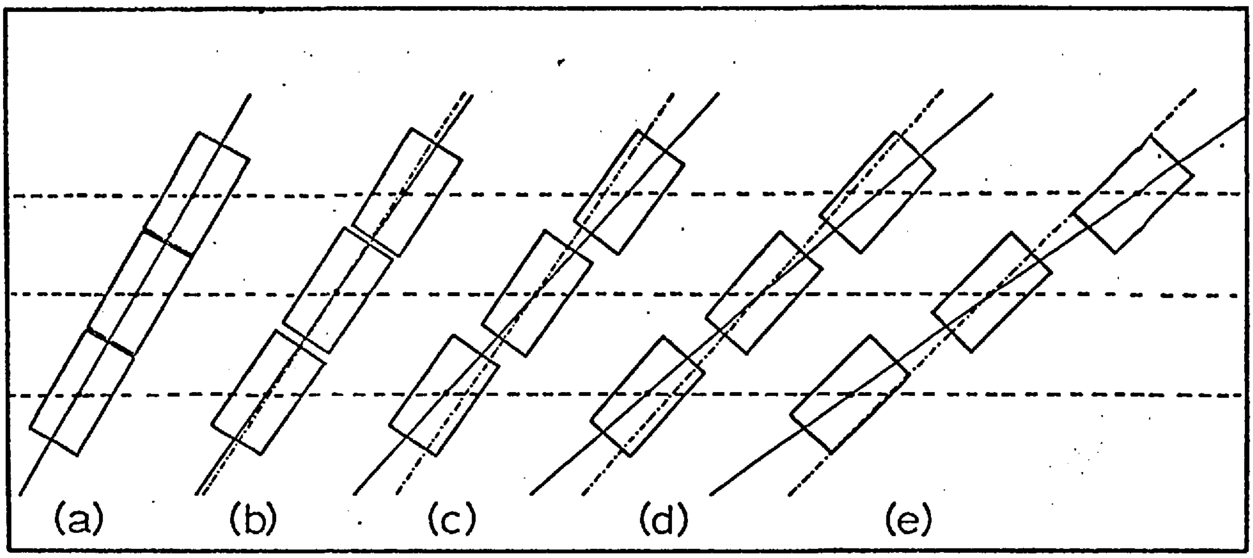

Fig. 7.4 An example of construction of a theoretical model of an extended belemnite undergoing progressive pure shear deformation.
(a) Undeformed; (b) $\sqrt{\lambda_1/\lambda_2} = 1.21$; (c) $\sqrt{\lambda_1/\lambda_2} = 1.61$;
(d) $\sqrt{\lambda_1/\lambda_2} = 2.08$; (e) $\sqrt{\lambda_1/\lambda_2} = 2.6$

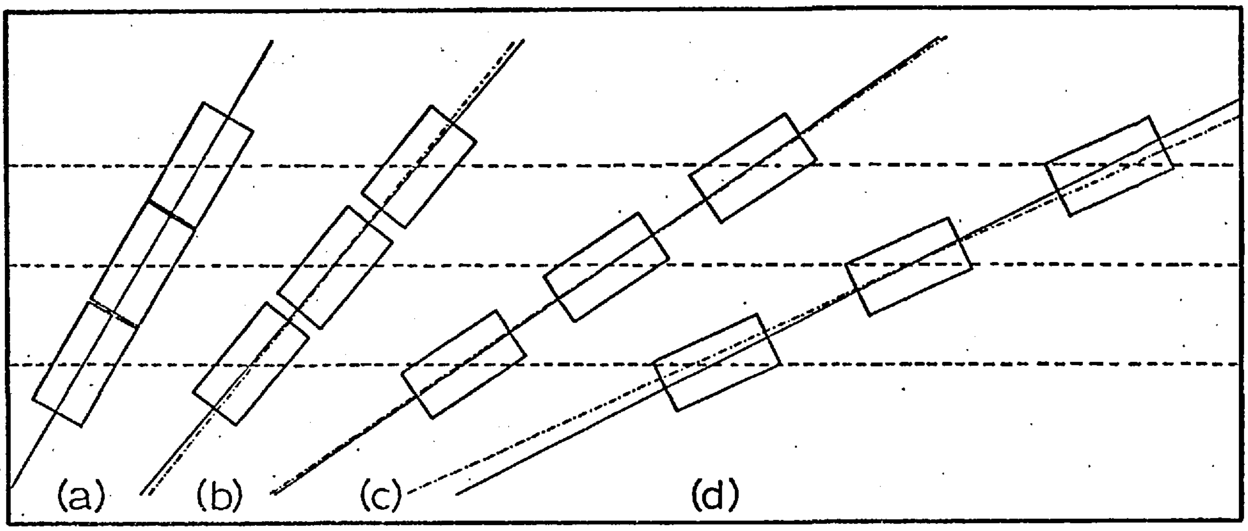

Fig. 7.5 An example of construction of a theoretical model of an extended belemnite undergoing progressive simple shear deformation.
(a) Undeformed; (b) $\gamma_s = 0.267$; (c) $\gamma_s = 0.876$; (d) $\gamma_s = 1.4$

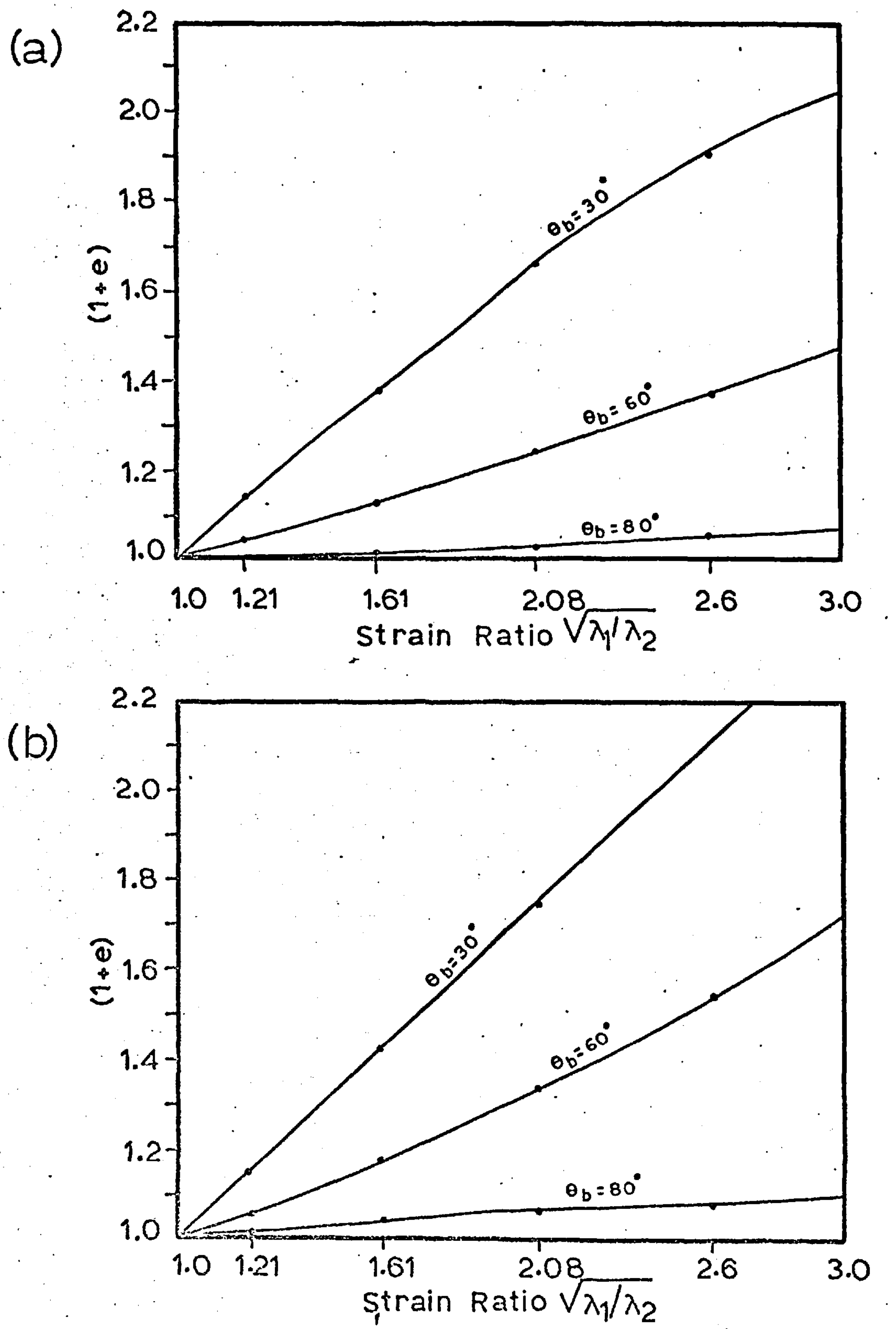

Fig. 7.6 Theoretical graphs for the elongation (1+e) of stretched belemnites being deformed during progressive pure shear. θ_b represents initial orientation of the specimen with reference to the principal extension direction.

(a) belemnite body a/b = 3:1; fragments a/b = 1:1

(b) belemnite body a/b = 6:1; fragments a/b = 2:1

to the principal extension direction). The graphs representing the behaviour of belemnite models during simple shear deformation demonstrate that the relationship between the extension of belemnite models and their initial orientation (θ_b) (fig. 7.7, a, b) cannot be expressed as simply as in the case of irrotational strain deformation. For a particular value of θ_b the amount of extension for a given amount of strain is seen to depend on the axial ratio of the specimen. Comparing graphs presented in (a) and (b) of fig. 7.7 it is observed that the curve of $\theta_b = 60^\circ$ for belemnite model with a/b = 6:1 do not agree with that for belemnite model a/b = 3:1. This curve (representing $\theta_b = 60^\circ$) indicates a lower amount of extension in fig. 7.7,a and a higher amount of extension in fig. 7.7,b than that for $\theta_b = 30^\circ$.

It is observed (theoretically and experimentally) in chapter 4 that the major principal axis of the strain ellipse, produced by the simple shear deformation, rotates progressively from 45° to 28.5° during deformation up to $\gamma_s = 1.4$. The principal extension direction and the extension field, therefore, rotate during simple shear deformation. The rotation of any inclusion set in a matrix undergoing simple shear deformation is the result of two effects. There are the tendency for a body to rotate towards the principal extension direction and the tendency of a body to rotate towards the shearing direction. Depending on the initial orientation of the belemnite body these two effects may oppose or compliment each other. The tendency of a body to rotate towards the shearing direction due to the movement of the surrounding matrix increases as the axial ratio of the specimen increases.

Results derived from the theoretical models demonstrate that a belemnite specimen having a/b = 3:1, when situated initially at $\theta_b = 30^\circ$ tends to remain within the extension field during subsequent deformation and thus suffer a large amount of extension (fig.7.7,a).

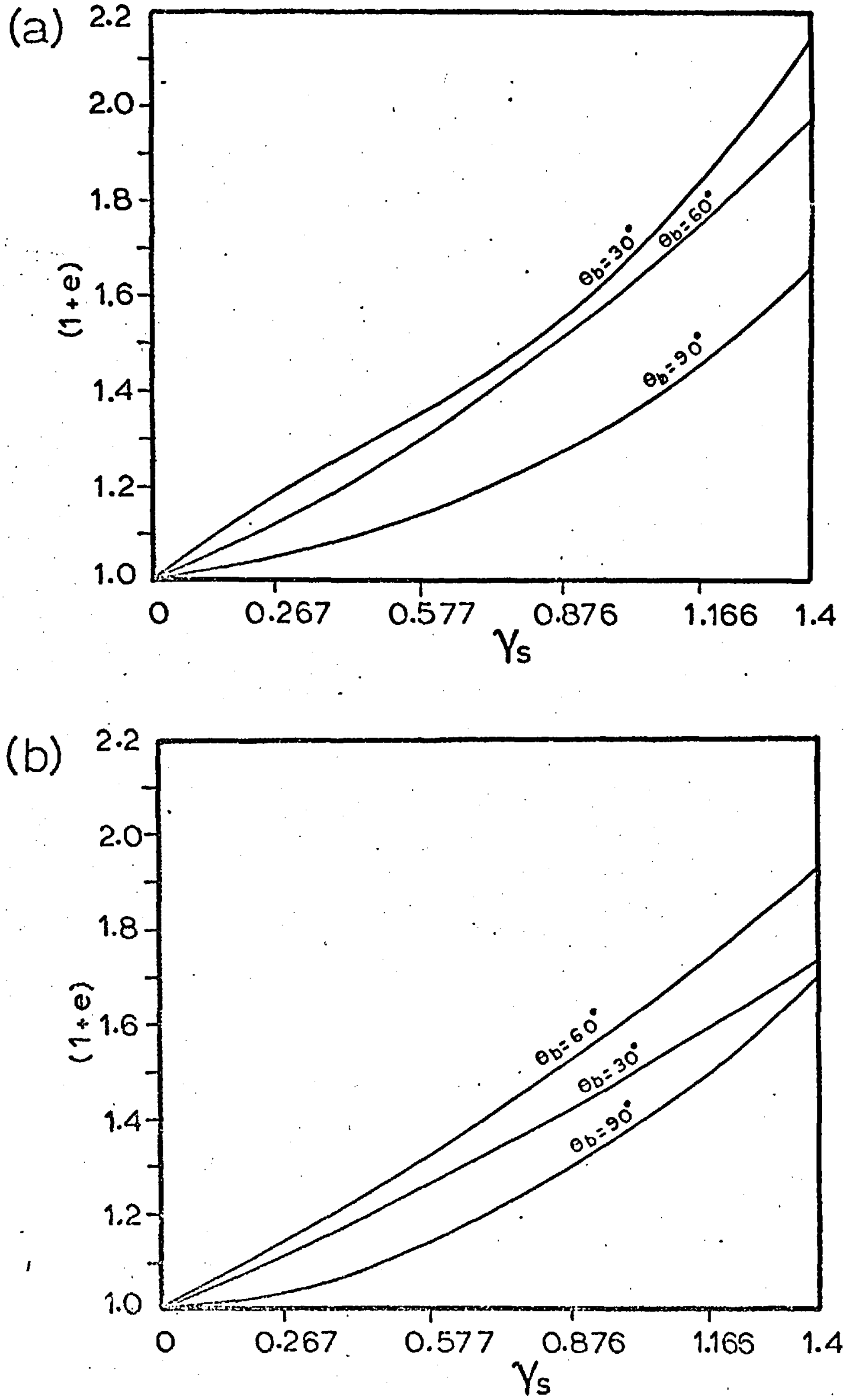

Fig. 7.7 Theoretical graphs for the elongation of stretched belemnites undergoing progressive simple shear deformation. θ_b represents the initial orientation of the specimen with respect to the shearing direction.

(a) belemnite body a/b = 3:1; fragments a/b = 1:1

(b) belemnite body a/b = 6:1; fragments a/b = 2:1

A belemnite specimen having a/b = 6:1, when situated initially at $\theta_b = 30^\circ$ shows much less extension (fig. 7.7,b) than the belemnite with smaller axial ratio (a/b = 3:1). This is because the belemnite with the larger axial ratio rotates towards the shearing direction faster than the belemnite with the smaller axial ratio and actually moves out of the extension field of the strain ellipse.

Theoretical studies also indicate that the individual fragments behave differently to the whole belemnite model. The en-echelon type of structure developed in stretched belemnite forms due to the differential amount of rotation between the individual fragments and the whole belemnite specimen (fig. 7.4 and 7.5).

The conclusions drawn from these studies may not provide accurate results as certain factors have not been taken into consideration in the theoretical analysis. The amount of extension has been calculated from θ_b and θ_b' considering a belemnite model with an a/b ratio that is fixed throughout the different increments of deformation. In a real situation the a/b ratio of a belemnite changes with each increment of deformation and the flow of the matrix inside the spaces created between the fragments by stretching modifies the strain state. These two factors could not be incorporated into the theoretical model and therefore the model did not completely satisfy the field situation.

CHAPTER 8. EXPERIMENTAL VERIFICATIONS OF THE BEHAVIOUR OF STRETCHED BELEMNITES

8.1 INTRODUCTION

Experimental model deformation simulating the development of stretched belmnites has been performed in order to verify the evolution and the theoretical analysis of distorted belmnites. Twenty-nine experimental runs were made varying the type of deformation (irrotational strain or simple shear), initial orientation (θ_b) and the axial ratio of the belmnite models. The results are quantitatively analysed and in the light of these results, a few methods of interpreting available field data are suggested.

The model materials, experimental procedure and the strain boxes used for the experiments, were described in chapter 4. The experimental results are not in complete agreement with the theoretical results. A possible explanation for this disagreement is given and in conclusion, it is suggested that the measured elongation of belemnites is always less than the actual elongation that has been suffered by the surrounding matrix.

8.2 PROGRESSIVE DEVELOPMENT OF STRETCHED BELEMNITES

The development of extended belemnites can be reproduced experimentally. Twenty-nine experiments were performed in order to obtain a quantitative understanding of the different aspects of stretched belemnites. Of these 29 experiments, two carried out in an irrotational strain box are selected for detailed discussion.

Three wooden strips (a/b = 2:1) were placed inside a matrix of putty in such a way that they resembled a belemnite body embedded in a matrix (fig. 8.1,a). The contacts between the fragments are assumed

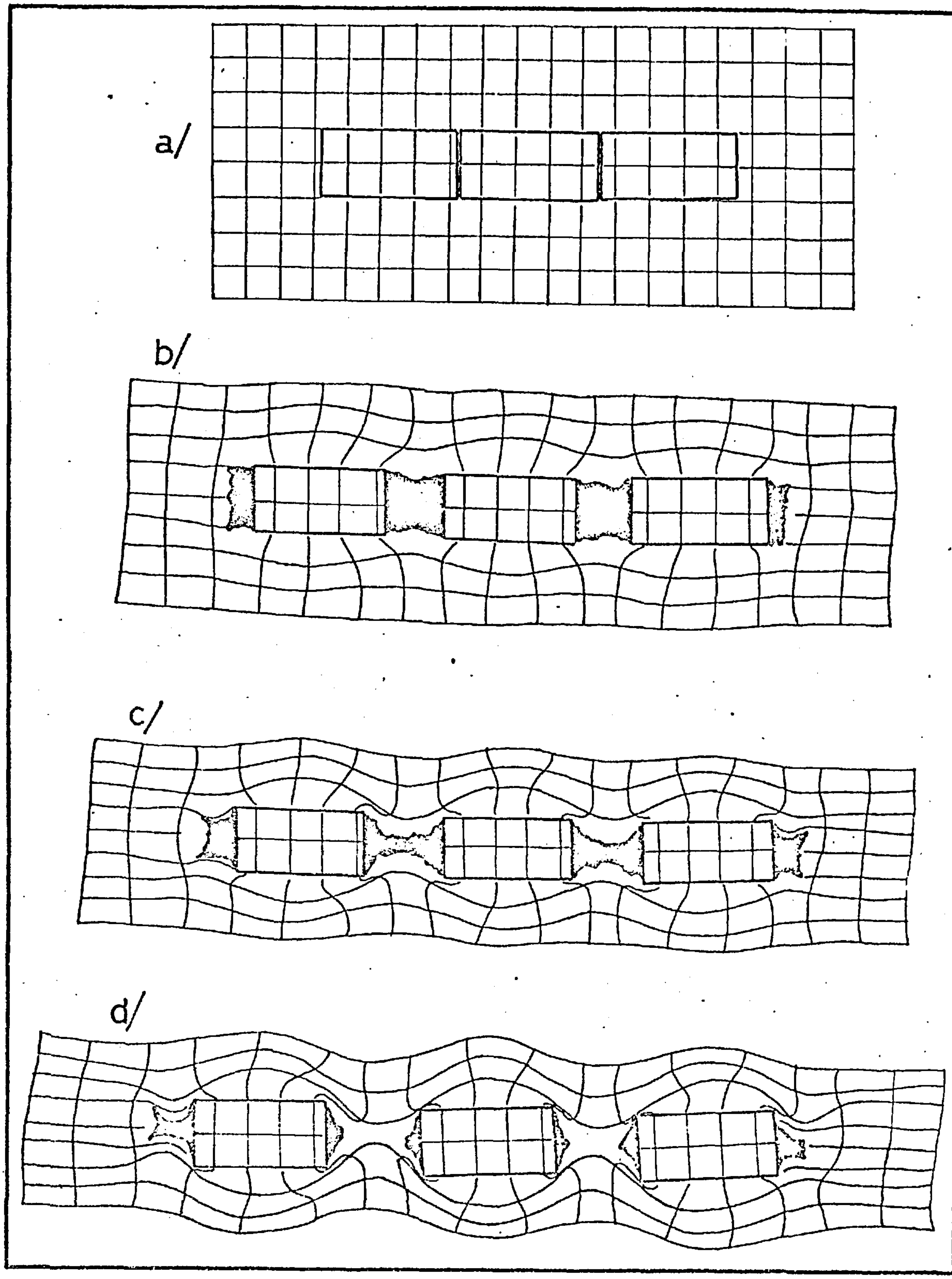

Fig. 8.1 Progressive separation of fragments simulating extension of a belemnite specimen lying initially parallel to the principal extension direction undergoing progressive irrotational strain deformation.

to be the contact between the belemnite guards. In one experiment, the wooden strips were placed parallel to the extension direction of the strain box and the matrix was deformed by irrotational strain. The stretching of the body started as soon as the compression normal to the length of the body was applied. Figure 8.1 illustrates the progressive stages in the deformation. It can also be compared to the development of boudinage which may develop in a layer lying parallel to the maximum extension direction of the strain ellipse. The deformed grids in the matrix around the body specimen show that the deformation near the fragments is inhomogeneous (fig. 8.1, b,c,d and 8.2, b,c,d). From the distorted grids, it can be seen that during deformation the matrix material moves towards the embedded body in a direction perpendicular to its long axis. The flow of the surrounding matrix produces a tensile stress on the boundary of the fragments which leads to their separation (fig. 8.1, b,c,d). The 'open spaces' formed in between the fragments are filled by the surrounding matrix during the later stages of deformation. This 'open space' can be correlated with the space between the fragments of belemnites which are usually filled with quartz or calcite (or both).

Another common type of structure developed in stretched belemnites is the 'en-echelon' type of structure (figs. 8.2 and 9.5). This structure was found to develop in experiments in which the long axis of wooden strip was at an angle to the extension direction. The specimen (belemnite model) was deformed inside an irrotational strain box. Figure 8.2 illustrates how the separating fragments develop an 'en-echelon' type of structure during progressive deformation. When allowed to deform, the body starts to rotate towards the extension direction. The individual fragments move away from each other and rotate. It has been established in chapter 5 that the surrounding

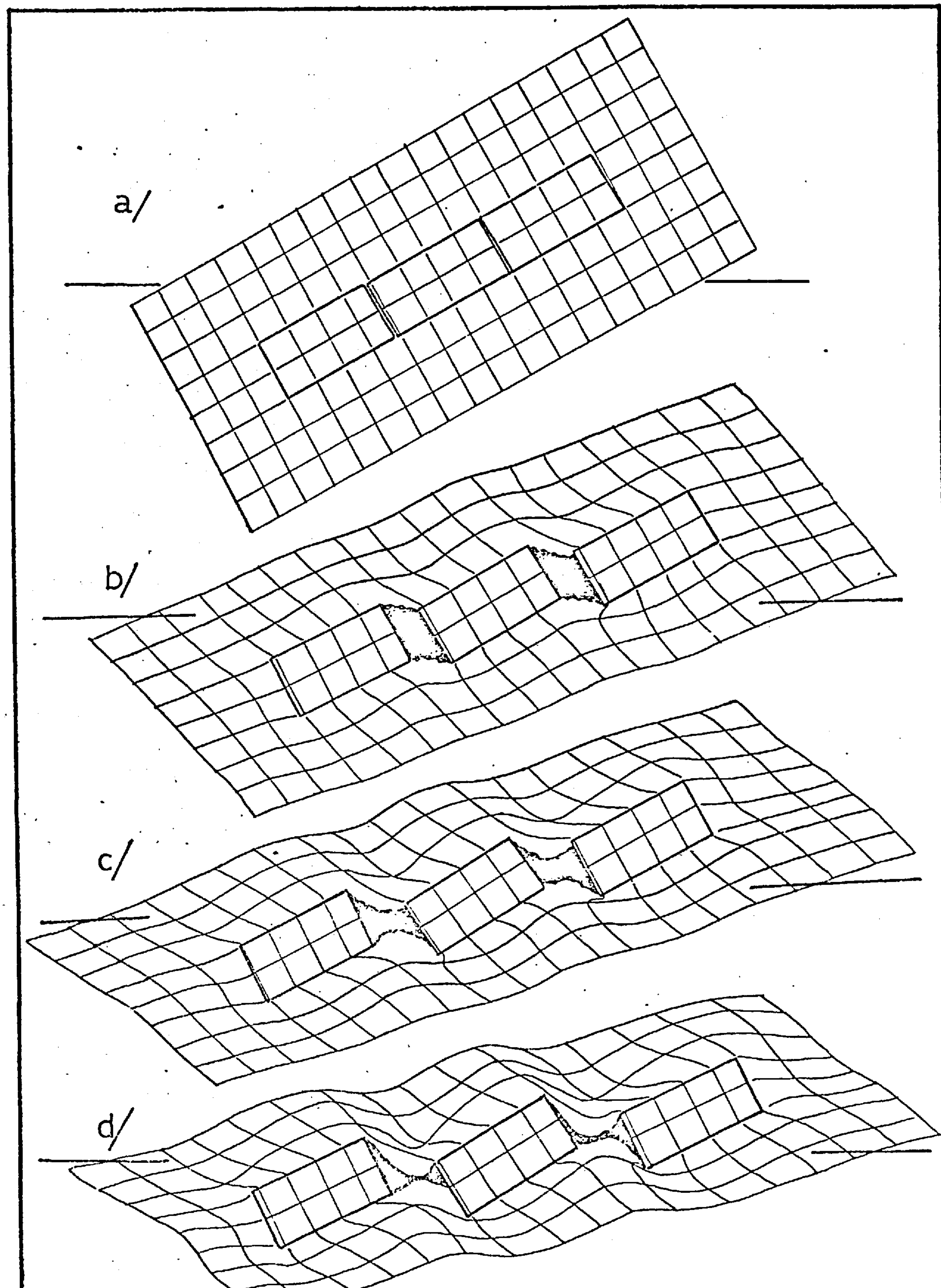

Fig. 8.2 Progressive development of 'en-echelon' structure in a layer simulating a belemnite specimen oriented initially oblique to the extension direction during progressive irrotational strain deformation.

matrix rotates faster than any inclusion when subjected to irrotational strain deformation and that the smaller the axial ratio of the inclusion the slower it rotates. Hence, the matrix material forces the whole body to rotate along with it whereas the fragments, being smaller in size, rotate less than the whole body. This differential amount of rotation of the whole body compared to the individual fragments causes the development of the 'en-echelon' type of structure. The above experimental observations show that the formation of the 'en-echelon' type of structure is due to the symmetry axes of the whole belemnite body being at an angle to the principal extension or compression.

8.3 RESULTS FROM THE EXPERIMENTS UNDERGOING IRROTATIONAL STRAIN

Twelve experiments simulating the development of stretched belemnites were performed in the irrotational strain box. Five of these are shown in plates XXII to XXVI. Measurements were taken from the photographic records of the experiments and the results are presented in table 13, a,b,c (in Appendix D). The experiments have been divided into three groups based on the axial ratio of both the body specimen and the fragments. The results of the elongation $(1 + e)$ and the amount of rotation obtained from these experiments are presented in fig. 8.3 along with the theoretically predicted results.

Inspection of fig. 8.3 shows that the amount of elongation increases with the decrease of initial orientation (θ_b) of the specimen body with reference to the extension direction of the box. $\theta_b = 0^o$ represents the condition when a specimen body is parallel to the extension direction of the bulk strain ellipse. Hence, the graph for $\theta_b = 0^o$ records the largest amount of elongation. The experimental results presented in fig. 8.3, a,b,c, show that considerable differences exist between the experimental and theoretical results. The probable

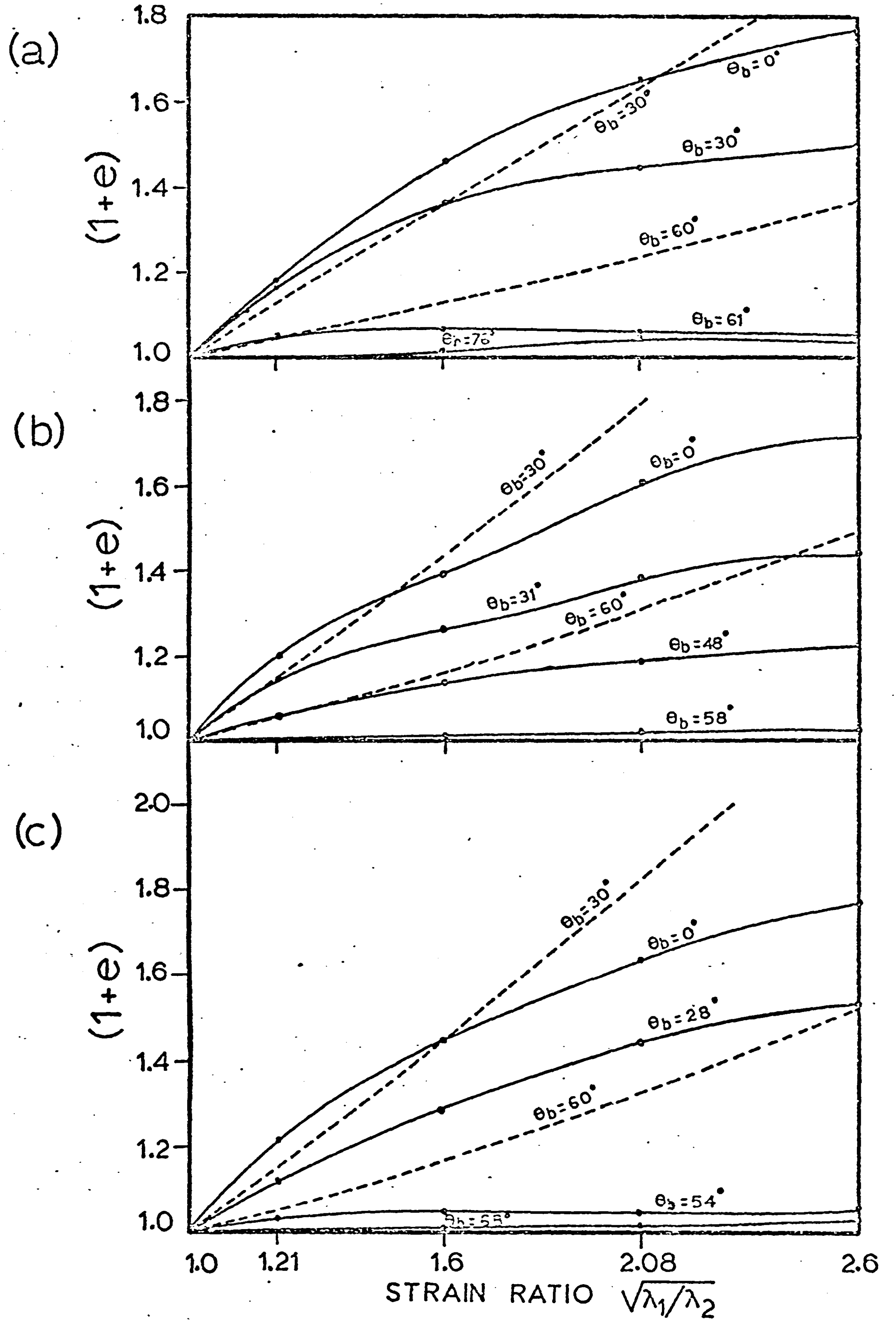

Fig. 8.3 Experimental graphs for the elongation (1+e) of extended belemnites undergoing progressive irrotational strain deformation. Solid lines and broken lines represent experimental and theoretical graphs respectively. θ_b is the initial orientation of the whole belemnite body with reference to the principal extension direction. (a) belem. body a/b=3:1; frags. a/b=1:1; (b) belem. body a/b=6:1; frags. a/b=2:1; (c) belem. body a/b=9:1; frags. a/b=3:1

reason for the difference of the results will be discussed in section 8.5.

Observation of fig. 8.4 demonstrates that the amount of rotation of the whole body during progressive deformation is dependent on its θ_b value. From the graphs of fig. 8.4, it can be seen that for low values of θ_b (i.e. $\theta_b < 65^\circ$ approximately), the amount of rotation increases with the increase of θ_b (measured with reference to the principal extension direction). This relationship does not hold if the specimen is situated initially at a higher angle (i.e. $\theta_b > 65^\circ$) to the principal extension direction. A specimen lying at a low angle to the compression direction, suffers relatively little rotation. In figure 8.4,a, the graph for $\theta_b = 61^\circ$ exhibits greatest amount of rotation, whereas, the curve for $\theta_b = 76^\circ$ shows that the amount of rotation is even less than that for $\theta_b = 30^\circ$. The distribution of the other graphs in fig. 8.4,b and c for different a/b ratio of the body specimen also follow a similar pattern.

8.4 RESULTS FROM THE EXPERIMENTS DURING SIMPLE SHEAR DEFORMATION

Four sets of experiments were performed in the simple shear box, each set being characterised by particular axial ratios of the fragments. The axial ratios chosen for the fragments for the first 3 sets of experiments were a/b = 1:1; a/b = 2:1; and a/b = 3:1 respectively. In the fourth set of experiments, fragments of different a/b ratio were used. Seventeen experimental runs were performed in the simple shear box and various values for θ_b (initial orientation of a belemnite body with reference to the shearing direction) were used in the 4 sets of experiments. Six of these are illustrated in plates XXVIII to XXXII. The amounts of elongation (1 + e) and rotation recorded during the experiments are shown in table 14,a,b,c (in Appendix D)

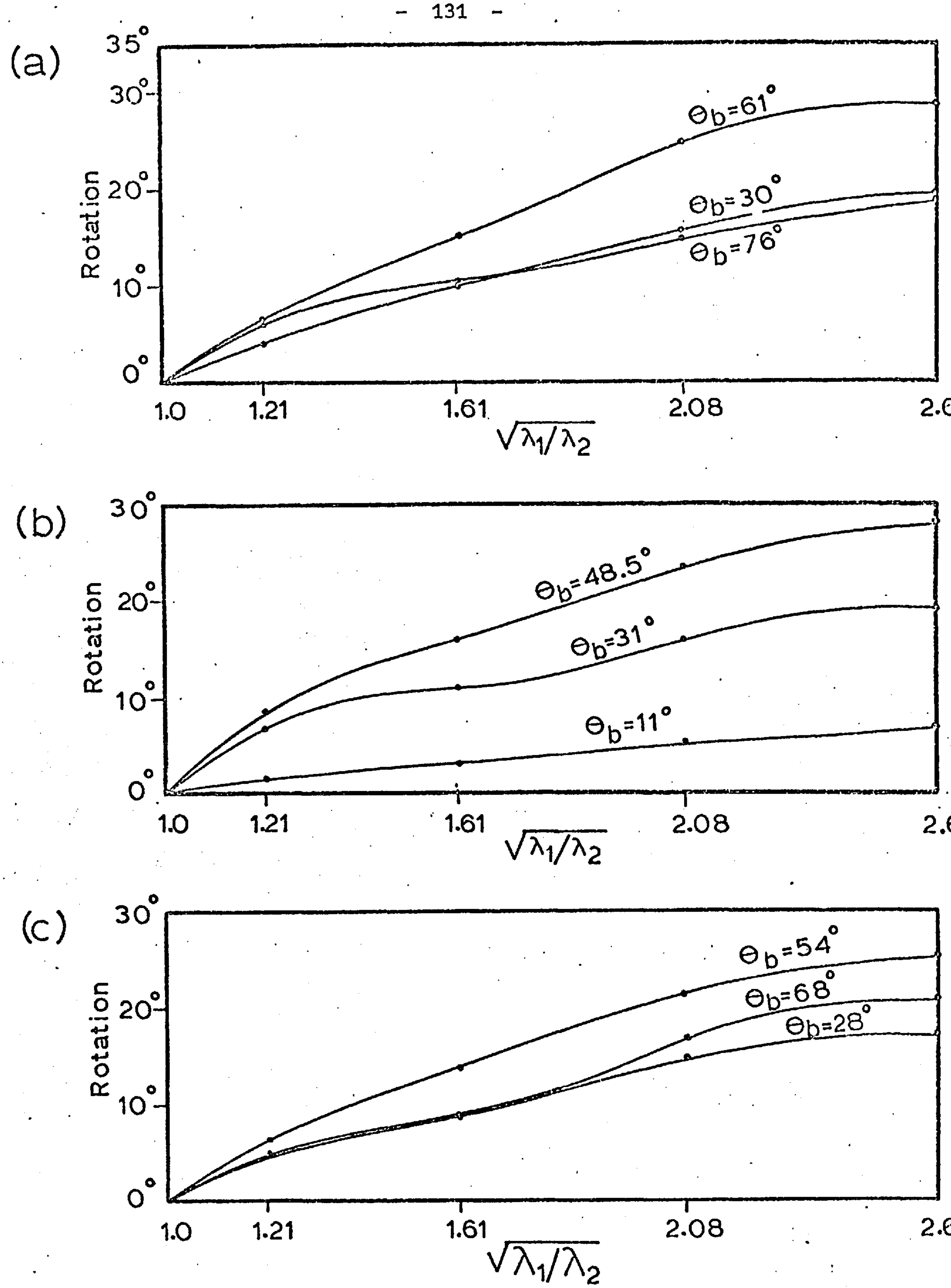

Fig. 8.4 Experimental graphs for the rotation of belemnite body set in a matrix undergoing progressive irrotational strain. θ_b represents the initial orientation of the specimen with reference to the principal extension direction.

(a) belemnite body a/b = 3:1; fragments a/b = 1:1

(b) belemnite body a/b = 6:1; fragments a/b = 2:1

(c) belemnite body a/b = 9:1; fragments a/b = 3:1

and are graphically presented in fig. 8.5. The theoretical curves are also shown.

The graphs in fig. 8.5, a,b,c show the relationship between the elongation and the shear strain for the specimens (with a/b = 3:1; a/b = 6:1; a/b = 9:1) containing fragments with axial ratios of a/b = 1:1; a/b = 2:1 and a/b = 3:1 respectively. It can be seen from the similarity of the graphs that the axial ratio of the fragment does not effect the deformation history very significantly. Fig. 8.5,a shows that the greatest elongation of the belemnite occurs when $\theta_b = 64.5^\circ$. A most interesting feature of these experiments illustrated by the graphs (fig. 8.5,a,b,c) is the cross over of the two curves $\theta_b = 91^\circ$ and $\theta_b = 30^\circ$ at a late stage in the deformation history. The specimen oriented initially at $\theta_b = 120^\circ$, when subject to deformation, started to rotate but did not elongate. Slight elongation of the specimen body began at a late stage in the deformation history. Inspection of the other graphs (fig. 8.5,b,c) derived from the experimental runs where the axial ratio of the fragments were a/b = 2:1 and a/b = 3:1, are similar to those derived from experiments with the ratio of fragments, a/b = 1:1 (i.e. the axial ratio of the whole body a/b = 3:1). The slight variation in the amount of elongation is due to the variation of the axial ratio of the specimen. It can also be seen from these graphs (fig. 8.5,a,b,c) that a specimen body lying parallel to the shearing direction (i.e. $\theta_b = 0^\circ$) shows very little or no extension.

The amount of rotation of the specimen body during progressive deformation was also measured and the results are shown in fig. 8.6, a,b and c. In all three cases the pattern of the graphs are similar and the amount of rotation is largest for largest θ_b (with reference to the shearing direction).

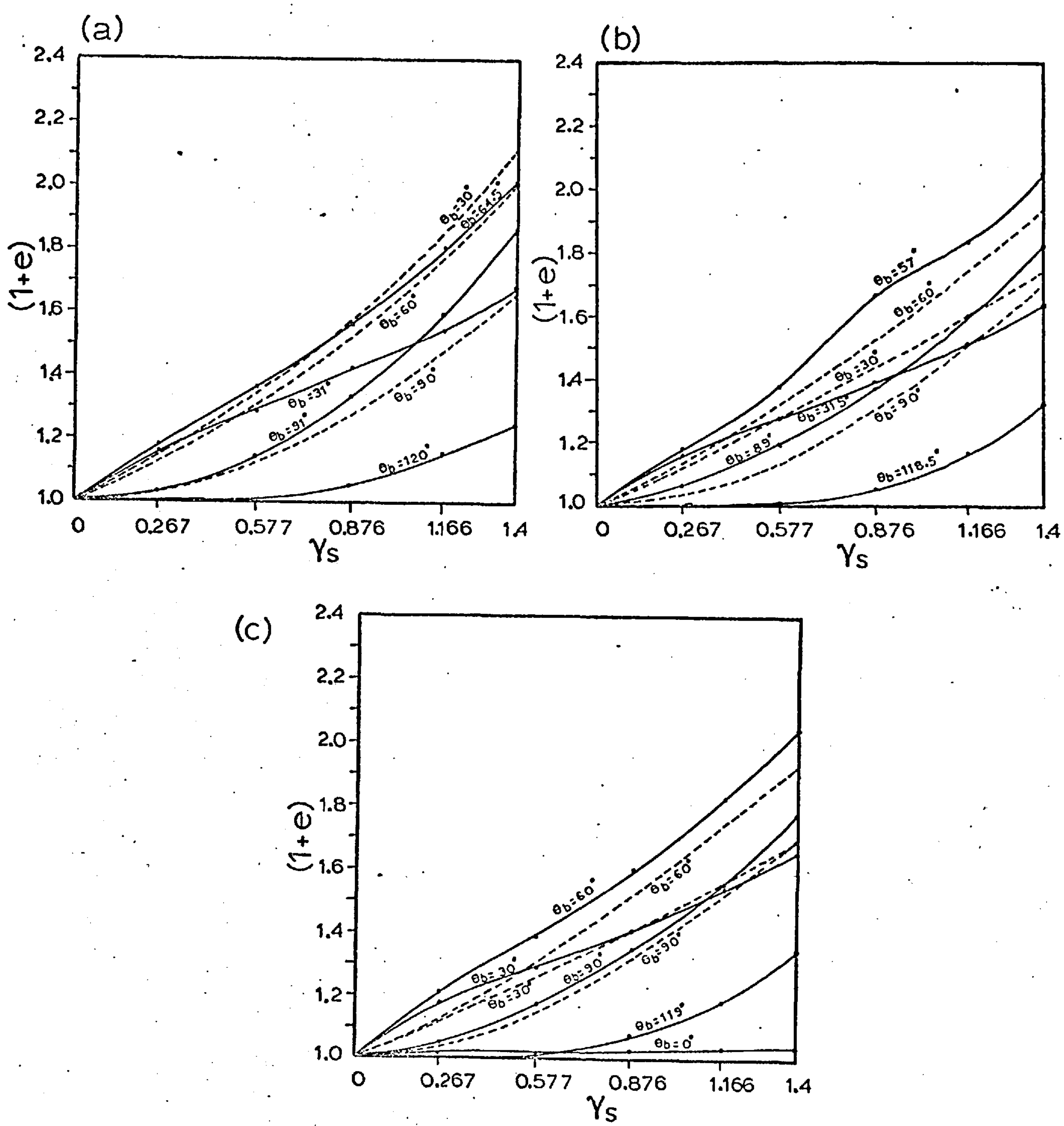

Fig. 8.5 Experimental graphs for the elongation (1+e) of stretched belemnites set in a matrix undergoing progressive simple shear deformation. γ_s represents the amount of simple shear and θ_b is the initial orientation of a specimen with reference to the shearing direction. Solid and broken lines are experimental and theoretical graphs respectively.

(a) belemnite body a/b = 3:1; fragments a/b = 1:1

(b) belemnite body a/b = 6:1; fragments a/b = 2:1

(c) belemnite body a/b = 9:1; fragments a/b = 3:1

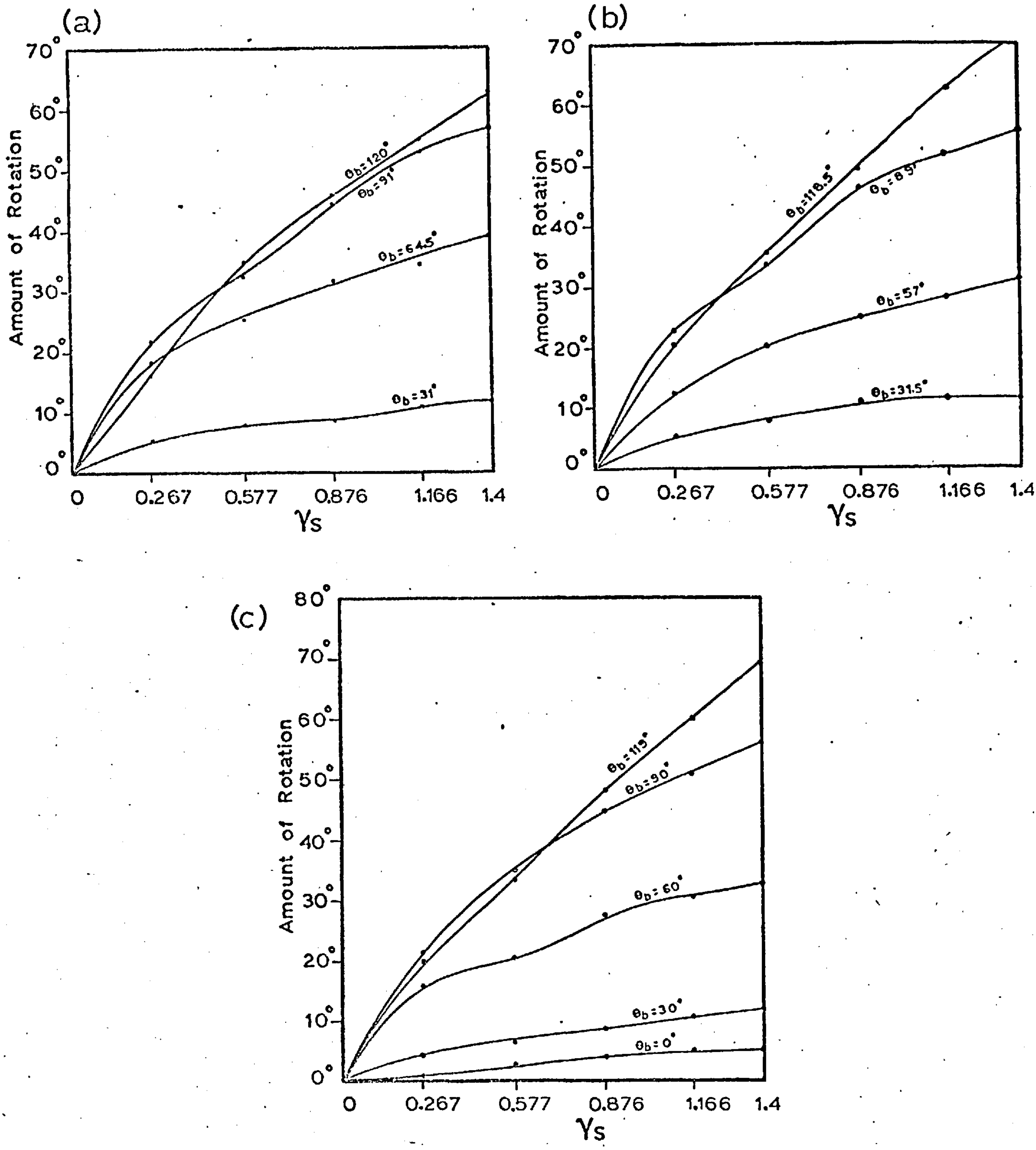

Fig. 8.6 Experimental graphs for the rotation of belemnite specimens set in a matrix undergoing progressive simple shear deformation. γ_s is the amount of simple shear and θ_b is the initial orientation of the specimen with reference to the shearing direction.

(a) belemnite body a/b = 3:1; fragments a/b = 1:1

(b) belemnite body a/b = 6:1; fragments a/b = 2:1

(c) belemnite body a/b = 9:1; fragments a/b = 3:1

In addition to above observation, three more experiments were performed in which the individual fragments had dissimilar a/b ratios. The results are presented in fig. 8.7a,b. It shows that the pattern of the curves and their distributions for elongation and rotation are similar to the results presented figs. 8.5 and 8.6. This suggests that dissimilar sizes of fragments which may exist in a specimen do not significantly influence its elongation and rotation.

8.5 DISCUSSION OF THE RESULTS

The discrepancy between the experimental and theoretical results is discussed in this section. Inspection of figs. 8.3 and 8.5 shows that the experimental results (solid lines in the graphs) for both type of deformation do not agree with the theoretically predicted results (broken lines). These discrepancies are greater in the irrotational strain experiments than in the simple shear experiments.

In theoretical analysis, the rotations and extension of the belemnite specimen were calculated assuming that the specimen body of belemnite deform passively with the matrix. The effect of the flow of the surrounding material into the space that opened up between the fragments and the possibility of relative displacement of the fragments along their contacts normal to the long axis of the specimen body was ignored.

The displacement vectors in the matrix around the specimen derived from the experiments for both the irrotational and simple shear are shown in figs. 8.8 and 8.9. When deformed under irrotational strain, a specimen body whose long axis is oblique to the compression direction and which lies in the extension field of the strain ellipse, undergoes rotation and extension. The surrounding matrix tends to

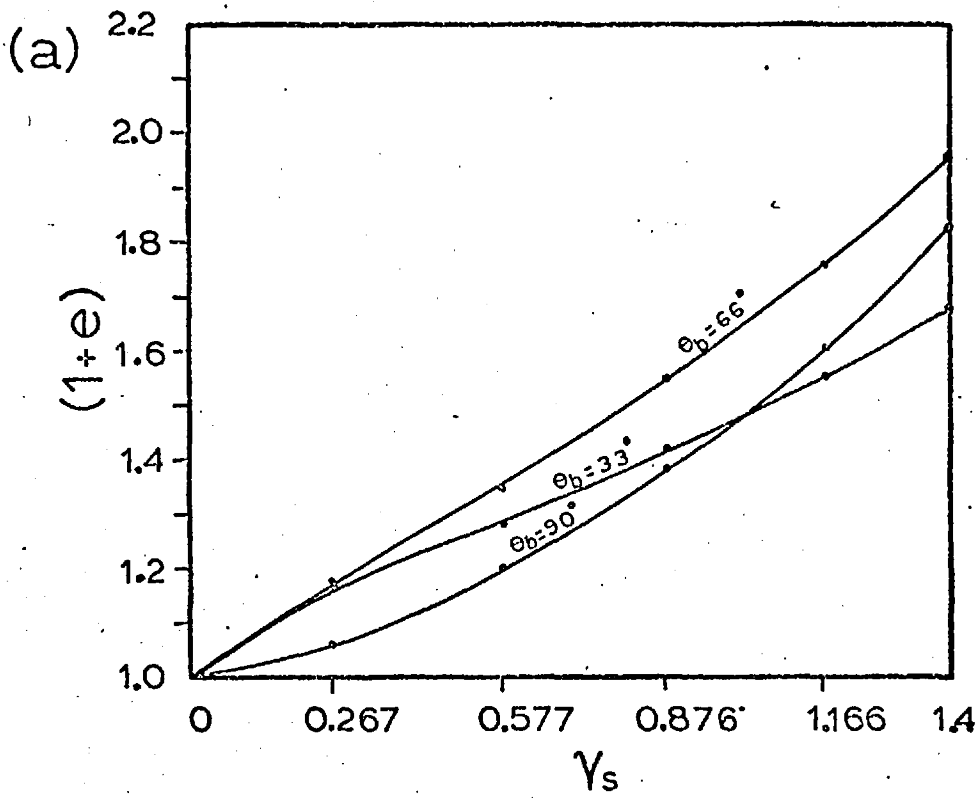

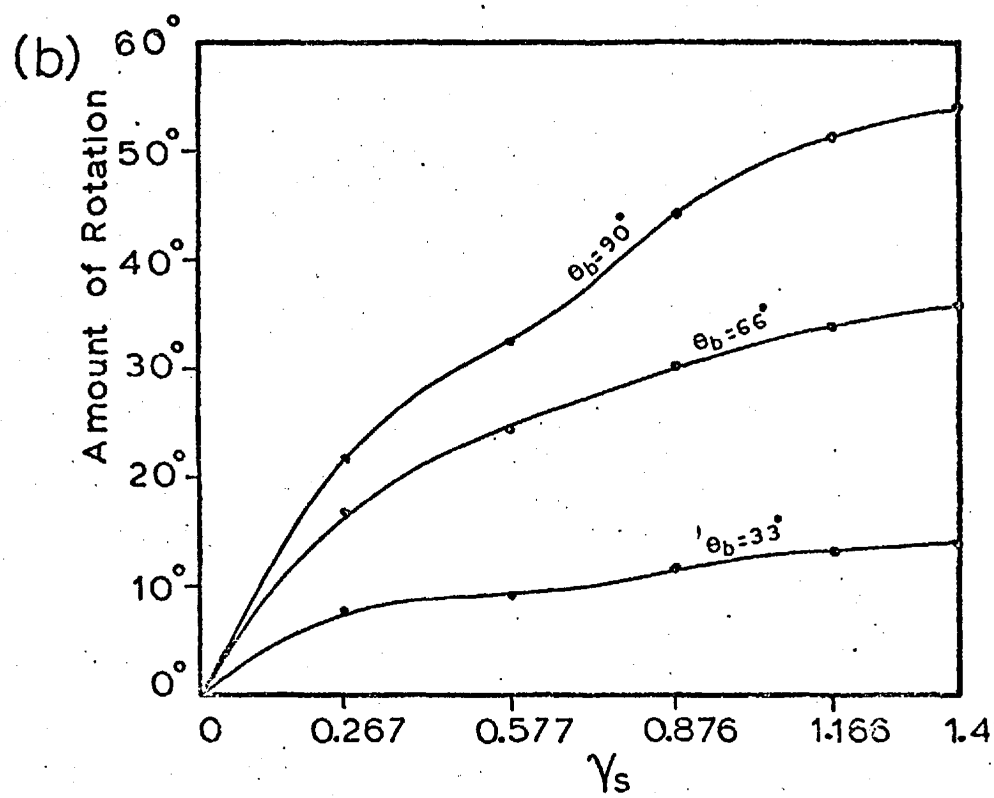

Fig. 8.7 (a) Experimental graphs for the elongation (1+e) of belemnite specimens having fragments of dissimilar axial ratio (a/b) during progressive simple shear deformation.

(b) Experimental graphs for the rotation of belemnite specimens having fragments of dissimilar axial ratio (a/b) set in a matrix undergoing progressive simple shear deformation.

γ_s – Amount of simple shear

θ_b – Initial orientation with reference to the shearing direction.

flow into the spaces that open up between the fragments. In addition to this, adjacent fragments may suffer slight relative displacement (figs. 8.2, 9.5 and plates XXIII to XXXII). Fig. 8.8 representing progressive deformation of a belemnite model set in a matrix undergoing irrotational strain shows that the flow lines in the matrix generally moves towards the specimen from both sides in a direction parallel to the compression direction. The force exerted on the fragments by the matrix may cause some shearing along the line of fracture between the fragments. The tensile stress that is built up along the common boundary of the fragments due to this force will partly be resolved by the development of shear. The experimental observations show that the infilling of the spaces that open up between the fragments of the specimen by the surrounding matrix causes maximum disturbance of the homogeneous strain state that develops when a homogeneous material is subjected to an irrotational strain. The amount of strain that is needed for the slip along the fragment contacts and the flow of the matrix into the space created by the separation of the fragments is to be deduced from the total predicted strain. Slip along the fragment boundaries and flow of the matrix into the spaces which open up between the fragments, are mainly responsible for the elongation observed experimentally being less than that predicted theoretically.

In simple shear deformation, the matrix flows parallel to the shearing direction as shown by the flow lines in fig. 8.9. This configuration of flow lines enables the specimen to rotate easily and does not force the matrix into the spaces which open up between the specimen fragments (compare figs. 8.8 and 8.9). The relative displacement along the plane of fracture, in this case, is less pronounced than that in the experiments involving irrotational strain. In experiments involving simple shear the differences

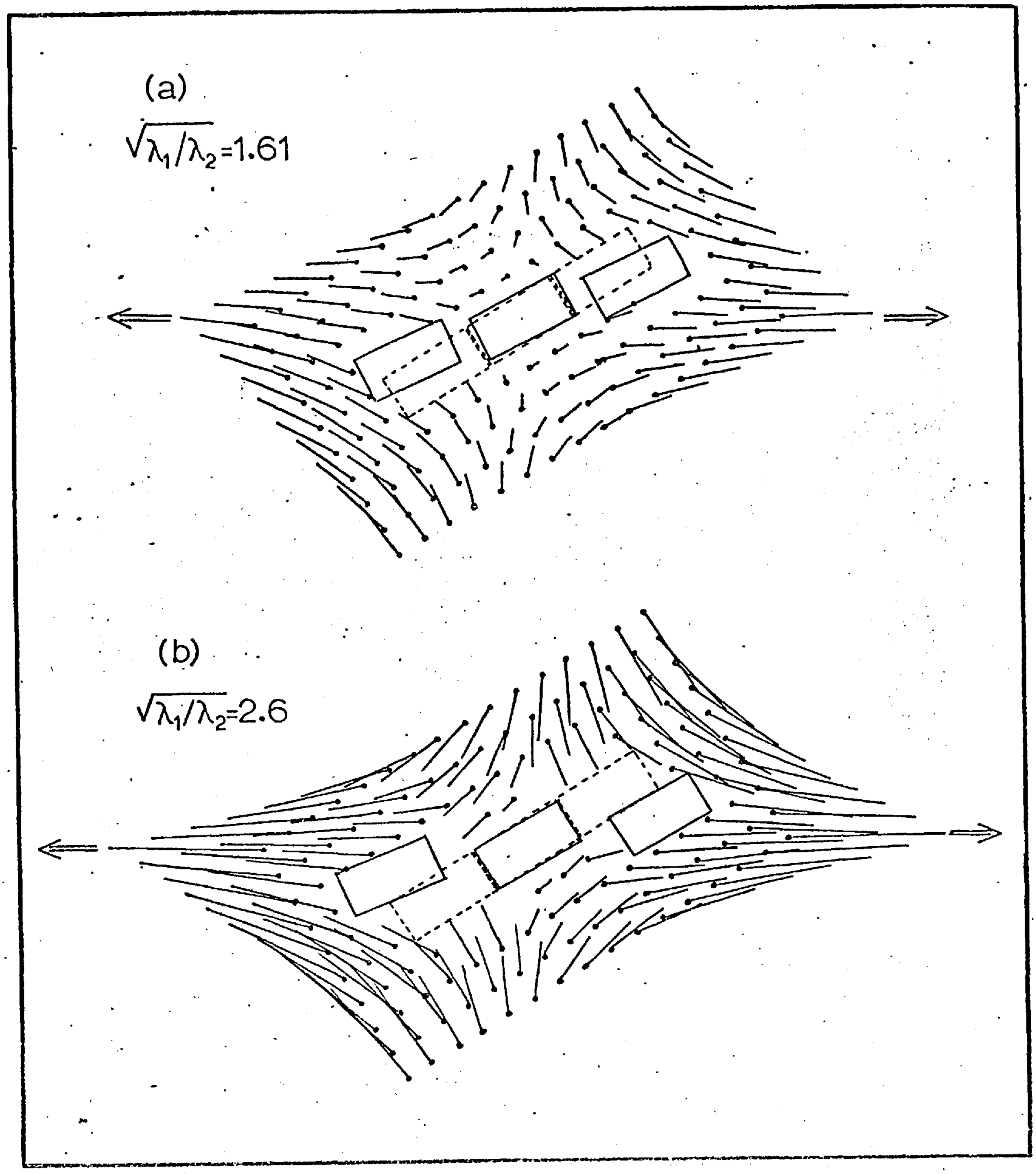

Fig. 8.8 Displacement of matrix material around a belemnite specimen undergoing irrotational strain deformation.

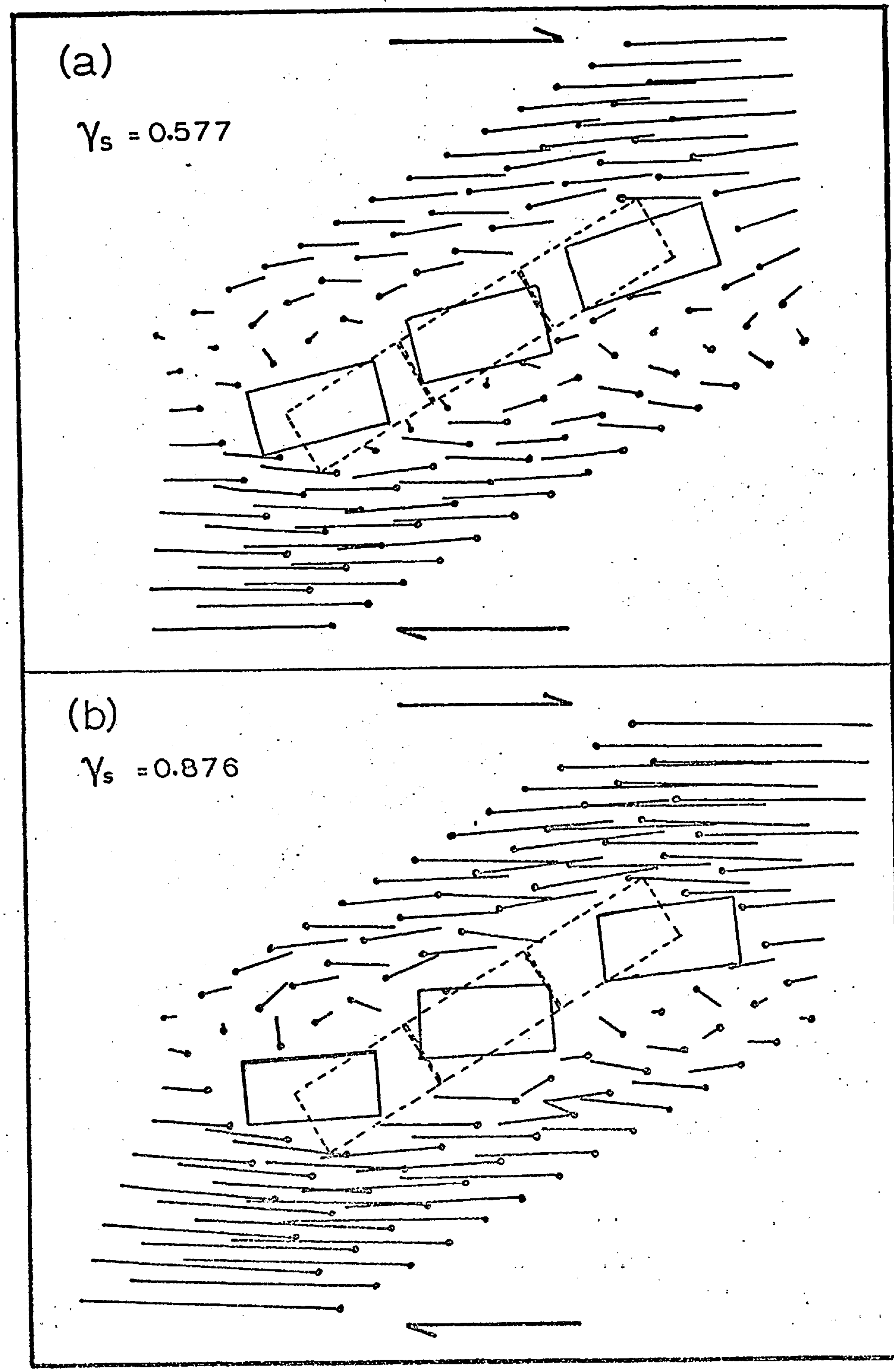

Fig. 8.9 Displacements of matrix material around a belemnite specimen undergoing simple shear deformation.

between the experimental and predicted results are somewhat less than those obtained from irrotational strain experiments.

In order to determine how closely the strain produced by the two deformation boxes approximated to pure shear and simple shear, experimental runs were performed in both the irrotational strain box and simple shear box with no inclusion set in the matrix. Strain markers stamped on the matrix showed that the strain patterns developed in both the boxes were in close agreement to the theoretically predicted strain pattern (figs. 4.7 and 4.17 in chapter 4). Theoretically, the amount of elongation of a belemnite specimen would be equal to the elongation that has developed in the matrix. However, the experiments described in section 8.3 and 8.4 show that the measured elongation is always less than that expected. The experimental production of stretched belemnites indicate that values of elongation determined from stretched belemnites will always be less than the elongation suffered by the surrounding material.

8.6 INTERPRETATION OF THE EXPERIMENTAL RESULTS

The analyses of the results in the previous sections (8.3 and 8.4) indicate that the experimental and theoretical results are not consistent. The behaviour of the model experiments of stretched belemnite are probably very like those of naturally stretched belemnites. There is almost certainly a closer correlation of behaviour than that predicted theoretically. Hence, an attempt is made to use the experimental results rather than the theory to determine strain state from the examples of stretched belemnites.

8.6.1 Effect of a/b ratio of fragments on elongation

It is commonly observed in the field that the fragments of broken belemnite guards are of dissimilar a/b ratio. In the light of these field observations, one might ask whether the accuracy of measurements of elongation from stretched belemnites depend on the a/b ratio of the individual fragments. This problem has been investigated experimentally. The specimens in these experiments were orientated at the same angle to the extension direction but the a/b ratio of the fragments was different in each experiment (i.e. a/b = 1:1; a/b = 2:1 and a/b = 3:1). The results obtained from these experiments are presented graphically in figs. 8.10 and 8.11. These figures indicate that during both irrotational strain and simple shear, the relationship between the elongation and the strain is, within the limits of experimental error, independent of the a/b ratio of the fragments.

8.6.2 Relationship between θ'_b and θ'_f

In examples of naturally stretched belemnites the final orientation of the whole specimen body (θ'_b) and that of the fragments (θ'_f), are generally not parallel. These two parameters, θ'_b and θ'_f, can easily be measured in the field and hence, an attempt is made to establish a relationship between them.

The final orientations of the specimen body and their fragments were measured from all the experiments undergoing both irrotational strain and simple shear deformation. The results are presented in figs. 8.12 and 8.13 which show a non-linear relationship between θ'_b and θ'_f. Inspection of the graphs in fig. 8.12 demonstrate that all the curves for irrotational strain deformation pass through the origin. This observation indicates that any specimen of belemnite situated initially parallel to the extension direction, in the case of irrotational strain, will show parallelism of θ'_b and θ'_f for any value of strain. This is not so in the case of simple shear. However, in

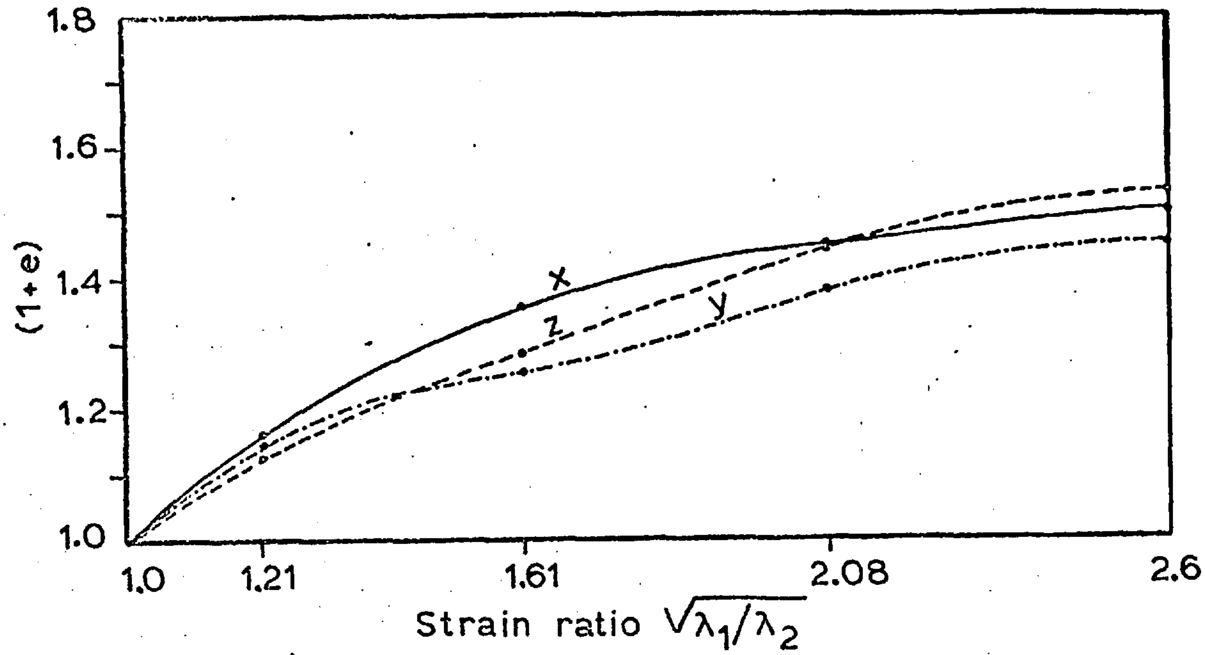

Fig. 8.10 Effect of the axial ratio (a/b) of individual fragments of a belemnite specimen on the amount of elongation during progressive irrotational strain deformation.

x - fragment a/b = 1:1; y - fragment a/b = 2:1;

z - fragment a/b = 3:1

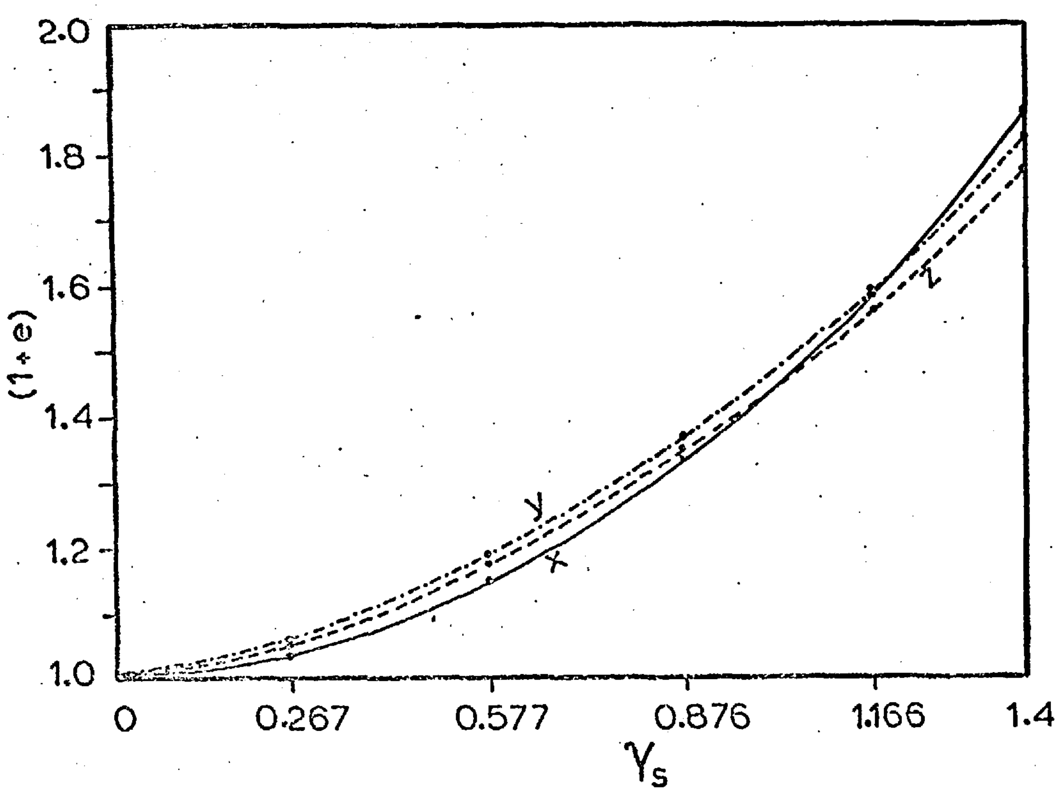

Fig. 8.11 Effect of the axial ratio (a/b) of the individual fragments of a belemnite specimen on the amount of elongation (1+e) during progressive simple shear deformation.

x - fragment a/b = 1:1; y - fragment a/b = 2:1

z - fragment a/b = 3:1

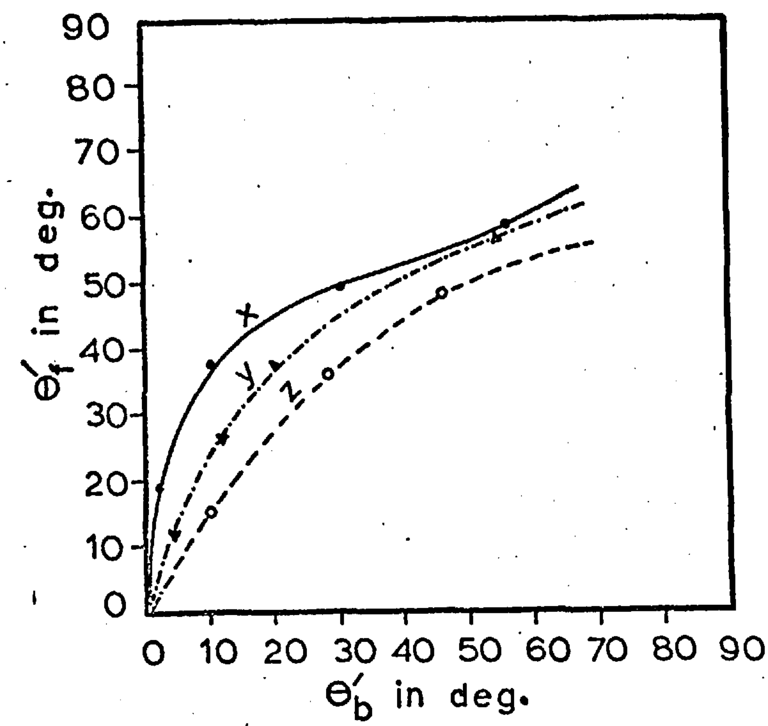

Fig. 8.12 Relationship between the final orientation of the whole belemnite specimen (θ_b') and that of the individual fragments (θ_f') after finite irrotational strain deformation ($\sqrt{\lambda_1/\lambda_2}$ = 2.6).

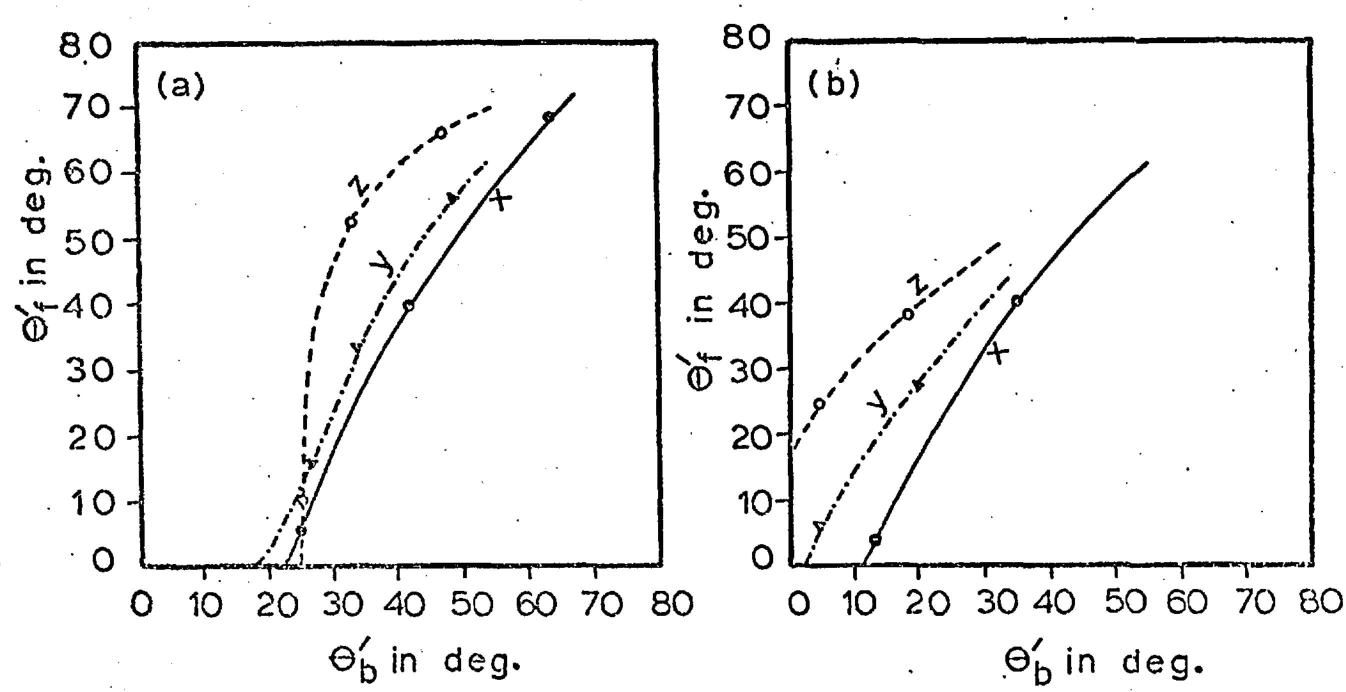

Fig. 8.13 Relationship between the final orientation of the whole specimen (θ_b') and that of the individual fragments after finite simple shear deformation (γ_s = 1.4).

(a) Orientations measured with reference to the shearing direction.

(b) Orientations measured with reference to the principal extension direction.

simple shear, a specimen originally at 45° to the shearing direction (i.e. parallel to the extension direction of the strain ellipse for the first increment of shear) does not remain at 45° to the shearing direction for the subsequent increments and therefore, θ'_b and θ'_f will not remain parallel to each other. For this reason, no curve in fig. 8.13 passes through the origin. This essential difference between the two types of deformation can be used in conjunction with field data to determine whether deformation was by progressive irrotational strain or alternatively by some rotational strain processes like that of simple shear.

8.6.3 Relationship between elongation and final orientation (θ'_b) of extended belemnites

The amount of elongation $(1 + e)$ and final orientation (θ'_b) can easily be measured from the field. Hence, the analysis of the experimental results using final orientation of the whole belemnite body (θ'_b) and the amount of elongation (calculated from the measurements of extension) is undertaken. The measurements of θ'_b were taken with reference to the extension direction of the strain ellipse from the experiments undergoing both irrotational strain and simple shear deformation.

The history of deformation on the surface of the matrix inside both the strain boxes shows that the deformation falls into field 2 (i.e. the strain ellipse has one principal extension and one principal contraction; Ramsay, 1967, fig. 3.54, p.112 and also shown in fig. 8.14,a). On the basis of the above observation, the deformation effects on linear elements can be either compressional or extensional (fig. 8.14,b).

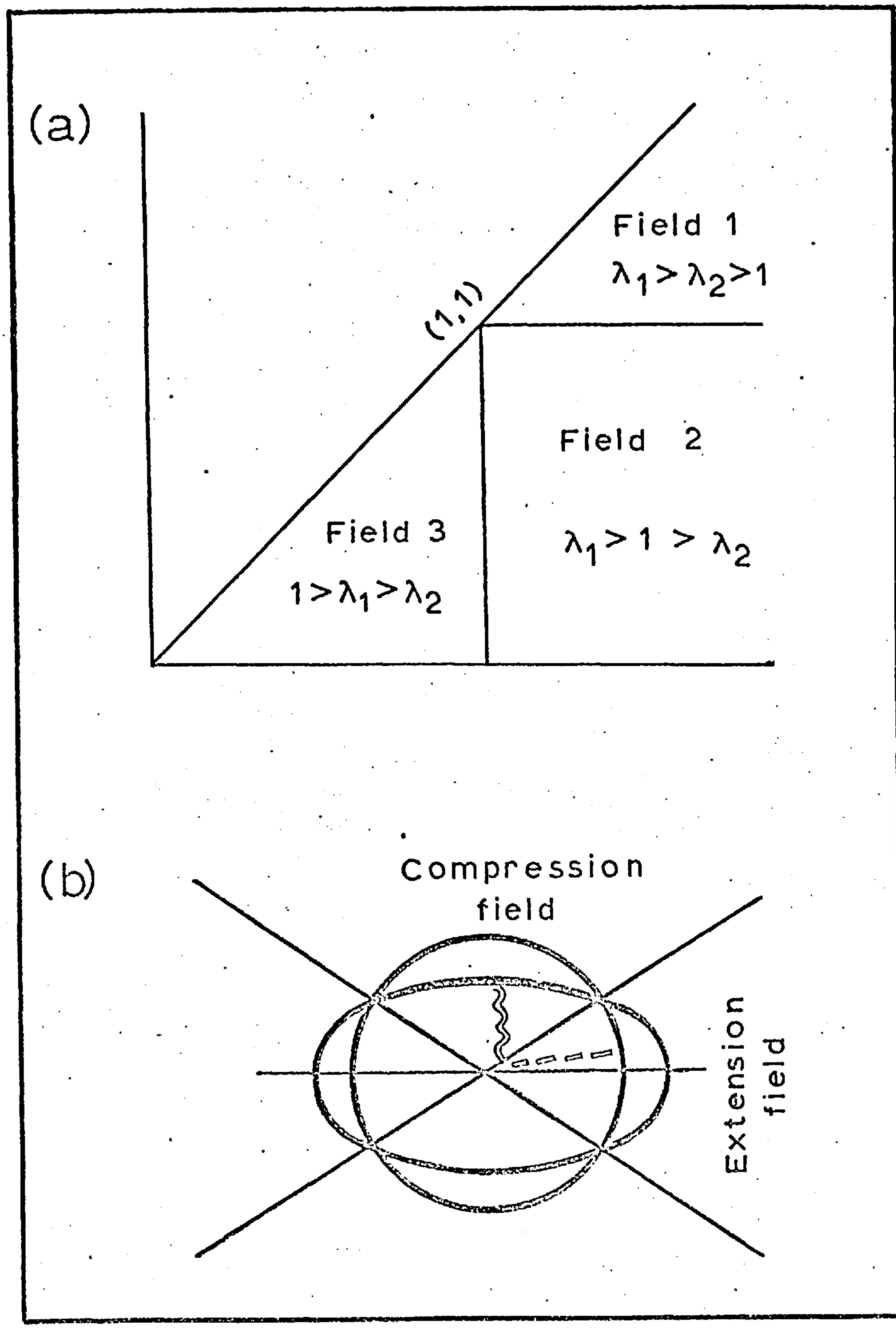

Fig. 8.14 (a) Strain state in the three fields of strain ellipse (after Ramsay, 1967, fig. 3-54).

(b) Relationship between the compression and extension field in a strain ellipse.

Any competent layer undergoing deformation is likely to be folded in the compression field and boudinaged (extended) in the extension field. Belemnite guards are rigid and resist folding. The amount of compression ($\sqrt{\lambda_2}$ of the strain ellipse) cannot, therefore, be evaluated from the belemnites lying in the compression field. The measurement of any belemnite specimen from this field can give only its initial length and is not useful data for the strain analysis. However, all the measurements of extension from the experiments were limited to the extension field and are used here for the present analysis.

The results obtained from the experiments undergoing both irrotational strain and simple shear are graphically presented in figures 8.15 and 8.16 respectively. These figures indicate the results measured from the extension field of the strain boxes and demonstrate that the amount of elongation decreases with the increase of θ_b'. The value of $\sqrt{\lambda_1}$ can easily be evaluated from the interpretation of the curves (figs. 8.15 and 8.16) as $\theta_b' = 0$ represent extension direction of the strain ellipse. Theoretically, the same curve should record $\sqrt{\lambda_2}$ when it meets $\theta_b' = 90^{\circ}$. This is not feasible in this present analysis due to the experimental condition. However, the determination of $\sqrt{\lambda_1}$ and $\sqrt{\lambda_2}$, using the relationship between elongation and θ_b' can be undertaken from the stretched belemnites where they deform in the field 1 (i.e. $\sqrt{\lambda_1} > \sqrt{\lambda_2} > 1$, fig. 8.14,a).

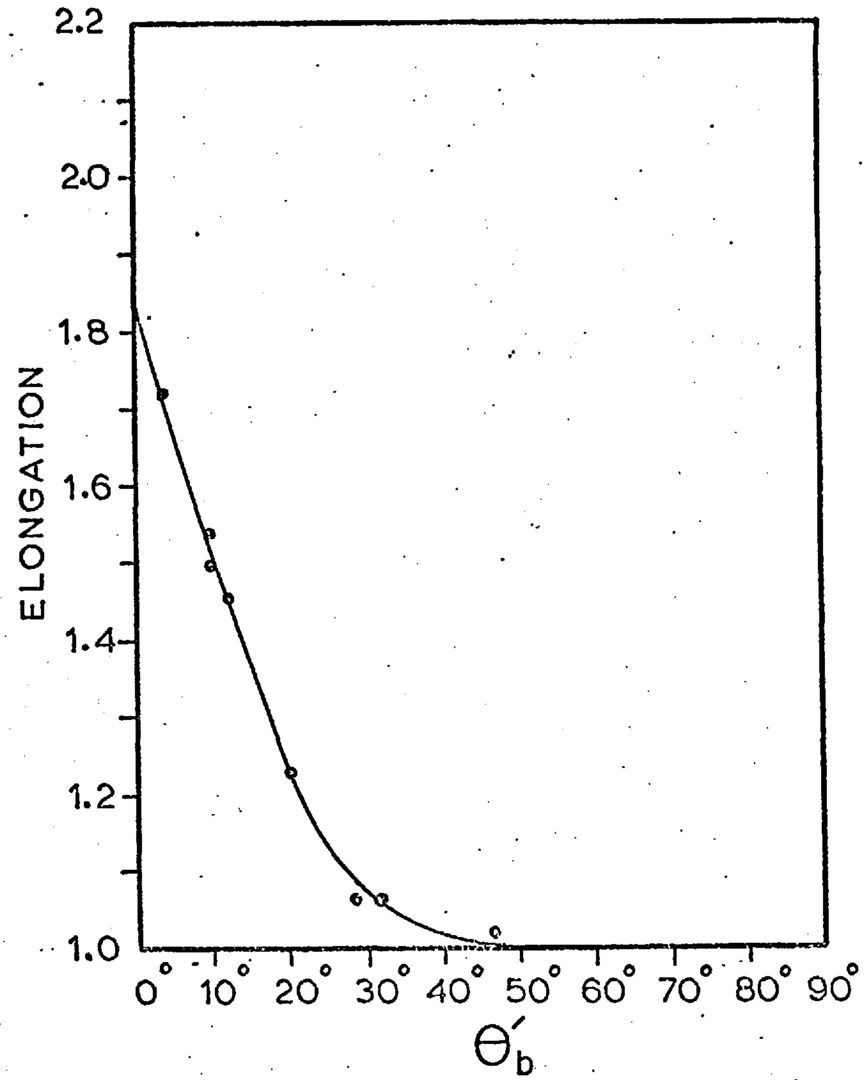

Fig. 8.15 Experimental relationship between the elongation $(1 + e)$ and the final orientation (θ_b') of stretched belemnites at the finite irrotational strain deformation $(\sqrt{\lambda_1/\lambda_2} = 2.6)$.

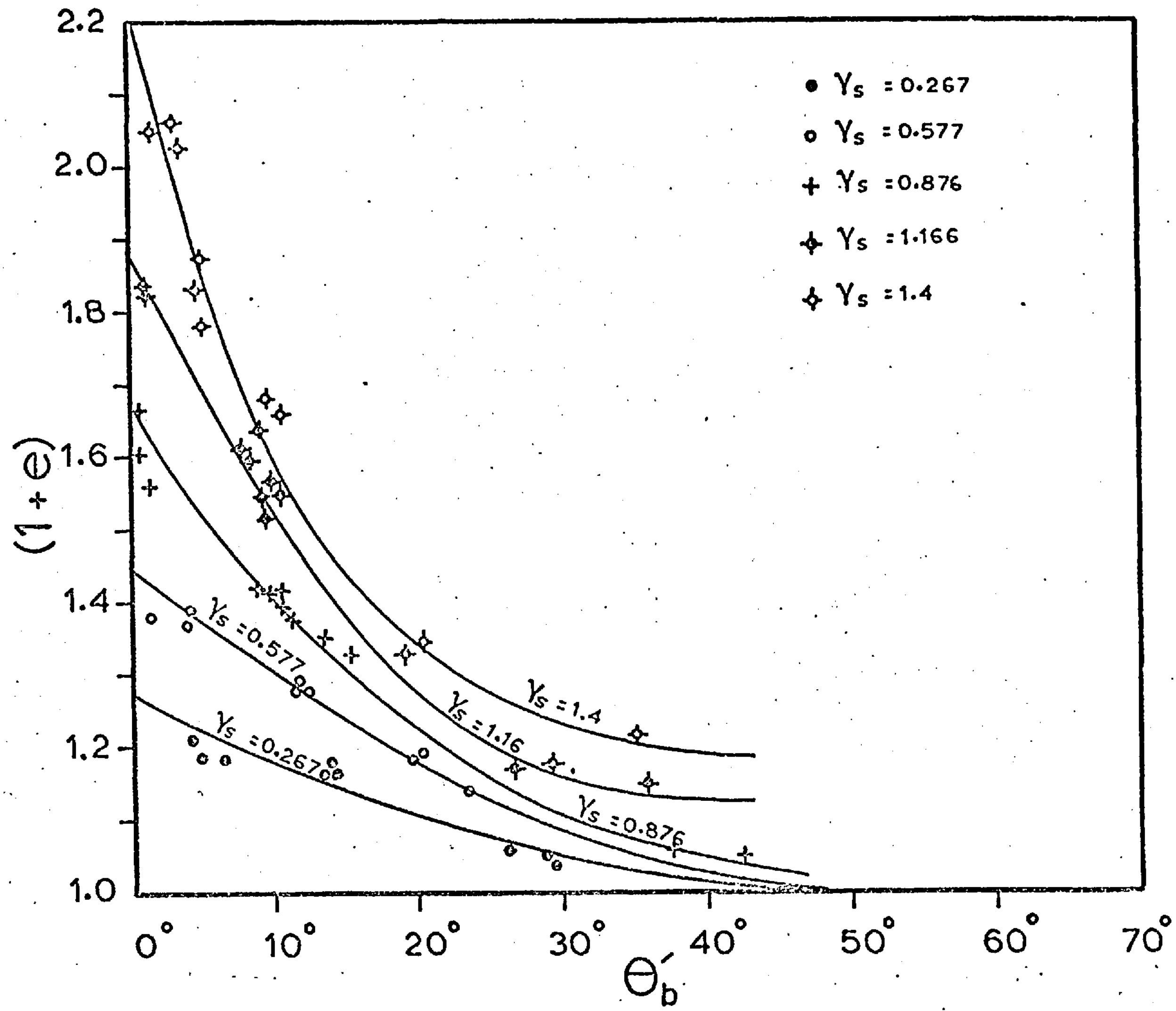

Fig. 8.16 Experimental relationship between the elongation (1 + e) and final orientation (θ_b') of stretched belemnites undergoing simple shear deformation.

CHAPTER 9. FIELD EXAMPLES OF STRETCHED BELEMNITES FROM LEYTRON, VALAIS, SWITZERLAND

9.1 INTRODUCTION

This chapter deals with field applications of the theoretical and experimental studies on the behaviour of stretched belemnites. An analysis of the behaviour of stretched belemnites from Leytron was undertaken in the light of various methods of interpretation of results discussed in the previous chapters (chapters 7 and 8). A statistical method for the determination of strain from the field data is introduced and is believed to give more accurate results than those obtained by other methods.

Analyses of the behaviour of extended belemnites and strain determinations using them were made on the Liassic slates of Leytron (fig. 9.1). These slates contain an abundance of stretched belemnites and have a well developed stretching lineation. The angle (θ_b') between the stretching direction and the stretched belemnite axis was measured. The field data was collected by two methods. Sixty-two specimens were directly measured in the field and 134 specimens were recorded by tracing them onto tracing paper from which the required measurements were later taken. Only 26 of the 196 specimens were measured insitu.

9.2 EXPOSURE AT LEYTRON

Leytron, a small wine producing village in Valais, Switzerland, is geologically reknowned for the impressive number of well preserved stretched belemnites in the Liassic slates of the area. They are best exposed in the Leytron slate quarries. These are situated on the Ardève mountain which constitutes the Liassic core of the Morcles nappe. The geographical situation of the area is shown in the location map (fig. 9.1).

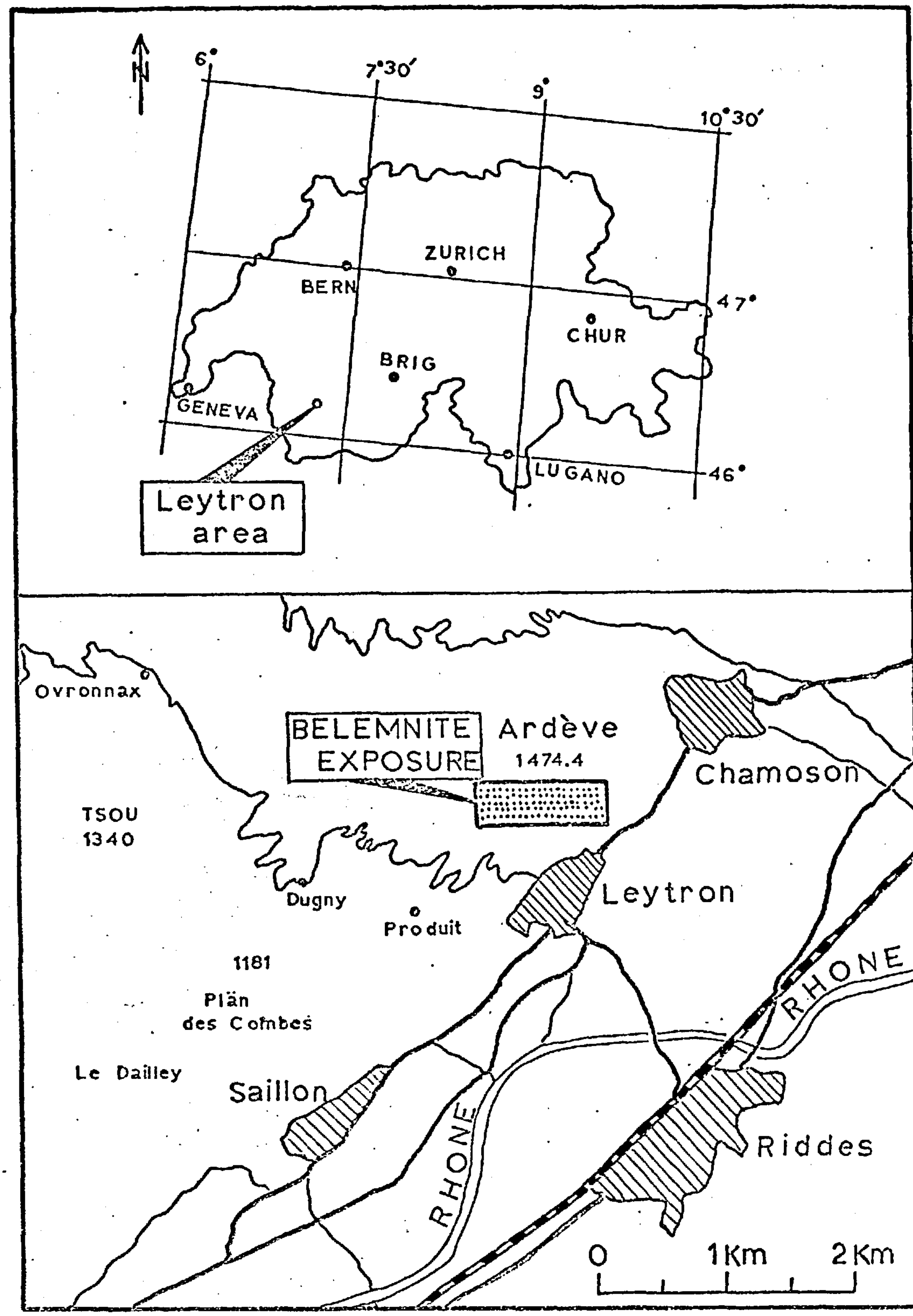

Fig. 9.1 Location map of the exposure of stretched belemnites in Leytron.

The photograph (fig. 9.2) taken from the bank of the Rhone shows the village of Leytron and the Ardève mountain. The physical features of the mountain face show that there are areas of accessible outcrop and screes, areas of vertical cliff and areas that are covered with vegetation.

The belemnite specimens lie in the bedding surfaces which are almost parallel to the planes of schistosity, the folds here being almost isoclinal. They are randomly orientated. The general geology, stratigraphy and major structures of the adjoining areas of Leytron was summarised by Durney (1972) on the basis of the works by Lugeon (1937, 1940); Badoux et al (1959); Badoux et al (1962) and Badoux (1963). According to Badoux (1963), the folds of the Ardève mountain are tight and plunging towards N.E. The schistosity shows a very distinct stretching lineation directed towards N.E. which is approximately parallel to the axis of folding.

9.3 GENERAL DESCRIPTION OF LEYTRON BELEMNITES

The belemnites found in Leytron, are generally cylindrical with a circular or oval rostrum. A natural weakness in the guard causes the specimen to break up into fragments during deformation (figs. 9.3 and 9.4). The spaces created between the fragments are filled by quartz and calcite. The quartz occurs in a band across the centre of the space and is separated from the belemnite fragment by two bands of calcite (fig. 9.5). Although the belemnites have been fragmented it is possible for the fragments to be fitted together to reconstruct the original length of the undeformed belemnite. The fragments have not undergone any destruction at the interface between adjacent fragments and hence the initial length of the specimen can be evaluated by suming the lengths of the individual fragments. This

Fig. 9.2 A view of the Mountain Ardève from the bank of the Rhone.

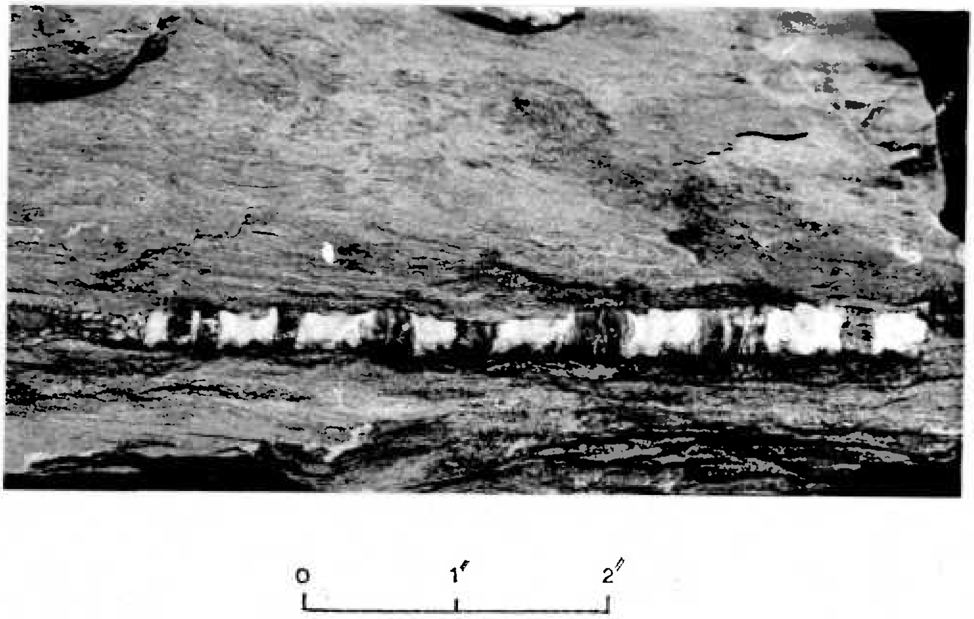

Fig. 9.3 Natural example of a stretched belemnite from Leytron, Valais, Switzerland.

Fig. 9.4 Development of 'en-echelon' type of structure in a stretched belemnite specimen, Leytron, Valais, Switzerland.

observation also demonstrates that the calcite crystals in the space between the fragments did not originate by the partial transformation of the shell. The calcite seems to have been derived by pressure solution transfer from adjacent limestone and marl (Durney, 1972).

A belemnite body situated oblique to the stretching lineation, after deformation, shows an en-echelon type of structure (fig. 9.4). This type of en-echelon arrangement of the fragments was reproduced in the experiments where the specimen was placed at an angle to the extension direction (fig. 8.2 in chapter 8). The en-echelon arrangement is the result of the synchronous occurance of rotation and extension.

9.4 DETERMINATION OF THE AMOUNT OF EXTENSION

The total length after deformation (belemnite fragments + quartz + calcite) and the initial length ($l = \sum l_o$) for each specimen were measured (fig. 9.6) and the extension of each sample calculated using the following equation.

$$e = \frac{\text{total length - initial length}}{\text{initial length}} = \frac{l_1 - l}{l}$$

The finite orientation of each belemnite (θ_b') was also measured with respect to the stretching lineation which is taken to represent the direction of principal extension of the strain ellipsoid (Badoux, 1963). From the field observation, it was found that the specimens lying parallel to the stretching lineation generally showed the largest amount of extension (except in some special cases). The values of extension for the 196 field specimens studied are recorded in table 15 (in Appendix E) and are shown graphically in figure 9.7.

The plots of the extension against the final orientation of belemnites (fig. 9.7) exhibit a considerable scatter. But the general

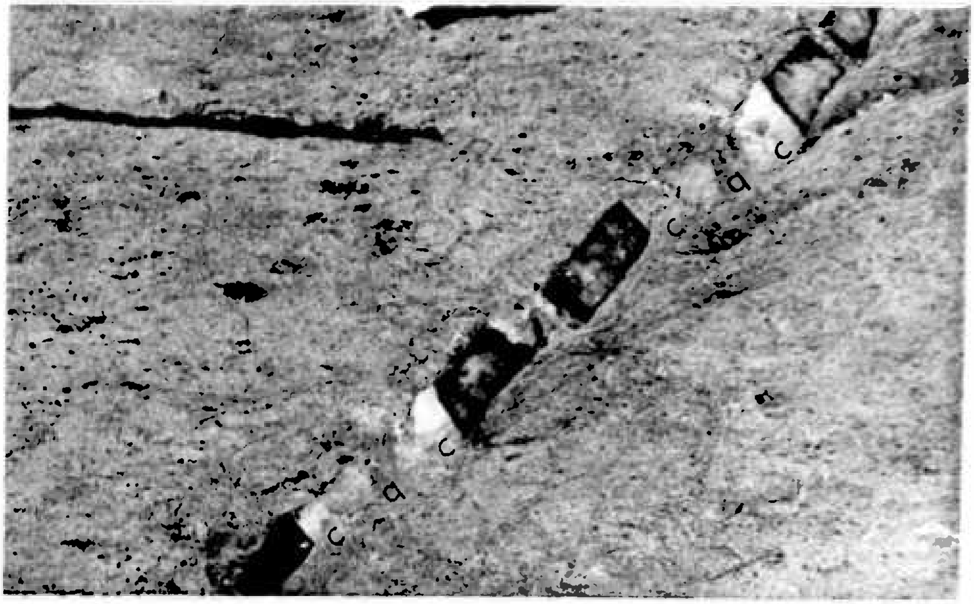

Fig. 9.5 Close up of a stretched belemnite specimen showing quartz (q) and calcite (c) infilling in the space between fragments.

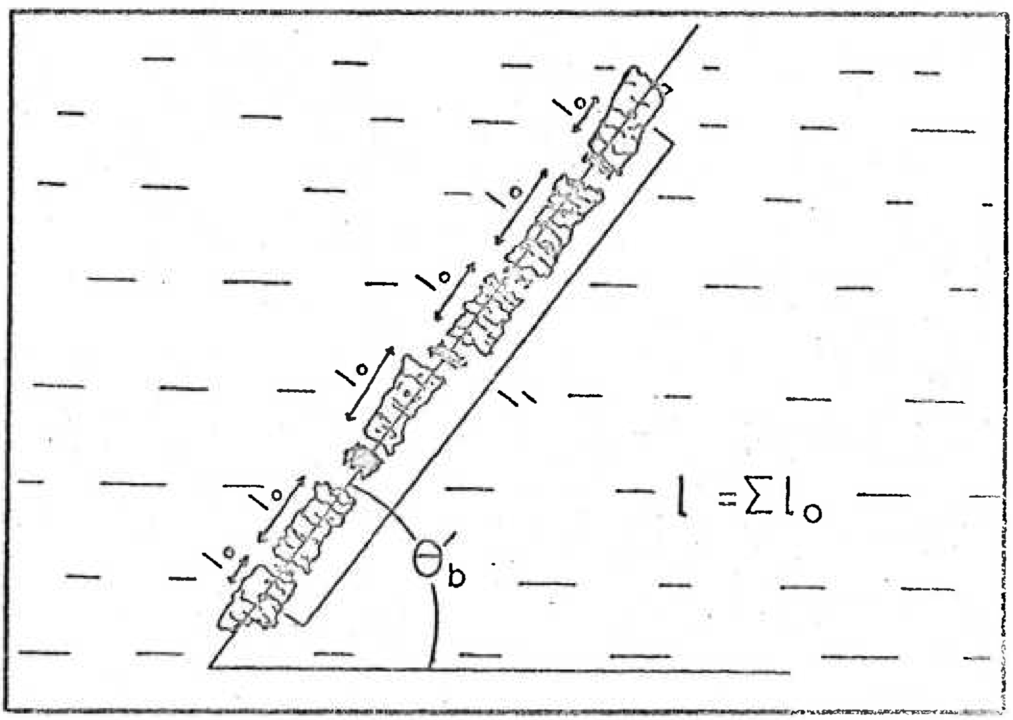

Fig. 9.6 Method of the measurement of extension from a stretched belemnite specimen.

trend of the distribution reveals that the amount of extension decreases with the increase of θ_b'. This observation agrees well with that of Badoux (1963, fig. 2).

An attempt has been made to determine the reason for such a scatter of the field data about their field of distribution in fig. 9.7. It is generally assumed that the most reliable values for extension are obtained when the belemnite has broken into a large number of fragments. In order to determine whether or not the scatter was due to the plotting of data from stretched belemnites with various number of fragments, the data was replotted (fig. 9.8) with the number of fragments marked on each point. Inspection of fig. 9.8 shows that the data obtained from belemnites broken into same number of fragments still shows a large scatter about their field of distribution. It is suggested thatthe scatter of data is not due to inaccuracies in measurement but is a feature related to real variations of the values of the finite deformation of the Liassic slates.

9.5 DETERMINATION OF STRAIN

Two methods have been used to evaluate the strain from the field data : (i) the "average elongation" method and (ii) the "statistical analysis". Principal elongations ($\sqrt{\lambda_1}$ and $\sqrt{\lambda_2}$) can also be calculated by a Mohr circle construction (Ramsay, 1967, p.79-80). However, this method is lengthy and time consuming and is not used in the present study.

9.5.1 The 'Average elongation' method

The amount of extension is transformed into elongation ($\sqrt{\lambda}$ = 1 +e) for the convenience of the analysis. The average of the elongation are calculated considering the specimens lying between

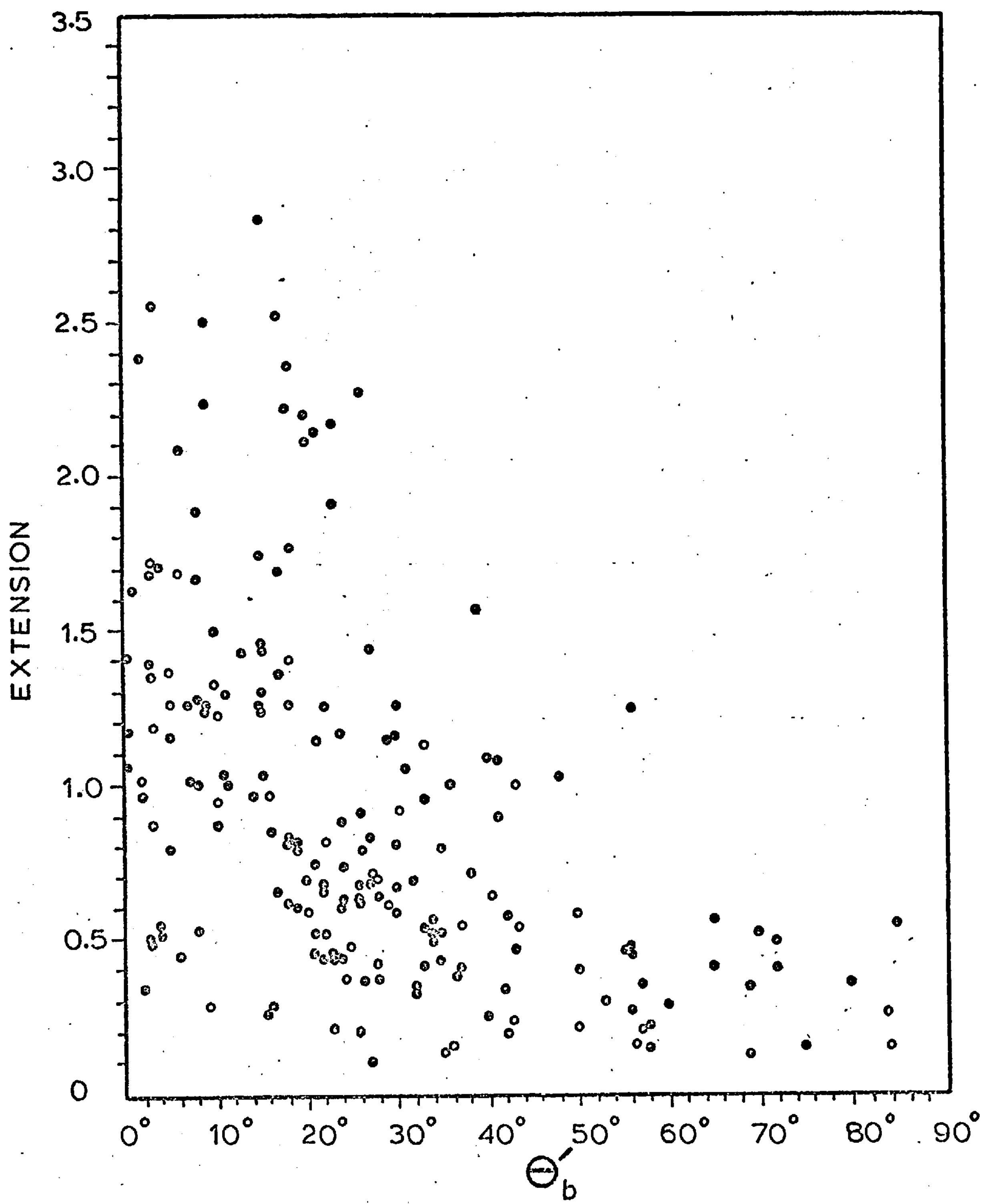

Fig. 9.7 Relationship between extension and finite orientation (θ_b') of Leytron belemnites. θ_b' measured with reference to the stretching lineation.

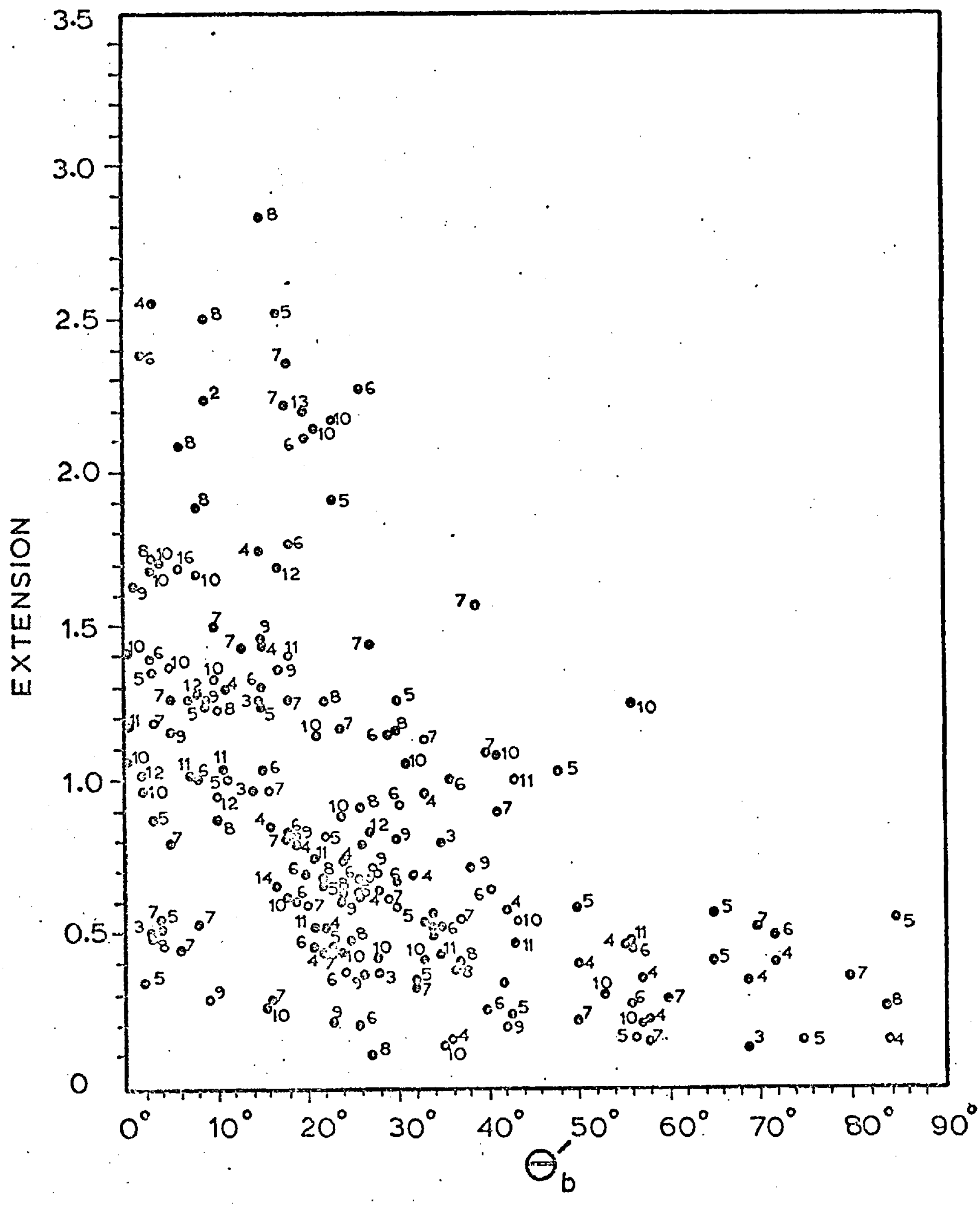

Fig. 9.8 Reliability of the field data used in the analyses. Numerical numbers shown in the plot represent the number of fragments involved in the measurement of extension of a specimen.

$\theta_b' = 0^\circ - 2.5^\circ$; $\theta_b' = 2.5^\circ - 7.5^\circ$; $\theta_b' = 7.5^\circ - 12.5^\circ$ etc. and by taking their arithmetic mean. This mean value was calculated for both elongation and final orientation (θ_b'). The average elongations, calculated from 196 specimens are recorded in table 16 and are graphically presented in figure 9.9.

It is clearly seen from the field observations and also from the figures 9.7 and 9.9 that the belemnites show extension even if they lie normal to the stretching lineation. Theoretically, if the Leytron slates suffered deformation in field 2 (i.e. extension in one direction and contraction in the other), the data cannot be used to obtain extension values in the direction normal to the stretching lineation. Inspection of these figures (figs. 9.7, 9.8 and 9.9) suggests that the Leytron belemnites stretched in two directions (i.e. deformed in field 1, fig. 8.14,a). The pattern of the graph (especially in the region between $\theta_b' = 45^\circ$ and $\theta_b' = 90^\circ$) in fig. 9.9 is not like that obtained from the experiments (fig. 8.15 in chapter 8). The maximum amount of compression cannot be measured from this type of 2D field data (i.e. data collected on a plane containing the maximum and intermediate principal axes of extension).

The amount of strain that has been suffered by the belemnites embedded in the planes of schistosity can only be obtained from this method. The two principal strains $\sqrt{\lambda_1}$ and $\sqrt{\lambda_2}$ being represented by the curve in fig. 9.9 at $\theta_b' = 0^\circ$ and $\theta_b' = 90^\circ$ respectively are evaluated and the strain ratio in this place is calculated as $\sqrt{\lambda_1/\lambda_2} = 2.382$.

9.5.2 <u>The "statistical method"</u>

The value of the reciprocal quadratic elongation in a direction θ_b' to the extension direction can be expressed in terms of

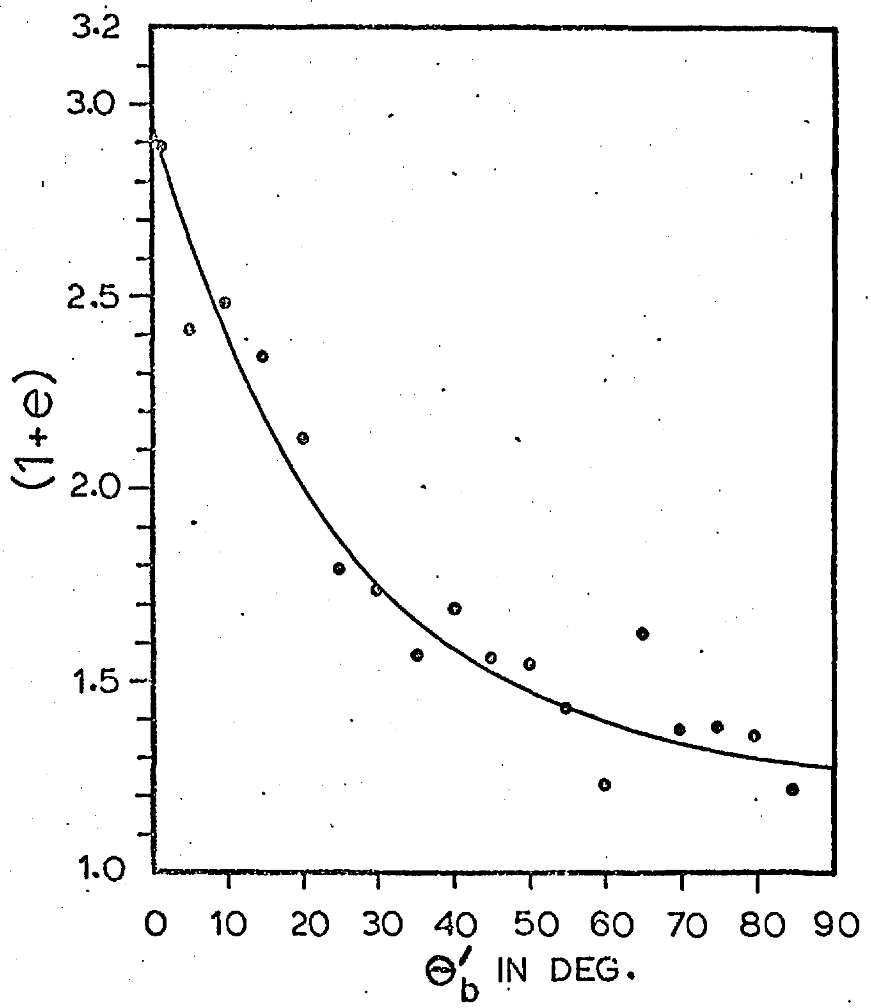

Fig. 9.9 Relationship between the average elongation (1+e) and finite orientation (θ_b') of Leytron belemnites. θ_b' measured with reference to the stretching lineation.

the two principal reciprocal quadratic elongations λ'_1 and λ'_2,

$$\lambda' = \lambda'_1 \operatorname{Cos}^2\theta'_b + \lambda'_2 \operatorname{Sin}^2\theta'_b \tag{9.1}$$

The "statistical method" of determining the principal strain is based on using field data to solve this equation (9.1). For any stretched belemnite θ'_b and λ' can be measured. Theoretically only two stretched belemnites at different orientation to the principal extension are required in order to calculate the two unknown (λ'_1 and λ'_2) of equation 9.1. In practice however, this technique is of little use as in areas where many samples of stretched belemnites are available for measurement, it is found that widely varying values for λ'_1 and λ'_2 can be obtained depending on how the pairs of belemnites are selected. However, the relationship expressed by equation 9.1 can be used in conjunction with the widely varying field data to determine the best apparent values of principal strain.

Equation 9.1 can be rewritten as

$$\lambda'/\operatorname{Cos}^2\theta'_b = \lambda'_1 + \lambda'_2\tan^2\theta'_b \tag{9.2}$$

Putting $\lambda'/\operatorname{Cos}^2\theta'_b = y$, $\lambda'_1 = c$, $\lambda'_2 = m$ and $\tan^2\theta'_b = x$, equation 9.2 becomes

$$y = c + mx \tag{9.3}$$

the equation of a straight line.

The physical significance of equation 9.2 is illustrated in fig. 9.10 which shows that the value of λ'_2 and λ'_1 can be derived from the slope of the line and the point of contact of the line with the y-axis respectively.

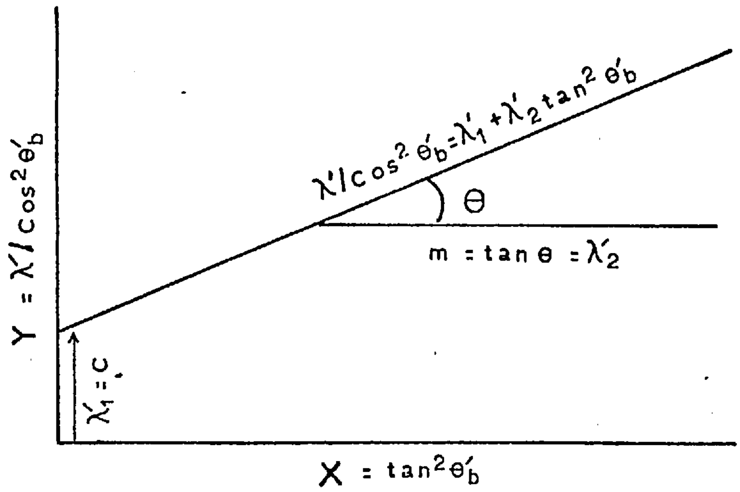

Fig. 9.10 Straight line concept for the determination of the principal strains.

The data obtained from the 196 belemnites has been graphically represented by plotting values of $\tan^2\theta'_b$ against $\lambda'/\text{Cos}^2\theta'_b$ for each specimen (fig. 9.11). The graph shows a large scatter of points about its best fit straight line. A method of least square is used to obtain the best fit straight line through these scattered points (Moroney, 1951). A relationship is established by Moroney (1951, p.284) to determine 'm' and 'c' of the best fit straight line through such a scatter of points.

$$m = \frac{\Sigma xy - \frac{(\Sigma x)(\Sigma y)}{N}}{\Sigma x^2 - \frac{(\Sigma x)^2}{N}} \tag{9.4}$$

$$c = \frac{(\Sigma x)(\Sigma xy) - (\Sigma y)(\Sigma x^2)}{(\Sigma x)^2 - N(\Sigma x^2)} \tag{9.5}$$

N is the number of points involved in the calculation.

Using these expressions (eqs. 9.4 and 9.5) the 196 values of x and y ($x = \tan^2\theta'_b$, $y = \lambda'/\cos^2\theta'_b$) determined from the field data, can be used to derive 'm' (λ'_2) and 'c' (λ'_1). Applying this method, the value of 'm' and 'c' for the Leytron belemnites are 0.547 and 0.135

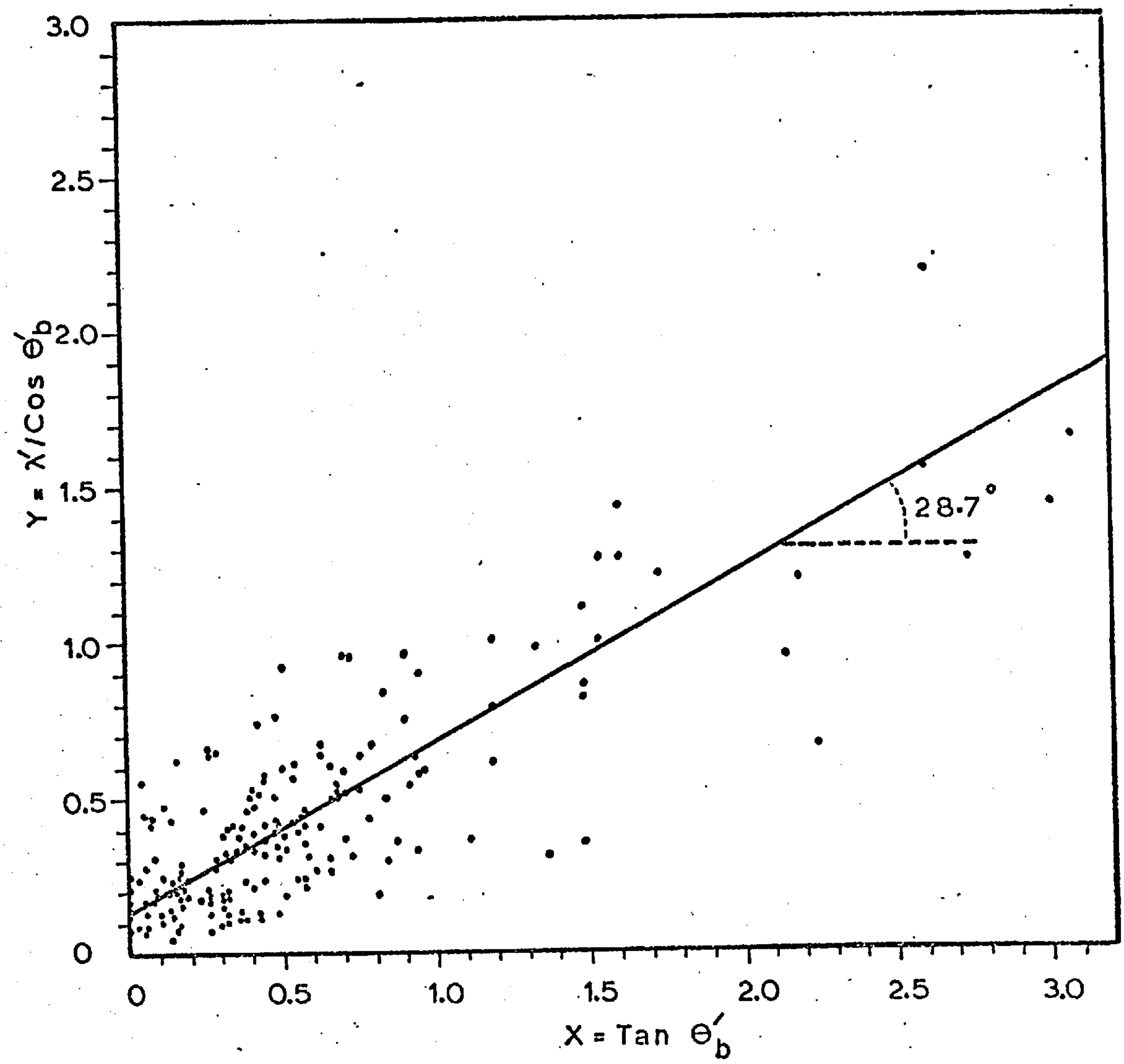

Fig. 9.11 Determination of the principal strains by the statistical method (using straight line concept and field data from 196 specimens).

respectively. Once 'm' is known, the slope of the best fit straight line is determined (m = tan θ). It is shown in figure 9.11. The strain ratio obtained by this method is $\sqrt{\lambda_1/\lambda_2} = 2.013$.

The value of the strain ratio determined using the 'statistical method' is slightly lower than that obtained using the method of 'Average elongation'. Durney (1972) studied 85 specimens of belemnites from the same area. He used the method described by Badoux (1963) and obtained a value of 2.083 for $\sqrt{\lambda_1/\lambda_2}$, a value encouragingly close to the result obtained by the 'statistical method'.

9.6 RELATIONSHIP BETWEEN θ'_b AND θ'_f

Thirty specimens, composed of fragments of varying a/b ratio were selected for determining the relationship between θ'_b and θ'_f. The fragments were divided into two groups based on the a/b ratios of their fragments : (i) a/b $<$ 2:1 and (ii) a/b $>$ 2:1. Measurements for both θ'_b and θ'_f were taken from the selected specimens and the results are shown in figure 9.12.

This figure (9.12) shows that the a/b ratio of the fragments does not influence the distribution of the points. However, this may be due to very low variation (2:1 $<$ a/b $<$ 4:1) of the a/b ratio of the fragments involved in the plot. The distribution of the points in fig. 9.12 also indicates that the relationship between θ'_b and θ'_f is slightly non-linear. This agrees with that obtained from the experiments (fig. 8.12). An 'eyeballed-in' curve drawn through these points passes through or close to the origin which signified that θ'_b and θ'_f are both zero when the specimen lies parallel to the extension direction (stretching lineation). Comparing figure 9.12 with experimental curve in fig. 8.12 (in chapter 8) and following the same argument used to interpret the experimental observation, it is suggested

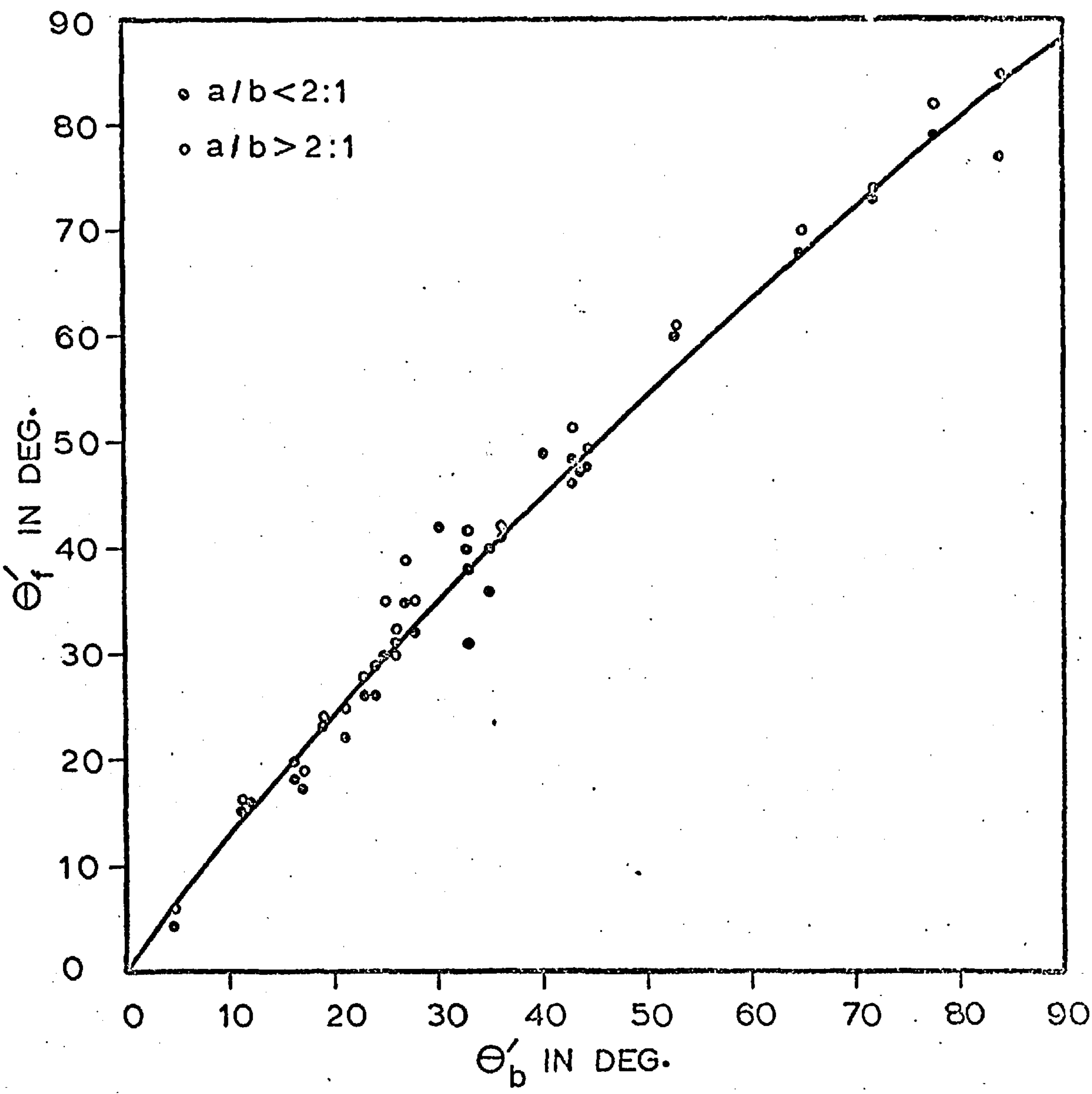

Fig. 9.12 Relationship between the finite orientation of the fragments (θ_f') and that of the whole specimen (θ_b') of Leytron belemnites.

that Leytron belemnites have probably suffered deformation of an irrotational type.

9.7 DETERMINATION OF THE INITIAL ORIENTATION OF THE LEYTRON BELEMNITES

The initial orientation of any line deformed by pure shear (irrotational strain) can be obtained if the final orientation with respect to the extension direction of strain ellipsoid and the amount of strain that causes the distortion are known. By assuming that the stretched belemnites can be treated as 'lines', then if the strain state is known, an attempt can be made to derive the initial orientation of the 196 specimens of Leytron belemnites.

After subjecting a circle to homogeneous deformation it becomes an ellipse. The position of a point (x, y) on the circle is transformed to a new position (x', y') and the angle θ between the x-axis and a line joining that point to the origin is changed to θ' (fig. 9.13).

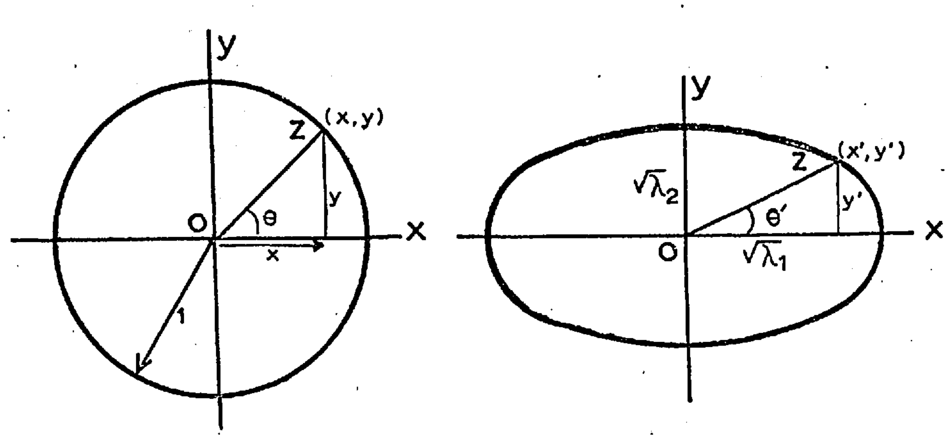

Fig. 9.13. Relationship of the initial and final orientation of a line stamped in a matrix undergoing homogeneous deformation. (After Ramsay, 1967, fig. 3.8).

The new position of the line 'OZ' in the ellipse can be described by

$$x' = x\sqrt{\lambda_1}$$
$$y' = y\sqrt{\lambda_2} \qquad (9.6)$$

and the new angle θ' is expressed as

$$\tan \theta' = y'/x' \qquad (9.7)$$

substituting equation 9.6 into equation 9.7 and replacing y/x by tan θ, the relationship between the initial and final orientation of a line is obtained.

$$\tan \theta = R \tan \theta'$$
$$\text{where} \quad R = \sqrt{\lambda_1/\lambda_2} \qquad (9.8)$$

(Ramsay, 1967, eq. 3.34)

With the help of a computer, eq. 9.8 was used to construct a series of curves relating θ and θ' for various values of finite strain ratio R. These curves are shown in fig. 9.14.

As θ'_b and the strain state for the field example are known, equation 9.8 or the reference graph (fig. 9.14) can be used to determine the initial orientation of each belemnite from Leytron.

If the belemnites originally had a random orientation on the bedding plane (now parallel to the cleavage), a histogram of their distribution (number plotted against orientation) would have been a straight line parallel to the orientation axis. The superposition of an irrotational homogeneous deformation would cause the belemnites to rotate towards the principal extension direction. A histogram of belemnite distribution in the strained state would therefore peak around the principal extension direction.

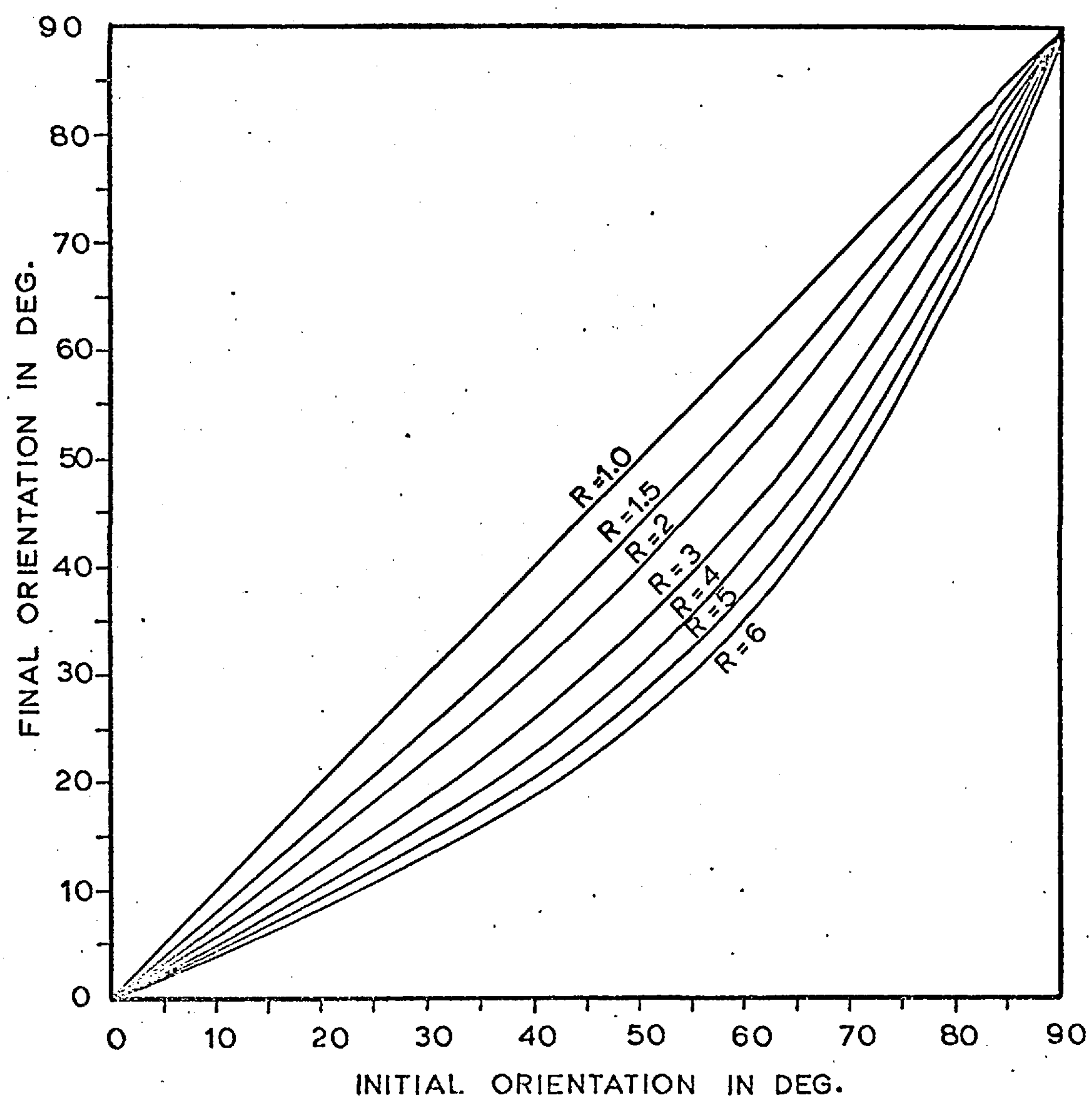

Fig. 9.14 Graphs showing the relationship between the initial and final orientation of a line for several stages of deformation. R represents the applied principal strain ratio $(\sqrt{\lambda_1/\lambda_2})$.

A histogram showing the distribution of Leytron belemnites in the strained state is shown in fig. 9.15. Using the field data and equation 9.8 the initial orientation of each of the 196 stretched belemnites was determined for the apparent finite strain ($\sqrt{\lambda_1/\lambda_2}=2.013$). The results are illustrated in fig. 9.16. Fig. 9.16 shows that although the belemnites were not originally completely randomly oriented, no important prefered orientation existed prior to deformation. The prefered orientation of the belemnites shown up in fig. 9.15 is probably a consequence of the deformation.

9.8 DISCUSSION AND CONCLUSIONS

The observations from the field examples show that the development of stretched belemnites agree well with the mechanism predicted by the theoretical and experimental analyses. It is found that most of the belemnite specimens are obliquely oriented with reference to the stretching lineation and thus exhibited an 'en-echelon' type of structure.

From experimental work it has been shown that the strain determination made from stretched belmenites is often lower than the actual strain that has been suffered by the matrix material. Following a similar argument as made in the interpretation of the experimental results, it has been found that the amount of strain obtained from the field is also considerably less than the true strain. This opinion is supported by Durney (1972) who also studied belemnites from the Leytron area. Durney also determined the finite strain ellipse by direct measurement of micro-boudinage. This is thought to give a closer approximation to the true strain of Leytron slates. These studies indicate that the belemnites give on average, only about 50% of the true elongation.

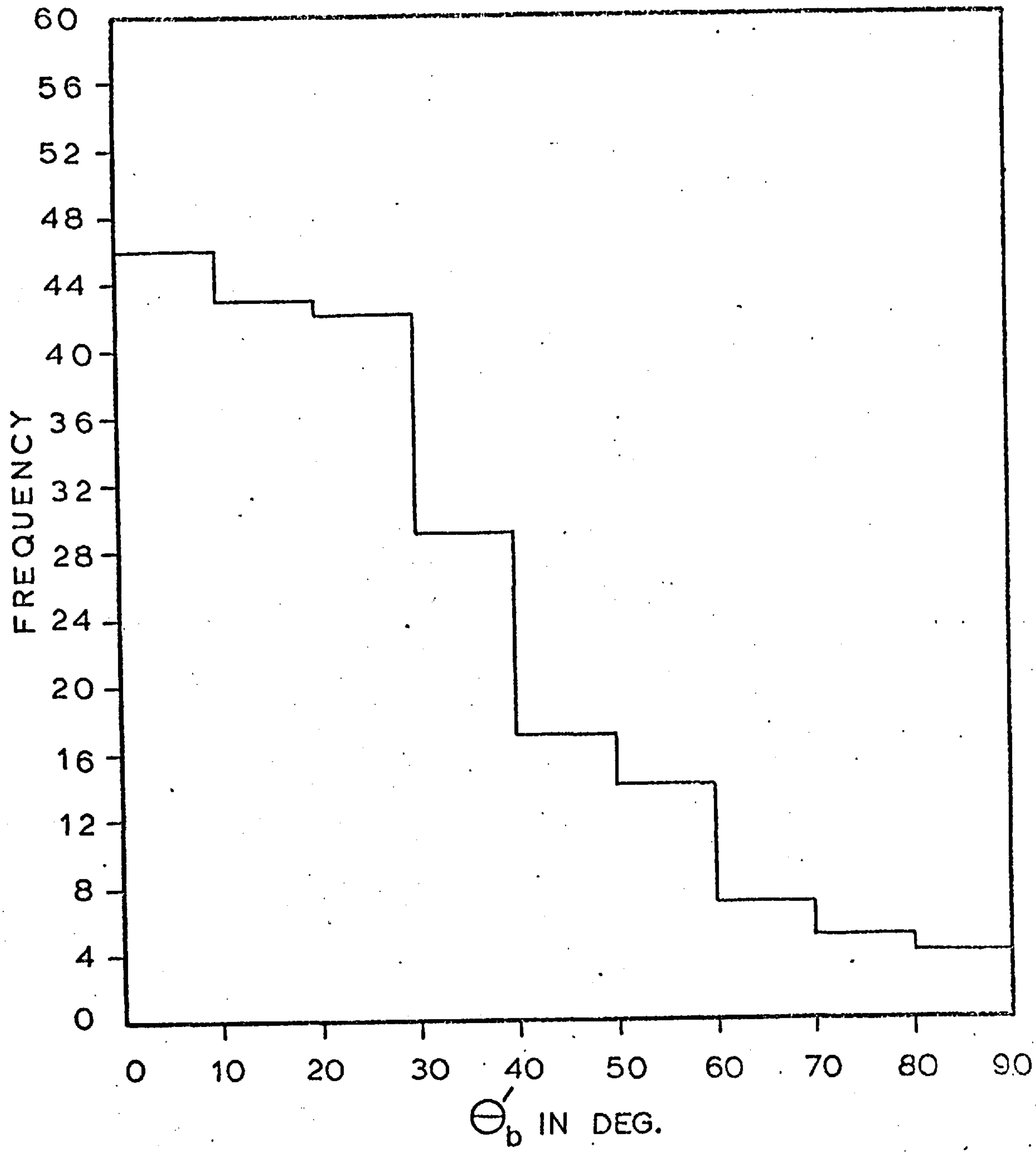

Fig. 9.15 Histogram showing the prefered finite orientation of the Leytron belemnites towards the stretching lineation.

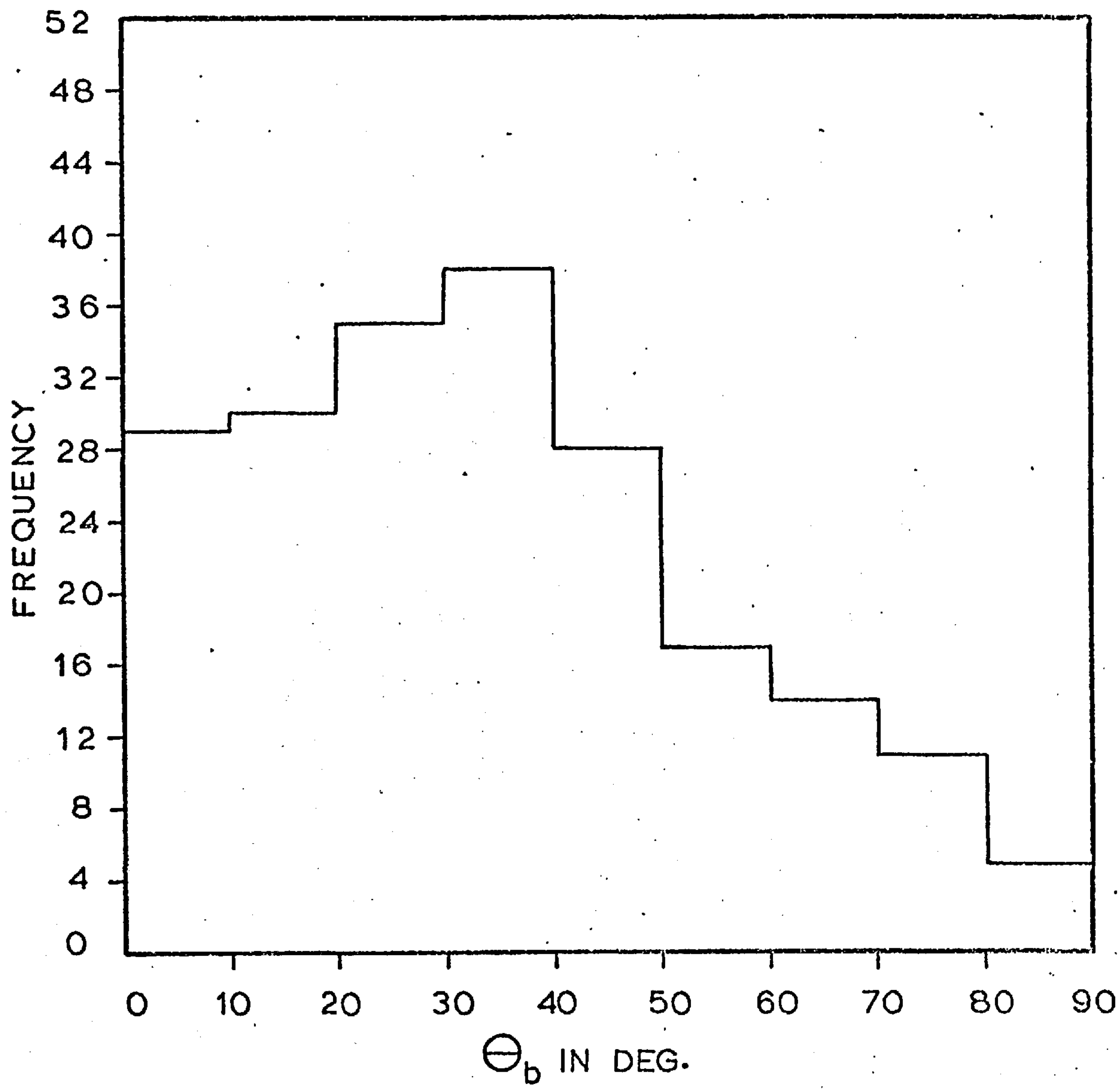

Fig. 9.16 Histogram showing the frequency of numbers of belemnite specimen against the initial orientation (θ_b) of Leytron belemnites. Calculation of θ_b were made considering that the Leytron belemnites have suffered extension due to strain $\sqrt{\lambda_1/\lambda_2} = 2.013$.

It may be concluded from the experimental work and the field studies that,

(a) The development of the stretched belemnites is the result of extension along the test of belemnites.

(b) The en-echelon type of structure developed in the distorted belemnites is due to the oblique situation of the specimen with respect to the extension direction of the strain ellipse.

(c) Observing the field relationship between θ'_b and θ'_f, and comparing it with the experimental observation (compare figs. 9.12 and 8.12), it can be stated that the Leytron slates have probably been deformed by a strain with nearly irrotational properties.

(d) Both the experimentations and the field observations suggest that the value of apparent strain evaluated from the extension (e) of stretched belemnites is considerably lower than the actual strain that has been suffered by the matrix materials.

(e) The initial orientation of the Leytron belemnites represented in fig. 9.16 shows that no important prefered orientation of the belemnites existed before deformation. The prefered finite orientation of Leytron belemnites shown in fig. 9.15 is primarily a consequence of deformation.

PART III

CHAPTER 10. SUMMARY AND CONCLUSIONS

10.1 On rotated porphyroblasts

10.2 On extended belemnites

CHAPTER 10. SUMMARY AND CONCLUSIONS

This thesis presents the geological implications and the results of a theoretical and experimental investigation into the behaviour and geometrical properties of rotated porphyroblasts (Part I) and extended belemnites (Part II) during irrotational strain and simple shear deformation. The experimental simulation of rotated porphyroblasts and extended belemnites was performed in an irrotational strain (Lozenge-shpaed) box and simple shear box. The results obtained from the experiments have been quantitatively analysed and compared with those derived from theory.

10.1 ON ROTATED PORPHYROBLASTS

(1) Published works on the geometry and nomenclature of rotated structures have been briefly reviewed. The present study supports the refinements of nomenclature of these structures proposed by Spry (1969). This work is also in agreement with the method of calculation of the differential rotations between porphyroblasts and matrix using S_i and S_e from thin sections cut perpendicular to the axis of rotation suggested by Powell and Treagus (1967, 1970).

(2) The confusion of the terms 'pressure shadows' and 'pressure fringes' used to describe the inhomogeneities around porphyroblasts has been discussed and the terms have been used in accordance with Spry (1969). Pressure shadows are defined as the relatively unstrained areas composed of randomly oriented minerals adjacent to the rigid object and being protected from deformation by the presence of the object. Pressure fringes consist of fibrous oriented new minerals (such as quartz, calcite and chlorite) grown as a result of the pulling away of the matrix from the porphyroblast.

(3) In chapter 3 the theory of motion of a rigid inclusion during deformation and the accuracy of the equations derived by Jeffery (1922) and used by Gay (1966, 1968) have been reviewed. An equation for the motion of a rigid object set in a matrix undergoing pure shear is obtained,

$$\ln \tan \theta_{fe} = \ln \tan \theta_{ie} + \frac{a^2 - b^2}{a^2 + b^2} \cdot \ln\sqrt{\lambda_2/\lambda_1}$$

This equation indicates that an equidimensional object does not rotate, and that the amount of rotation of an elliptical inclusion increases with the increase of its axial ratio a/b. The amount of rotation is also dependent on the initial orientation of the object. The amount of rotation per strain increment is greatest when $\theta_i = 40^\circ$–70° and least when $\theta_i = 0^\circ$ and $\theta_i = 90^\circ$.

(4) The equation for the motion of an elliptical particle inside a matrix undergoing simple shear derived by previous workers has been modified and a more complete solution relating the final and initial orientation of the inclusion with the deformation is derived.

$$\text{Cot } \theta_{fs} = a/b \tan \left[\frac{a \cdot b}{a^2+b^2} \gamma_s + \tan^{-1}(b/a \cot \theta_{is})\right]$$

This equation indicates that an equidimensional object rotates at a constant rate and that the motion of an elliptical inclusion is dependent on its initial orientation. The greatest amount of rotation occurs in elliptical objects when the long axis of the object lie at a high angle to the shearing direction.

(5) Geometry and the deformation history inside the irrotational strain (Lozenge-shaped) box and simple shear box designed to perform all the experiments have been studied both theoretically and experimentally. The results obtained from the theory and experiment are in complete agreement. Experimental observations show that the strains

developed in the central region of both the boxes are fairly homogeneous.

(6) The measurements of the amount of shear γ_s made by Gay (1966) from the geometry of the simple shear box are shown to be inaccurate and a modified method of determining γ_s is suggested.

$$\gamma_s = \frac{\text{Sin } \beta}{\text{Sin}(\alpha_o - \beta).\text{Sin } \alpha_o}$$

This equation relates the angular deflection (β) caused by the change of apical angle of the box and the initial apical angle (α_o) of the box.

(7) In order to test the theoretical predictions of the motion of rigid inclusions in a viscous matrix, 31 experimental runs using inclusions of different shapes have been performed in both the irrotational strain box and simple shear box. The results obtained from these experiments show that the motion of the inclusions depends on many factors, e.g. the initial orientation, the shape of the object and the type of deformation (irrotational strain or simple shear) they undergo. The results obtained from the experiments have been compared with those predicted from the theory and within the limit of experimental error, a close agreement is found. The model studies reaffirmed the conclusion that equidimensional inclusions do not rotate when set in matrix deforming by irrotational strain and rotate at a constant rate when set in a matrix deforming by simple shear.

(8) The experiments show that the behaviour of elliptical inclusion depends mainly on the orientation of the object with respect to the axes of finite strain ellipse. For irrotational strain, the amount of rotation for an elliptical object approches zero as θ_i (the angle between the long axis of the object and the major principal

extension direction) approaches either 0° or 90°. For simple shear deformation, the amount of rotation for an elliptical object increases with the increase of θ_i (the angle between the long axis of the object and the shearing direction).

(9) The study of the effect of shape defined by the axial ratio of the object shows that the rotation of elliptical inclusions when deformed under irrotational strain is greatest where the axial ratio a/b of the object is largest. However, this axial ratio of elliptical inclusions has very little influence on the rotation of the inclusions in the case of simple shear deformation.

(10) Generally, it is seen that the matrix materials rotate faster than the included object. This behaviour is always observed in the case of irrotational strain deformation. But the models deformed in simple shear show a very little amount of $S_i \wedge S_e$ and sometimes the included object rotates more than that of the matrix.

(11) The strain patterns in the matrix around the rigid inclusion with respect to the principal extension direction have been experimentally determined from the distorted grids; they are similar for both irrotational strain and simple shear deformation. In order to investigate the movement of the material around the rigid inclusions, the flow lines associated with both irrotational strain and simple shear have been constructed. The flow lines produced in the irrotational strain experiments indicate that the material moves towards the compressive direction in the compression field and towards principal extension direction in the extension field. However, the flow lines obtained from simple shear experiments moved towards the shearing direction. The study of $S_i \wedge S_e$ from the experiments seems to provide a feature that can be used to distinguish whether the matrix has

undergone irrotational strain or simple shear deformation. During deformation by irrotational strain $S_i \wedge S_e$ is generally large and during simple shear, the value of $S_i \wedge S_e$ is very small even for high strains provided the inclusions suffer rotation under the condition as set up in the experiments.

(12) It has been possible to simulate experimentally the formation of pressure shadows and pressure fringes which in nature develop adjacent to the rigid inclusions. The progressive development of the 'open spaces' that formed around an inclusion shows that the shape of the 'spaces' depends on the shape of the inclusion. The low strain regions, where the pressure shadows are thought to develop, show up in the experiments as regions of relatively widely spaced grid lines adjacent to the inclusions.

(13) The state of stress in the matrix around a rigid circular inclusion has been studied mathematically. The basic equations (Jaeger and Cook, 1969), have been extended to obtain solutions for the resolved stresses in the material around a rigid circular object loaded under plane strain. The solutions are

(i) For uniaxial stress

$$\sigma_r = \frac{1}{2} P_1 + \frac{1}{2} P_1 (1 + \frac{4R^2}{r^2} - \frac{3R^4}{r^4}) \text{ Cos } 2\theta$$

$$\sigma_\theta = \frac{1}{2} P_1 - \frac{1}{2} P_1 (1 - \frac{3R^4}{r^4}) \text{ Cos } 2\theta$$

$$\tau_{r\theta} = - \frac{1}{2} P_1 (1 - \frac{2R^2}{r^2} + \frac{3R^4}{r^4}) \text{ Sin } 2\theta$$

(ii) For biaxial stress

$$\sigma_r = \frac{1}{2}(P_1 + P_2) + \frac{1}{2} (P_1 - P_2)(1 + \frac{4R^2}{r^2} - \frac{3R^4}{r^4}) \text{Cos } 2\theta$$

$$\sigma_\theta = \frac{1}{2}(P_1 + P_2) - \frac{1}{2}(P_1 - P_2)(1 - \frac{3R^4}{r^4})\text{Cos } 2\theta$$

$$\tau_{r\theta} = -\frac{1}{2}(P_1 - P_2)(1 - \frac{2R^2}{r^2} + \frac{3R^4}{r^4})\text{Sin } 2\theta$$

The distribution of principal stresses (σ_1 and σ_3) and the direction of the maximum principal stress have been evaluated with the help of a computer using the above equations. The stress trajectories, the distribution of maximum principal stress, maximum shearing stresses (differential stresses) and mean stresses have also been determined.

(14) The principal stress trajectories constructed in the matrix around a circular inclusion show a marked deflection around the object. These trajectories have been used to evaluate the fracture patterns which are likely to develop if the matrix underwent brittle failure. The distribution of magnitude of σ_1 shows that the largest local stresses occur on the side of the object facing the regional pressure. High local tensile stresses occur on the sides perpendicular to the greatest regional compression. These tensile zones are the regions in which pressure fringes and pressure shadows are likely to form.

(15) The study of mean stress in the material around a circular rigid inclusion demonstrates that the highest value of the mean stress lies along the plane parallel to the direction of greatest regional pressure and the lowest value lies along the plane normal to the direction of greatest regional pressure. The areas of low mean stress and areas of tensile stress are found to coincide. During geological deformation, pressure shadows and pressure fringes are formed in the low mean stress regions around an object as a consequence of minerals migrating from high pressure (high mean stress) regions to low pressure (low mean stress) regions.

10.2 ON EXTENDED BELEMNITES

(1) The behaviour of extended belemnites has been studied both theoretically and experimentally in conjunction with field examples from Leytron, Valais, Switzerland. A theoretical study of the geometric properties of stretched belemnites has been made using the solutions for the motion of rigid elliptical inclusion set in a viscous matrix undergoing homogeneous deformation (both irrotational strain and simple shear).

(2) The theoretical analysis predicts that during pure shear deformation, the amount of extension of belemnite models lying within the extension field increases as the initial orientation of belemnites (θ_b with reference to the major extension direction) decreases. However, in simple shear deformation a more complex history of extension of belemnites is observed.

(3) It is seen from the theoretical studies that the individual fragments of a belemnite specimen rotate independently of the whole specimen. The rotation of the fragments is governed by their a/b ratio. The difference in amount of rotation of individual fragments compared to the specimen as a whole is one of the mechanism by which an 'en-echelon' arrangement of the fragments occur.

(4) The change of a/b ratio of the whole specimen during deformation and the modification of strain state due to the flow of the matrix into the spaces created by the separation of fragments, have not been taken into account in the theoretical analysis. This may account for certain differences between the theoretical and experimental results.

(5) Twenty-nine runs of experiments simulating extended belemnites have been performed in the two strain boxes, varying the initial orientation (θ_b) and the axial ratio of belemnite models. Comparison

between the results determined from the theory and those obtained from the experiments shows that the experimental extension are always less than those derived from the theory. It is also observed from the experiments that the strain ($\sqrt{\lambda_1}$ and $\sqrt{\lambda_2}$) measured from the matrix undergoing a certain amount of finite deformation and having no inclusion is considerably higher than that measured from the experimental simulation of stretched belemnites undergoing same amount of deformation.

(6) Experimental reproduction of an 'en-echelon' arrangement of fragments in an extended belemnite reaffirmed the theoretical prediction that the 'en-echelon' arrangement develops as a result of different amount of rotation of the fragments compared to that of the specimen as a whole. Experimental studies demonstrate that the dissimilar axial ratio (a/b) of fragments do not influence significantly the behaviour of the whole specimen.

(7) Studying the relationship between the final orientation of the whole specimen (θ'_b) and the average finite orientation of the fragments (θ'_f) from the experiments, it is observed that during irrotational strain θ'_b and θ'_f remain the same when the specimen was initially parallel to the extension direction ($\theta_b = 0^o$). It is also observed from the experiments after simple shear deformation, regardless of the original orientation of the belemnite, θ'_b and θ'_f are never parallel.

(8) Because the belemnites act as fragmented rigid bodies, they can only be used to measure strain if they lie within the extension field of the strain ellipse. If they are situated in the compression field, they do not shorten and hence do not reflect the strain in the surrounding matrix.

(9) Hundred and ninety-six (196) specimens of extended belemnites from Leytron, Valais, Switzerland, have been measured and a strain analysis has been performed using the methods of interpretation of results derived from the theoretical and experimental studies. The field occurence of the 'en-echelon' arrangement in the fragments of belemnites that were not originally parallel to the extension direction and the dependence of the amount of offset of the individual fragments on the initial orientation of the belemnite are in good agreement with the experimental observation.

(10) The amounts of extension obtained from the field examples of stretched belemnites show that the Leytron belemnites suffered extension both in the direction parallel and normal to the stretching lineation. The strain determined normal to the stretching lineation is the strain parallel to the intermediate principal axis of the strain ellipse ($\sqrt{\lambda}_2$). The strain ratio determined on the schistosity plane is, therefore, $\sqrt{\lambda_1/\lambda_2}$. However, it has been experimentally demonstrated that the strain determinations made from extended belemnites are always considerably less than the actual strain that has been suffered by the surrounding matrix.

(11) The strain ($\sqrt{\lambda}_1$ and $\sqrt{\lambda}_2$) suffered by the Leytron slates on the schistosity plane has been determined from measurements of stretched belemnites, using two methods : (i) the 'average elongation' method and (ii) the 'statistical method'. The strain ratio calculated by the 'average elongation' method is 2.382 and that obtained by the 'statistical method' is 2.013. The value obtained by the 'statistical method' is close to the result obtained by Durney (1972) from the same area.

(12) The relationship between θ'_b and θ'_f has been studied from the field and the results have been compared with those obtained from the experiments. As a result of the comparison, it appears that the Leytron slates most probably underwent an irrotational strain deformation. Field study also agrees well with the experimental observation that the a/b ratio of the individual fragments of a belemnite have little effect on the behaviour of the whole specimen.

APPENDICES

Appendix A. Results predicted from the theory of the motion of rigid inclusions undergoing pure and simple shear deformation. (calculated by the help of a computer) (tables 1 - 3)

Appendix B. Experimental results of the motion of rigid inclusions undergoing irrotational strain and simple shear deformation. (tables 4 - 10)

Appendix C. Predicted results of the elongation (1+e) of stretched belemnites determined from the theoretical models. (tables 11 - 12)

Appendix D. Experimental results of extended belemnites. (tables 13 - 14)

Appendix E. Results obtained from the measurements of extended belemnites of Leytron, Valais, Switzerland. (tables 15 - 16)

Appendix F. Determination of strain from the distorted grids.

APPENDIX A. RESULTS PREDICTED FROM THE THEORY OF THE MOTION OF RIGID INCLUSIONS UNDERGOING PURE AND SIMPLE SHEAR DEFORMATION (CALCULATED BY THE HELP OF A COMPUTER)

Table 1. Results for the motion of rigid elliptical inclusions set in a viscous matrix undergoing pure shear deformation. Calculations were made from equation 3.8.

(a) $\theta_{ie} = 30^{\circ}$

$\sqrt{\frac{\lambda_1}{\lambda_2}}$	a/b = 2:1		a/b = 3:1		a/b = 4:1		a/b = 6:1	
	θ_{fe} in deg.	Rotation in deg.	θ_{fe} in deg	Rotation in deg.	θ_{fe} in deg.	Rotation in deg.	θ_{fe} in deg.	Rotation in deg.
1.0	30.0	0	30.0	0	30.0	0	30.0	0
1.21	27.25	2.75	26.37	3.63	26.01	3.99	25.74	4.26
1.61	23.45	6.55	21.53	8.47	20.77	9.23	20.20	9.80
2.08	20.41	9.59	17.82	12.18	16.83	13.17	16.11	13.89
2.60	18.03	11.97	15.05	14.95	13.95	16.05	13.16	16.84
3.0	16.63	13.37	13.48	16.52	12.35	17.65	11.54	18.46
3.5	15.23	14.77	11.97	18.03	10.82	19.18	10.01	19.99
4.0	14.11	15.89	10.78	19.22	9.64	20.36	8.84	21.16
4.5	13.18	16.82	9.83	20.17	8.71	21.29	7.92	22.08

(b) $\theta_{ie} = 60^{\circ}$

$\sqrt{\frac{\lambda_1}{\lambda_2}}$	a/b = 2:1		a/b = 3:1		a/b = 4:1		a/b = 6:1	
	θ_{fe} in deg.	Rotation in deg.	θ_{fe} in deg.	Rotation in deg.	θ_{fe} in deg.	Rotation in deg.	θ_{fe} in deg.	Rotation in deg.
1.0	60.00	0	60.00	0	60.00	0	60.00	0
1.21	57.09	2.91	56.08	3.92	55.66	4.34	55.34	4.66
1.61	52.47	7.53	49.80	10.20	48.69	11.31	47.83	12.17
2.08	48.15	11.85	43.96	16.04	42.23	17.77	40.91	19.09
2.60	44.32	15.68	38.89	21.11	36.71	23.29	35.05	24.95
3.0	41.86	18.14	35.73	24.27	33.31	26.69	31.50	28.50
3.5	39.25	20.75	32.45	27.55	29.84	30.16	27.91	32.09
4.0	37.02	22.98	29.75	30.25	27.01	32.99	25.02	34.98
4.5	35.09	24.91	27.48	32.52	24.68	35.32	22.66	37.33

(c) $\theta_{ie} = 85^{\circ}$

$\sqrt{\frac{\lambda_1}{\lambda_2}}$	a/b = 2:1		a/b = 3:1		a/b = 4:1		a/b = 6:1	
	θ_{fe} in deg.	Rotation in deg.	θ_{fe} in deg.	Rotation in deg.	θ_{fe} in deg.	Rotation in deg.	θ_{fe} in deg.	Rotation in deg.
1.0	85.0	0	85.0	0	85.0	0	85.0	0
1.21	84.40	0.60	84.18	0.82	84.09	0.91	84.02	0.98
1.61	83.36	1.64	82.71	2.29	82.42	2.58	82.19	2.81
2.08	82.27	2.73	81.08	3.92	80.53	4.47	80.09	4.91
2.60	81.19	3.81	79.37	5.63	78.52	6.48	77.83	7.17
3.0	80.41	4.59	78.12	6.88	77.03	7.97	76.13	8.87
3.5	79.50	5.50	76.61	8.39	75.22	9.78	74.06	10.94
4.0	78.65	6.35	75.17	9.83	73.47	11.53	72.04	12.96
4.5	77.84	7.16	73.78	11.22	71.77	13.23	70.08	14.92

Table 2. Results of the motion of rigid circular (equidimensional) object included in a viscous matrix deformed under simple shear. Calculations have been made from equation 3.15.

γ_s	Orientations W.R.T. Shearing Direction in Deg.			
	$\theta_{is} = 30^{\circ}$	$\theta_{is} = 50^{\circ}$	$\theta_{is} = 70^{\circ}$	$\theta_{is} = 90^{\circ}$
0	30.0	50.0	70.0	90.0
0.267	22.35	42.35	62.35	82.35
0.577	13.47	33.47	53.47	73.47
0.876	4.90	24.90	44.90	64.90
1.166	-3.40	16.6	36.60	56.60
1.4	-10.10	9.90	29.90	49.90

Table 3. Results of the motion of rigid elliptical inclusions set in a viscous matrix undergoing simple shear deformation. Results were derived from equation 3.20.

(a) $\theta_{is} = 10^{\circ}$

γ_s	a/b = 2:1		a/b = 3:1		a/b = 4:1	
	θ_{fs} in deg.	Rotation in deg.	θ_{fs} in deg.	Rotation in deg.	θ_{fs} in deg.	Rotation in deg.
0	10.0	0	10.0	0	10.0	0
0.267	6.74	3.26	8.16	1.84	8.74	1.26
0.577	3.11	6.89	6.17	3.83	7.39	2.61
0.876	-0.32	10.32	4.34	5.66	6.17	3.83
1.166	-3.66	13.66	2.63	7.37	5.05	4.95
1.4	-6.40	16.40	1.27	8.73	4.19	5.81

(b) $\theta_{is} = 30^{o}$

γ_s	a/b = 2:1		a/b = 3:1		a/b = 4:1	
	θ_{fs} in deg.	Rotation in deg.	θ_{fs} in deg.	Rotation in deg.	θ_{fs} in deg.	Rotation in deg.
0	30.0	0	30.0	0	30.0	0
0.267	24.98	5.02	25.80	4.20	26.12	3.88
0.577	19.88	10.12	21.72	8.28	22.43	7.57
0.876	15.51	14.39	18.40	11.60	19.50	10.50
1.166	11.64	18.36	15.60	14.40	17.08	12.92
1.4	8.70	21.30	13.58	16.42	15.37	14.63

(c) $\theta_{is} = 50^{o}$

γ_s	a/b = 2:1		a/b = 3:1		a/b = 4:1	
	θ_{fs} in deg.	Rotation in deg.	θ_{fs} in deg.	Rotation in deg.	θ_{fs} in deg.	Rotation in deg.
0	50.0	0	50.0	0	50.0	0
0.267	42.19	7.81	42.15	7.85	42.13	7.87
0.577	34.55	15.54	34.89	15.11	35.03	14.97
0.876	28.33	21.67	29.32	20.68	29.71	20.29
1.166	23.14	26.86	24.91	25.09	25.59	24.41
1.4	19.60	30.40	21.88	28.12	22.81	27.19

(d) $\theta_{is} = 70^{\circ}$

γ_s	a/b = 2:1		a/b = 3:1		a/b = 4:1	
	θ_{fs} in deg.	Rotation in deg.	θ_{fs} in deg.	Rotation in deg.	θ_{fs} in deg.	Rotation in deg.
0	70.0	0	70.0	0	70.0	0
0.267	59.46	10.54	58.59	11.41	58.23	11.77
0.577	48.93	21.07	47.76	22.24	47.33	22.67
0.876	40.45	29.55	39.56	30.44	39.25	30.75
1.166	33.53	36.47	33.24	36.76	33.18	36.82
1.4	28.70	41.30	29.03	40.97	29.23	40.77

(e) $\theta_{is} = 90^{\circ}$

γ_s	a/b = 2:1		a/b = 3:1		a/b = 4:1	
	θ_{fs} in deg.	Rotation in deg.	θ_{fs} in deg.	Rotation in deg.	θ_{fs} in deg.	Rotation in deg.
0	90.0	0	90.0	0	90.0	0
0.267	77.90	12.10	76.46	13.54	75.88	14.12
0.577	64.83	25.17	62.32	27.68	61.35	28.65
0.876	53.84	36.16	51.09	38.91	50.09	39.91
1.166	44.80	45.20	42.42	47.58	41.61	48.39
1.4	38.57	51.43	36.74	53.26	36.18	53.82

APPENDIX B. EXPERIMENTAL RESULTS OF THE MOTION OF RIGID INCLUSIONS UNDERGOING IRROTATIONAL STRAIN AND SIMPLE SHEAR DEFORMATION

Table 4. Results to verify the deformation history of the matrix inside Lozenge-shaped irrotational strain box.

Apical angle α	Predicted from the geometry of the box			Measured from the Experiment		
	$\sqrt{\lambda_1}=1+e_1$	$\sqrt{\lambda_2}=1+e_2$	$R=\sqrt{\lambda_1/\lambda_2}$	$\sqrt{\lambda_1}=1+e_1$	$\sqrt{\lambda_2}=1+e_2$	$R=\sqrt{\lambda_1/\lambda_2}$
65°	1.0	1.0	1.0	1.0	1.0	1.0
75°	1.14	0.935	1.21	1.17	0.92	1.27
90°	1.34	0.83	1.61	1.40	0.82	1.70
105°	1.50	0.72	2.08	1.56	0.70	2.23
115°	1.62	0.62	2.6	1.65	0.63	2.63

Table 5. Results for the verification of the deformation history of the matrix being deformed in simple shear box.

Apical angle α	Predicted from the geometry of the box			Observed from the experiment	
	γ_s	$\sqrt{\lambda_1/\lambda_2}$	θ in deg.	$\sqrt{\lambda_1/\lambda_2}$	θ in deg.
125°	0	1.0	45.0	1.0	-
115°	0.176	1.192	42.1	1.3	40.87
105°	0.36	1.431	39.85	1.53	39.45
95°	0.577	1.765	36.15	1.91	35.08
85°	0.787	2.154	34.25	2.187	32.37
75°	0.967	2.540	32.1	2.567	30.54
65°	1.166	3.031	30.4	2.948	29.17
55°	1.4	3.692	27.5	3.63	28.50

θ - the orientation of the long axis of the strain ellipse.

Table 6. Experimental results on the motion of grid marker in and around equidimensional (circular) inclusion undergoing irrotational strain deformation.

$\sqrt{\lambda_1/\lambda_2}$	$\theta_{ie} = 36^{\circ}$				$\theta_{ie} = 62.5^{\circ}$				$\theta_{ie} = 90^{\circ}$			
	S_i		S_e		S_i		S_e		S_i		S_e	
	θ_{fe} in deg.	Rot. in deg.	θ_{fe} in deg.	Rot. in deg.	θ_{fe} in deg.	Rot. in deg.	θ_{fe} in deg.	Rot. in deg.	θ_{fe} in deg.	Rot. in deg.	θ_{fe} in deg.	Rot. in deg.
1.0	36	0	36.0	0	62.5	0	62.5	0	90	0	90	0
1.21	36	0	29.0	7.0	62.5	0	51.5	11.0	90	0	90	0
1.61	36	0	23.5	12.5	62.5	0	44.0	18.5	90	0	90	0
2.08	36	0	19.0	17.0	62.5	0	36.0	26.5	90	0	90	0
2.6	36	0	15.0	21.0	62.5	0	29.0	33.5	90	0	90	0

S_i – Grid lines inside the object

S_e – Grid line outside the object

Rot.– Amount of rotation

Table 7. Motion of an equidimensional inclusion and surrounding matrix undergoing simple shear deformation.

γ_s	large = 1.2" dia.		medium = 0.92" dia.		small = 0.72" dia.		Surrounding matrix	
	θ_{fs} in deg.	Rotation in deg.	θ_{fs} in deg.	Rotation in deg.	θ_{fs} in deg.	Rotation in deg.	θ_{fs} in deg.	Rotation in deg.
0	90.0	0	90.0	0	90.0	0	90.0	0
0.267	80.0	10.0	80.2	9.8	79.4	10.6	70.0	20.0
0.577	71.0	19.0	71.5	18.5	70.0	20.0	58.0	32.0
0.876	65.5	24.5	65.0	25.0	63.0	27.0	50.0	40.0
1.166	60.5	29.5	59.2	30.8	56.8	33.2	45.5	44.5
1.40	55.5	34.5	55.0	35.0	52.0	38.0	40.0	50.0

θ_{fs} - Finite orientation of the grid markers stamped inside and outside the inclusion.

Table 8. Results of the motion of rigid elliptical inclusions measured from the experiments undergoing irrotational strain.

(a) a/b = 2:1

$\sqrt{\lambda_1/\lambda_2}$	$\theta_{ie} = 0^\circ$		$\theta_{ie} = 30^\circ$		$\theta_{ie} = 58^\circ$		$\theta_{ie} = 90^\circ$	
	θ_{fe} in deg.	Rotation in deg.	θ_{fe} in deg.	Rotation in deg.	θ_{fe} in deg.	Rotation in deg.	θ_{fe} in deg.	Rotation in deg.
1.0	0	0	30.0	0	58.0	0	90.0	0
1.21	0	0	29.0	1.0	55.0	3.0	90.0	0
1.61	0	0	24.5	5.5	49.5	8.5	90.0	0
2.08	0	0	20.0	10.0	43.0	15.0	90.0	0
2.60	0	0	18.5	11.5	39.0	19.0	90.0	0

(b) a/b = 3:1

$\sqrt{\lambda_1/\lambda_2}$	$\theta_{ie} = 0^o$		$\theta_{ie} = 30^o$		$\theta_{ie} = 63^o$		$\theta_{ie} = 90^o$	
	θ_{fe} in deg.	Rotation in deg.	θ_{fe} in deg.	Rotation in deg.	θ_{fe} in deg.	Rotation in deg.	θ_{fe} in deg.	Rotation in deg.
1.0	0	0	30.0	0	63.0	0	90.0	0
1.21	0	0	26.5	3.5	58.0	5.0	90.0	0
1.61	0	0	22.0	8.0	51.5	11.5	90.0	0
2.08	0	0	16.0	14.0	43.5	19.5	90.0	0
2.60	0	0	15.0	15.0	38.0	25.0	90.0	0

(c) a/b = 4:1

$\sqrt{\lambda_1/\lambda_2}$	$\theta_{ie} = 0^o$		$\theta_{ie} = 30^o$		$\theta_{ie} = 58^o$		$\theta_{ie} = 90^o$	
	θ_{fe} in deg.	Rotation in deg.	θ_{fe} in deg.	Rotation in deg.	θ_{fe} in deg.	Rotation in deg.	θ_{fe} in deg.	Rotation in deg.
1.0	0	0	30.0	0	58.0	0	90.0	0
1.21	0	0	25.5	4.5	52.5	5.5	90.0	0
1.61	0	0	20.0	10.0	46.5	11.5	90.0	0
2.08	0	0	15.5	14.5	38.0	20.0	90.0	0
2.60	0	0	11.5	18.5	31.0	27.0	90.0	0

Table 9. Results for the motion of rigid elliptical inclusions set in a deforming matrix measured from the experiments performed during progressive simple shear deformation.

(a) a/b = 2:1

γ_s	$\theta_{is} = 126^\circ$		$\theta_{is} = 90^\circ$		$\theta_{is} = 60^\circ$		$\theta_{is} = 50^\circ$	
	θ_{fs} in deg.	Rotation in deg.	θ_{fs} in deg.	Rotation in deg.	θ_{fs} in deg.	Rotation in deg.	θ_{fs} in deg.	Rotation in deg.
0.00	126	0	90.0	0	60.0	0	50.0	0
0.267	112	14.0	73.5	16.5	47.0	13.0	39.5	10.5
0.577	99	27.0	60.5	29.5	37.5	22.5	33.0	17.0
0.876	87	39.0	52.5	38.5	33.5	26.5	28.5	21.5
1.166	74.5	51.5	44.0	46.0	28.0	32.0	26.0	24.0
1.4	63	63.0	40.0	50.0	24.0	36.0	21.5	28.5

(b) a/b = 3:1

γ_s	$\theta_{is} = 126^\circ$		$\theta_{is} = 90^\circ$		$\theta_{is} = 54^\circ$		$\theta_{is} = 33^\circ$	
	θ_{fs} in deg.	Rotation in deg.	θ_{fs} in deg.	Rotation in deg.	θ_{fs} in deg.	Rotation in deg.	θ_{fs} in deg.	Rotation in deg.
0.00	126	0	90.0	0	54.0	0	33.0	0
0.267	112	14	73.0	17.0	41.0	13.0	26.5	6.5
0.577	98	28	60.0	30.0	36.5	17.5	22.0	11.0
0.876	86	40	52	38	33	21	17.5	15.5
1.166	71	55	40.5	49.5	26.5	27.5	14.0	19.0
1.40	61	65	36.0	54.0	23.0	31.0	10.0	23.0

(c) a/b = 4:1

γ_s	$\theta_{is} = 126°$		$\theta_{is} = 90°$		$\theta_{is} = 57°$		$\theta_{is} = 33°$	
	θ_{fs} in deg.	Rotation in deg.	θ_{fs} in deg.	Rotation in deg.	θ_{fs} in deg.	Rotation in deg.	θ_{fs} in deg.	Rotation in deg.
0.00	126	0	90.0	0	57.0	0	33.0	0
0.267	108.5	17.5	67.0	23.0	44.0	13.0	24.0	9.0
0.577	93.0	33.0	55.5	34.0	38.0	19.0	18.0	15.0
0.876	80.0	46.0	48.5	41.5	30.0	27.0	16.0	17.0
1.166	67.0	59.0	41.5	48.5	27.0	30.0	14.5	18.5
1.40	52.0	74.0	36.0	54.0	-	-	12.5	20.5

Table 10. Measurements of the amount of rotation of rigid elliptical inclusions and their surrounding matrix deformed during progressive simple shear.

(a) a/b = 2:1

γ_s	$\theta_{is} = 126^\circ$				$\theta_{is} = 90^\circ$				$\theta_{is} = 60^\circ$				$\theta_{is} = 50^\circ$			
	Inclusion		Matrix		Inclusion		Matrix		Inclusion		Matrix		Inclusion		Matrix	
	θ_{fs} in deg.	Rot. in deg.	θ_{fs} in deg.	Rot. in deg.	θ_{fs} in deg.	Rot. in deg.	θ_{fs} in deg.	Rot. in deg.	θ_{fs} in deg.	Rot. in deg.	θ_{fs} in deg.	Rot. in deg.	θ_{fs} in deg.	Rot. in deg.	θ_{fs} in deg.	Rot. in deg.
0	126	0	126	0	90	0	90	0	60	0	60	0	50	0	50	0
0.267	112	14	112	14	73.5	16.5	71	19	47	13	45.5	14.5	39.5	10.5	40	10
0.577	99	27	100	26	60.5	29.5	56	34	37.5	22.5	35	25	33	17	36	14
0.876	87	39	91	35	52.5	38.5	49.5	40.5	33.5	26.5	33.5	26.5	28.5	21.5	33	17
1.166	74.5	51.5	76	50	44	46.0	40	50	28	32	29	31	26	24	31.5	18.5
1.40	63	63	62	64	40	50	37	63	24	36	26	34	21.5	28.5	29	21

(b) a/b = 3:1

γ_s	$\theta_{is} = 126^\circ$				$\theta_{is} = 90^\circ$				$\theta_{is} = 54^\circ$				$\theta_{is} = 33^\circ$			
	Inclusion		Matrix		Inclusion		Matrix		Inclusion		Matrix		Inclusion		Matrix	
	θ_{fs} in deg.	Rot. in deg.	θ_{fs} in deg.	Rot. in deg.	θ_{fs} in deg.	Rot. in deg.	θ_{fs} in deg.	Rot. in deg.	θ_{fs} in deg.	Rot. in deg.	θ_{fs} in deg.	Rot. in deg.	θ_{fs} in deg.	Rot. in deg.	θ_{fs} in deg.	Rot. in deg.
0	126	0	126	0	90	0	90	0	54	0	54	0	33	0	33	0
0.267	112	14	114	12	73	17	71	19	41	13	42	12	26.5	6.5	30	3
0.577	98	28	100.5	25.5	60	30	59	31	36.5	17.5	39	15	22	11	27	6
0.876	86	40	84.5	41.5	52	38	49	41	33	21	35.5	18.5	17.5	15.5	22	11
1.166	71	55	71	55	40.5	49.5	40	50	26.5	27.5	29.5	24.5	14	19	18	15
1.40	61	65	60	66	36	54	34.5	55.5	23	31	26	28	10	23	16.5	16.5

θ_{fs} - Finite orientation of the long axis of the elliptical inclusion and grid lines in the matrix with reference to the shearing direction.

Rot. - Amount of rotation in degrees.

APPENDIX C. PREDICTED RESULTS OF THE ELONGATION (1 + e) OF STRETCHED BELEMNITES DETERMINED FROM THE THEORETICAL MODELS

Table 11. Results from the models simulating stretched belemnites during pure shear deformation.

(a) Belemnite body a/b = 3:1; fragments a/b = 1:1

$\sqrt{\lambda_1/\lambda_2}$	$\theta_b = 30^\circ$		$\theta_b = 60^\circ$		$\theta_b = 80^\circ$	
	l_1 cm.	$\sqrt{\lambda}=(1+e)$	l_1 cm.	$\sqrt{\lambda}=(1+e)$	l_1 cm.	$\sqrt{\lambda}=(1+e)$
1.0	2.0	1.0	2.0	1.0	2.0	1.0
1.21	2.3	1.15	2.2	1.10	2.05	1.025
1.61	2.75	1.375	2.35	1.175	2.08	1.04
2.08	3.36	1.68	2.6	1.3	2.10	1.05
2.6	3.8	1.9	2.9	1.45	2.15	1.075

(b) Belemnite body a/b = 6:1; fragments a/b = 2:1

$\sqrt{\lambda_1/\lambda_2}$	$\theta_b = 30^\circ$		$\theta_b = 60^\circ$		$\theta_b = 80^\circ$	
	l_1 cm.	$\sqrt{\lambda}=(1+e)$	l_1 cm.	$\sqrt{\lambda}=(1+e)$	l_1 cm.	$\sqrt{\lambda}=(1+e)$
1.0	4.0	1.0	4.0	1.0	4.0	1.0
1.21	4.6	1.15	4.22	1.05	4.1	1.025
1.61	5.7	1.425	4.75	1.18	4.2	1.05
2.08	7.0	1.75	5.35	1.337	4.25	1.06
2.6	8.5	2.125	6.0	1.5	4.35	1.07

θ_b – Initial orientation of belemnite body with reference to the principal extension direction.

Table 12. Results from the models simulating stretched belemnites set in a matrix undergoing simple shear deformation.

(a) Belemnite body a/b = 3:1; fragments a/b = 1:1

γ_s	$\theta_b = 90^\circ$			$\theta_b = 60^\circ$			$\theta_b = 30^\circ$		
	l_1 cm.	e	$\sqrt{\lambda}$ = (1+e)	l_1 cm.	e	$\sqrt{\lambda}$ = (1+e)	l_1 cm.	e	$\sqrt{\lambda}$ = (1+e)
0	2.0	0	1.0	2.0	0	1.0	2.0	0	1.0
0.267	2.1	0.05	1.05	2.25	0.125	1.125	2.35	0.175	1.175
0.876	2.55	0.275	1.275	3.05	0.525	1.525	3.1	0.55	1.55
1.4	3.35	0.675	1.675	3.98	0.99	1.99	4.3	1.15	2.15

(b) Belemnite body a/b = 6:1; fragments a/b = 2:1

γ_s	$\theta_b = 90^\circ$			$\theta_b = 60^\circ$			$\theta_b = 30^\circ$		
	l_1 cm.	e	$\sqrt{\lambda}$ = (1+e)	l_1 cm.	e	$\sqrt{\lambda}$ = (1+e)	l_1 cm.	e	$\sqrt{\lambda}$ = (1+e)
0	4.0	0	1.0	4.0	0	1.0	4.0	0	1.0
0.267	4.13	0.032	1.032	4.55	0.137	1.137	4.45	0.112	1.112
0.876	5.25	0.312	1.312	6.15	0.537	1.537	5.75	0.437	1.437
1.4	6.85	0.712	1.712	7.68	0.92	1.92	6.9	0.725	1.725

θ_b = Initial orientation of the belemnite body with reference to the shearing direction.

APPENDIX D. EXPERIMENTAL RESULTS OF EXTENDED BELEMNITES

Table 13. Results obtained from the experiments simulating stretched belemnites undergoing irrotational strain.

(a) Belemnite body a/b = 3:1; fragments a/b = 1:1

Initial orientation θ_b in deg.	Applied strain $\sqrt{\lambda_1/\lambda_2}$	Length of the specimen l_1 cm.	Elongation (1+e)	Orient. of the whole belemn. θ_b' in deg.	Rotation of the whole belemn. specimen in deg.	Average orient. of fragments. θ_f' in deg.
76	1.0	2.95	1.0	76.0	0	76.0
	1.21	2.95	1.0	70.0	6.0	72.66
	1.61	3.0	1.017	65.5	10.5	69.33
	2.08	3.1	1.05	61.0	15.0	65.26
	2.60	3.1	1.05	56.5	19.5	58.66
61	1.0	3.0	1.0	61.0	0	61.0
	1.21	3.15	1.05	54.5	6.5	59.33
	1.61	3.2	1.06	46.0	15.0	57.33
	2.08	3.2	1.06	36.0	25.0	53.66
	2.60	3.2	1.06	32.0	29.0	49.16
30	1.0	3.0	1.0	30.0	0	30.0
	1.21	3.5	1.166	26.0	4.0	31.0
	1.61	4.1	1.366	20.0	10.0	33.33
	2.08	4.35	1.45	14.0	16.0	37.66
	2.60	4.5	1.5	10.0	20.0	38.83
0	1.0	3.0	1.0	0	0	0
	1.21	3.55	1.18	0	0	-0.5
	1.61	4.4	1.466	0	0	-2.43
	2.08	4.94	1.65	0	0	-4.76
	2.60	5.35	1.78	0	0	-6.66

(b) Belemnite body a/b = 6:1; fragments a/b = 2:1

Initial orientation θ_b in deg.	Applied strain $\sqrt{\lambda_1/\lambda_2}$	Length of the specimen l_1 cm.	Elongation $(1+e)$	Orient. of the whole belemn. θ_b' in deg.	Rotation of the whole belemn. specimen in deg.	Average orient. of fragments. θ_f' in deg.
58	1.0	6.0	1.0	58.0	0	58.0
	1.21	6.05	1.008	52.5	5.5	53.66
	1.61	6.1	1.01	45.0	13.0	49.166
	2.08	6.15	1.025	36.0	22.0	44.33
	2.6	6.2	1.03	30.0	28.0	39.66
48.5	1.0	6.0	1.0	48.5	0	48.5
	1.21	6.4	1.06	40.0	8.5	45.33
	1.61	6.8	1.133	32.5	16.0	43.0
	2.08	7.15	1.19	25.0	23.5	40.0
	2.6	7.4	1.23	20.5	28.0	38.0
31	1.0	5.9	1.0	31.0	0	31.0
	1.21	6.8	1.152	24.0	7.0	27.66
	1.61	7.45	1.26	20.0	11.0	27.33
	2.08	8.2	1.389	15.0	16.0	26.5
	2.6	8.6	1.457	12.0	19.0	26.33
11	1.0	6.0	1.0	11.0	0	11.0
	1.21	7.1	1.183	9.5	1.5	11.0
	1.61	8.5	1.416	7.0	3.0	10.0
	2.08	9.65	1.608	5.5	5.5	10.83
	2.6	10.35	1.725	4.0	7.0	12.0
0	1.0	5.8	1.0	0	0	0
	1.21	7.0	1.206	0	0	0
	1.61	8.1	1.396	0	0	0
	2.08	9.35	1.612	0	0	-0.75
	2.6	10.0	1.724	0	0	-1.50

(c) Belemnite body a/b = 9:1; fragments a/b = 3:1

Initial orientation θ_b in deg.	Applied strain $\sqrt{\lambda_1/\lambda_2}$	Length of the specimen l_1 cm.	Elongation (1+e)	Orient. of the whole belemn. θ_b' in deg.	Rotation of the whole belemn. specimen in deg.	Average orient. of fragments θ_f' in deg.
68	1.0	4.2	1.0	68.0	0	68.0
	1.21	4.2	1.0	63.0	5.0	63.75
	1.61	4.25	1.01	59.0	9.0	59.5
	2.08	4.3	1.02	51.0	17.0	51.75
	2.6	4.35	1.035	47.0	21.0	48.0
54	1.0	4.2	1.0	54.0	0	54.0
	1.21	4.35	1.035	47.5	6.5	49.75
	1.61	4.4	1.047	40.0	14.0	44.5
	2.08	4.4	1.047	32.5	21.5	39.75
	2.6	4.45	1.059	28.5	25.5	36.0
28	1.0	4.3	1.0	28.0	0	28.0
	1.21	4.85	1.128	23.0	5.0	24.5
	1.61	5.5	1.28	19.0	9.0	21.0
	2.08	6.25	1.45	13.0	15.0	16.25
	2.6	6.65	1.546	10.5	17.5	15.0
0	1.0	4.3	1.0	0	0	0
	1.21	5.25	1.22	0	0	0
	1.61	6.2	1.44	0	0	0
	2.08	7.05	1.64	0	0	0
	2.6	7.65	1.78	0	0	0

Table 14. Results obtained from the experiments simulating stretched belemnites during simple shear deformation.

(a) Belemnite body a/b = 3:1; fragments a/b = 1:1

Initial orientation θ_b in deg.	Applied shear strain γ_s	Length of the specimen l_1 cm.	Elongation (1+e)	Orient. of the whole belemn. θ_b' in deg.	Rotation of the whole belemn. specimen in deg.	Average orient. of fragments θ_f' in deg.
120.0	0	5.25	1.0	120.0	0	120.0
	0.267	5.25	1.0	104.0	16.0	104.0
	0.577	5.25	1.0	85.0	35.0	86.37
	0.876	5.55	1.057	74.0	46.0	78.62
	1.166	6.10	1.162	65.0	55.0	73.25
	1.4	6.55	1.247	63.5	56.5	69.0
91.0	0	5.25	1.0	91.0	0	91.0
	0.267	5.42	1.032	69.0	22.0	78.62
	0.577	6.0	1.143	58.5	32.5	78.62
	0.876	7.02	1.337	46.5	44.5	76.25
	1.166	8.4	1.60	38.0	53.0	76.25
	1.4	9.85	1.876	33.5	57.5	76.0
64.5	0	5.3	1.0	64.5	0	64.5
	0.267	6.3	1.188	46.0	18.5	51.87
	0.577	7.25	1.368	39.0	25.5	46.62
	0.876	8.30	1.566	32.5	32.0	37.0
	1.166	9.60	1.811	30.0	34.5	22.25
	1.4	10.75	2.028	25.0	39.5	16.50
31.0	0	5.3	1.0	31.0	0	31.0
	0.267	6.2	1.169	25.5	5.5	18.12
	0.577	6.8	1.283	23.0	8.0	4.25
	0.876	7.55	1.424	22.5	8.5	-11.12
	1.166	8.2	1.547	20.0	11.0	-29.4
	1.4	8.95	1.688	19.0	12.0	-41.75

(b) Belemnite body a/b = 6:1; fragments a/b = 2:1

Initial orientation θ_b in deg.	Applied shear strain γ_s	Length of the specimen l_1 cm.	Elongation (1+e)	Orient. of the whole belemn. θ_b' in deg.	Rotation of the whole belemn. specimen in deg.	Average orient. of fragments θ_f' in deg.
118.5	0	6.8	1.0	118.5	0	118.5
	0.267	6.85	1.007	98.0	20.5	98.0
	0.577	6.85	1.007	83.0	35.5	83.0
	0.876	7.2	1.058	69.0	49.5	74.16
	1.166	7.95	1.169	55.6	62.9	67.16
	1.4	9.05	1.331	47.5	71.0	66.5
89.0	0	6.8	1.0	89.0	0	89.0
	0.267	7.25	1.066	66.0	23.0	73.83
	0.577	8.15	1.198	55.5	33.5	69.33
	0.876	9.35	1.375	42.5	46.5	61.33
	1.166	10.9	1.603	37.0	52.0	58.26
	1.4	12.45	1.830	33.0	56.0	53.30
57.0	0	6.85	1.0	57.0	0	57.0
	0.267	8.15	1.189	44.5	12.5	45.83
	0.577	9.45	1.379	36.5	20.5	36.33
	0.876	11.45	1.671	32.0	25.0	28.5
	1.166	12.6	1.839	29.0	28.0	20.33
	1.4	14.15	2.065	25.5	31.5	11.161
31.5	0	6.8	1.0	31.5	0	31.5
	0.267	7.9	1.161	26.0	5.5	21.83
	0.577	8.7	1.279	24.0	7.5	13.83
	0.876	9.5	1.397	20.5	11.0	3.50
	1.166	10.3	1.514	20.0	11.5	-4.83
	1.4	11.15	1.639	20.0	11.5	-9.33
0	0	6.75	1.0	0	0	0
	0.267	6.75	1.0	0	0	-3.166
	0.577	6.75	1.0	0	0	-5.50
	0.876	6.77	1.003	0	0	-8.33
	1.166	6.81	1.016	0	0	-10.0
	1.4	6.81	1.016	0	0	-11.33

(c) Belemnite body a/b = 9:1; fragments a/b = 3:1

Initial orientation θ_b in deg.	Applied shear strain γ_s	Length of the specimen l_1 cm.	Elongation (1+e)	Orient. of the whole belemn. θ_b' in deg.	Rotation of the whole belemn. specimen in deg.	Average orient. of fragments θ_f' in deg.
119.0	0	9.7	1.0	119.0	0	119.0
	0.267	9.7	1.0	99.0	20.0	99.83
	0.577	9.8	1.01	85.5	33.5	87.16
	0.876	10.5	1.082	70.5	48.5	73.66
	1.166	11.5	1.185	58.5	60.5	64.0
	1.4	13.1	1.35	49.0	70.0	56.0
90.0	0	9.65	1.0	90.0	0	90.0
	0.267	10.2	1.056	68.5	21.5	73.16
	0.577	11.4	1.181	55.0	35.0	61.83
	0.876	13.05	1.352	45.0	45.0	51.83
	1.166	15.1	1.564	39.0	51.0	43.5
	1.4	17.2	1.782	33.5	56.5	34.66
60.0	0	9.7	1.0	60.0	0	60.0
	0.267	11.8	1.216	44.0	16.0	45.10
	0.577	13.5	1.391	39.5	20.5	39.83
	0.876	15.55	1.603	32.0	28.0	30.66
	1.166	17.75	1.829	29.3	30.7	23.66
	1.4	19.9	2.051	27.0	33.0	16.5
30.0	0	9.75	1.0	30.0	0	30.0
	0.267	11.55	1.184	25.5	4.5	22.66
	0.577	12.6	1.292	23.5	6.5	17.33
	0.876	13.8	1.415	21.0	9.0	10.5
	1.166	15.15	1.554	19.0	11.0	3.33
	1.4	16.2	1.661	18.0	12.0	0
0	0	9.7	1.0	0	0	0
	0.267	9.9	1.02	1.0	-1.0	-0.5
	0.577	9.9	1.02	3.0	-3.0	-2.33
	0.876	10.0	1.03	4.0	-4.0	-4.166
	1.166	10.05	1.036	5.0	-5.0	-6.83
	1.4	10.15	1.046	5.0	-5.0	-10.5

APPENDIX E. RESULTS OBTAINED FROM THE MEASUREMENTS OF EXTENDED BELEMNITES OF LEYTRON, VALAIS, SWITZERLAND

Table 15. Measurements of 196 specimens of stretched belemnites.

θ_b' – Angle between the finite orientation of the whole belemnite body and the stretching lineation.

l_o – Original length of the belemnite specimen derived by the addition of the length of individual fragments containing in a specimen.

l_1 – Total length including the space occupied by quartz and calcite (extended length).

Insitu specimens :

Serial No.	θ_b' in deg.	l_o cm.	l_1 cm.	$e=\frac{l_1-l_o}{l_o}$	$\sqrt{\lambda}=1+e$
1	29	8.5	13.7	0.611	1.611
2	10	6.05	11.8	0.95	1.95
3	43.5	3.1	4.8	0.548	1.548
4	30.5	3.75	7.2	0.92	1.92
5	84	3.45	4.0	0.159	1.159
6	3	2.9	6.9	1.72	2.72
7	24	4.3	5.9	0.372	1.372
8	40	1.9	3.1	0.631	1.63
9	16	2.65	5.2	0.96	1.96
10	22	1.6	2.9	0.81	1.81
11	27	5.2	8.9	0.71	1.71
12	10.5	3.55	7.9	1.22	2.22
13	37	3.5	5.4	0.54	1.54
14	33	3.05	6.5	1.13	2.13
15	5	4.05	9.6	1.37	2.37
16	18	3.7	8.9	1.40	2.40
17	42	4.55	5.4	0.186	1.186
18	43	9.2	18.7	1.03	2.03

Serial No.	θ_b' in deg.	l_o cm.	l_1 cm.	$e=\frac{l_1-l_o}{l_o}$	$\sqrt{\lambda}=1+e$
19	20	2.0	3.2	0.60	1.60
20	84	7.9	13.7	0.73	1.73
21	35	6.6	7.5	0.13	1.13
22	36	9.45	10.8	0.14	1.14
23	9	9.0	11.6	0.29	1.29
24	6	10.1	27.2	1.69	2.69
25	28.5	2.95	5.0	0.694	1.694
26	10	5.3	12.3	1.33	2.33

Specimens embedded in slates collected from scress :

Serial No.	θ_b' in deg.	l_o cm.	l_1 cm.	$e=\frac{l_1-l_o}{l_o}$	$\sqrt{\lambda}=1+e$
27	22	3.7	5.6	0.51	1.51
28	3	5.25	14.1	1.68	2.68
29	3	2.65	6.25	1.36	2.36
30	23	2.55	3.7	0.45	1.45
31	20	2.25	7.2	2.20	3.20
32	18	3.75	8.5	1.26	2.26
33	20	3.8	6.1	0.60	1.60
34	58	2.2	2.7	0.23	1.23
35	30	2.7	6.2	1.29	2.29
36	8	3.1	6.5	1.09	2.09
37	38.5	5.05	7.0	0.38	1.38
38	7	6.4	13.1	1.04	2.04
39	10	4.8	9.0	0.87	1.87
40	57	4.05	4.9	0.20	1.20
41	2	4.55	9.0	0.98	1.98
42	20	4.3	7.3	0.69	1.69
43	8	4.15	12.0	1.89	2.89
44	19	3.95	7.1	0.79	1.79
45	28	2.5	4.1	0.64	1.64
46	24	3.35	5.8	0.73	1.73
47	2	5.95	12.0	1.016	2.016

Serial No.	θ_b' in deg.	l_o cm.	l_1 cm.	$e=\frac{l_1-l_o}{l_o}$	$\sqrt{\lambda}=1+e$
48	18	3.15	10.6	2.36	3.36
49	22	3.2	5.3	0.65	1.65
50	56	5.5	7.0	0.27	1.27
51	8	5.6	8.6	0.53	1.53
52	15	2.95	6.8	1.30	2.30
53	72	3.5	4.9	0.40	1.40
54	38	6.4	11.0	0.72	1.72
55	0	2.0	5.6	1.80	2.80
56	9	4.9	11.1	1.26	2.26
57	30	2.9	4.6	0.58	1.58
58	2	1.4	10.2	-	-
59	69	7.3	8.3	0.136	1.136
60	70	4.6	7.0	0.52	1.52
61	15	2.4	9.2	2.83	3.83
62	15	3.7	9.1	1.46	2.46
63	9	3.2	11.2	2.50	3.50
64	11	2.35	5.4	1.29	2.29
65	10	4.2	10.5	1.5	2.5
66	21	3.5	11.0	2.14	3.14
67	57	3.9	5.3	0.36	1.36
68	32	5.4	7.3	0.35	1.35
69	14	4.45	8.8	0.97	1.97
70	18	2.85	9.2	2.23	3.23
71	3	2.0	7.1	2.55	3.55
72	20	2.7	8.4	2.11	3.11
73	0	5.95	12.2	1.05	2.05
74	15	2.9	7.1	1.45	2.45
75	26	3.85	6.2	0.61	1.61
76	50	4.7	7.5	0.59	1.59
77	19	2.55	4.6	0.80	1.80
78	3	4.8	9.0	0.87	1.87
79	6	3.3	10.2	2.09	3.09
80	0	7.95	19.3	1.43	2.43
81	3	6.8	10.2	0.5	1.5

Serial No.	θ_b' in deg.	l_o cm.	l_1 cm.	$e=\frac{l_1-l_o}{l_o}$	$\sqrt{\lambda}=1+e$
82	21	6.5	14.0	1.15	2.15
83	16	2.7	5.0	0.85	1.85
84	50	7.5	9.1	0.21	1.21
85	30	5.55	10.0	0.80	1.80
86	40	3.1	6.5	1.09	2.09
87	5	6.7	14.5	1.16	2.16
88	2	3.95	13.4	2.39	3.39
89	25.2	3.77	5.6	0.48	1.48
90	.4	5.25	14.2	1.70	2.70
91	22	3.35	7.6	1.27	2.27
92	8	4.95	11.3	1.28	2.28
93	26	4.3	7.7	0.79	1.79
94	28	2.7	3.7	0.37	1.37
95	19	3.8	6.1	0.60	1.60
96	17	1.9	6.7	1.31	2.31
97	5	3.75	8.5	1.26	2.26
98	9	3.3	7.4	1.24	2.24
99	60	2.7	3.5	0.29	1.29
100	37	4.95	7.0	0.41	1.41
101	22	4.45	7.5	0.68	1.68
102	42	6.7	9.0	0.34	1.34
103	33	6.3	8.9	0.41	1.41
104	33	3.7	5.7	0.54	1.54
105	28	7.8	11.1	0.42	1.42
106	50	4.0	5.6	0.4	1.4
107	21	6.25	9.5	0.52	1.52
108	13	2.75	6.7	1.43	2.43
109	30	3.35	5.6	0.67	1.67
110	34	7.2	11.0	0.53	1.53
111	35	1.5	2.7	0.80	1.80
112	35	6.1	8.8	0.44	1.44
113	69	3.8	5.1	0.34	1.34
114	43	7.75	11.4	0.47	1.47
115	80	3.8	5.2	0.36	1.36
116	20	6.65	21.3	2.20	3.20

Serial No.	θ_b' in deg.	l_o cm.	l_1 cm.	$e=\frac{l_1-l_o}{l_o}$	$\sqrt{\lambda}=1+e$
117	23	2.05	6.5	2.17	3.17
118	1	3.65	9.6	1.63	2.63
119	9	4.2	13.6	2.23	3.23
120	32	5.3	7.0	0.32	1.32
121	26	2.75	4.5	0.63	1.63
122	36	1.45	2.9	1.0	2.0
123	75	3.55	4.2	0.18	1.18
124	87	6.9	8.8	0.27	1.27
125	3	1.75	2.6	0.48	1.48
126	21.5	3.35	4.9	0.46	1.46
127	8	2.55	12.2	3.78	4.78
128	17	6.65	17.9	1.69	2.69
129	24	4.1	6.7	0.63	1.63
130	18	2.45	6.8	1.77	2.77
131	15	5.6	12.7	1.26	2.26
132	26	4.45	7.5	0.68	1.68
133	56	4.6	6.7	0.45	1.45
134	5	4.35	7.8	0.79	1.79
135	7	4.5	10.2	1.26	2.26
136	26.5	6.2	8.5	0.37	1.37
137	15	3.5	7.9	1.25	2.25
138	14.5	4.5	5.8	0.28	1.28
139	18	3.3	6.0	0.81	1.81
140	3	1.5	3.6	1.40	2.40
141	23	3.4	9.9	1.91	2.91
142	33	2.65	5.3	0.96	1.96
143	15	3.2	8.8	1.75	2.75
144	11	4.3	8.8	1.04	2.04
145	44	8.6	13.2	0.53	1.53
146	27	5.15	8.7	0.68	1.68
147	24	4.65	7.5	0.61	1.61
148	56	4.9	7.3	0.49	1.49
149	41	7.2	14.7	1.04	2.04
150	26	4.45	8.5	0.91	1.91
151	58	5.3	6.1	0.15	1.15

Serial	θ_b' in deg.	l_o cm.	l_1 cm.	$e=\frac{l_1-l_o}{l_o}$	$\sqrt{\lambda}=1+e$
152	40	4.0	5.0	0.25	1.25
153	15	2.6	5.3	1.03	2.03
154	56	3.3	4.8	0.45	1.45
155	65	2.4	3.8	0.58	1.58
156	18	3.9	6.3	0.61	1.61
157	27	2.9	7.1	1.44	2.44
158	2.5	3.5	4.7	0.34	1.34
159	31	5.15	10.6	1.05	2.05
160	23.5	3.3	4.8	0.45	1.45
161	27	13.4	24.5	0.82	1.82
162	26	3.05	10.0	2.27	3.27
163	0	5.2	11.3	1.17	2.17
164	48	3.2	6.5	1.03	2.03
165	53	11.5	15.0	0.30	1.30
166	21	4.5	7.9	0.75	1.75
167	65.5	3.3	4.7	0.42	1.42
168	35	3.8	5.8	0.52	1.52
169	27	8.4	9.3	0.11	1.11
170	17	8.75	14.5	0.65	1.65
171	24	6.1	8.5	0.39	1.39
172	22	5.6	8.1	0.44	1.44
173	8	4.0	10.7	1.67	2.67
174	16	6.9	8.7	0.26	1.26
175	4	5.5	8.3	0.51	1.51
176	85	2.55	4.0	0.56	1.56
177	39	3.5	9.0	1.57	2.57
178	26	6.2	7.5	0.21	1.21
179	24	4.45	9.7	1.18	2.18
180	32	3.3	5.6	0.69	1.69
181	23	6.35	8.7	0.21	1.21
182	42.5	3.6	5.7	0.58	1.58
183	43.5	6.6	8.2	0.24	1.24
184	17	6.0	14.2	1.36	2.36
185	66	5.55	10.7	0.92	1.92
186	24	5.9	11.2	0.89	1.89

Serial No.	θ_b' in deg.	l_o cm.	l_1 cm.	$e=\frac{l_1-l_o}{l_o}$	$\sqrt{\lambda}=1+e$
187	56	4.0	9.0	1.25	2.25
188	18	3.3	6.0	0.82	1.82
189	29.5	4.15	9.0	1.17	2.17
190	34	4.15	6.2	0.49	1.49
191	41	3.15	6.0	0.90	1.90
192	6.5	6.1	8.9	0.46	1.46
193	4	5.1	7.9	0.55	1.55
194	34	4.85	7.5	0.54	1.54
195	72	4.45	6.7	0.50	1.50
196	29	4.4	9.5	1.16	2.16

Table 16. Average elongation of Leytron belemnites

Average θ_b' in deg.	Average e	Average $\sqrt{\lambda}$ = (1+e)
1.25	1.90	2.90
5	1.41	2.41
10	1.49	2.49
15	1.34	2.34
20	1.31	2.13
25	0.79	1.79
30	0.73	1.73
35	0.57	1.57
40	0.69	1.69
45	0.56	1.56
50	0.55	1.55
55	0.47	1.47
60	0.23	1.23
65	0.64	1.64
70	0.37	1.37
75	0.38	1.38
80	0.36	1.36
85	0.21	1.21

APPENDIX F. DETERMINATION OF STRAIN FROM THE DISTORTED GRIDS

Square grids were stamped on the surface of the inclusion and surrounding matrix as strain markers. Displacement vectors describing flow lines of the matrix and the magnitude and orientation of principal strains can be evaluated from the distorted grids.

Two different methods : (i) The "graphical method" developed by Ramsay (personal communication) and (ii) The "shift image" method presented by Durelli, Park and Feng (1967) were used to evaluate strains and displacements from the grid data. A detailed description of the graphical method is given in (Hossain, 1970). The "shift image" method involves the shifting of the image of the distroted grid over another image of the undistorted grid, or the shifting of the image of the distorted grid over another image of the same distorted grid in order to obtain the displacement components and the derivatives of displacement components respectively. The strain can be determined directly from these displacement components. Both the "graphical method" and "shift image method" are tedious, time consuming and inaccurate.

A new technique of evaluating grid data using a computer has been developed in collaboration with Cobbold (1973). The magnitude and the orientation of principal strains developed in the matrix material has been determined from the displacement gradients using simple equations (Ramsay, 1967, Section 3-4). This computer technique is very accurate and fast. Another advantage of this technique over the two other methods is that it produces automatic plots of the magnitude and orientation of the major and minor axes of the strain ellipses.

The technique involves two stages. The first stage is the recording of the co-ordinates of the nodes (points of intersection of the grid lines) using the digital pencil follower (D-MAC). This was done using photographs of the experiments. A photograph was placed on the 'D-MAC' table and the co-ordinates of the nodes were automatically punched into the computer cards using the pencil follower. This was done in sequence from left to right for each row. The analysis of strain for the successive stages of deformation of an experiment can be made by repeating the procedure of recording co-ordinates from successive photographs.

The second stage of the technique is the determination of strains using the displacement gradients calculated from the co-ordinates of the nodes. A computer programme has been developed to read the node data punched onto the cards and to determine and plot the magnitude and orientation of the major and minor axes of the strain ellipses. This computer technique has been described in detail by Cobbold (1973, Appendix C). The computer programme developed for this purpose is enclosed with this appendix.

```
              PROGRAM GRID(INPUT,OUTPUT,TAPE62,TAPE5=INPUT,TAPE6=OUTPUT)
000002        COMMON X,Y,NIX,NIY,XINC,YINC,NNF,NNT,NNX,NNY
000002        COMMON XO,YO
000002        DIMENSION X(25,25),Y(25,25)
        C
        C      CARRIAGE CONTROL
000002        WRITE (6,9999)
        C
        C      SET INITIAL PARAMETERS
        C
000006        NNF=10
000007        NIX=24
000010        NIY=24
000011        XINC=20.8/24
000013        YINC=XINC
000014        NNX=NIX+1
000016        NNY=NIY+1
000017        XO=20.0
000021        YO=5.0
        C
        C      START PLOT
000023        CALL START(2)
        C
        C
        C      SET SCALE IN INCHES, NOT CENTIMETRES
000024        FACT = 1.0 / 2.5399978
000026        CALL FACTOR(FACT)
        C
        C      READ IN COORDINATE DATA OF NODES
000027        CALL READXY
        C
        C      PLOT ARRAY OF NODES
000030        CALL GPLOT
        C
        C      CALCULATE FINITE STRAINS
000031        CALL FINSTR
        C
        C      END PLOT
000032        CALL ENPLOT
        C
        C      CARRIAGE CONTROL
000033        WRITE (6,9999)
        C
000037   9999 FORMAT (1H1)
000037        STOP
000041        END

UNUSED COMPILER SPACE
031700
```

```
                 SUBROUTINE READXY
          C
          C       READS IN COORDINATE DATA, FROM PUNCHED CARDS
          C       EACH CARD CONTAINS NNF GROUPS OF X,Y COORDINATES,
          C       CORRESPONDING TO CONSECUTIVE NODES. EACH NODE
          C       HAS AN ADDRESS IX,IY, THE NUMBERING PROCEDING
          C       ALONG X-ROWS.
          C
000001           COMMON X,Y,NIX,NIY,XINC,YINC,NNF,NNT,NNX,NNY
000001           COMMON XO,YO
000001           DIMENSION X(25,25),Y(25,25)
000001           DIMENSION T(30)
          C
          C       SET INITIAL PARAMETERS
          C
000001           IX=0
000002           IY = 1
000003           NNT= NNX*NNY
000005           NFC= NNT/NNF
000010           NNR= NNT- (NNF*NFC)
000013       100 NNZ= NNF*2
          C
          C       READ IN ARRAYS X,Y
          C
000015           DO 104 N=1,NFC
000016           READ (5,1000)(T(J),J=1,NNZ)
000024           DO 103 M=1,NNF
000026           IX=IX+1
000027           MY= M*2
000030           MX= MY-1
000031           IF (IX - NNX) 102,102,101
000033       101 IX=1
000034           IY= IY+1
000042       102 X(IX,IY) = T(MX)
000043           Y(IX,IY) = T(MY)
000046       103 CONTINUE
000050       104 CONTINUE
000053           IF (NNR) 106,106,105
000054       105 NFC=1
000055           NNF= NNR
000056           NNR= 0
000057           GO TO 100
          C
          C       WRITE OUT ARRAYS X,Y
          C
000060       106 WRITE (6,1001)
000064           WRITE (6,1002) ((X(I,J),I=1,NNX),J=1,NNY)
000102           WRITE (6,1003)
000106           WRITE (6,1002) ((Y(I,J),I=1,NNX),J=1,NNY)
          C
000124      1000 FORMAT(20F4.2)
000124      1001 FORMAT(16H0 ARRAY X(NNX,NNY))
000124      1002 FORMAT(1X,18F7.2)
000124      1003 FORMAT(16H0 ARRAY Y(NNX,NNY))
          C
000124           RETURN
000125           END
```

```
                  SUBROUTINE GPLOT
           C
           C       PRODUCES A PLOT, IN WHICH EACH NODE IS
           C       JOINED TO ITS NEIGHBOURS BY STRAIGHT LINES
           C
000001            COMMON X,Y,NIX,NIY,XINC,YINC,NNF,NNT,NNX,NNY
000001            COMMON X0,Y0
000001            DIMENSION X(25,25),Y(25,25)
000001            DIMENSION XR(30),YR(30),XC(30),YC(30)
           C
           C       LINK THE NODES IN EACH ROW
           C
000001            DO 101 IY=1,NNY,NIY
000003            DO 100 IX=1,NNX
000015            XR(IX) = X(IX,IY) - X0
000016            YR(IX) = Y(IX,IY) - Y0
000017        100 CONTINUE
000020            CALL ARKIST(XR,YR,1,NNX,50,1.0,1.0,0.0,0.0,2,1)
000033        101 CONTINUE
           C
           C       LINK THE NODES IN EACH COLUMN
           C
000036            DO 103 IX=1,NNX,NIX
000037            DO 102 IY=1,NNY
000050            XC(IY) = X(IX,IY) - X0
000051            YC(IY) = Y(IX,IY) - Y0
000053        102 CONTINUE
000054            CALL ARKIST(XC,YC,1,NNY,50,1.0,1.0,0.0,0.0,2,1)
000066        103 CONTINUE
           C
000071            RETURN
000071            END

UNUSED COMPILER SPACE
031600
```

```
                 SUBROUTINE FINSTR
            C
            C     CALCULATES FINITE STRAIN PARAMETERS OF EACH
            C     ELEMENT, GIVEN THE INITIAL AND FINAL
            C     COORDINATES OF THE NODES.
            C
000001           COMMON X,Y,NIX,NIY,XINC,YINC,NNF,NNT,NNX,NNY
000001           COMMON X0,Y0
000001           DIMENSION X(25,25),Y(25,25)
000001           DIMENSION E(2), ALPH(2)
000001           DIMENSION IW(3,2),F(3,4)
            C
000001           WRITE (6,1001)
000005           N4 = NIX*NIY / 4
000010           NN4= N4*4
            C
            C     SET SCALE FACTOR
000012           SKALE = 0.25
            C
            C
000014           DO 114 IY=1,NIY
000015           DO 113 IX=1,NIX
000025           IX1=IX+1
000026           IY1=IY+1
            C
            C     RETRIEVE FINAL COORDINATES OF NODES
            C
000026           X1 = X(IX,IY)
000027           X2 = X(IX,IY1)
000032           X3 = X(IX1,IY)
000034           X4 = X(IX1,IY1)
000040           Y1 = Y(IX,IY)
000042           Y2 = Y(IX,IY1)
000045           Y3 = Y(IX1,IY)
000046           Y4 = Y(IX1,IY1)
            C
            C     CALCULATE COORDINATES (XC,YC) OF CENTROID
            C
000051           XC = (X1 + X2 + X3 + X4) / 4.0
000055           YC = (Y1 + Y2 + Y3 + Y4) / 4.0
000061           XC0 = XC - X0
000063           YC0 = YC - Y0
            C
            C     CALCULATE ELEMENTS OF DISPLACEMENT GRADIENT MATRIX
            C
000065           A = 0.5 * (X3-X1 + X4 - X2)/ XINC
000073           B = 0.5 * (X2 - X1 + X4 - X3) / YINC
000077           C = 0.5 *(Y3 - Y1 + Y4 - Y2) / XINC
000104           D = 0.5 * ( Y2 - Y1 + Y4 - Y3) / YINC
            C
            C     CALCULATE INVARIANTS
            C
000111           AUX1 = (A * C) + (B * D)
000114           AUX2 = (A**2) + (B**2) - (C**2) - (D**2)
000120           AUX3 = ABS(A*D - B*C)
            C
            C     CALCULATE PRINCIPAL ORIENTATION
            C     CHECK FOR ZERO DIVISOR
```

```
              C
000126              IF (AUX1) 101,100,101
000127          100 ALPH(1) = 0.0
000130              GO TO 104
000131          101 IF (AUX2) 103,102,103
000132          102 ALPH(1) = -0.7854
000134              GO TO 104
000134          103 TEMP = 2.0 * (AUX1 / AUX2)
000136              ALPH(1) = 0.5 * ATAN(TEMP)
000142          104 ALPH(2) = ALPH(1) + 1.5708
              C
              C      CALCULATE PRINCIPAL EXTENSIONS
              C
000144              DO 105 I=1,2
000146              SA = SIN(ALPH(I))
000150              CA = COS(ALPH(I))
000154              TEMP1 = (D * CA) - (B * SA)
000157              TEMP2 = (A * SA) - (C * CA)
000162              BOT = SQRT(TEMP1**2 + TEMP2**2)
000166              E(I) = AUX3 / BOT
000171          105 CONTINUE
              C
000173              IF (E(1) - E(2)) 106,107,107
000175          106 EXT1 = E(2)
000176              EXT2 = E(1)
000200              RATIO=EXT1/EXT2
000201              ALPHA = ALPH(2)
000202              GO TO 108
000203          107 EXT1 = E(1)
000204              EXT2 = E(2)
000206              RATIO=EXT1/EXT2
000207              ALPHA = ALPH(1)
000210              IF (RATIO .LT. 1.2 .AND. RATIO .GT. 0.9) GO TO 108
              C
              C      PLOT THE LONG AND SHORT AXES
              C      OF THE FINITE STRAIN ELLIPSOID
              C
000221              DO 200 I=1,2
000222              EMOD = E(I) * SKALE
000224              XADD=EMOD*COS(ALPH(I))
000227              YADD=EMOD*SIN(ALPH(I))
000234              XP = XCO + XADD
000235              YP = YCO + YADD
000240              CALL PLOT(XP,YP,3)
000242              XP = XCO - XADD
000244              YP = YCO - YADD
000246              CALL PLOT(XP,YP,2)
000251          200 CONTINUE
              C
              C      CONVERT PRINCIPAL ORIENTATION TO DEGREES
              C
000253          108 ALPHA = (ALPHA / 3.1416) * 180.0
              C
              C      CALCULATE VOLUME CHANGE
              C
              C      DELTA = AUX3 - 1.0
              C
              C      WRITE OUT PARAMETERS
```

```
          C
000256       109 L = (IY - 1) * NIX + IX
000262           IF (L - NN4) 110,111,112
000265       110 L4 = L / 4
000266           LR = L - (L4*4)
000270           IF (LR .EQ. 0) GO TO 111
000273           IW(LR,1) = IX
000274           IW(LR,2) = IY
000275           F(LR,1) = EXT1
000277           F(LR,2) = EXT2
000300           F(LR,3) = RATIO
000302           F(LR,4) = ALPHA
000304           GO TO 113
000304       111 WRITE (6,1002) IW(1,1),IW(1,2),F(1,1),F(1,2),F(1,3),F(1,4)
                1 IW(2,1),IW(2,2),F(2,1),F(2,2),F(2,3),F(2,4),
                2 IW(3,1),IW(3,2),F(3,1),F(3,2),F(3,3),F(3,4),
                3 IX,IY,EXT1,EXT2,RATIO,ALPHA
000370           GO TO 113
000371       112 WRITE (6,1003) IX,IY,EXT1,EXT2,RATIO,ALPHA
000411       113 CONTINUE
000414       114 CONTINUE
000416      1001 FORMAT(26H0 FINITE STRAIN PARAMETERS// 1X,
                1 4(8H ELEMENT,6H  EXT1,6H  EXT2,6H RATIO,6H ALPHA))
000416      1002 FORMAT (1X,4(1X,I3,1H-,I3,3F6.2,F6.1))
000416      1003 FORMAT (2X,I3,1H-,I3,3F6.2,F6.1)
000416           RETURN
000417           END

UNUSED COMPILER SPACE
030100
```

REFERENCES

BADOUX, H. 1963 "Les bélemnites tronçonées de Leytron (Valais)", Bull. Lab. Geol., Mineral, Geophys. Musée Geol. Univ. Lausanne, 138; 1-7.

BADOUX, H., BONNARD, E. G., BURRI, M. & VISCHER, A., 1959, Atlas géologique de la suisse, 1:25.000, St. Léonard, Sheet 35.

BADOUX, H. & LOMBARD, A. 1962. Notice Explicative, Lenk Sheet, Atlas geologique de la Suisse.

BAILY, E. B. 1923. The metamorphism of the South West Highlands. Geol. Mag., 60; 317-331.

BAIN, G. W. 1933. Wall-rock mineralization along Ontario gold deposits, Econ. Geol., 28; 705-743.

BARTOK, W. & MASON, S. G. 1958. Particle motions in sheared suspensions, VII. Internal circulation in fluid droplets (Theoretical)., J. Colloid. Sci., 13; 293-307.

BECKE, F. 1924. "Struktur und Klüftung", Fort. Miner. Krist. Petrogr., 9; 185-196.

BECKER, G. F. 1904. Experiments on schistosity and slaty cleavage. Bull. U.S. geol. Surv., No. 241, 34.

BEECH, S. H. 1969. Buckling of single and multi-layer oblique to the principal compressive stress and its bearing on the problem of asymmetrical fold formation. Unpublished M.Sc. dissertation, Univ. London.

BIOT, M. A., ODE, H. & ROEVER, W. L. 1961. Experimental verification of the folding of stratified viscoelastic media., Geol. Soc. Am. Bull., 72; 1621-1632.

BRACE, W. F. 1960. Analysis of large two-dimensional strain in deformed rocks., 21st Int.Geol.Congr. Copenhagen, 18,261-269.

BUCHER, W. H. 1956. Role of gravity in orogenesis. Bull. Geol. Soc. Am., 67; 1295-1318.

CADELL, H. M. 1888. Experimental researches in mountain building. Trans. Roy. Soc. Edinburgh, 35; 337-357.

CHADWICK, B. 1965. The structural and metamorphic geology of the Lukmanier region, Ticino-Grisons, Switzerland. Unpublished Ph.D. thesis, Univ. London.

CLOOS, E. 1955. Experimental analysis of fracture patterns., Bull. geol. Soc. Am., 66; 241-256.

COBBOLD, P. R. 1973. Initiation and development of folds in rocks. Unpublished Ph.D. thesis, Univ. London.

COBBOLD, P. R., COSGROVE, J. W. & SUMMERS, J. M. 1971. Development of internal structures in deformed anisotropic rocks. Tectonophysics, 12; 23-53.

COLLETTE, B. J. 1959. On helicitic structures and the occurance of elongate crystals in the direction of the axis of a fold. Proc. K. Ned. Åkad. Wet., Ser.B, 62(3); 161-171.

COUTINHO, A. 1949. Theory of an experimental method for determining stresses not requiring an accurate knowledge of the elasticity modulus, Third Congr. Int.Ass.Bridge struct. Engng. Liege.

COX, F. C. 1969. Inclusions in garnet: discussion and suggested mechanism of growth for syntectonic garnets. Geol.Mag., 106; 57-62.

CURRIE, J. B. 1966. Experimental structural geology, Earth Sciences reviews, 1; 51-67.

DAUBRÉE, M. 1876. "Expériences sur la schistosité des roches et sur les deformations des fossils, etc.; BSGF 3^{e} ser. t. IV.

DONATH, F. A. 1968. Experimental study of Kink-band development in Martinsburg slate. In: A. J. Baer and D. K. Norris (Editors), Proc.Conf.Res.Tectonics.Geol.Surv.Can. Paper, 68; 52; 255-292.

DURELLI, A. J., PARKS, V. J. & FENG, H. 1967. Evaluation of grid data to determine displacements and strains., J. Strain Analysis, 2(3), 181-187.

DURNEY, D. W. 1968. Some experiments on putty and plasticine., Unpublished M.Sc. dissertation, Univ. London.

DURNEY, D. W. 1972. Deformation history of the Western Helvetic Nappes, Valais, Switzerland. Unpublished Ph.D. thesis, Univ. London.

EINSTEIN, A. 1896. "Ein neue Bestimmung der Molekudimensioneu". Ann. d. Physik, 19; 289-306. with a correction in Vol.34 p.591 (1911).

ESHELBY, J. D. 1957. The determination of the elastic field of an ellipsoidal inclusion, and related problems., Proc. Roy. Soc. London, A 241; 376-396.

FAIRBAIRN, H. W. 1950. Pressure shadows and relative movement in shear zone. Trans.Am.Geophys. Union, 31; 914-916.

FAVRE, M. A. 1878. Bibliotheque Universelle. Arch. Sc. (Geneva), 246 pp.

FLETT, J. G. 1912. Geology of Ben Wyvis, Carn Chuinneag, etc., Mem. geol. Surv. Scotland, 93; p.111.

FRANKEL, J. J. 1957. Abraded pyrite crystals from the Witwatersrand gold mines, Mineralog. Mag., 31; 392-401.

GAY, N. C. 1966. The deformation of inhomogeneous materials and consequent geological implication., Unpublished Ph.D. thesis, Univ. London.

GAY, N. C. 1968. **The motion of the rigid particles embedded in a viscous fluid during pure shear deformation of the fluid. Tectonophysics, 5(2); 81-88.**

GOODIER, J. N. 1933. Concentration of stress around spherical inclusions and flows.; Trans. Am. Soc. Mech. Engrs., 55; 39-44.

GOSH, S. K. 1968. Experiments of buckling of multilayers which permit interlayer gliding; Tectonophysics, 6(3), 207-249.

GRESENS, R. L. 1966. The effect of structurally produced gradients on diffusion in rocks.; J.Geol., 74; 307-321.

HAFNER, W. 1951. Stress distributions and faulting; Bull.Geol.Soc. Am., 62; 373-398.

HALL, J. 1815. On the vertical position and convolutions of certain strata and their relation with granite. Trans. Roy. Soc. Edinburgh, 7; 79-108.

HARKER, A. 1939. Metamorphism. Methuen, London. 362 p.

HARKER, A. 1889. Geol. Mag. New ser. decade - 3, 6; 396. Mentioned by Frankel, 1957.

HEIM, A. 1919."Undersuchungen über den Mechanismus der Gebirgsbeldung". Geologie der Schweiz. Tauchwitz, Leipzig.

HOSSAIN, K. M. 1970. Experimental work on boudinage structure.; Unpublished M.Sc. thesis, Univ. London.

HOWKINS, J. B. 1961. Helicitic textures in garnets from Moine rocks of Moidart.; Trans. geol. Soc. Edinb., 18(3); 315-324.

HUBBERT, M. K. 1937. Theory of scale models as applied to the study of geologic structures., Bull. Geol. Soc. Am., 48; 1459-1520.

HUBBERT, M. K. 1951. Mechanical basis for certain familiar geologic structure. Bull. Geol. Soc. Am., 62; 355-372.

JAEGER, J. C. & COOK, N. G. W. 1969. Fundamentals of Rock Mechanics. Chapman and Hall, 515 pp.

JEFFERY, G. B. 1922. The motion of ellipsoidal particles immersed in a viscous fluid. Proc. Roy. Soc., A, 102; 161-179.

JOHNSON, M. R. W. 1963. Some time-relations of movement and metamorphism in the Scottish Highlands., Geologic Mijnb., 42; 121-142.

JOPLIN, G. A. 1968. A petrography of Australian Metamorphic rocks.; Angus & Robertson, Sydney.

KNOPF, A. 1929. The mother Lode system of California., U.S. Geol. Surv. prof. Paper, 157; 41-42.

KREIG, L. 1918. "Petrographische Untersunchungen Val Piora Und Umbegung. Ecolgae Geol. Helv., 14; 519-654.

LAMB, H. 1932. Hydrodynamics. 6th ed., Cambridge University Press, 738 pp.

LUGEON, M., ARGAND, E., OULIANOFF, N., REINHARD, M., & POLDINI, E. 1937. Atlas géologique de la Suisse, 1:25.000, Saxon-Morcles, sheet 16.

LUGEON, M. 1940. Atlas géologique de la Suisse, 1:25.000, Diablerets, sheet 19, and Notice Explicative.

MILES, K. R. 1945. Metamorphism of the Jesper bars of W. Australia., Q.J. Geol. Soc. London, 52; 115-

MORONEY, M. J. 1951. Facts from figures. Penguin books Ltd. 472 pp.

MOSS, F. A. 1927. The Geology of Carson Hill. Eng. and Mining J., 124; 1010-1012.

MUGGE, O. 1930. "Bewegungen von porphyroblasten in phylliten und ihre Messung". Neus Jahrb. Miner. Beibl., 61A; 469-510.

MUSKHELISHVILI, N. I. 1953. Some basic problems of the mathematical theory of elasticity. P. Noordhoff Ltd., Groningen, Holland, 704 pp.

NADAI, A. 1950. Theory of flow and fracture of solids, Vol.1, 2nd ed.; McGraw-Hill Book Company, Inc., New York, Toronto, London, 572 pp.

NIGGLI, P. 1912. "Die chloritoid schiefer und die sedimentäre zone am Nordostrand des Gotthard massives". Beotr. geol. Karte. Schweiz., 36.

PABST, A. 1931. Pressure shadows and the measurement of the orientation of minerals in rocks., Am. Mineral., 16; 55-70.

PAULKE, W. 1912. "Das Experiment in der Geologie.", Borntraeger, Berlin, 108 pp.

PEACEY, J. S. 1961. Rolled garnets from Morar, Inverness-shire. Geol. Mag., 98; 77-80.

POWELL, D. 1966. On preferred crystallographic orientation of garnet in some metamorphic rocks, Mineralog. Mag., 35, 1094-1109.

POWELL, D & TREAGUS, J. E. 1967. On the geometry of S-shaped inclusion trails in garnet porphyroblasts. Mineralog. Mag., 36(279), 453-456.

POWELL D. & TREAGUS, J. E. 1970. Rotational fabrics in metamorphic minerals. Mineralog. Mag., 37; 801-814.

RAMBERG, H. 1952. The origin of Metamorphic and Metasomatic Rocks. Univ. of Chicago Press, Chicago, Ill., 317 pp.

RAMBERG, J. G. 1955. Natural and experimental boudinage and Pinch-and-swell structures. J. Geol., 63; 512-526.

RAMBERG, H. 1959. Evolution of Ptygmatic folding., Norsk. Geol. Tidsskr., 39; 99-151.

RAMBERG, H. 1961. A study of veins in caledonian rocks around Trondheim Fjord, Norway, Nor. Geol. Tidsskr., 41; 1-44.

RAMSAY, J. G. 1962. The geometry and mechanics of formation of 'similar' type of folds. J. Geol., 70; 309-327.

RAMSAY, J. G. 1967. Folding and Fracturing of Rocks. McGraw-Hill. New York, 568 pp.

RAMSCHEIDT, F. D. & MASON, S. G. 1961. Particle motions in sheared suspensions, XI. Internal circulation in fluid droplets (experimental)., J. Colloid. Sci., 16; 210-237.

RAST, N. 1958. Metamorphic history of the Schichallion complex. Trans. Roy. Soc. Edinburgh, 63; 413-432.

SANFORD, A. R. 1959. Analytical and experimental study of simple geologic structure. Bull.Geol.Soc.Am., 70; 19-52.

SAVIN, G. N. 1961. Stress concentration around holes. Pergamon Press, Oxford, London, New York, Paris, 430 pp.

SCHMIDT, W. 1918. "Bewegungsspuren in porphyroblasten Kristalliner Schiefer," Sver. Akad. Wiss. Wien, 1, 127.

SEZAWA, K. 1933. The effect of local heterogeneity on the stress distribution in solid. Engineering, 135; 695-696.

SPRY, A. 1963. The origin and signigicance of snowball structure in garnet. J. Petrol., 4; 211-222.

SPRY, A. 1969. Metamorphic textures. Pergamon Press, Oxford, 350 pp.

STRÖMGÅRD, K. E. 1972. Stress distribution during formation of boudinage and pressure shadows. Tectonophysics, 16; 215-248.

TAYLOR, G. I. 1932. The viscosity of a fluid containing small drops of another fluid. Proc. Roy. Soc., A. 138; 41-48.

TAYLOR, G. I. 1934. The formation of emulsions in definable fields of flow. Proc. Roy. Soc. A., 146; 501-523.

TREVELYAN, B. J. & MASON, S. G. 1951. Particle motions in sheared suspensions, I. Rotations. J. Colloid. Sci., 6: 345-367.

TURNER, F. J. 1948. Mineralogical and structural evolution of the metamorphic rocks., Mem. geol. Soc. Am., 30.

WILSON, A. H. 1961. A laboratory investigation of a high modulus borehole plug gage for the measurement of rock stress. Proc. Fourth Symp. Rock Mech., Penn. State Univ., 185-195.

WILSON, M. R. 1971. On syntectonic porphyroblast growth., Tectonophysics, 11, 239-260.

ZWART, H. J. 1960. Relation between folding and metamorphism in the Central Pyrenees and their chronological succession. Geol. en Mijnbouw, 22; 163-180.

ZWART, H. J. 1962. On the determination of polymetamorphic mineral associations and its application to the Bossost Area (Central Pyrenees). Geol. Rundschau, 52; 38-65.

LIST OF PLATES

irrotational strain deformation.
(a) Undeformed; (b) $\sqrt{\lambda_1/\lambda_2} = 1.61$; (c) $\sqrt{\lambda_1/\lambda_2} = 2.08$;
(d) $\sqrt{\lambda_1/\lambda_2} = 2.6$

Plate VII Successive stages of an experiment showing the behaviour of the matrix and an elliptical inclusion (a/b = 2:1) oriented initially at $\theta_{ie} = 90^{\circ}$ during progressive irrotational strain deformation.
(a) Undeformed; (b) $\sqrt{\lambda_1/\lambda_2} = 1.61$; (c) $\sqrt{\lambda_1/\lambda_2} = 2.08$;
(d) $\sqrt{\lambda_1/\lambda_2} = 2.6$

Plate VIII Successive stages of an experiment showing the behaviour of the matrix and an inclusion (a/b = 3:1) oriented initially at $\theta_{ie} = 0$ (i.e. parallel to the principal extension direction) during progressive irrotational strain deformation.
(a) Undeformed; (b) $\sqrt{\lambda_1/\lambda_2} = 1.61$; (c) $\sqrt{\lambda_1/\lambda_2} = 2.08$;
(d) $\sqrt{\lambda_1/\lambda_2} = 2.6$

Plate IX Successive stages of an experiment showing the behaviour of the matrix and an inclusion (a/b = 4:1) oriented initially at $\theta_{ie} = 30^{\circ}$ during progressive irrotational strain deformation.
(a) Undeformed; (b) $\sqrt{\lambda_1/\lambda_2} = 1.61$; (c) $\sqrt{\lambda_1/\lambda_2} = 2.08$;
(d) $\sqrt{\lambda_1/\lambda_2} = 2.6$

Plate X Successive stages of an experiment showing the behaviour of the matrix and an inclusion (a/b = 4:1) oriented initially at $\theta_{ie} = 90^{\circ}$ during progressive irrotational strain deformation.
(a) Undeformed; (b) $\sqrt{\lambda_1/\lambda_2} = 1.61$; (c) $\sqrt{\lambda_1/\lambda_2} = 2.08$
(d) $\sqrt{\lambda_1/\lambda_2} = 1.6$

Plate XI Successive stages of an experiment showing the behaviour of the matrix and a rigid equidimensional inclusion deformed inside simple shear box.
(a) Undeformed; (b) $\gamma_s = 0.577$; (c) $\gamma_s = 0.876$; (d) $\gamma_s = 1.4$

Plate XII Successive stages of an experiment showing the behaviour of the matrix around a rigid equidimensional object during simple shear deformation.
(a) Undeformed; (b) $\gamma_s = 0.577$; (c) $\gamma_s = 0.876$; (d) $\gamma_s = 1.4$

Plate XIII Rigid rotation of an elliptical inclusion (a/b = 2:1) oriented initially at $\theta_{is} = 126^{\circ}$ (measured with reference to the shearing direction) and the behaviour of the matrix during simple shear deformation.
(a) Undeformed; (b) $\gamma_s = 0.577$; (c) $\gamma_s = 0.876$; (d) $\gamma_s = 1.4$

Plate XIV The behaviour of the matrix and an inclusion (a/b = 2:1) oriented at $\theta_{is} = 60^{\circ}$ deformed inside the simple shear box.
(a) Undeformed; (b) $\gamma_s = 0.577$; (c) $\gamma_s = 0.876$; (d) $\gamma_s = 1.4$

Plate XV The behaviour of the matrix and an inclusion (a/b = 3:1) oriented initially at $\theta_{is} = 121^{\circ}$ deformed inside the simple shear box.
(a) Undeformed; (b) $\gamma_s = 0.577$; (c) $\gamma_s = 0.876$; (d) $\gamma_s = 1.4$

Plate XVI Behaviour of the matrix and an inclusion (a/b = 3:1) oriented initially at $\theta_{is} = 57^{\circ}$ during simple shear deformation.
(a) Undeformed; (b) $\gamma_s = 0.577$; (c) $\gamma_s = 0.876$, (d) $\gamma_s = 1.4$

Plate XVII Behaviour of the matrix and an inclusion (a/b = 4:1) oriented at $\theta_{is} = 126^{\circ}$ after deformation inside the simple shear box.
(a) Undeformed; (b) $\gamma_s = 0.577$; (c) $\gamma_s = 0.876$; (d) $\gamma_s = 1.4$

Plate XVIII Behaviour of the matrix and an inclusion (a/b = 4:1) oriented initially at $\theta_{is} = 57^{\circ}$ after deformation inside the simple shear box.
(a) Undeformed; (b) $\gamma_s = 0.577$; (c) $\gamma_s = 0.876$; (d) $\gamma_s = 1.4$

Plate XIX Experimental simulation of the development of pressure fringe regions around a rigid circular inclusion undergoing simple shear deformation.

Plate XX Another example of the formation of 'open spaces' simulating pressure fringe regions around a circular inclusion during simple shear deformation.

Plate XXI Experimental simulation of the progressive development of pressure fringe regions around a rectangular inclusion during irrotational strain deformation.

Plate XXII Successive stages of an experiment simulating a stretched belemnite oriented initially parallel to the principal extension direction during progressive irrotational strain deformation.
(a) Undeformed; (b) $\sqrt{\lambda_1/\lambda_2} = 1.61$; (c) $\sqrt{\lambda_1/\lambda_2} = 2.08$; (d) $\sqrt{\lambda_1/\lambda_2} = 2.6$

Plate XXIII Successive stages of an experiment simulating a stretched belemnite oriented initially at $\theta_b = 31^{\circ}$ during progressive irrotational strain deformation.
(a) Undeformed; (b) $\sqrt{\lambda_1/\lambda_2} = 1.61$; (c) $\sqrt{\lambda_1/\lambda_2} = 2.08$; (d) $\sqrt{\lambda_1/\lambda_2} = 2.6$

Plate XXIV Successive stages of an experiment simulating a stretched belemnite oriented initially at $\theta_b = 48.5^{\circ}$ during irrotational strain deformation.
(a) Undeformed; (b) $\sqrt{\lambda_1/\lambda_2} = 1.61$; (c) $\sqrt{\lambda_1/\lambda_2} = 2.08$; (d) $\sqrt{\lambda_1/\lambda_2} = 2.6$

Plate XXV Successive stages of an experiment simulating a stretched belemnite oriented initially at $\theta_b = 58^{\circ}$ during irrotational strain deformation.
(a) Undeformed; (b) $\sqrt{\lambda_1/\lambda_2} = 1.61$; (c) $\sqrt{\lambda_1/\lambda_2} = 2.08$; (d) $\sqrt{\lambda_1/\lambda_2} = 2.6$

Plate XXVI Successive stages of an experiment simulating a stretched belemnite oriented initially at $\theta_b = 74^{\circ}$ during irrotational strain deformation.
(a) Undeformed; (b) $\sqrt{\lambda_1/\lambda_2} = 1.61$; (c) $\sqrt{\lambda_1/\lambda_2} = 2.08$; (d) $\sqrt{\lambda_1/\lambda_2} = 2.6$

Plate XXVII An experiment simulating a stretched belemnite oriented initially at $\theta_b = 0^o$ (measured with reference to the shearing direction) undergoing simple shear deformation.
(a) Undeformed; (b) $\gamma_s = 0.577$; (c) $\gamma_s = 0.876$; (d) $\gamma_s = 1.4$

Plate XXVIII An experiment simulating a stretched belemnite having $\theta_b = 31.5^o$ during progressive simple shear deformation.
(a) Undeformed; (b) $\gamma_s = 0.577$; (c) $\gamma_s = 0.876$; (d) $\gamma_s = 1.4$

Plate XXIX An experiment simulating a stretched belemnite having $\theta_b = 57^o$ during progressive simple shear deformation.
(a) Undeformed; (b) $\gamma_s = 0.577$; (c) $\gamma_s = 0.876$; (d) $\gamma_s = 1.4$

Plate XXX An experiment simulating a stretched belemnite having $\theta_b = 89^o$ during progressive simple shear deformation.
(a) Undeformed; (b) $\gamma_s = 0.577$; (c) $\gamma_s = 0.876$; (d) $\gamma_s = 1.4$

Plate XXXI An experiment simulating a stretched belemnite having $\theta_b = 119^o$ during progressive simple shear deformation.
(a) Undeformed; (b) $\gamma_s \pm 0.577$; (c) $\gamma_s = 0,876$; (d) $\gamma_s = 1.4$

Plate XXXII An experiment simulating a stretched belemnite having fragments of dissimilar axial ratio (a/b) and $\theta_b = 90^o$ deformed during progressive simple shear.

Plate I.

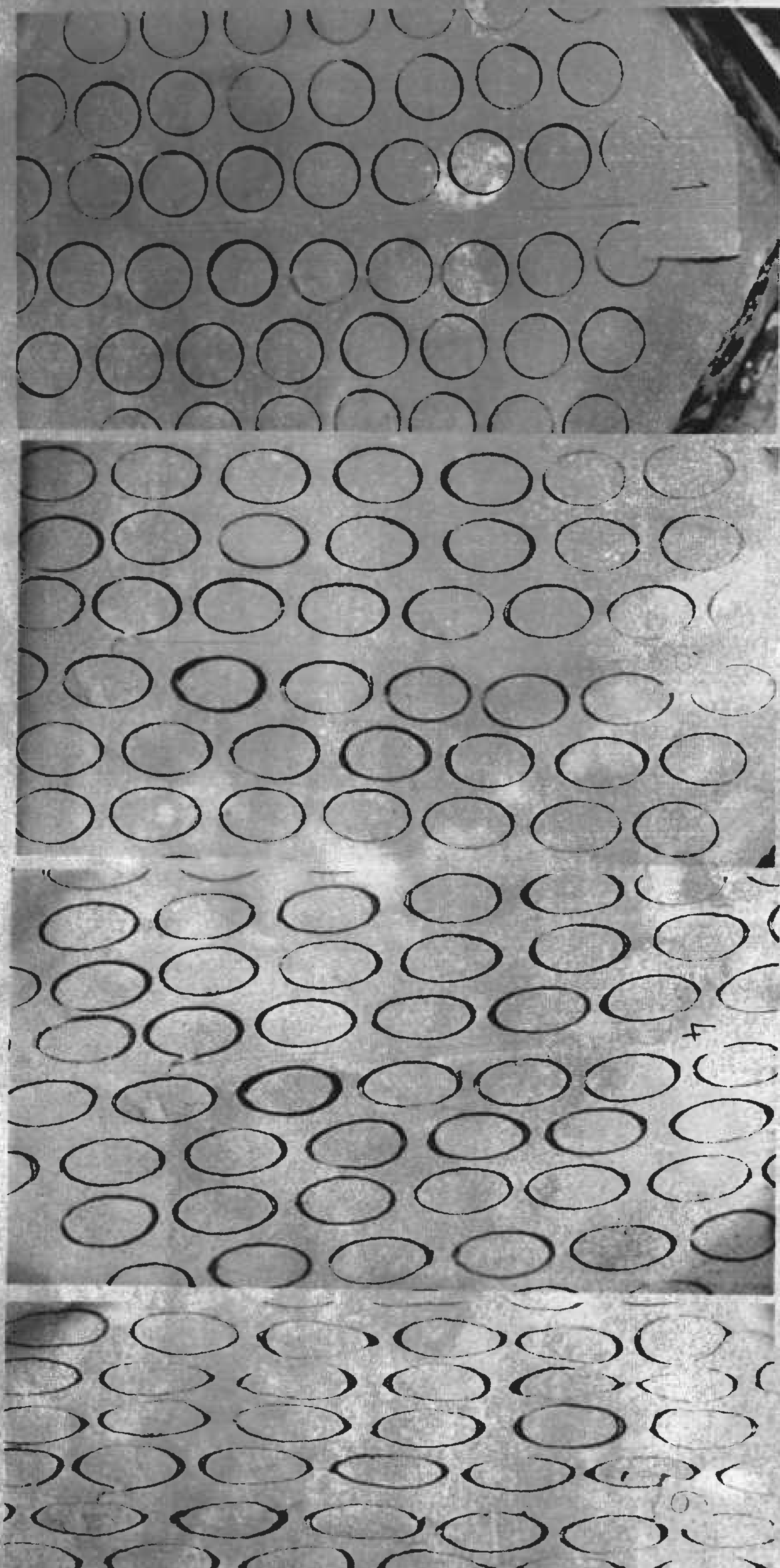

(a)

(b)

(c)

(d)

Plate II.

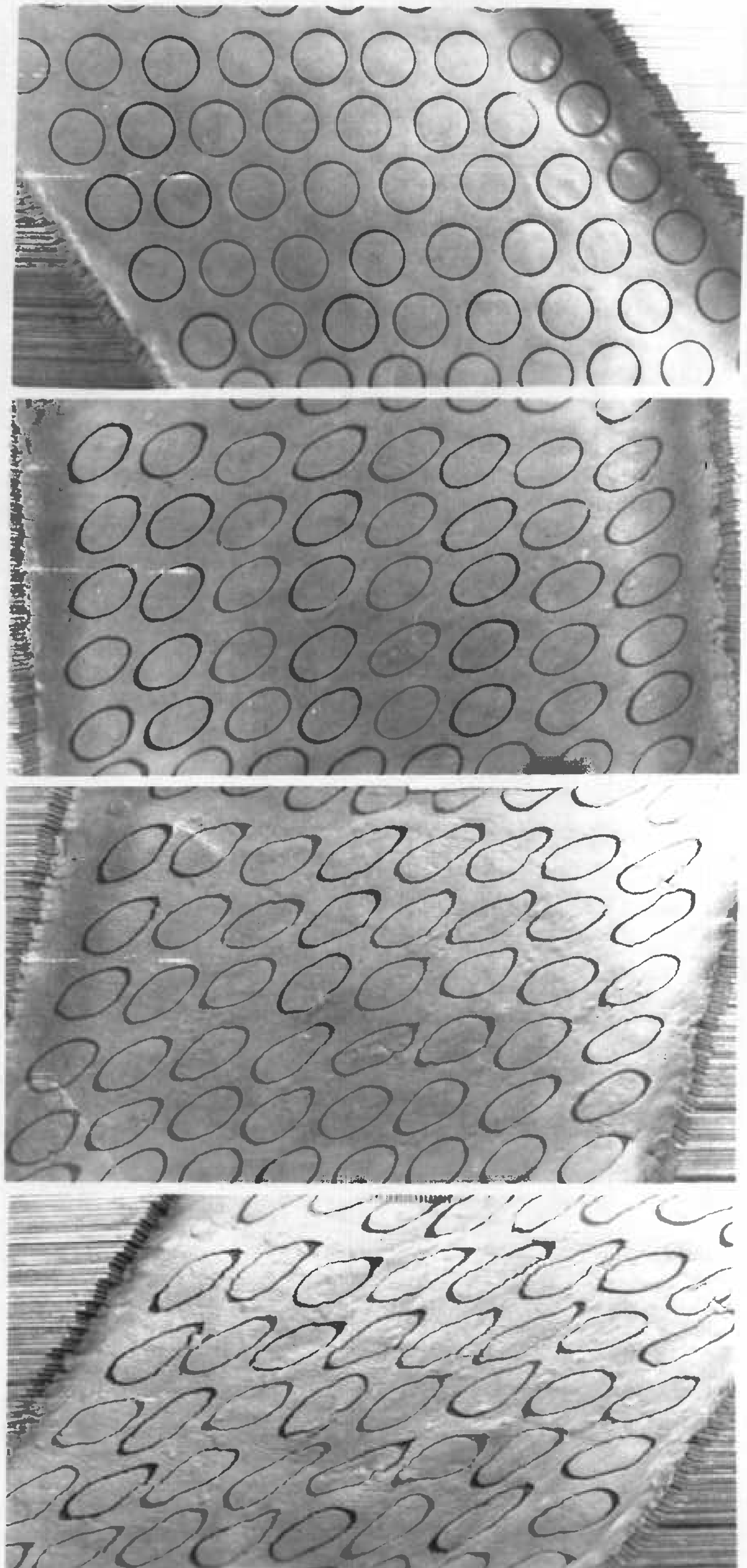

(a)

(b)

(c)

(d)

Plate III.

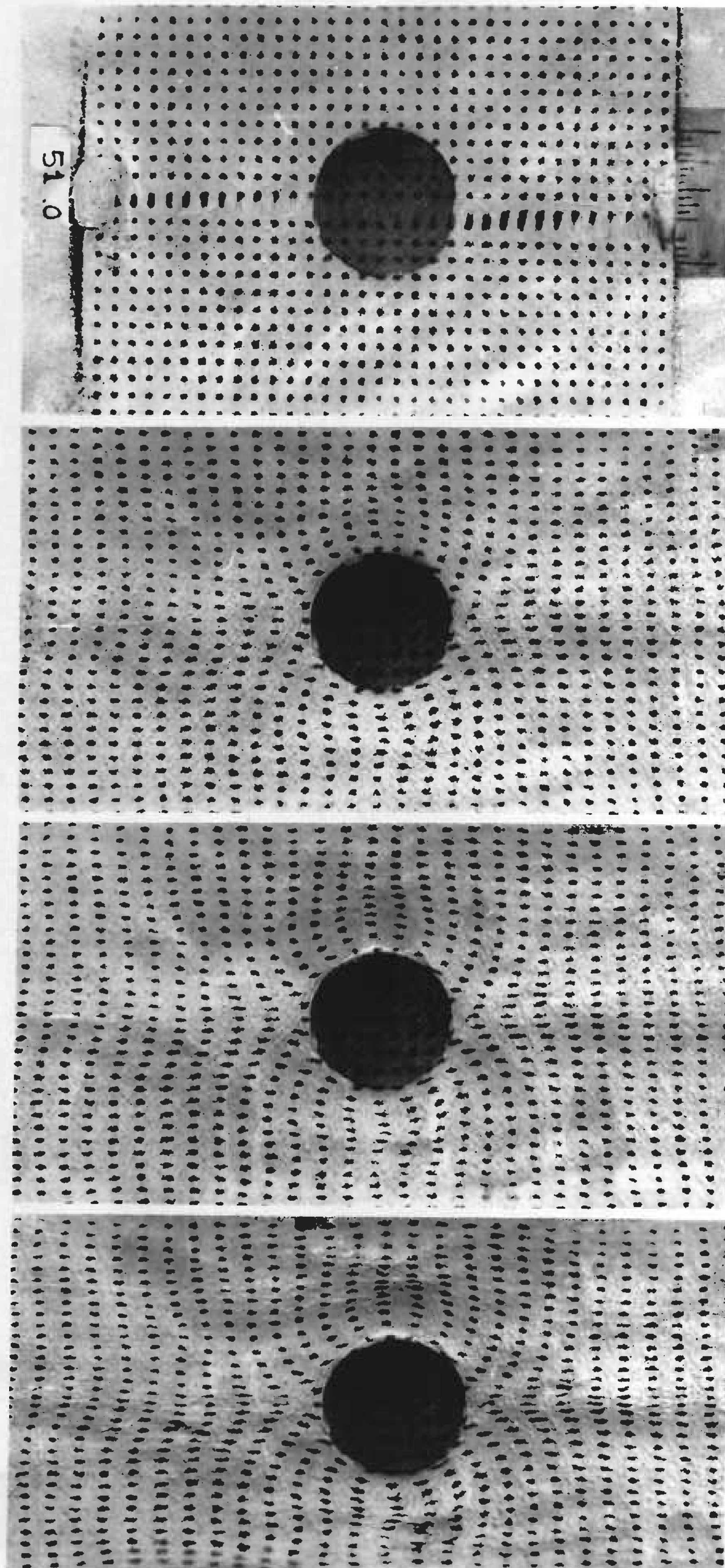

(a)

(b)

(c)

(d)

Plate IV.

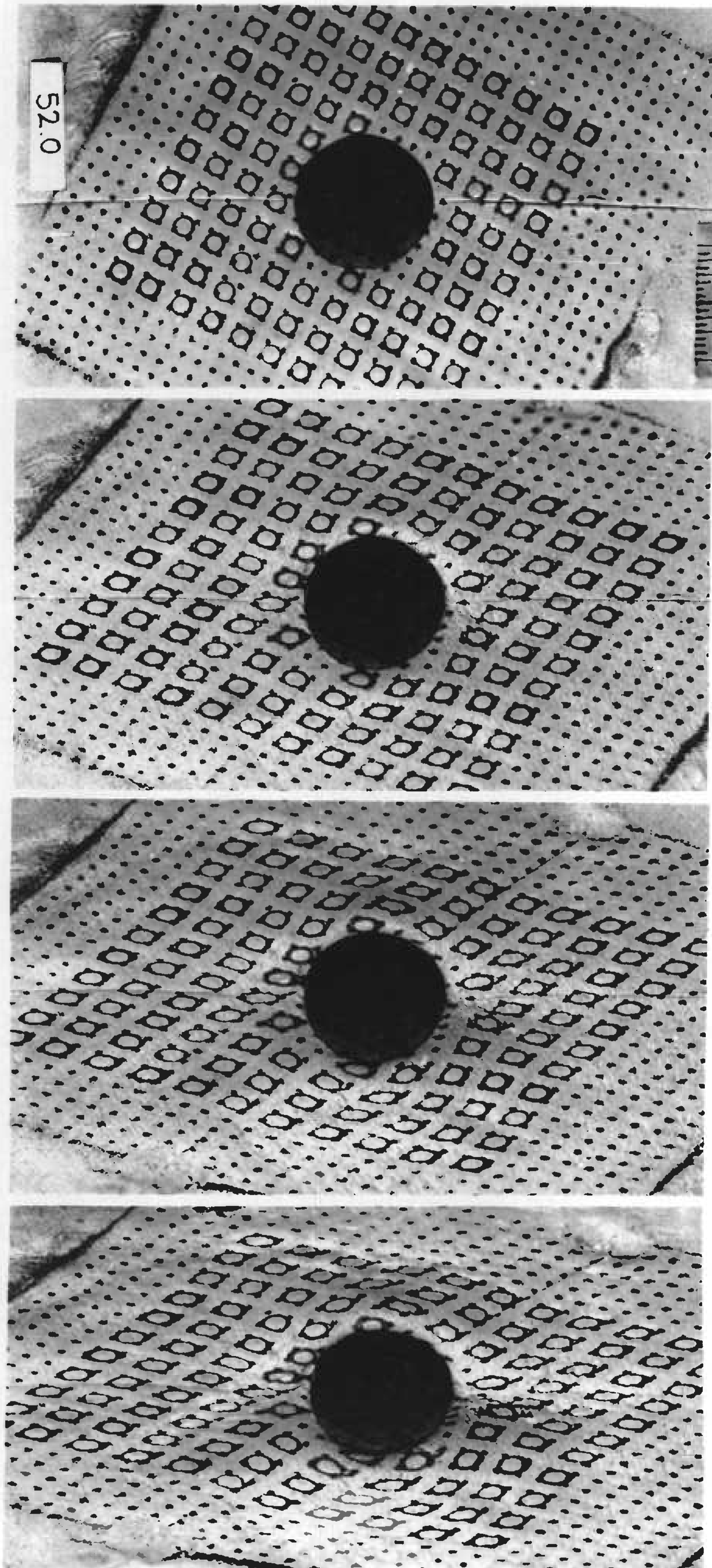

(a)

(b)

(c)

(d)

Plate V.

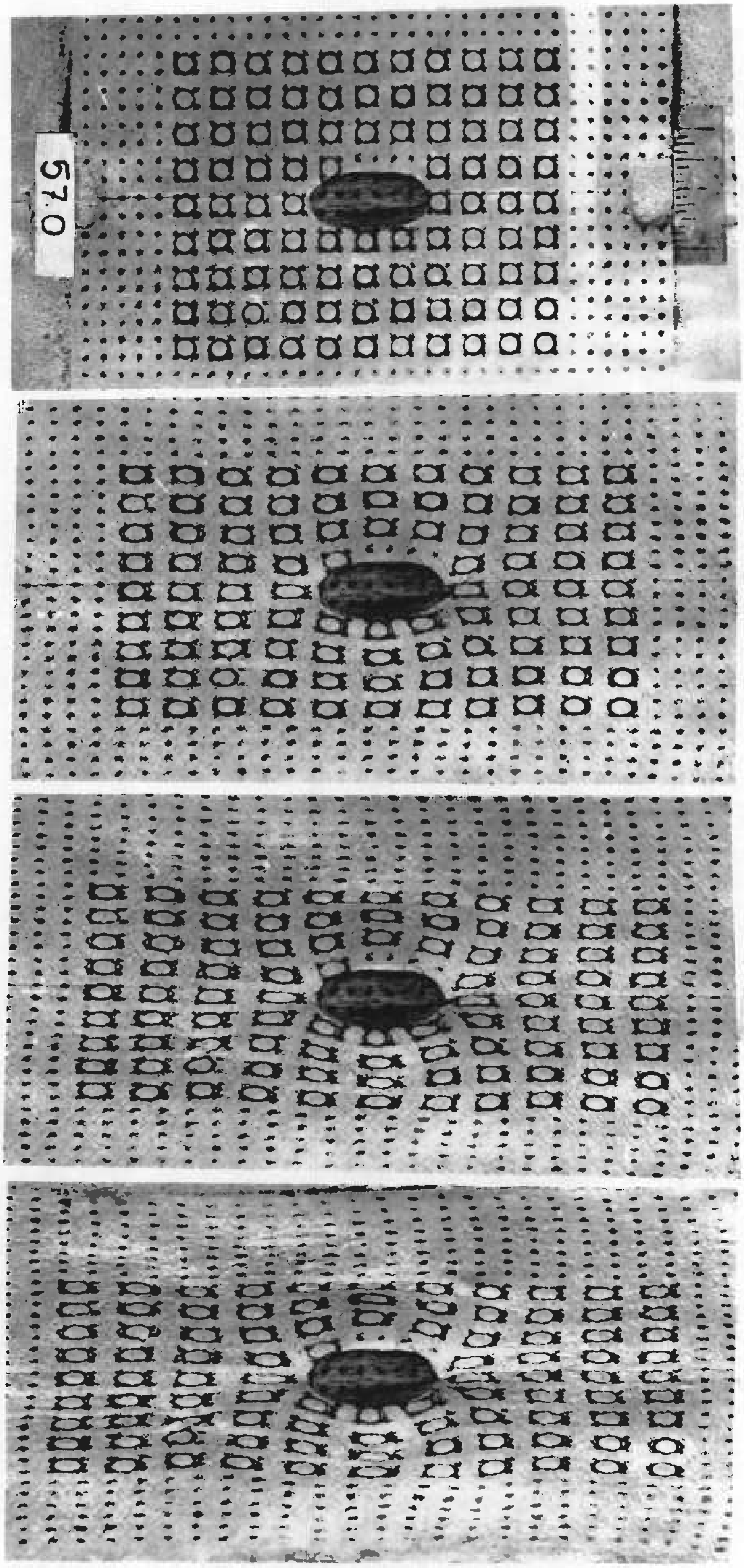

(a)

(b)

(c)

(d)

Plate VI.

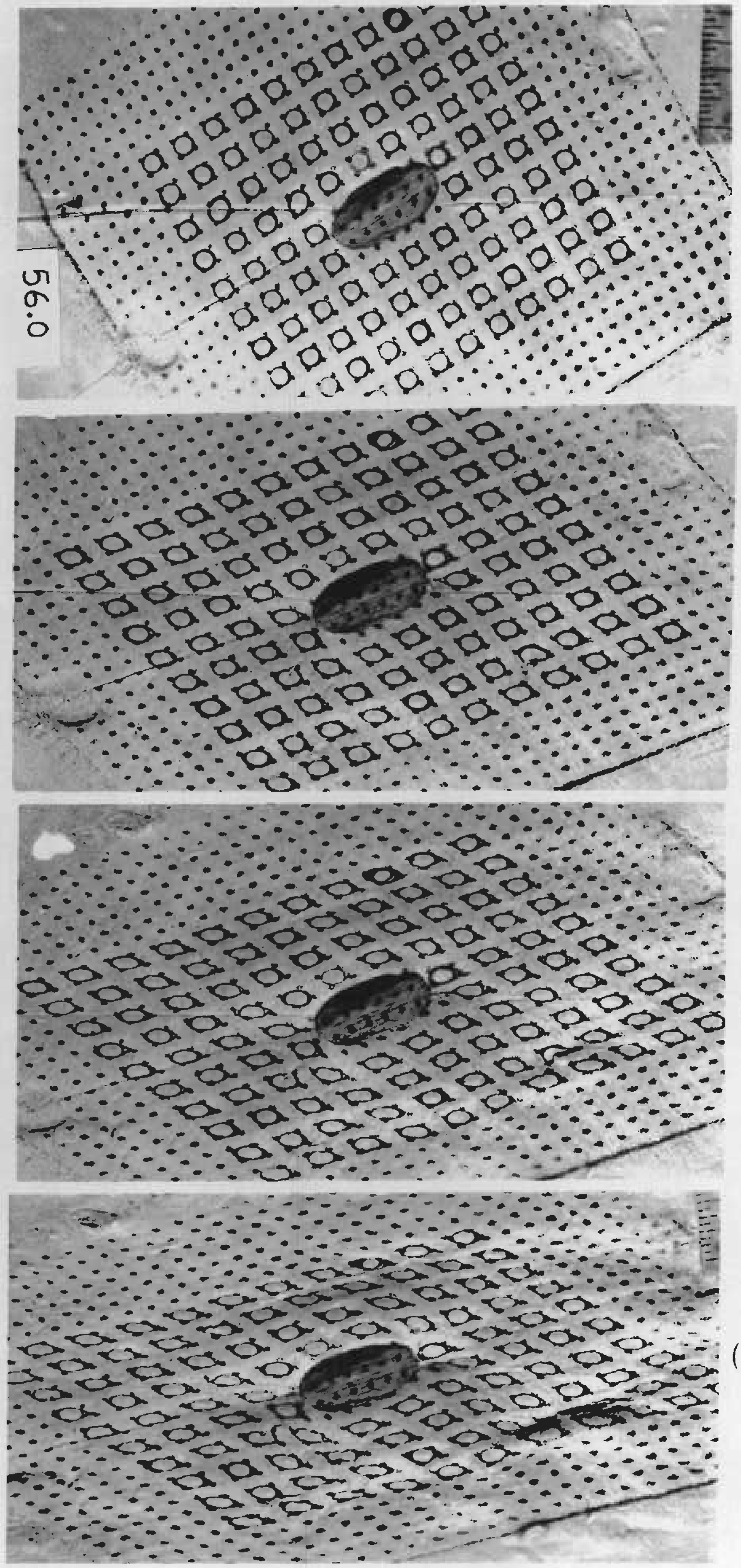

(a)

(b)

(c)

(d)

Plate VII.

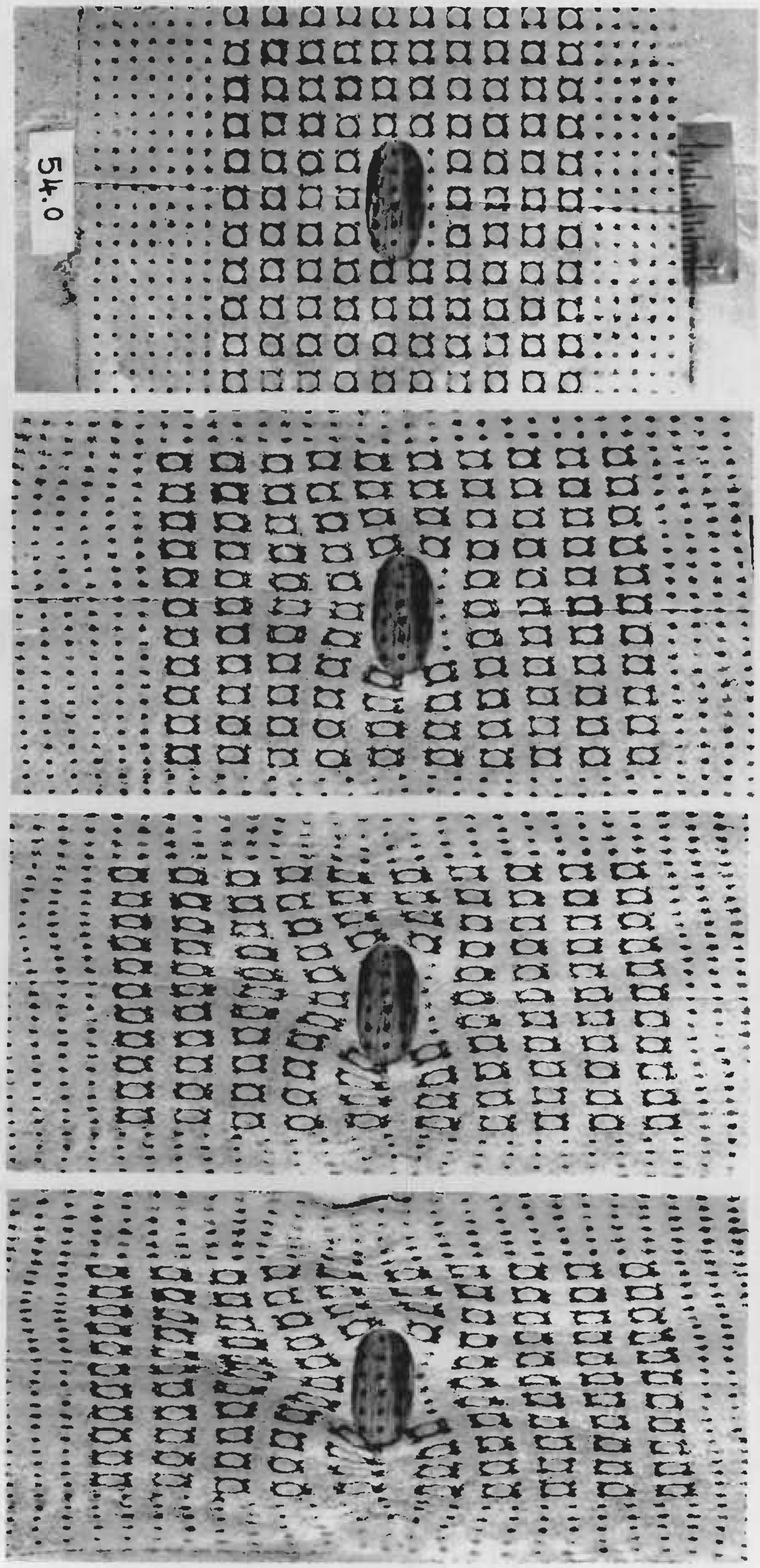

(a)

(b)

(c)

(d)

Plate VIII.

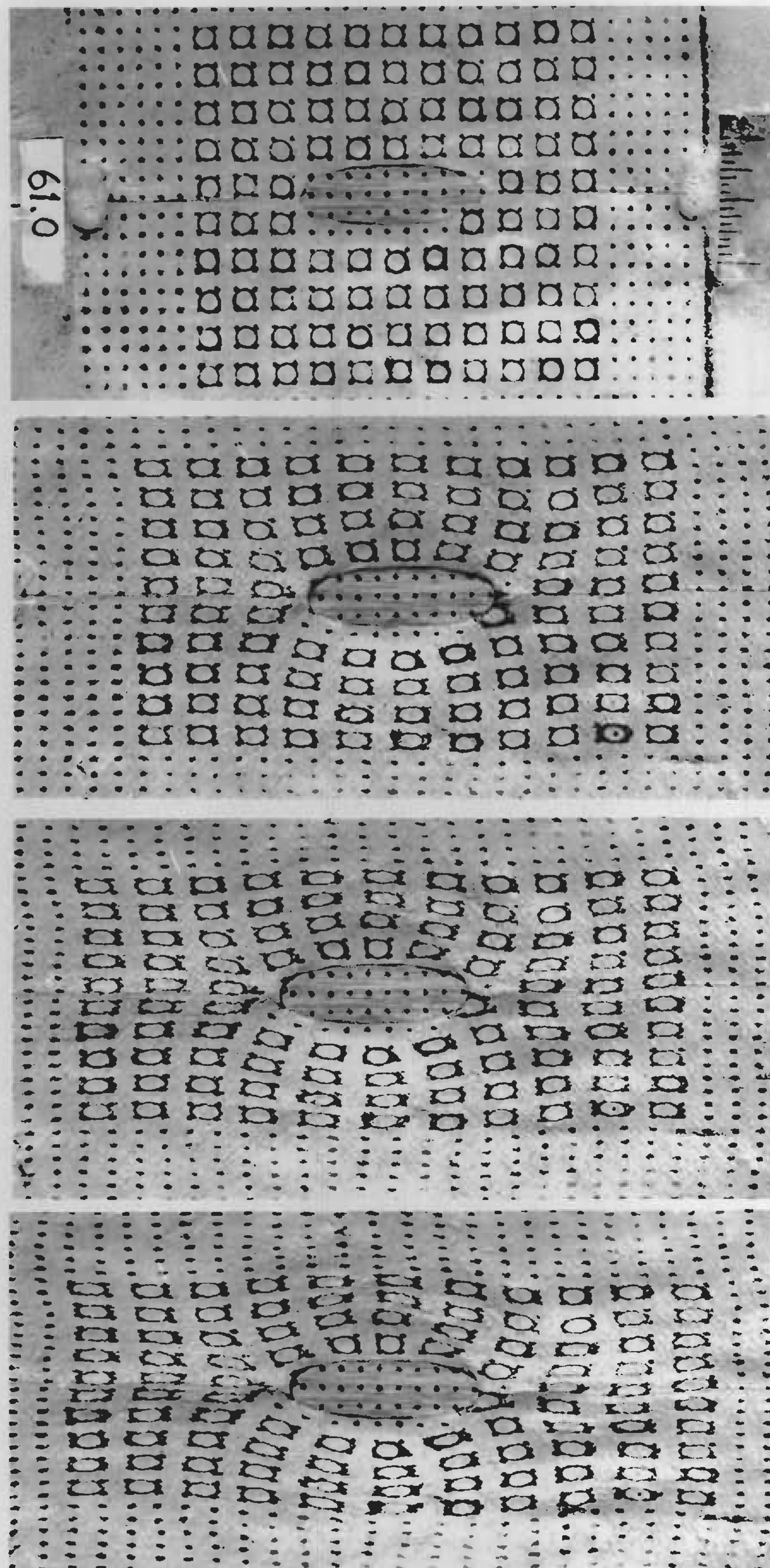

(a)

(b)

(c)

(d)

Plate IX.

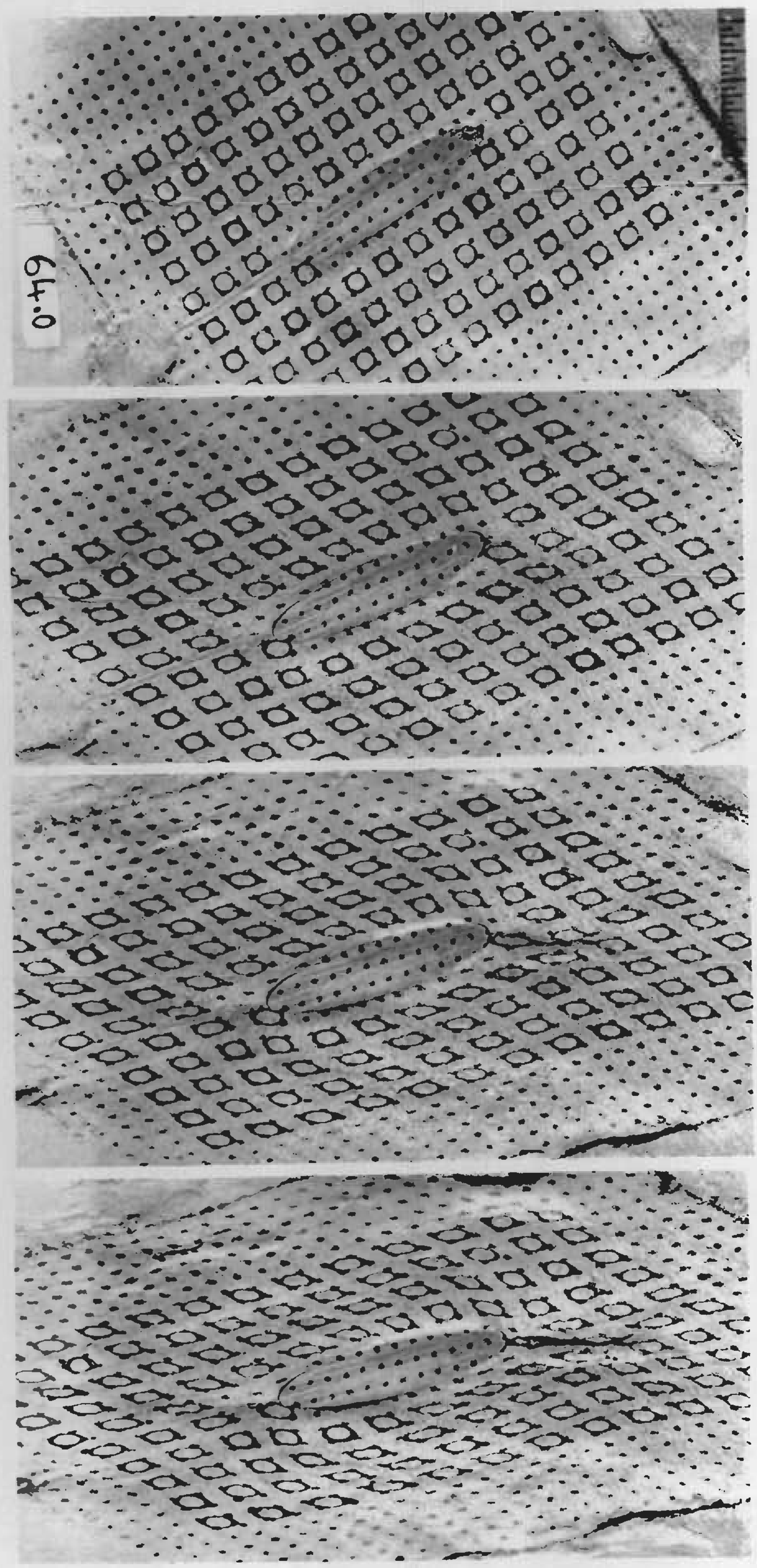

(a)

(b)

(c)

(d)

Plate X.

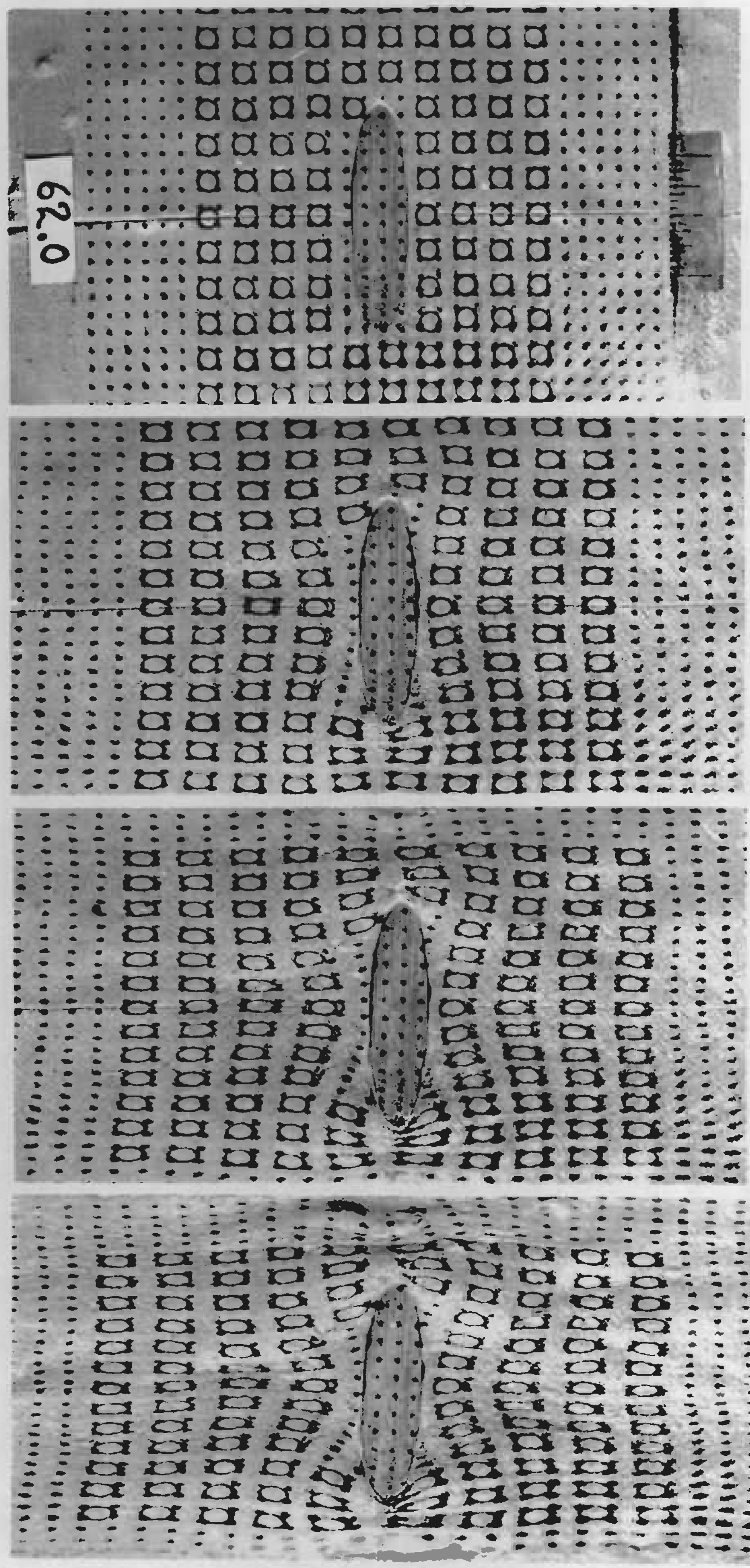

(a)

(b)

(c)

(d)

Plate XI.

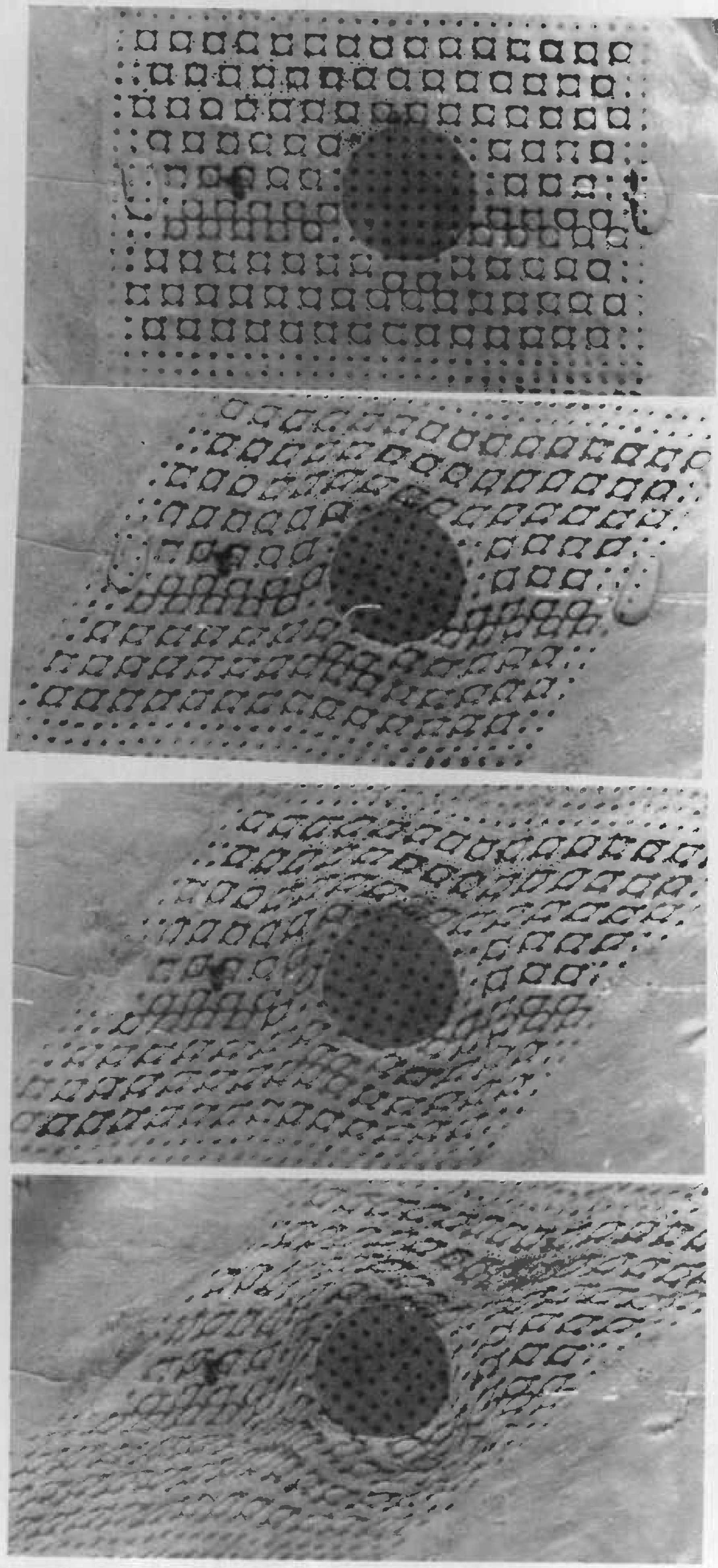

(a)

(b)

(c)

(d)

Plate XII.

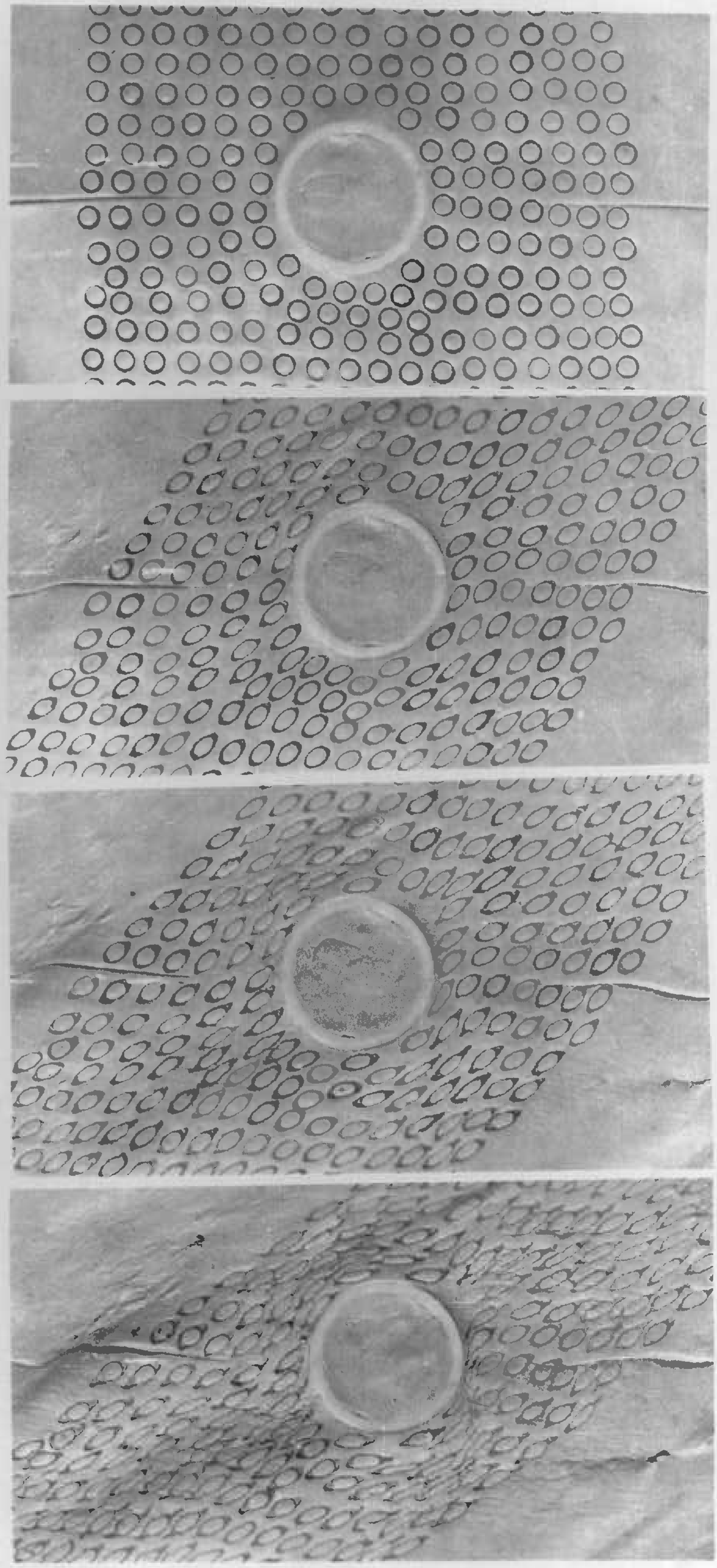

(a)

(b)

(c)

(d)

Plate XIII.

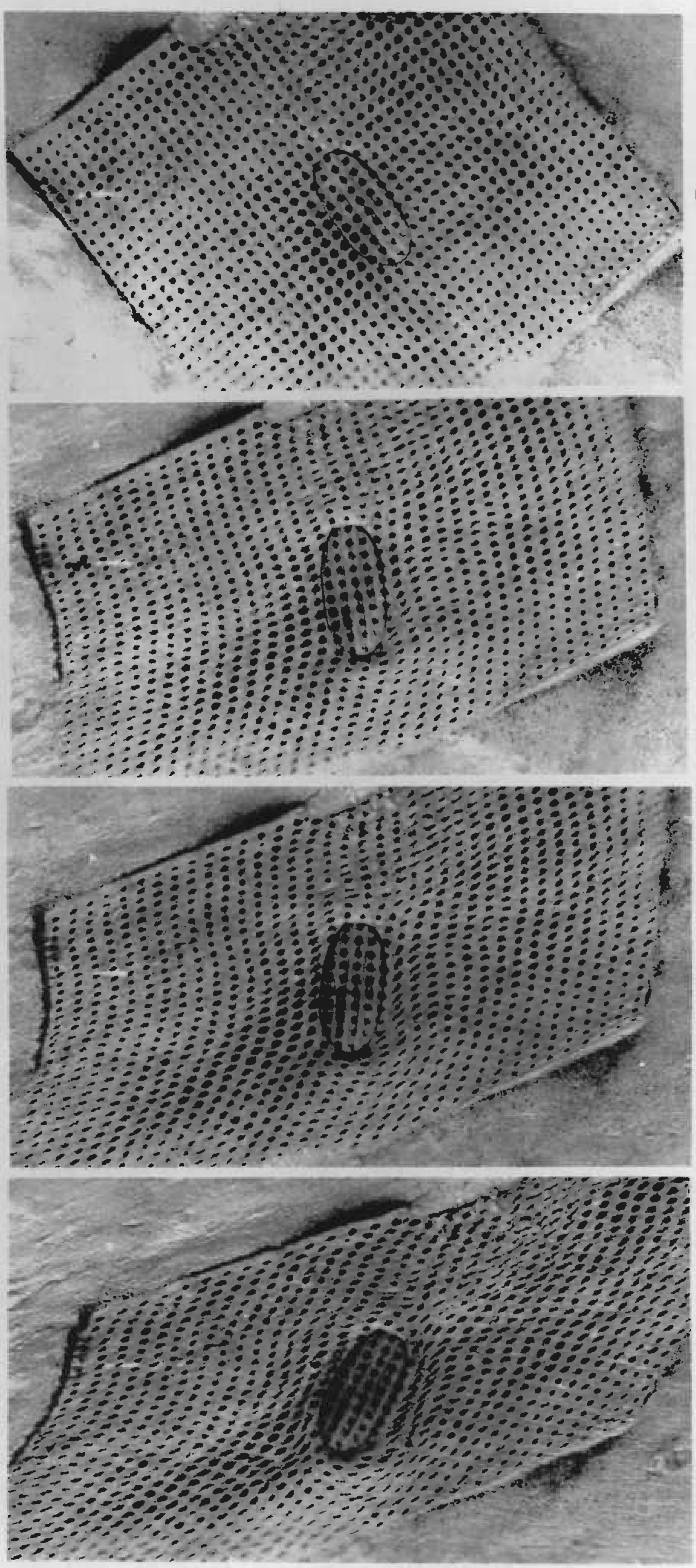

(a)

(b)

(c)

(d)

Plate XIV.

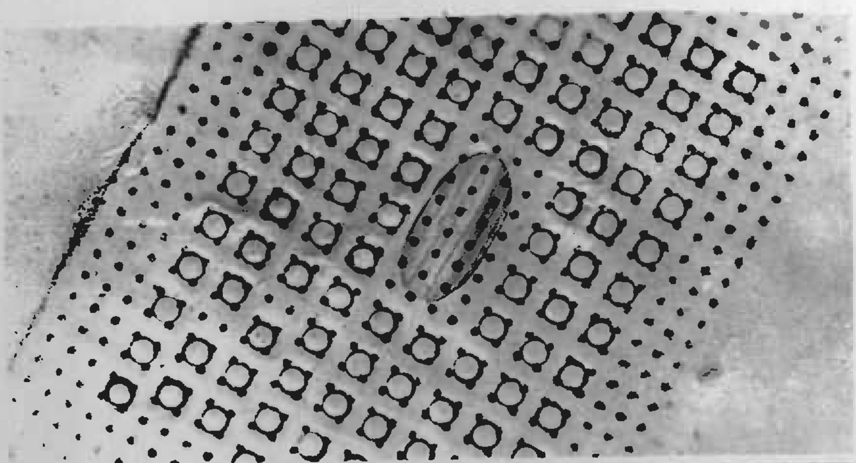

(a)

(b)

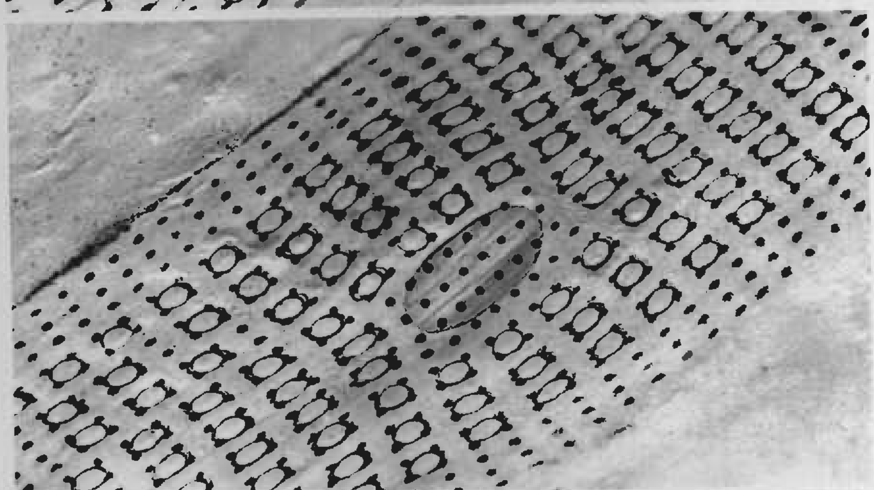

(c)

(d)

Plate XV.

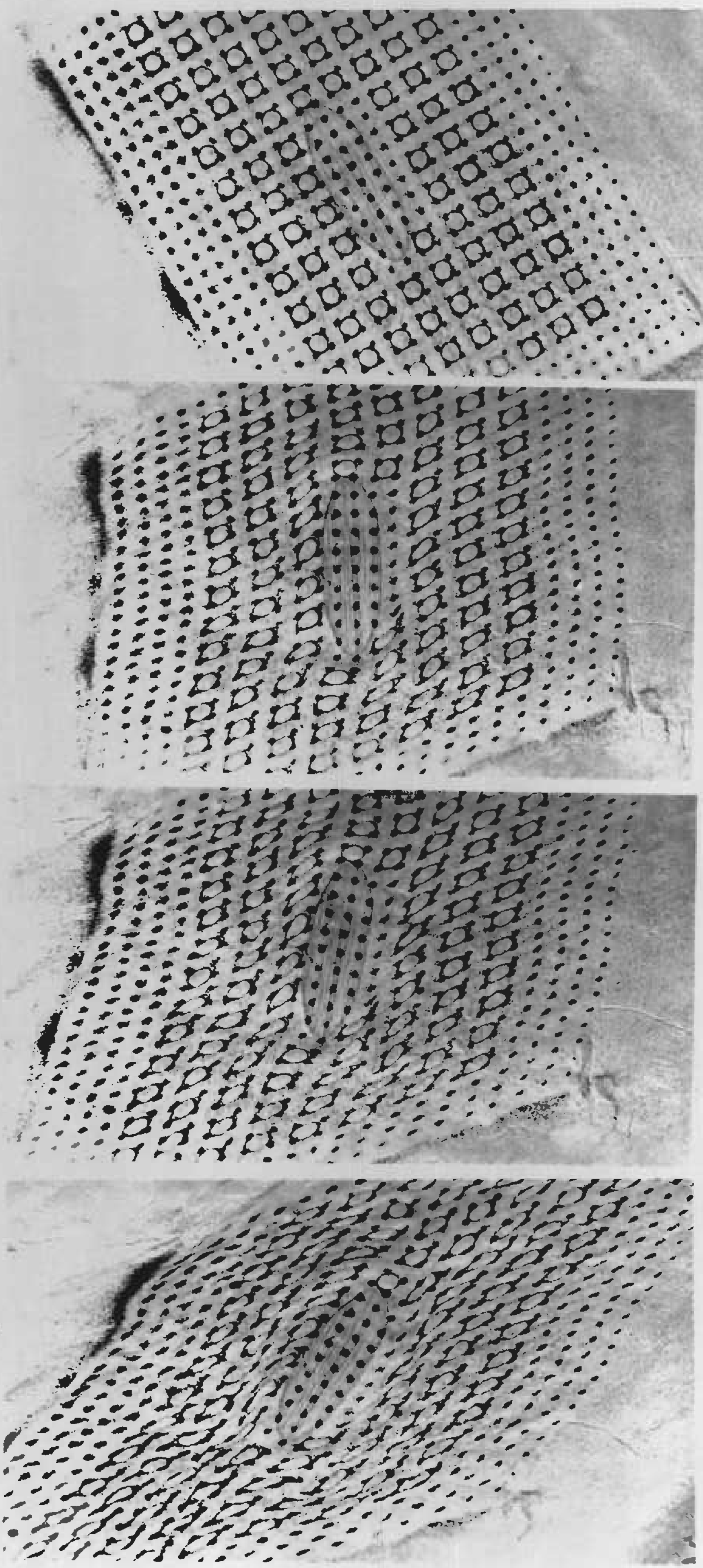

(a)

(b)

(c)

(d)

Plate XVI.

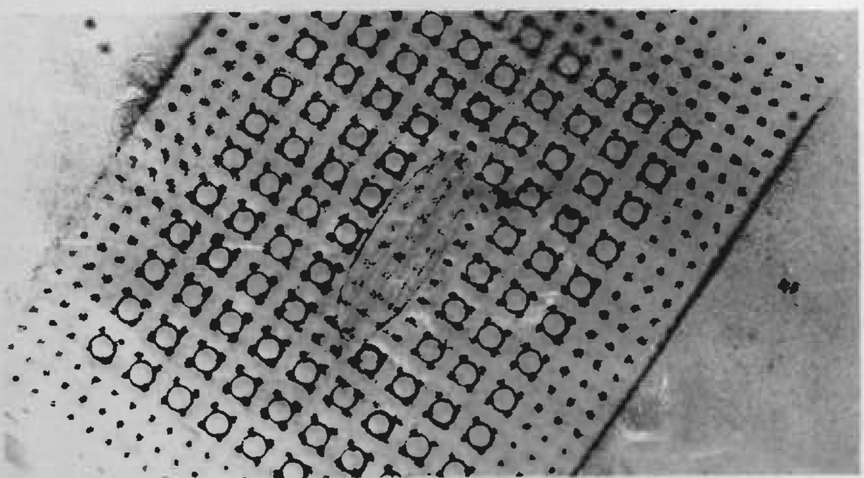

(a)

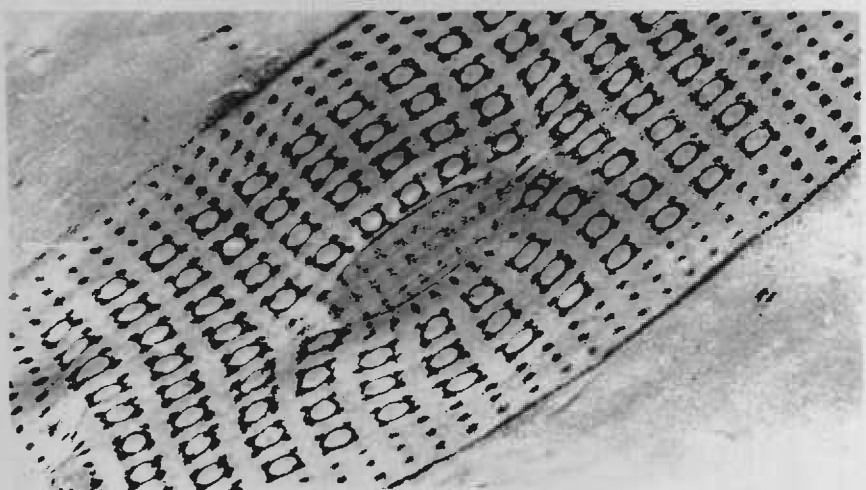

(b)

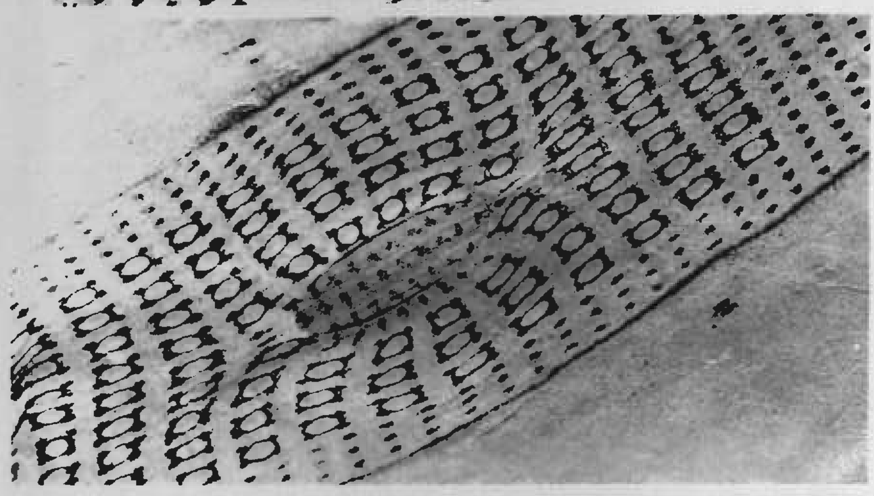

(c)

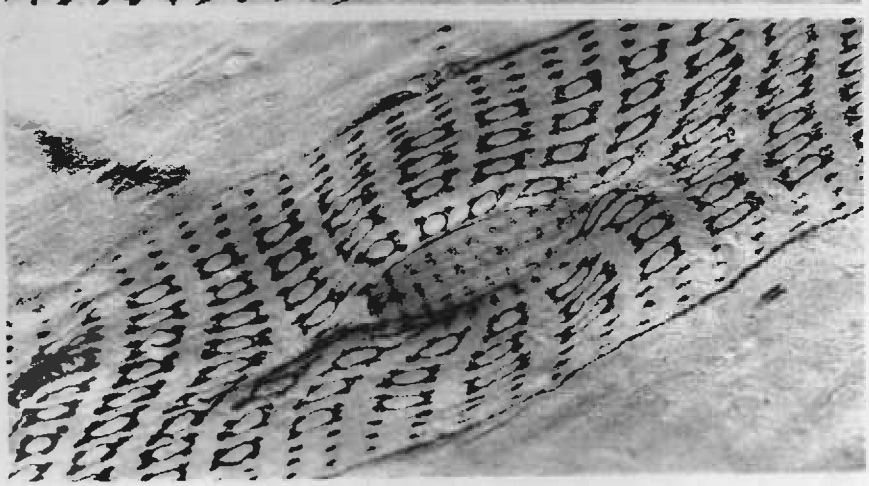

(d)

Plate XVII.

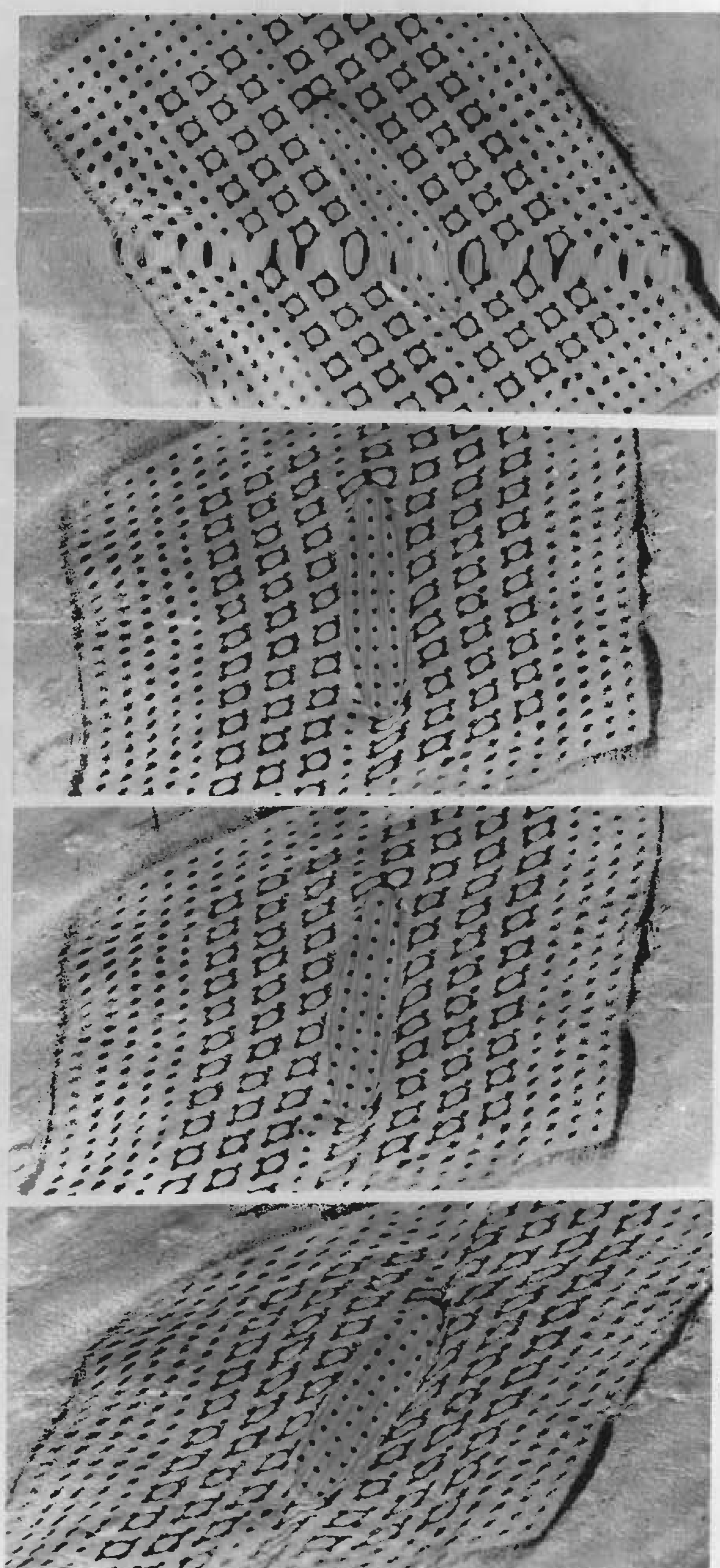

(a)

(b)

(c)

(d)

Plate XVIII

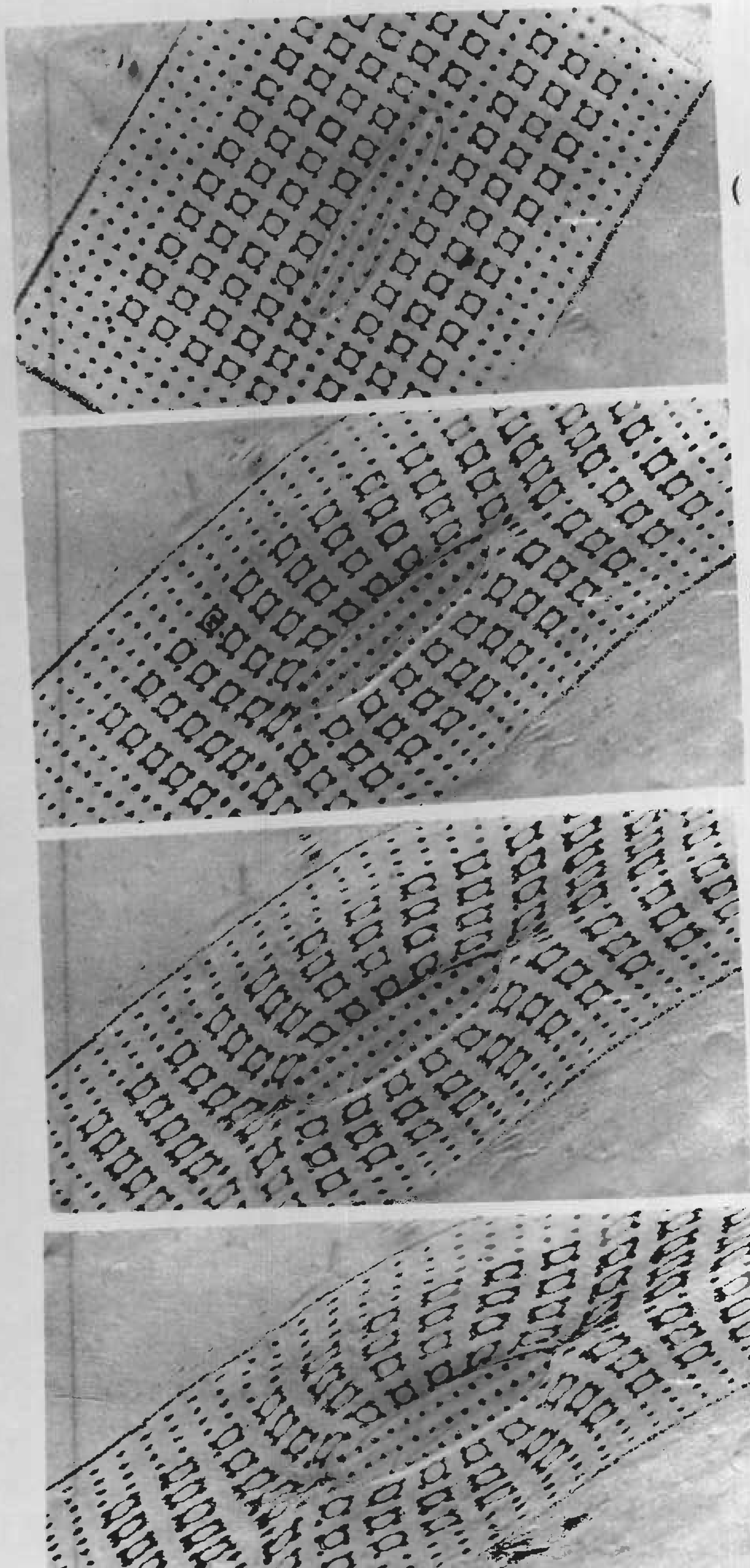

(a)

(b)

(c

(d)

Plate XIX.

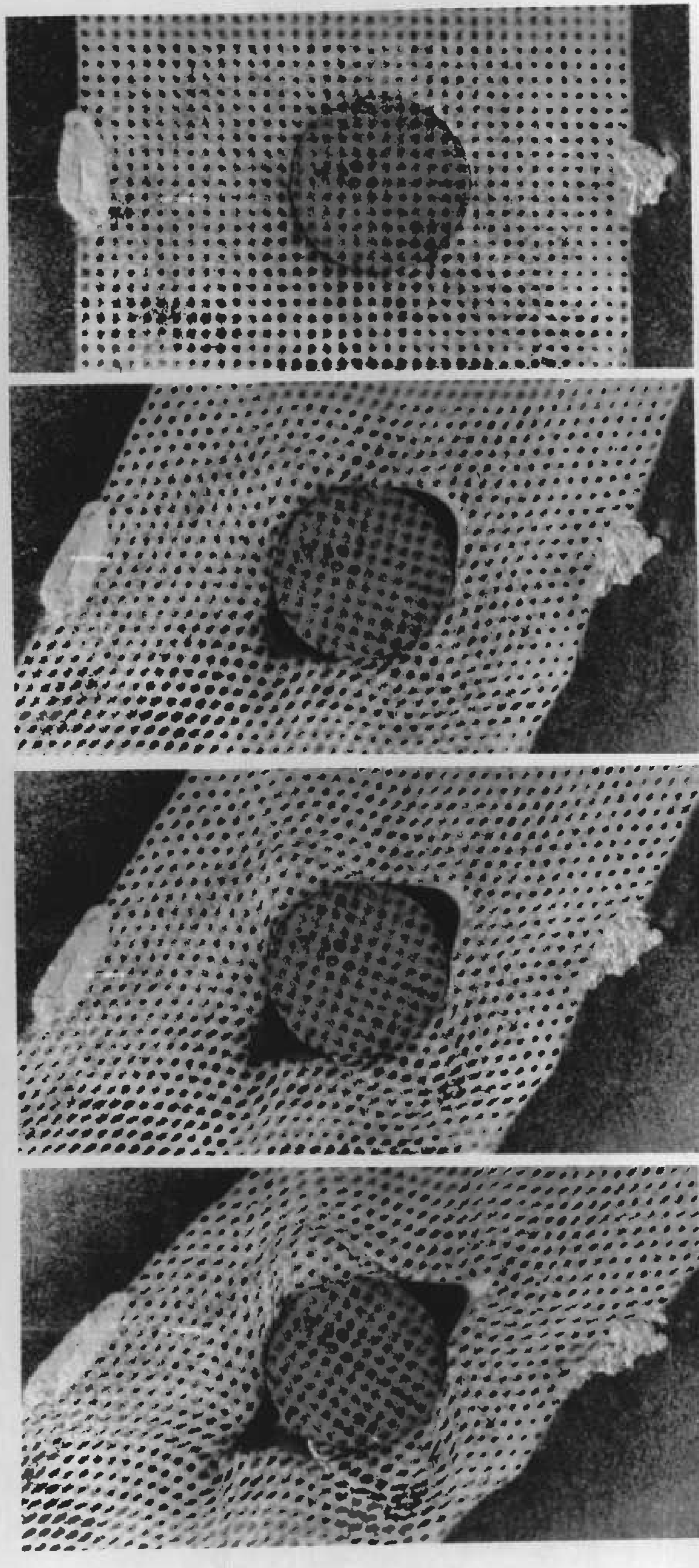

(a)

(b)

(c)

(d)

Plate XX

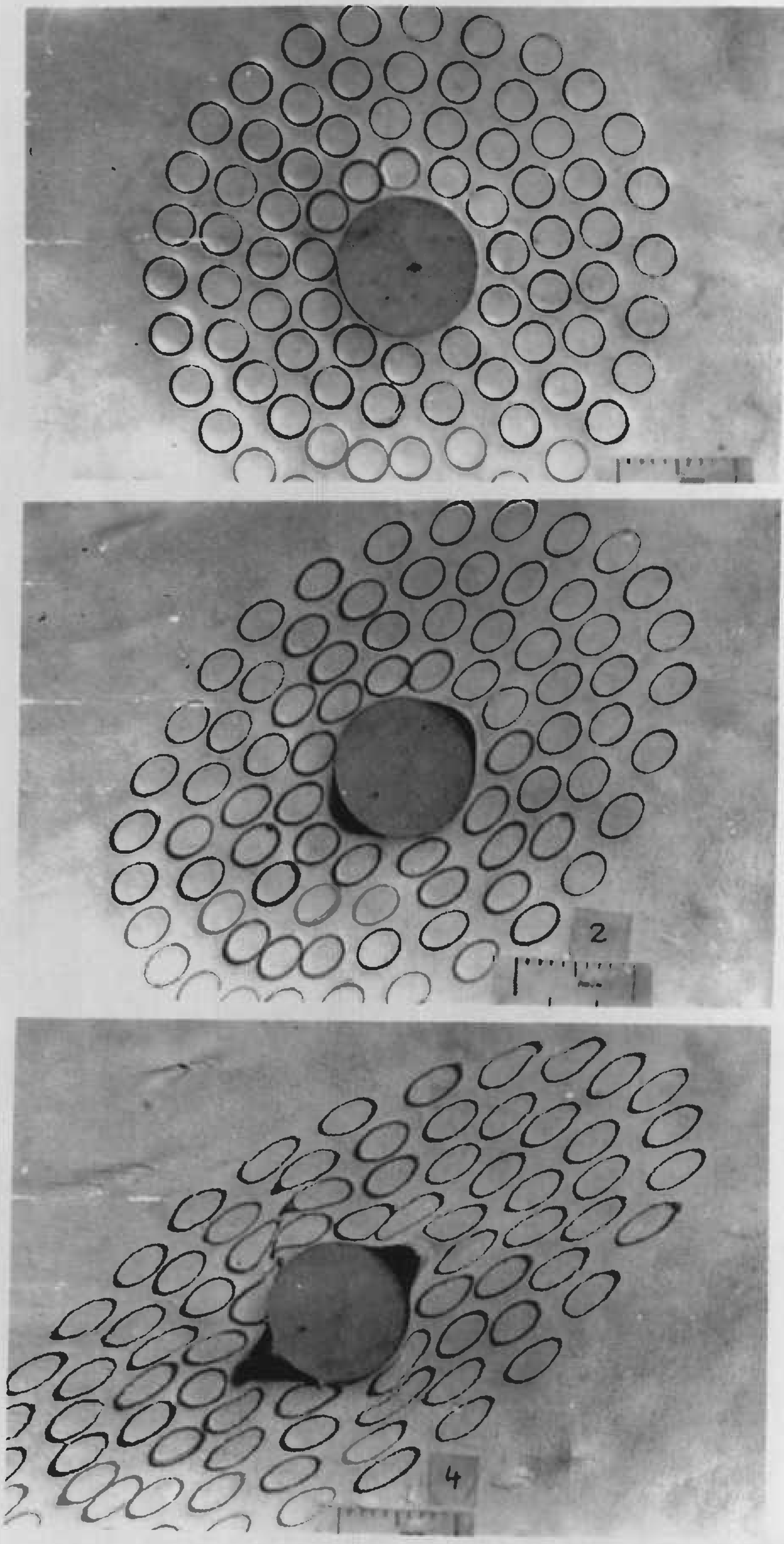

(a)

(b)

(c)

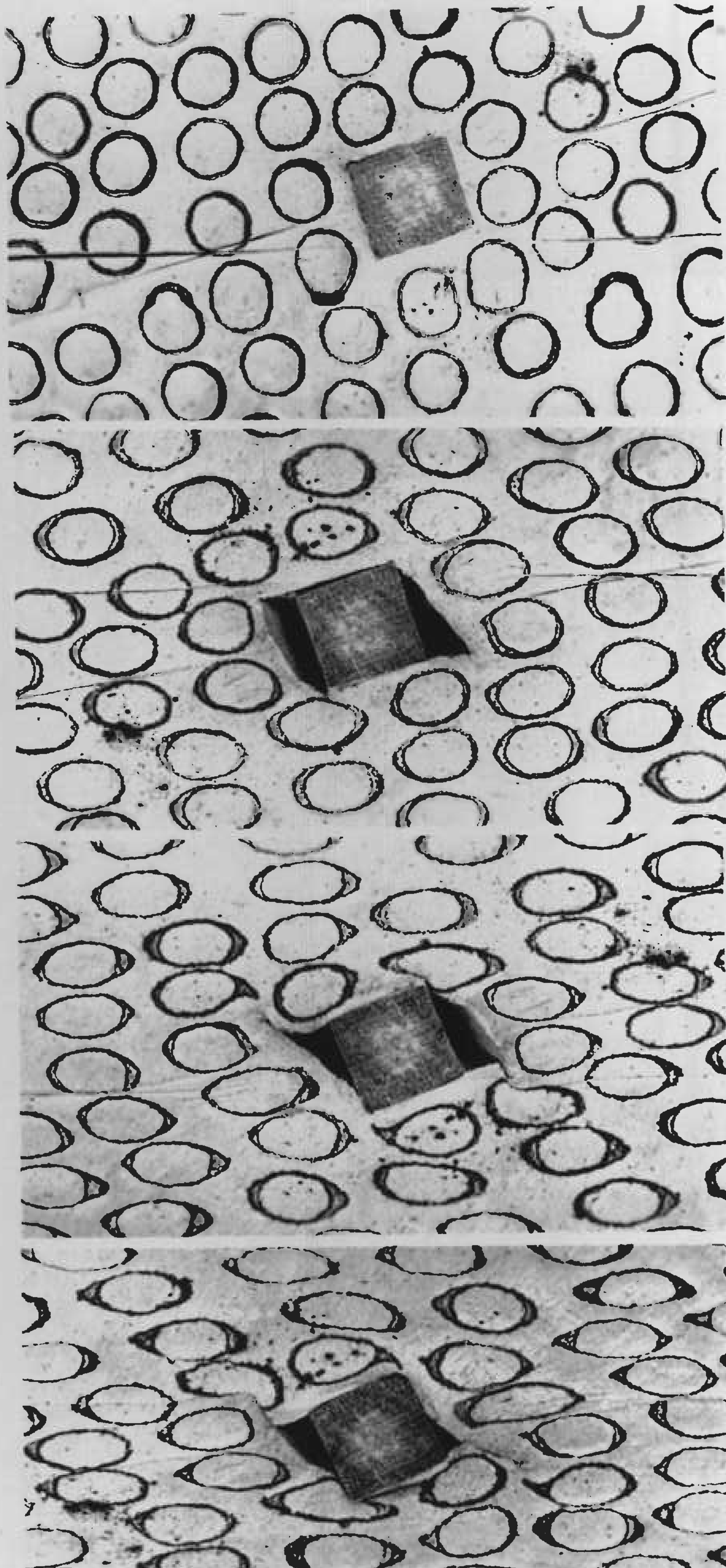

(a)

(b)

(c)

(d)

Plate XXII.

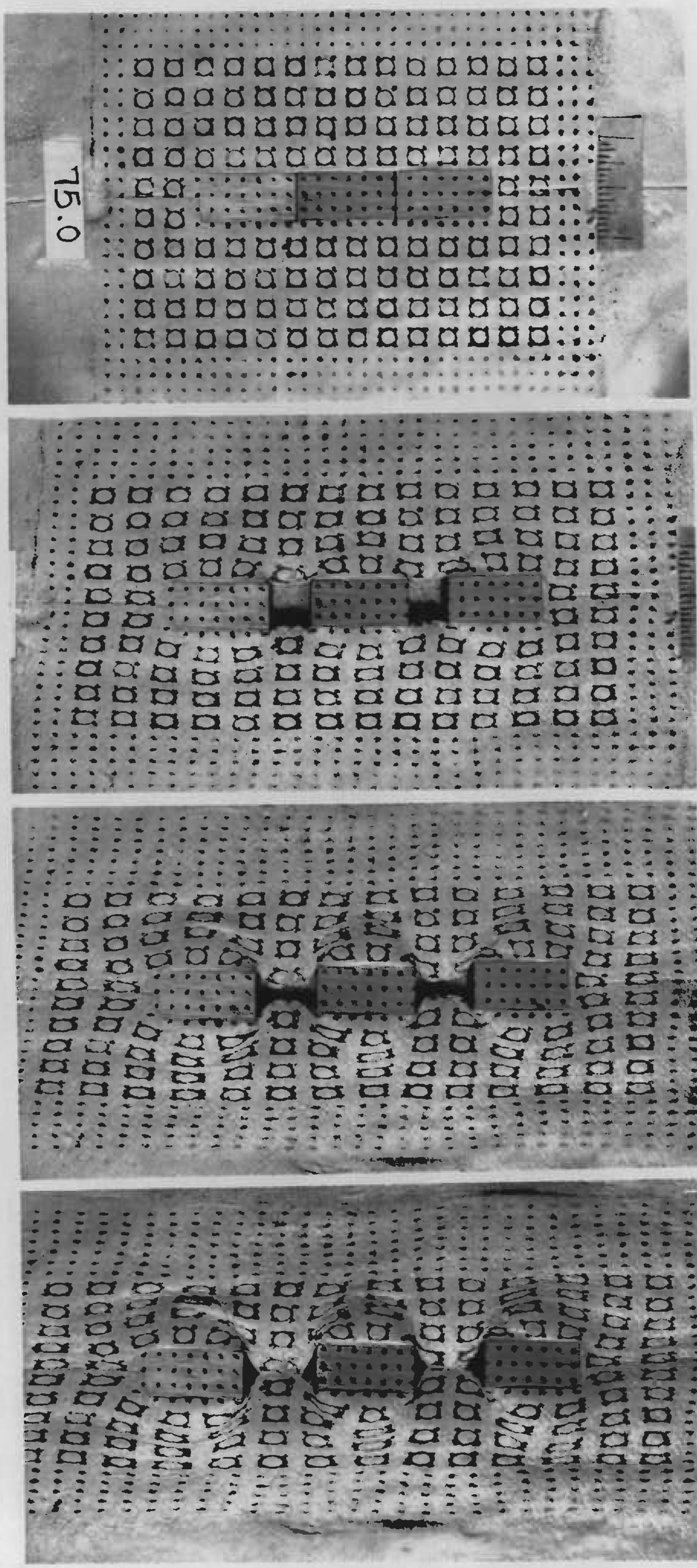

(a)

(b)

(c)

(d)

Plate XXIII

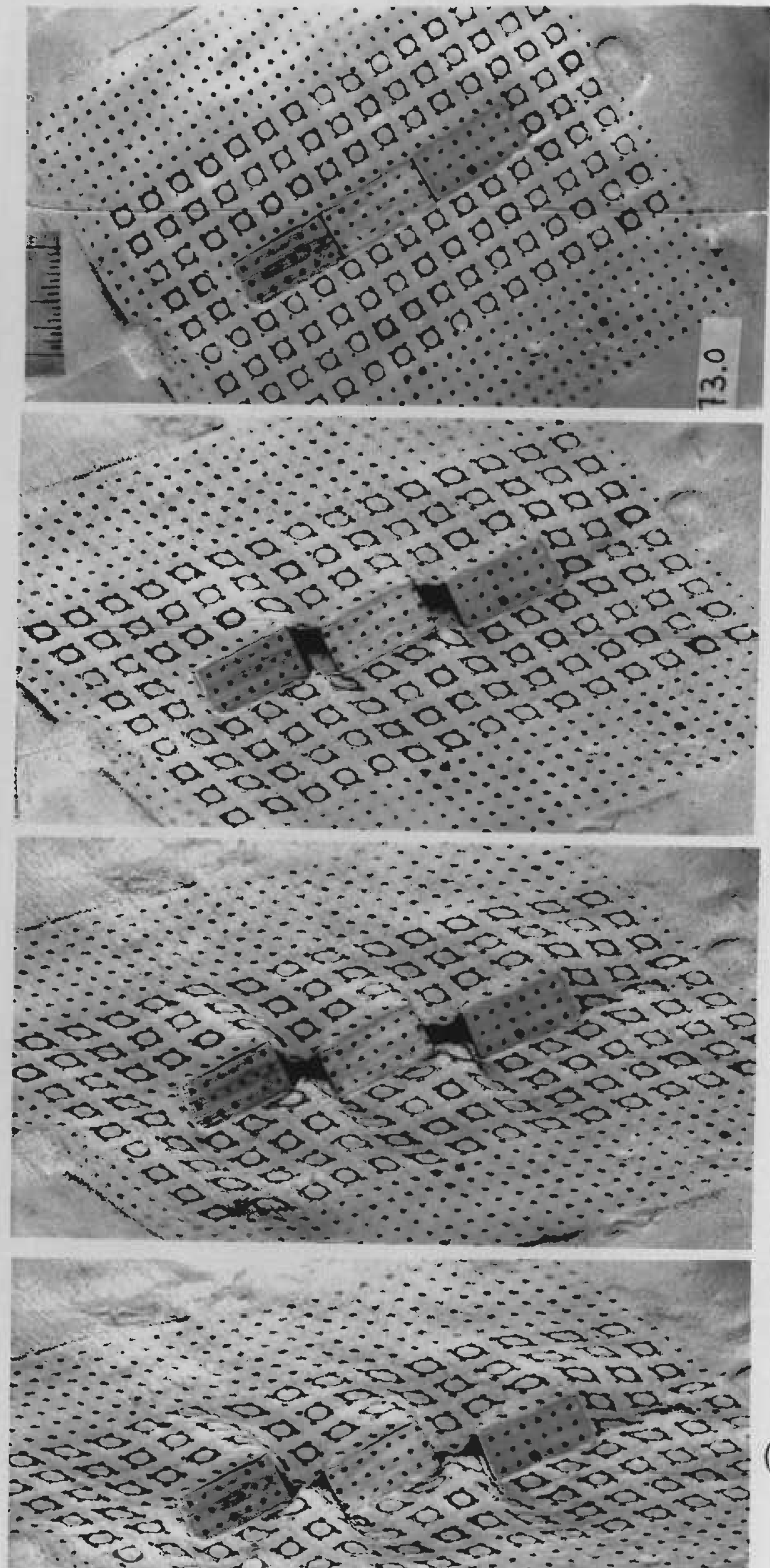

(a)

(b)

(c)

(d)

Plate XXIV.

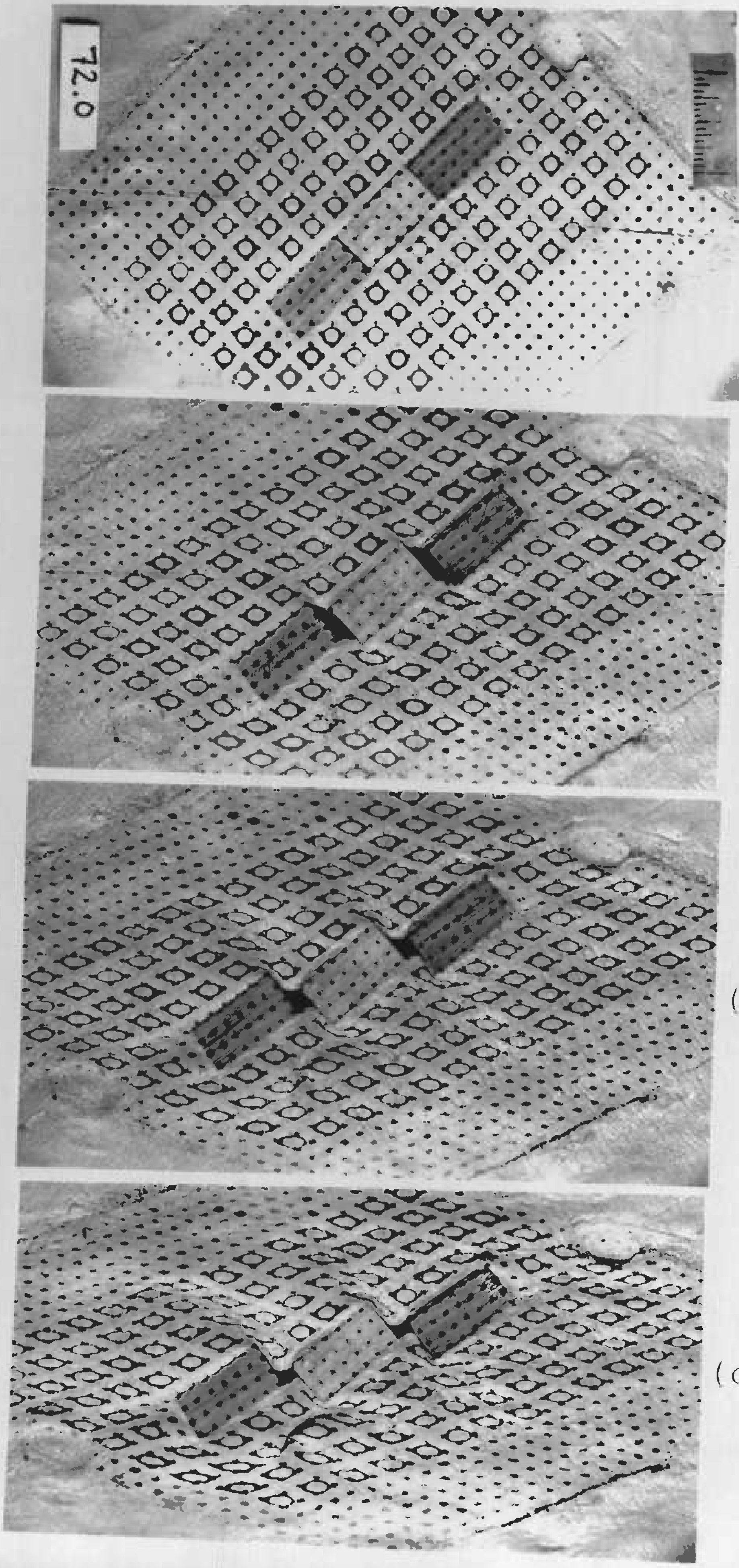

(a)

(b)

(c)

(d)

Plate XXV

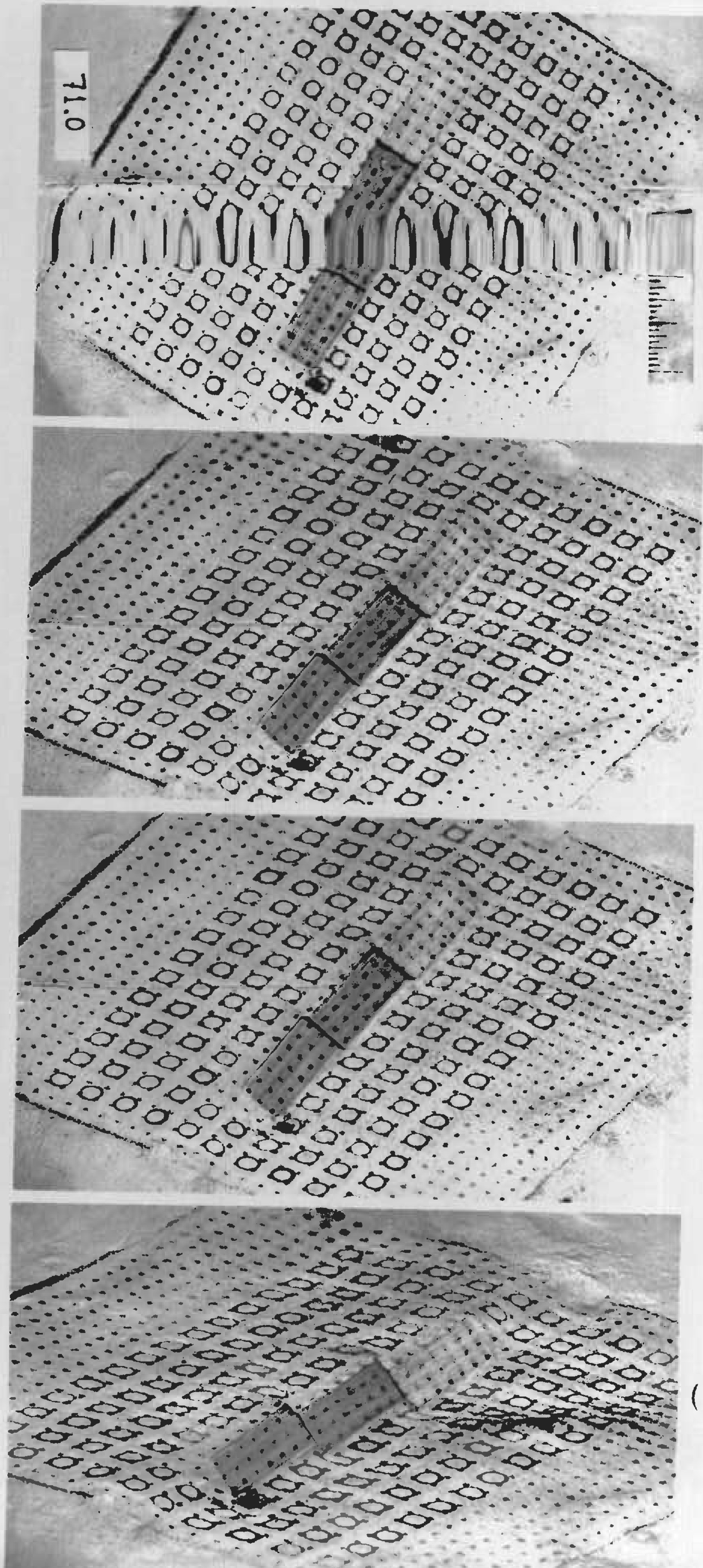

(a)

(b)

(c)

(d)

Plate XXVI

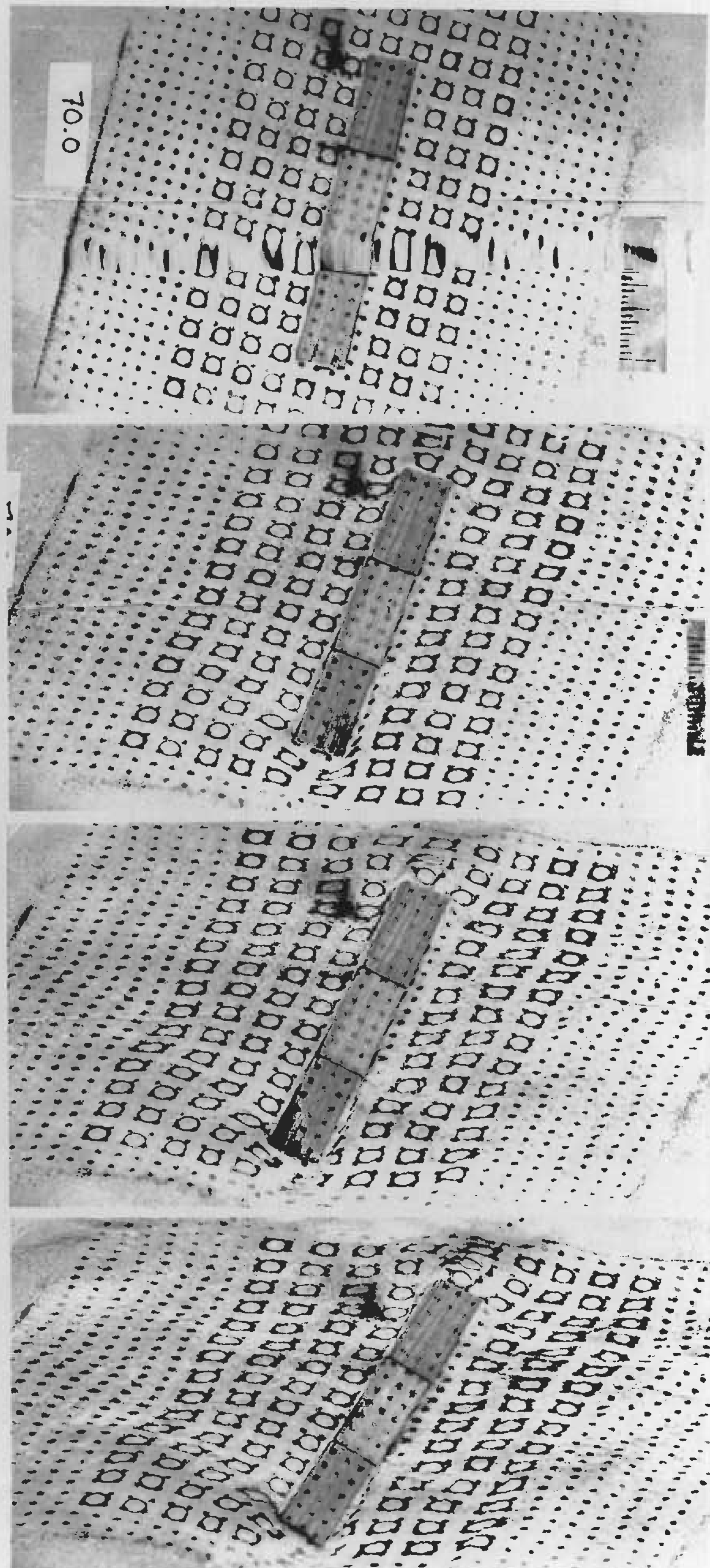

(a)

(b)

(c)

(d)

Plate XXVII

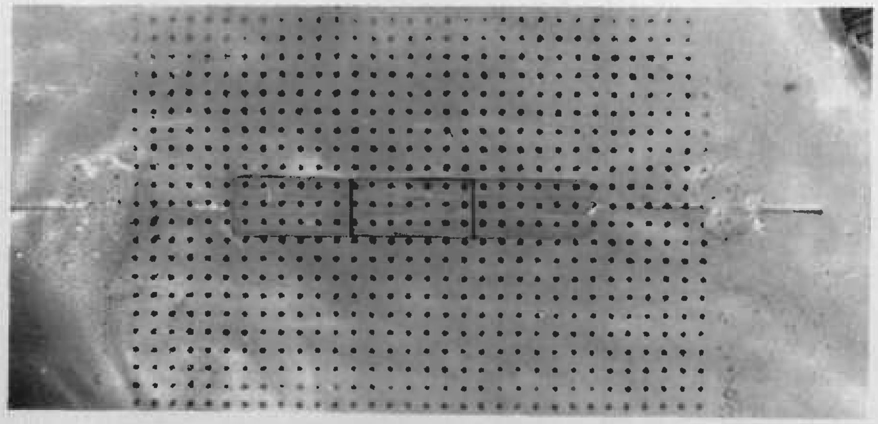

(a)

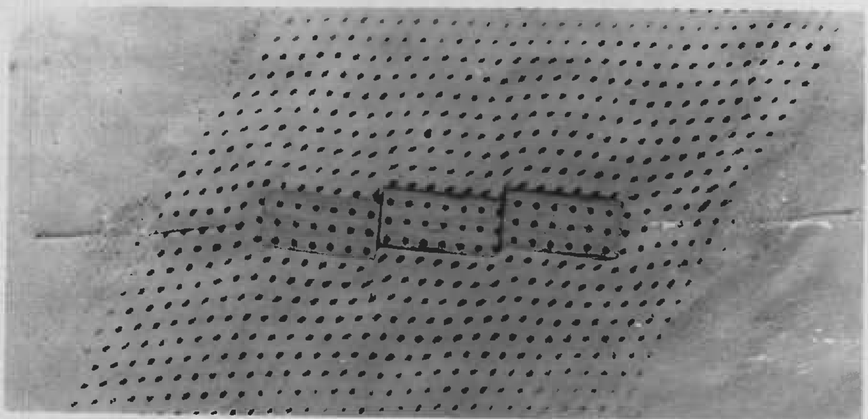

(b)

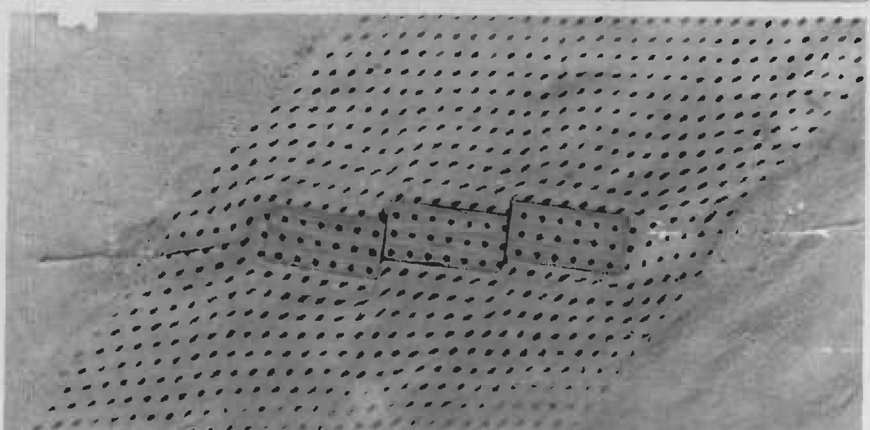

(c)

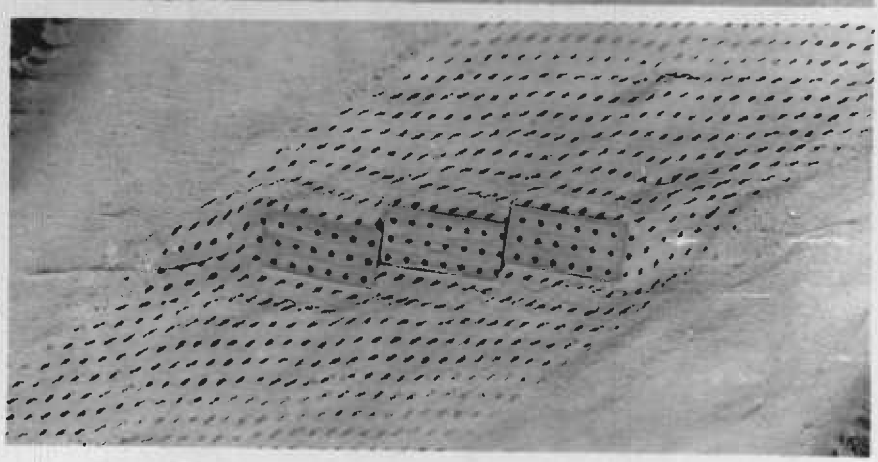

(d)

Plate XXVIII

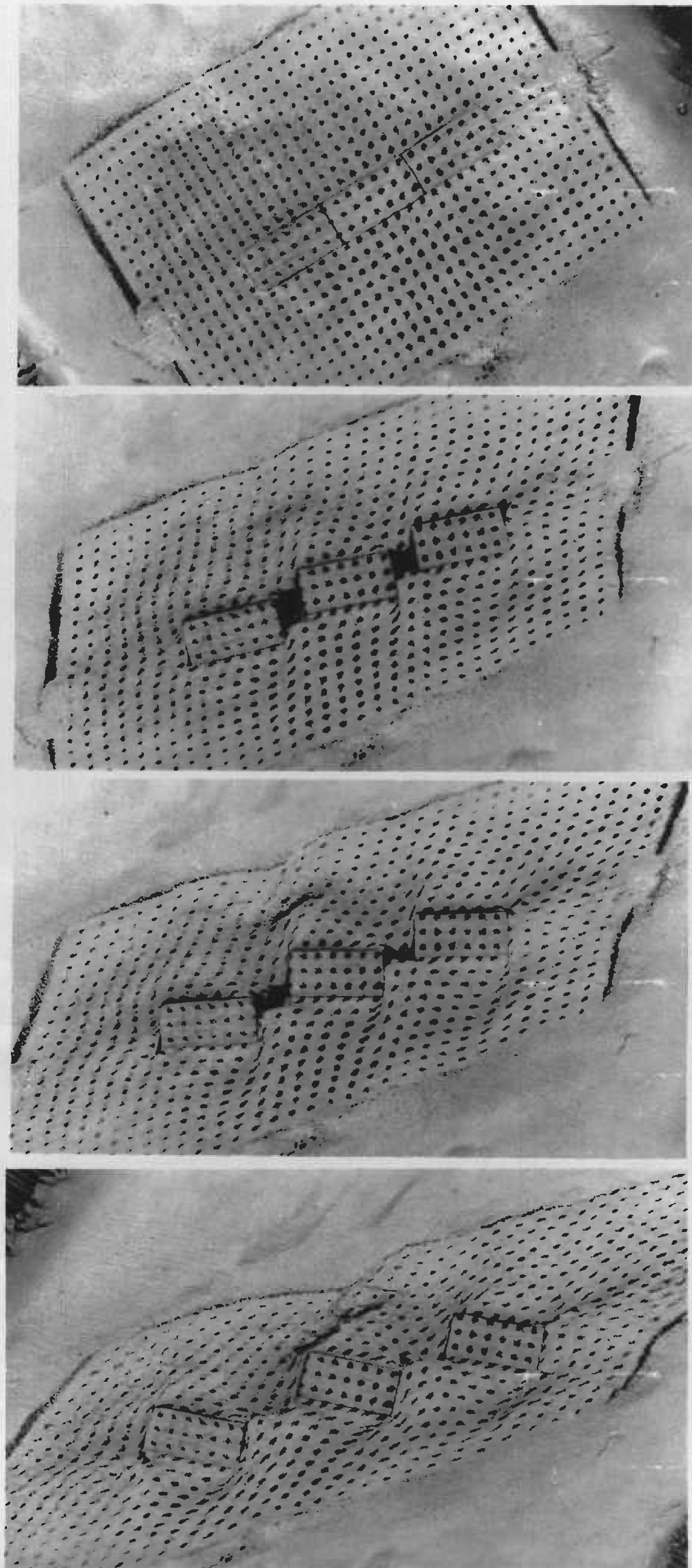

(a)

(b)

(c)

(d)

Plate XXIX

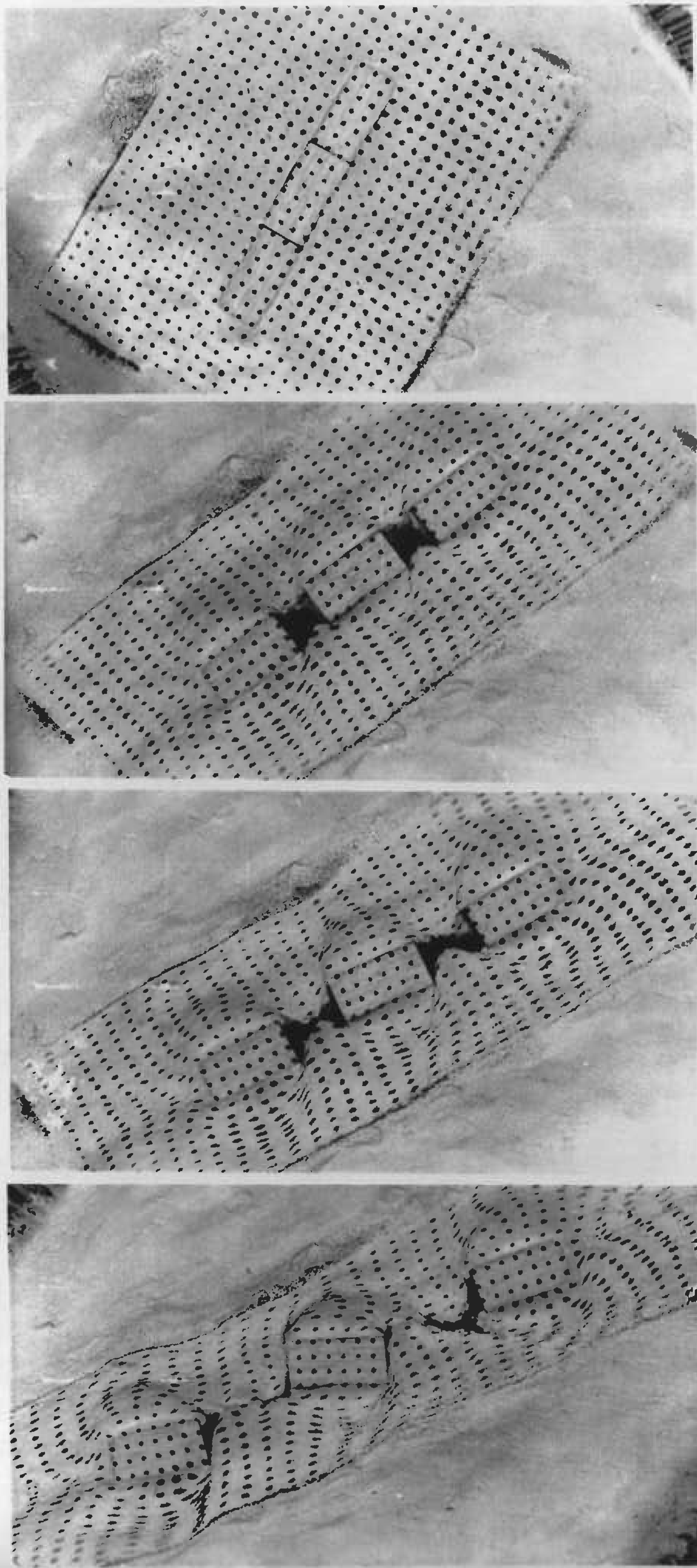

(a)

(b)

(c)

(d)

Plate XXX

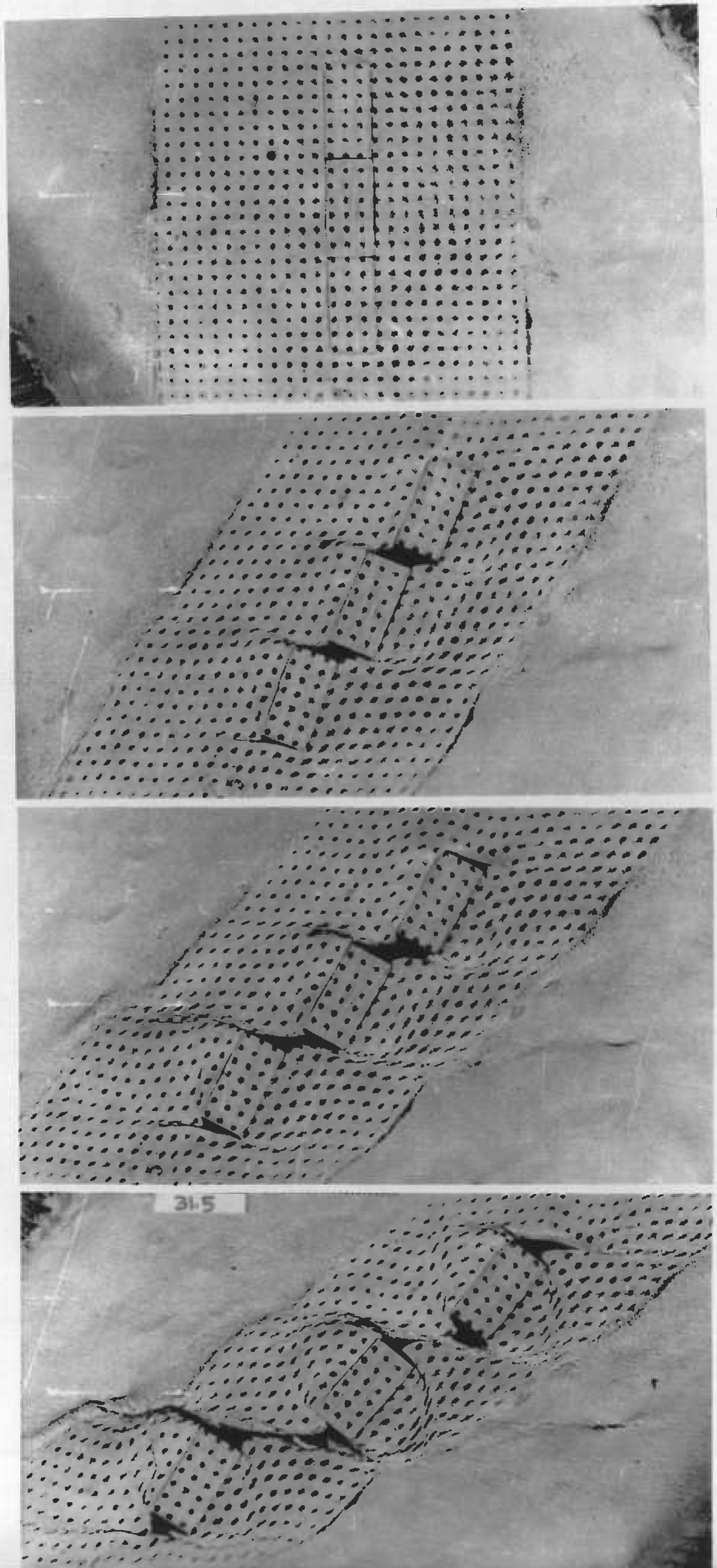

(a)

(b)

(c)

(d)

Plate XXXI.

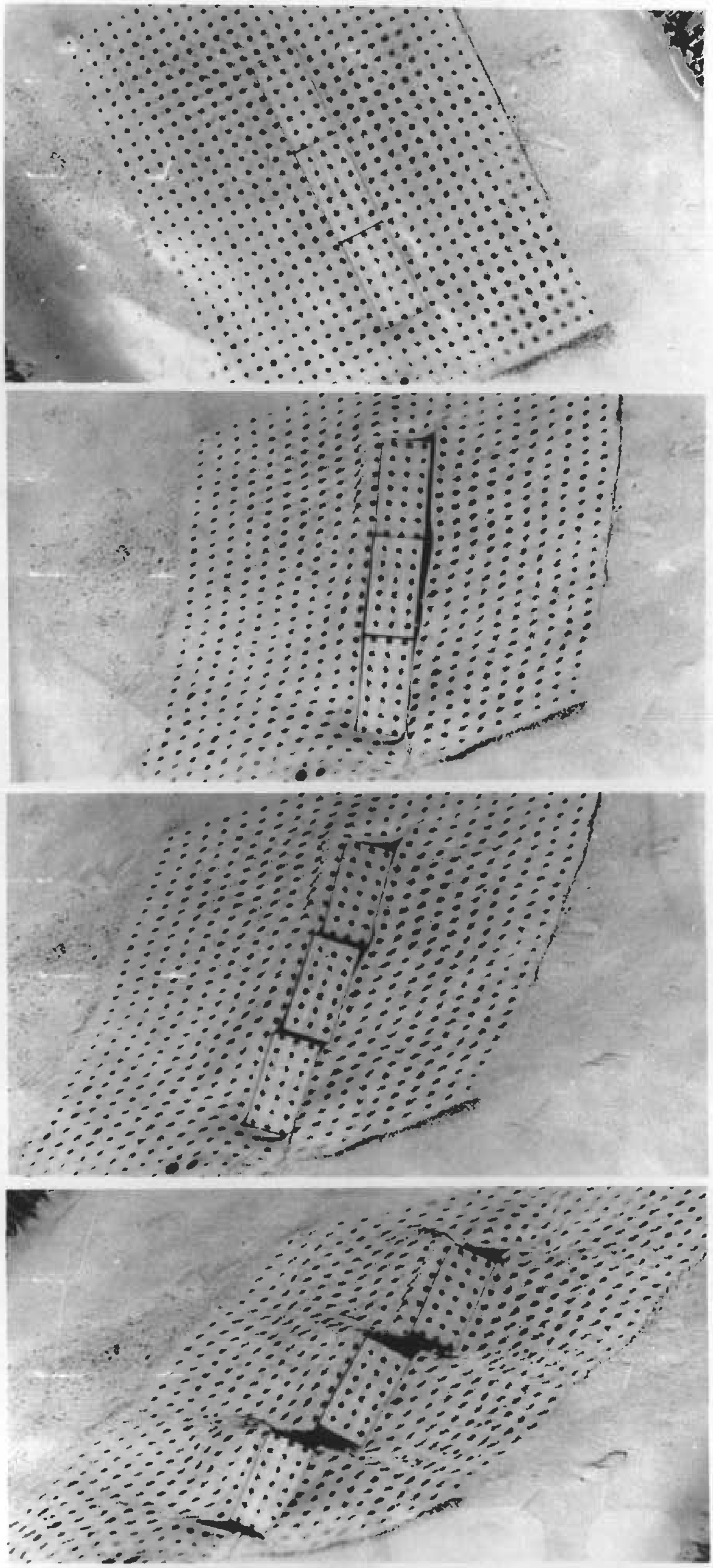

(a)

(b)

(c)

(d)

Plate XXXII

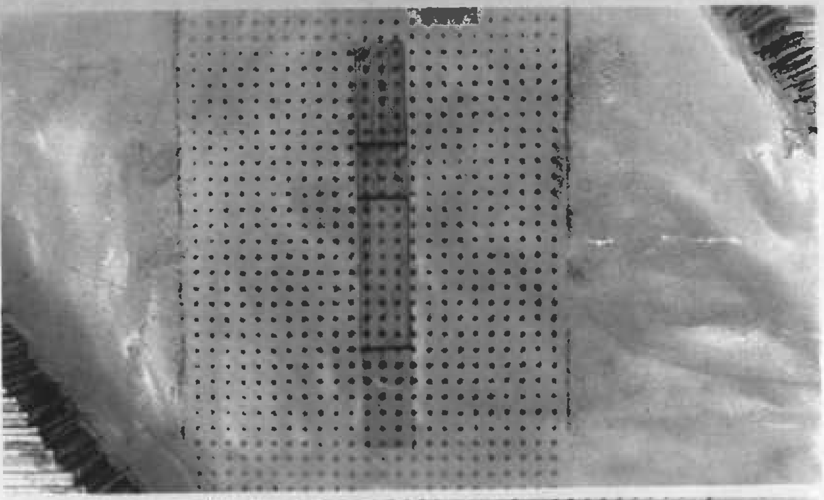

(a)

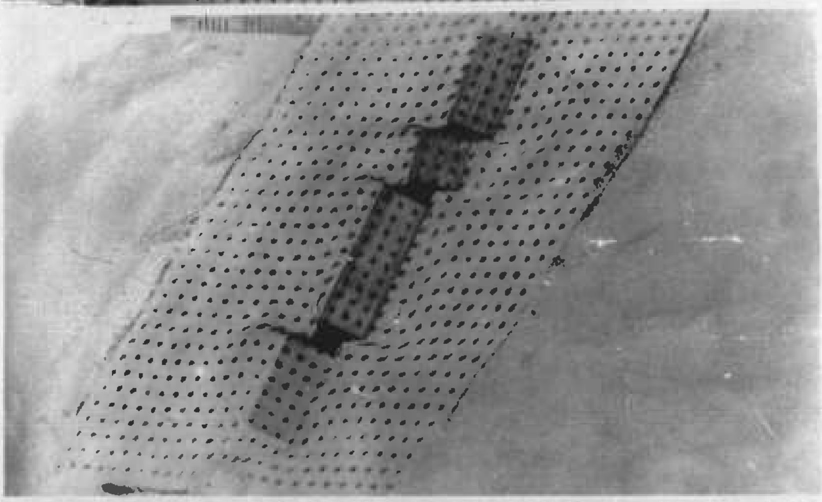

(b)

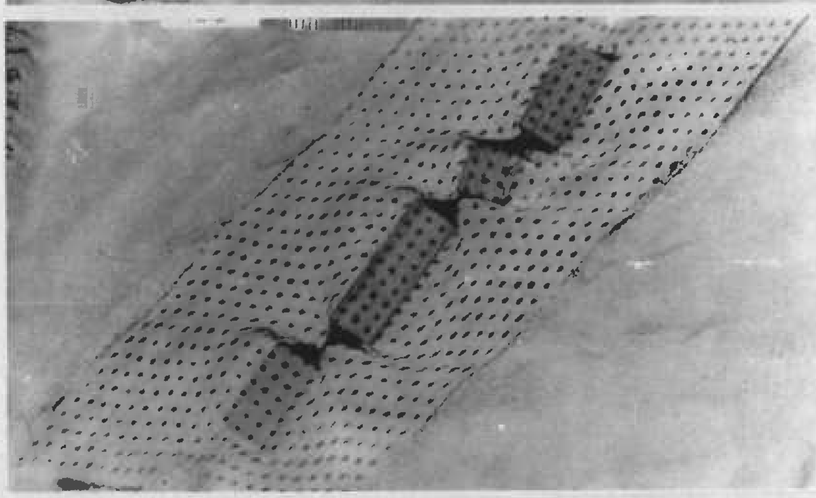

(c)

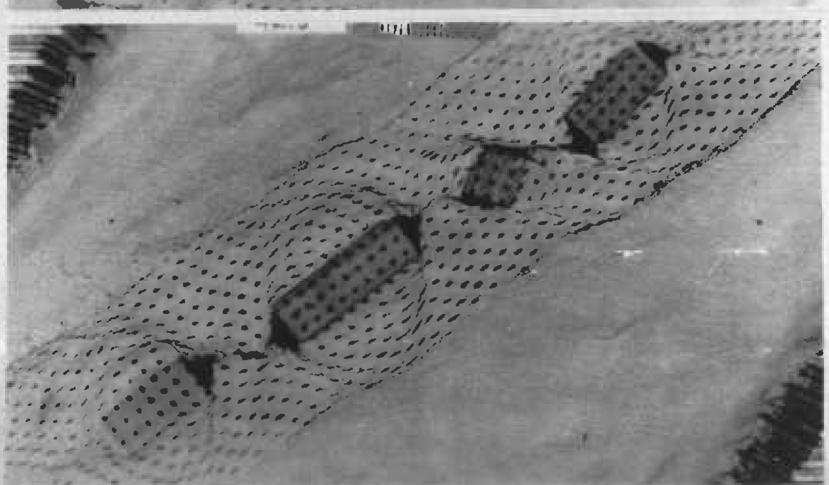

(d)